

**NEW QUANTITATIVE PHASE IMAGING MODALITIES ON
STANDARD MICROSCOPE PLATFORMS**

A Thesis
Presented to
The Academic Faculty

by

Micah H. Jenkins

In Partial Fulfillment
of the Requirements for the Degree
Doctor of Philosophy in the
School of Electrical and Computer Engineering

Georgia Institute of Technology
December 2015

Copyright © 2015 by Micah H. Jenkins

NEW QUANTITATIVE PHASE IMAGING MODALITIES ON STANDARD MICROSCOPE PLATFORMS

Approved by:

Professor Thomas K. Gaylord,
Advisor, Committee Chair
School of Electrical and Computer
Engineering
Georgia Institute of Technology

Professor John A. Buck
School of Electrical and Computer
Engineering
Georgia Institute of Technology

Dr. Donald D. Davis
School of Electrical and Computer
Engineering
Georgia Institute of Technology

Professor Gee-Kung Chang
School of Electrical and Computer
Engineering
Georgia Institute of Technology

Professor Phillip First
School of Physics
Georgia Institute of Technology

Dr. Sorin Tibuleac
ADVA Optical Networking

Date Approved: 9 November 2015

ACKNOWLEDGEMENTS

The work documented in this thesis would not have been possible without the support and encouragement of family, friends, and colleagues during my time at Georgia Tech.

My wife, Sarah, has been a light in my life. She has helped me to improve in many ways and has helped me focus on what matters most in life. Her commitment and support have perhaps been most evident in her role as a mother and caretaker to our beautiful daughters, Natalie and Angela, whom she consistently influences for the better. She is the love of my life and continuously provides me with the motivation to achieve more. I look forward to spending an eternity with her by my side.

I thank my parents, Martin and Charlotte, for providing encouragement and direction throughout my life. They encouraged my interest in math and science from a very young age, which led me to engineering as a field of study. My parents were especially supportive of my wrestling career in high school. Through wrestling, I learned the importance of hard work and setting goals, which has blessed me throughout my life and helped me to complete this degree.

It has been a true honor to have Dr. Tom Gaylord as an advisor. In addition to his role as a technical advisor and major contributor to this work, he has been a mentor, role model, and friend throughout my time at Georgia. I will forever benefit from the emphasis on technical communication which he continuously fosters and is greatly needed in the world in which we find ourselves. Lastly, I thank Dr. Gaylord for his constant positive attitude and for believing in me when I doubted myself.

I thank my committee members, Dr. John Buck, Dr. Don Davis, Dr. Gee-Kung Chang, Dr. Phillip First, and Dr. Sorin Tibuleac, for the great interest and support they showed in this work and the time they took to discuss it in great detail.

The Optics Lab has been an ideal environment for graduate school. I appreciate all of the helpful associations and interactions which it has enabled throughout my time at Georgia Tech. This work is only a building block on the previous efforts put forth by Dr. Mike Hutsel, who in addition to providing an excellent base off of which to build, has also been a mentor and a friend. I also acknowledge Dr. Matthieu Leibovici, who has contributed greatly to the presentation of these difficult concepts and with whom it has been a pleasure to work and associate with. I also thank those who have graduated during my time in the Optics Lab for their examples and mentorship, including Dr. Chien-I Lin, Dr. Matt Burrow, Dr. Jon Maikisch, and Don Sedivi. In addition, those who I had the opportunity to work with personally were especially helpful, including Dr. Ting Feng, Pengfei Wang, Joshua Long, Austin Sutlief, and Yijun Bao.

I am also grateful for Dr. Stephen Goldman and Dr. Timothy Kassis for their help with securing the experimental results on live cells. Their knowledge and expertise were absolutely critical in this regard.

Lastly, I thank my Father in Heaven for His grace and unconditional love which has sustained me throughout my life. Of myself, I can do nothing, but by trusting in Him, I can all things according to His will.

MICAH H. JENKINS

Georgia Institute of Technology

November 2015

TABLE OF CONTENTS

	Page
ACKNOWLEDGEMENTS	iii
LIST OF TABLES	x
LIST OF FIGURES	xi
LIST OF SYMBOLS	xvi
LIST OF ABBREVIATIONS	xxv
SUMMARY	xxix
1 INTRODUCTION	1
1.1 Background.....	1
1.2 Motivation and Impact.....	2
1.3 Literature Review.....	4
1.3.1 Two-Dimensional Quantitative Phase Imaging Methods.....	4
1.3.1.1 Phase-Shifting Interferometry.....	5
1.3.1.2 Off-Axis Interferometry.....	6
1.3.1.3 Phase Retrieval.....	7
1.3.1.4 Two-Dimensional Quantitative Phase Imaging Method Comparison.....	8
1.3.2 Three-Dimensional Quantitative Phase Imaging Methods.....	9
1.3.2.1 Projection Tomography	10
1.3.2.2 Diffraction Tomography.....	11
1.3.2.3 Three-Dimensional Deconvolution.....	12
1.3.2.4 Three-Dimensional Quantitative Phase Imaging Method Comparison.....	13
1.3.3 Optical Fiber Characterization.....	14

1.3.3.1	Active Large-Mode-Area Fiber Characterization	15
1.3.3.2	Fusion Splice Characterization	16
1.3.3.3	Long-Period Fiber Grating Characterization	17
1.4	What is needed?	18
1.4.1	Quantitative Phase Imaging	18
1.4.2	Optical Fiber Characterization	20
1.5	Research Objectives.....	21
1.6	Thesis Overview	22
2	MULTIFILTER PHASE IMAGING WITH PARTIALLY COHERENT LIGHT	25
2.1	Introduction.....	25
2.2	Principles of Multifilter Phase Imaging.....	28
2.2.1	Optimal Frequency Selection.....	28
2.2.2	Partially Coherent Multifilter Phase Imaging.....	29
2.3	Simulation Results	36
2.4	Experimental Results	42
2.5	Summary.....	47
3	QUANTITATIVE PHASE MICROSCOPY VIA OPTIMIZED INVERSION OF THE PHASE OPTICAL TRANSFER FUNCTION	49
3.1	Introduction.....	49
3.2	Quantitative Phase Microscopy via Inversion of the Weak Object Transfer Function	54
3.2.1	Coherent Phase Optical Transfer Function Recovery.....	54
3.2.2	Partially Coherent Phase Optical Transfer Function Recovery	57
3.3	Simulation Results	64
3.4	Experimental Results	70

3.5	Conclusions.....	78
3.5.1	Discussion.....	78
3.5.2	Summary.....	80
4	THREE-DIMENSIONAL QUANTITATIVE PHASE IMAGING VIA TOMOGRAPHIC DECONVOLUTION PHASE MICROSCOPY.....	82
4.1	Introduction.....	83
4.2	Principles of Tomographic Deconvolution Phase Microscopy	87
4.2.1	Relationship to First-Order Diffraction Tomography.....	87
4.2.2	Tomographic Deconvolution Phase Microscopy Refractive Index Recovery	92
4.3	Simulation Results	103
4.3.1	Modified Split-Step Beam Propagation Method.....	103
4.3.2	Simulated Tomographic Deconvolution Phase Microscopy Reconstructions.....	106
4.4	Experimental Results	111
4.5	Summary	117
5	JOINT RESIDUAL STRESS/REFRACTIVE INDEX CHARACTERIZATION OF LARGE-MODE-AREA ERBIUM-DOPED FIBERS.....	119
5.1	Introduction	120
5.2	Experimental Methods.....	121
5.3	Experimental Results	122
5.3.1	Unperturbed Fiber Characterization	123
5.3.2	Cleaved end-face Characterization	128
5.3.3	Fusion Splice Characterization	133
5.4	Summary.....	138
6	ARC FUSION SPLICING EFFECTS IN LARGE-MODE-AREA SINGLE- MODE YTTERBIUM-DOPED FIBERS.....	140

6.1	Introduction.....	140
6.2	Experimental Methods.....	142
6.3	Experimental Results.....	143
6.4	Summary.....	151
7	RESEARCH SUMMARY.....	153
7.1	Summary of Results and Accomplishments.....	154
7.1.1	New Two-Dimensional Quantitative Phase Imaging Methods.....	154
7.1.2	New Three-Dimensional Quantitative Phase Imaging Method.....	155
7.1.3	Large-Mode-Area Erbium- and Ytterbium-Doped Fiber Characterization.....	157
8	FUTURE WORK.....	159
8.1	Multifilter Phase Imaging with Partially Coherent Light.....	159
8.1.1	Development.....	159
8.1.2	Verification.....	165
8.1.3	Characterization.....	168
8.1.4	Application.....	170
8.2	Phase Optical Transfer Function Recovery.....	171
8.2.1	Development.....	171
8.2.2	Verification.....	173
8.2.3	Characterization.....	175
8.2.4	Application.....	177
8.3	Tomographic Deconvolution Phase Microscopy.....	178
8.3.1	Development.....	178
8.3.2	Verification.....	180
8.3.3	Characterization.....	181
8.3.4	Application.....	182

8.4	Long-Period Fiber Grating Applications	183
8.4.1	Characterization of Arc-Induced Long-Period Fiber Gratings	184
8.4.2	Modeling of Measured Refractive Index/Residual Stress Data	186
9	CONCLUDING REMARKS	188
	APPENDIX A: DERIVATION OF GENERALIZED LINEARIZATION CONDITIONS FOR PHASE OPTICAL TRANSFER FUNCTION RECOVERY	189
	REFERENCES.....	192
	VITA.....	214

LIST OF TABLES

	Page
Table 1.1: Characteristic summary for representative 2D QPI methods.	9
Table 1.2: Characteristic summary for representative 3D QPI methods.	14
Table 1.3: Decomposition of QPI method design.	19
Table 7.1: Characteristic review for representative PR methods.	158
Table 7.2: Characteristic review for representative 3DD methods.	160

LIST OF FIGURES

	Page
Figure 1.1: Representations of 2- and 3D QPI data.....	2
Figure 1.2: Block diagram representation of phase-shifting interferometry (PSI).....	5
Figure 1.3: Block diagram representation of off-axis interferometry (OAI).....	6
Figure 1.4: Block diagram depicting experimental configuration for deterministic phase retrieval (PR).....	8
Figure 1.5: Diagram representation of projection tomography (PT).....	10
Figure 1.6: Diagram representation of diffraction tomography (DT).....	12
Figure 1.7: Diagram representation of 3D deconvolution (3DD).....	13
Figure 2.1: Block diagram representation of the multifilter phase imaging (MFPI) method.....	29
Figure 2.2: Normalized phase optical transfer functions (POTFs) for various SGDF orders m and coherence parameters S	33
Figure 2.3: Normalized cut-off frequencies for various SGDF orders m and coherence parameters S	34
Figure 2.4: Phase transfer functions (PTFs) for various SGDF orders m and coherence parameters S	35
Figure 2.5: Simulated phase object.....	37
Figure 2.6: Recovered phases for various SGDF orders m and coherence parameters S as well as for MFPI-PC.....	38
Figure 2.7: Recovered phase for $S = 0.5$ and optimal frequency selection (OFS).....	39
Figure 2.8: Phase root mean squared error (RMSE) as a function of normalized noise standard deviation σ for various SGDF orders m and coherence parameters S as well as for MFPI-PC.....	41
Figure 2.9: Visible transmission grating phase measurement results.....	43
Figure 2.10: Various representations of optical fiber tomography experimental data processed using conventional TIE recovery with various defocus distances as well as the established OFS method and the proposed MFPI-PC method.....	45

Figure 3.1: Block diagram representation of defocus-based phase optical transfer function (POTF) recovery.....	56
Figure 3.2: Magnitude of off-axis phase optical transfer functions (POTFs) for Nomarski differential interference contrast (DIC) and defocus.....	62
Figure 3.3: Partially coherent phase optical transfer functions (POTFs) and weighting functions used to define partially coherent POTF recovery.....	64
Figure 3.4: Partially coherent phase imaging simulation results.....	66
Figure 3.5: Root mean squared error (RMSE) of simulations corresponding to Fig. 3.4 under varying amounts of additive white Gaussian noise σ	68
Figure 3.6: Simulation emulating reconstruction of adherent HeLa cell.....	69
Figure 3.7: Experimental results for microlens array (MLA) validating the accuracy of POTF recovery.	71
Figure 3.8: Simulated and measured optical path length (OPL) RMSE's resolved in the frequency domain.	73
Figure 3.9: Snapshot of live bovine mesenchymal stem cell cluster taken from Media 3.1	75
Figure 3.10: Snapshot of live endothelial cells taken from Media 3.2.	77
Figure 4.1: Magnitudes of the on-axis coherent 3D absorption- and phase optical transfer function (AOTF and POTF) derived from simulating the scattered complex field amplitude due to a point scatterer.	94
Figure 4.2: Partially coherent 3D absorption- and phase optical transfer function (AOTF and POTF) plotted as a function of normalized frequency coordinates.....	95
Figure 4.3: Image of Gaussian fit to the objective back-focal-plane with no sample in place serving as the input source distribution in the calculation of optical transfer functions (OTFs) shown in Fig. 4.2.	96
Figure 4.4: Block diagram representation of tomographic deconvolution phase microscopy (TDPM) refractive index (RI) recovery for high spatial frequencies.....	100
Figure 4.5: Block diagram representation of tomographic deconvolution phase microscopy (TDPM) RI recovery for low spatial frequencies.....	103
Figure 4.6: Normalized mean squared errors (NMSEs) of various split-step beam propagation method (SS-BPM) simulations with and without obliquity factor (OF) correction.....	106

Figure 4.7: RI contrast $\Delta n(\mathbf{r})$ of modified Shepp-Logan phantom.....	108
Figure 4.8: Reconstructions obtained using filtered backpropagation (FBPP) under the first Born and Rytov approximations as well as tomographic deconvolution phase microscopy (TDPM).	109
Figure 4.9: TDPM reconstructions obtained with additive noise σ	111
Figure 4.10: 2D TDPM cross-sectional tomograms obtained on various optical fibers.	114
Figure 4.11: RI modification induced via CO ₂ -laser exposure.....	116
Figure 4.12: Line profiles showing axial variation of RI in selected regions of CO ₂ -exposed SMF	117
Figure 5.1: Cross-sectional residual stress (RS) distribution and profile of unperturbed large-mode-area erbium-doped fiber (LMA EDF).....	126
Figure 5.2: Cross-sectional changes in radial refractive index (RI) resulting from manufacturing induced RS.	128
Figure 5.3: Cross-sectional RI distribution and profile of unperturbed LMA EDF.	129
Figure 5.4: Average stress and index profiles, with associated non-uniformities, of unperturbed LMA EDF.	130
Figure 5.5: Cross-sectional RS distribution and profile 5 μm from the end-face of the LMA EDF.....	131
Figure 5.6: Mean axial stress inside the LMA EDF at various lengths from the cleaved end-face.	132
Figure 5.7: Cross-sectional RI distribution and profile 5 μm from the end-face of the LMA EDF.....	133
Figure 5.8: Cross-sectional RS distribution and profile of the LMA EDF 100 μm from the splicing point.	134
Figure 5.9: Arc fusion splicing induced RS distribution along the LMA EDF and <i>SMF-28</i>	135
Figure 5.10: Change in radial RI, Δn_r , induced by the RS change along the fusion splice between the LMA EDF and the <i>SMF-28</i>	136
Figure 5.11: RI distribution along the LMA EDF and <i>SMF-28</i>	137
Figure 5.12: RI profiles at various lengths along the transition region from the fusion splicing point.	138

Figure 5.13: Finite-difference beam propagation method (FD-BPM) simulation of the fusion splice between the LMA EDF and the <i>SMF-28</i>	140
Figure 6.1: Cross-section of <i>LIEKKI™ Yb1200-10/125-DC</i> as observed in a bright-field microscope.....	146
Figure 6.2: The residual stress (RS) distribution along the <i>LIEKKI™ Yb1200-10/125-DC</i> and the <i>SMF-28</i> after arc fusion splicing.	147
Figure 6.3: Cross-sectional RS distribution in <i>LIEKKI™ Yb1200-10/125-DC</i> 20 μm from the splicing point.	149
Figure 6.4: Change of radial refractive index (RI), Δn_r , induced by the RS change along the fusion splice between the <i>LIEKKI™ Yb1200-10/125-DC</i> and the <i>SMF-28</i>	150
Figure 6.5: The RI distribution along the <i>LIEKKI™ Yb1200-10/125-DC</i> and the <i>SMF-28</i> after arc fusion splicing.	151
Figure 6.6: Cross-sectional RI distribution in <i>LIEKKI™ Yb1200-10/125-DC</i> 20 μm from the splicing point.	152
Figure 6.7: Finite-difference beam propagation method (FD-BPM) simulation of a fusion splice between the <i>LIEKKI™ Yb1200-10/125-DC</i> and the <i>SMF-28</i> using the measured RI data.	153
Figure 8.1: Simulation showing the power of transport-of-intensity equation (TIE) phase recovery for strong objects with correlated phase and absorption.	164
Figure 8.2: Simulation showing the error associated with the use of the paraxial approximation in the transport-of-intensity equation (TIE).	166
Figure 8.3: Commercial microlens array (<i>Thorlabs, MLA150-5C</i>) with chrome in the interstitial regions.	171
Figure 8.4: Experimental reconstruction showing the potential benefit of satisfying numerical boundary conditions by symmetric padding.	173
Figure 8.5: Simulation showing the importance of symmetric, as opposed to single-sided, defocus in phase recovery.	175
Figure 8.6: Block diagram representation of real-time high-speed phase optical transfer function (POTF) recovery software implementation.	177
Figure 8.7: Simulation demonstrating phase optical transfer function (POTF) recovery based on differential interference contrast (DIC) microscopy.	178

Figure 8.8: Simulation demonstrating the possibility of single-sided multiple distance POTF recovery.	181
Figure 8.9: The effect of iterative constraint algorithms on tomographic deconvolution phase microscopy (TDPM) refractive index (RI) data.	183
Figure 8.10: Sample configuration for fixed cell tomographic deconvolution phase microscopy (TDPM) measurement.	184
Figure 8.11: Changes in phase contrast owing to the use of annular, as opposed to circular, diaphragms in the condenser back-focal-plane.	186
Figure 8.12: Axial variation of residual stress (RS) within a <i>Corning SMF-28</i> exposed to electric arc discharge.	189
Figure 8.13: Transmission spectra modeled using coupled mode theory (CMT) and split-step beam propagation method (SS-BPM).	190

LIST OF SYMBOLS

$A(\mathbf{r})$	2D object absorption (dimensionless)
$A(\boldsymbol{\rho})$	2D Fourier transform of $A(\mathbf{r})$ (μm^2)
a_j	Normalized SGDF coefficient corresponding to j^{th} defocus distance (dimensionless)
a_2	Optical fiber cladding radius (μm)
α	POTF regularization parameter (μm^4)
α	TDPM regularization parameter (μm^4)
B	Background intensity average (μm^{-2})
β	Amplitude corresponding to object absorption A (dimensionless)
C_1	Stress-optic constant corresponding to σ_r (MPa^{-1})
C_2	Stress-optic constant corresponding to σ_θ and σ_z (MPa^{-1})
c	Scalar function defining ratio between absorption A and phase ϕ (dimensionless)
χ	MFPI-PC filter cut-off ratio (dimensionless)
D	Diameter of potential phase objects (μm)
d	Depth of field (μm)
Δ	Normalized RI difference between optical fiber core and cladding (dimensionless)
Δ_{DIC}	Differential interference contrast shear magnitude (μm)
$\Delta I_z(\mathbf{r})$	Intensity difference between $\pm z$ defocus planes (μm^{-2})
$\Delta I_z(\boldsymbol{\rho})$	2D Fourier transform of $\Delta I_z(\mathbf{r})$ (dimensionless)
$\Delta\lambda$	Full width at half maximum bandwidth of quasi-monochromatic source (μm)
Δn	RI difference between object and surrounding material n_0 (RI units)

Δn_{cc}	RI difference between optical fiber core and cladding (RI units)
Δn_{max}	Maximum RI difference between object and surrounding material n_0 (RI units)
Δn_r	Change in n_r (RI units)
$\Delta\theta$	TDPM object rotational increment (rad)
Δr	Lateral grid resolution used in TDPM (μm)
$\Delta\sigma_z$	Change in axial RS (MPa)
Δx	Grid resolution in x direction used in TDPM (μm)
Δy	Grid resolution in y direction used in TDPM (μm)
Δz	Distance between defocus planes used in MFPI-PC (Chapter 2, μm)
Δz	Down-sampled longitudinal grid resolution used in TDPM (Chapter 4, μm)
∇	Gradient operator acting on spatial coordinates (x,y,z) (μm^{-1})
∇_{\perp}	Gradient operator acting on lateral spatial coordinates (x,y) (μm^{-1})
δ	Dirac delta function (units depend on units and dimensionality of the argument)
δz	Magnitude of defocus distance (μm)
E	Complex electric field amplitude ($\text{V}/\mu\text{m}$)
ε	Proportionality constant defining ratio between absorption and phase (dimensionless)
ϵ	Frequency domain minimization parameter used in POTF recovery (Chapter 3, dimensionless)
ϵ	Frequency domain minimization parameter used in TDPM (Chapter 4, μm^6)
$G(\boldsymbol{\rho})$	3D Fourier transform of $g(\mathbf{r})$ (μm^2)
$G'(\boldsymbol{\rho})$	3D Fourier transform of $g'(\mathbf{r})$ (μm^2)
$g(\mathbf{r})$	3D Green's function (μm^{-1})
$g'(\mathbf{r})$	Effective 3D coherent point spread function (μm^{-1})

$\hat{\Gamma}$	Operator defining higher order derivatives in non-paraxial transport of intensity equation
γ	Refractive increment of protein (g/mL)
$H_A^{(3)}(\boldsymbol{\rho}, \rho_z)$	3D AOTF used in MFPI-PC (dimensionless)
$H_A(\boldsymbol{\rho})$	2D AOTF used in POTF recovery (Chapter 3, μm^{-2})
$H_A(\boldsymbol{\rho})$	3D AOTF used in TDPM (Chapter 4, dimensionless)
$H_A^{OA}(\boldsymbol{\rho})$	Off-axis 2D AOTF (dimensionless)
$H_{hp}(\boldsymbol{\rho})$	High-pass filter used in TDPM (dimensionless)
$H_{lp}(\boldsymbol{\rho})$	Low-pass filter used in TDPM (dimensionless)
$H_P(\boldsymbol{\rho})$	3D POTF used in TDPM (dimensionless)
$H_{P_j}(\boldsymbol{\rho})$	3D POTF used in TDPM rotated to angle θ_j (dimensionless)
$H_P^{(2)}(\boldsymbol{\rho})$	2D POTF used in MFPI-PC describing transfer between phase and axial intensity derivative (μm^{-3})
$H_{PTIE}^{(2)}(\boldsymbol{\rho})$	2D POTF used in MFPI-PC describing transfer between phase and axial intensity derivative inherent in the TIE (μm^{-3})
$H_{PW}^{(2)}(\boldsymbol{\rho})$	2D POTF used in MFPI-PC describing transfer between phase and axial intensity derivative assuming weak defocus (μm^{-3})
$H_P^{(3)}(\boldsymbol{\rho}, \rho_z)$	3D POTF used in MFPI-PC (dimensionless)
$H_\phi(\boldsymbol{\rho})$	2D POTF used in POTF recovery (μm^{-2})
$H_\phi^{OA}(\boldsymbol{\rho})$	Off-axis 2D POTF (dimensionless)
$H'_\phi(\boldsymbol{\rho})$	2D POTF for complex object assuming absorption/phase proportionality ε (μm^{-2})
$H_{SG}(e^{i2\pi\rho_z\Delta z})$	SGDF frequency response, discrete-time Fourier transform of $h_{SG}[j]$ (μm^{-1})
$H_z^C(\boldsymbol{\rho})$	POTF corresponding to defocus distance z for coherent illumination in the paraxial approximation (μm^{-2})

$H_z^{PC}(\boldsymbol{\rho})$	POTF corresponding to defocus distance z for partially coherent illumination (μm^{-2})
$h(\mathbf{r})$	Coherent point spread function corresponding to inverse 2D Fourier transform of $P(\boldsymbol{\rho})$ (μm^{-2})
h_A	3D absorption intensity point spread function corresponding to inverse 3D Fourier transform of $H_A(\boldsymbol{\rho})$ (μm^{-3})
h_p	3D phase intensity point spread function corresponding to inverse Fourier transform of $H_p(\boldsymbol{\rho})$ (μm^{-3})
$h_{SG}[j]$	SGDF coefficients $a_j/\Delta z$ (μm^{-1})
$I(\mathbf{r})$	Intensity of total wave field (μm^{-2})
$I(\boldsymbol{\rho})$	2D Fourier transform of $I(\mathbf{r})$ (Chapter 3, dimensionless)
$I(\boldsymbol{\rho})$	3D Fourier transform of $I(\mathbf{r})$ (Chapter 4, μm)
$I(\mathbf{r}, \boldsymbol{\rho}')$	Intensity corresponding to off-axis illumination point $\boldsymbol{\rho}'$ normalized by unit intensity (dimensionless)
$I(\boldsymbol{\rho}, \boldsymbol{\rho}')$	3D Fourier transform of $I(\mathbf{r}, \boldsymbol{\rho}')$ (μm^3)
$I_A(\mathbf{r})$	Intensity due to scattering from homogeneous cylinder calculated by rigorous analytical solution (μm^{-2})
\bar{I}_A	Mean value of I_A (μm^{-2})
$I_R^{im}(\mathbf{r}, \boldsymbol{\rho}')$	Intensity at the image plane in the first-order Rytov approximation due to off-axis illumination point $\boldsymbol{\rho}'$ normalized by unit intensity (dimensionless)
$I_S(\mathbf{r})$	Intensity due to scattering from homogeneous cylinder simulated by split-step beam propagation method (μm^{-2})
$I_z(\mathbf{r})$	Intensity at defocus plane z (μm^{-2})
$I_z(\boldsymbol{\rho})$	2D Fourier transform of $I_z(\mathbf{r})$ (dimensionless)
$I_z^C(\mathbf{r}, \mathbf{0})$	Intensity at defocus plane z assuming on-axis coherent illumination ($\boldsymbol{\rho}' = \mathbf{0}$) normalized by unit intensity (dimensionless)
$I_z^C(\boldsymbol{\rho}, \mathbf{0})$	2D Fourier transform of $I_z^C(\mathbf{r}, \mathbf{0})$ (μm^2)
$I'_z(\mathbf{r}, \boldsymbol{\rho}')$	Intensity at defocus plane z corresponding to off-axis illumination point $\boldsymbol{\rho}'$ normalized by unit intensity (dimensionless)

$I'_z(\boldsymbol{\rho}, \boldsymbol{\rho}')$	2D Fourier transform of $I'_z(\mathbf{r}, \boldsymbol{\rho}')$ (μm^2)
i	Imaginary unit $\sqrt{-1}$ (dimensionless)
j	Summation index used to express convolution with SGDF (dimensionless)
j	Summation index corresponding to defocus distances in POTF recovery (dimensionless)
j	Summation index corresponding to rotation angles in TDPM (dimensionless)
k	Wave vector magnitude in medium of RI n (μm^{-1})
k_0	Free-space wave vector magnitude (μm^{-1})
κ	Radial spatial frequency threshold defining regions of validity between high-frequency and low-frequency TDPM algorithms (μm^{-1})
Λ	Blazed transmission grating period (Chapter 2, μm)
Λ	Azimuthally asymmetric LPFG period (Chapter 4, μm)
λ	Free-space wavelength of monochromatic wave field (μm)
$\bar{\lambda}$	Central wavelength of quasi-monochromatic wave field (μm)
m	SGDF polynomial order (dimensionless)
N	Half-data length of SGDF (Chapter 2, dimensionless)
N	Number of defocus plane pairs used in POTF recovery (Chapter 3, dimensionless)
N	Number of rotation angles in TDPM (Chapter 4, dimensionless)
NA	Optical fiber numerical aperture (dimensionless)
NA_c	Numerical aperture of illuminating condenser lens (dimensionless)
NA_c^{in}	Numerical aperture corresponding to inner diameter of annular condenser diaphragm (dimensionless)
NA_c^{out}	Numerical aperture corresponding to outer diameter of annular condenser diaphragm (dimensionless)
NA_o	Numerical aperture of imaging objective lens (dimensionless)
n	Spatial distribution of RI (Chapters 2-4, RI units)

n	Taylor series expansion index (Chapter 8, dimensionless)
n_r	RI seen by radially polarized light in optical fiber (RI units)
n_x	RI of material x (RI units)
OF	Obliquity factor used in modified SS-BPM (dimensionless)
$P(\boldsymbol{\rho})$	Pupil function describing coherent image transfer between object and image planes (dimensionless)
Φ	Differential interference contrast phase bias (rad)
$\phi(\mathbf{r})$	Phase of optical wave field (rad)
$\phi(\boldsymbol{\rho})$	2D Fourier transform of $\phi(\mathbf{r})$ (rad- μm^2)
$\hat{\phi}_z(\boldsymbol{\rho})$	Fourier spectrum of phase estimate corresponding to defocus distance z in POTF recovery (rad- μm^2)
$\varphi(\mathbf{r})$	Auxiliary function used to define curl-free component of power flow vector $[I_0(\mathbf{r})\nabla\phi(\mathbf{r})]$ (μm^{-2})
$\varphi(\boldsymbol{\rho})$	2D Fourier transform of $\varphi(\mathbf{r})$ (dimensionless)
θ_B	Blaze angle of transmission grating (degrees)
θ_c	Angle of marginal illumination ray (rad)
θ_j	Angle corresponding to j^{th} rotational increment in TDPM (rad)
\mathbf{r}	Spatial coordinate vector defined in either two or three dimensions (μm)
r	Radial spatial coordinate corresponding to magnitude of lateral spatial coordinates (x,y) (μm)
$\boldsymbol{\rho}$	Spatial frequency coordinate vector conjugate to \mathbf{r} defined in either two or three inverse dimensions (μm^{-1})
ρ	Radial spatial frequency coordinate corresponding to the magnitude of lateral spatial frequency coordinates (ρ_x,ρ_y) (μm^{-1})
ρ_c	Marginal illumination ray spatial frequency magnitude (μm^{-1})
ρ_{co}	MFPI-PC radial spatial frequency cut-off (μm^{-1})
ρ^N	Normalized radial spatial frequency coordinate (dimensionless)

ρ_{co}^N	Normalized MFPI-PC radial spatial frequency cut-off (dimensionless)
ρ_o	Spatial frequency magnitude at edge of NA_o (μm^{-1})
ρ_x	Spatial frequency coordinate vector conjugate to x (μm^{-1})
$\widehat{\rho}_x$	Unit vector for ρ_x (dimensionless)
ρ_{xz}	Spatial frequency magnitude distance from ρ_y -axis (μm^{-1})
ρ_y	Spatial frequency coordinate conjugate to y (μm^{-1})
$\widehat{\rho}_y$	Unit vector for ρ_y (dimensionless)
ρ_z	Spatial frequency coordinate conjugate to z (μm^{-1})
$\widehat{\rho}_z$	Unit vector for ρ_z (dimensionless)
$\boldsymbol{\rho}'$	Spatial frequency coordinates in the source plane (μm^{-1})
$\widehat{\boldsymbol{\rho}}'$	Unit vector in the direction of $\boldsymbol{\rho}'$ (dimensionless)
ρ'_x	Source plane spatial frequency coordinate conjugate to x (μm^{-1})
$\widehat{\rho}'_x$	Unit vector for ρ'_x (dimensionless)
ρ'_y	Source plane spatial frequency coordinate conjugate to y (μm^{-1})
$\widehat{\rho}'_y$	Unit vector for ρ'_y (dimensionless)
ρ'_z	Source plane spatial frequency coordinate conjugate to z (μm^{-1})
$\widehat{\rho}'_z$	Unit vector for ρ'_z (dimensionless)
$\boldsymbol{\rho}_\perp$	Lateral spatial frequency coordinates conjugate to (x,y) (μm^{-1})
S	Coherence parameter defining ratio of condenser and objective lens numerical apertures (Chapters 2-4, dimensionless)
S	Source function defining normalized intensity in the illumination pupil (Chapter 3-4, dimensionless)
σ	Normalized noise standard deviation (dimensionless)
σ_θ	Azimuthal component of RS (MPa)
σ_r	Radial component of RS (MPa)

σ_z	Axial component of RS (MPa)
$\overline{\sigma_z}$	Cross-sectional mean of axial RS (MPa)
T	2D complex transmittance function describing object absorption and phase (dimensionless)
T_z	Diffracted wave field amplitude at defocus distance z (μm^{-1})
t	Time in time-lapse image series (sec)
U	Step function (dimensionless)
U_0	Amplitude of incident plane wave (μm^{-1})
$u(\mathbf{r})$	Complex amplitude of total wave field (μm^{-1})
$u(\mathbf{r}, \boldsymbol{\rho}')$	Complex amplitude of total wave field due to off-axis illumination point $\boldsymbol{\rho}'$ normalized by unit amplitude (dimensionless)
$u^{im}(\mathbf{r}, \boldsymbol{\rho}')$	Complex amplitude of total wave field at the image plane due to off-axis illumination point $\boldsymbol{\rho}'$ normalized by unit amplitude (dimensionless)
$u_B(\mathbf{r})$	Complex amplitude of wave field scattered by an object in the first-order Born approximation (μm^{-1})
$u_B^{im}(\mathbf{r}, \boldsymbol{\rho}')$	Complex amplitude of scattered wave field at the image plane in the first-order Born approximation due to off-axis illumination point $\boldsymbol{\rho}'$ normalized by unit amplitude (dimensionless)
$u_R^{im}(\mathbf{r}, \boldsymbol{\rho}')$	Complex amplitude of scattered wave field at the image plane in the first-order Rytov approximation due to off-axis illumination point $\boldsymbol{\rho}'$ normalized by unit amplitude (dimensionless)
$u_s(\mathbf{r})$	Complex amplitude of wave field scattered by an object (μm^{-1})
$u_0(\mathbf{r})$	Complex amplitude of wave field incident on an object (μm^{-1})
$u_0(\mathbf{r}, \boldsymbol{\rho}')$	Complex amplitude of wave field incident on an object due to off-axis illumination point $\boldsymbol{\rho}'$ normalized by unit amplitude (dimensionless)
$u_0^{im}(\mathbf{r}, \boldsymbol{\rho}')$	Complex amplitude of incident wave field at the image plane due to off-axis illumination point $\boldsymbol{\rho}'$ normalized by unit amplitude (dimensionless)
$V(\mathbf{r})$	Complex scattering potential (μm^{-2})
$V_A(\mathbf{r})$	Imaginary part of complex scattering potential corresponding to absorption (μm^{-2})

$V_A(\boldsymbol{\rho})$	3D Fourier transform of $V_A(\mathbf{r})$ (μm)
$V_P(\mathbf{r})$	Real part of complex scattering potential corresponding to phase (μm^{-2})
$V_P(\boldsymbol{\rho})$	3D Fourier transform of $V_P(\mathbf{r})$ (μm)
$\overline{V_{PB}}$	Mean of V_P in background region outside V' (μm^{-2})
V'	Region of 3D object support ($\mu\text{m} \times \mu\text{m} \times \mu\text{m}$)
Ω	Region of 3D measurement support in TDPM ($\mu\text{m} \times \mu\text{m} \times \mu\text{m}$)
Ω_z	Length of Ω in the z direction (μm)
x	Spatial coordinate perpendicular to optical axis (z) and rotational axis (y) (μm)
\hat{x}	Unit vector for x (dimensionless)
$\xi_z(\boldsymbol{\rho})$	Frequency domain weighting function corresponding to defocus distance z in POTF recovery (dimensionless)
y	Spatial coordinate defining rotational axis for tomography (μm)
\hat{y}	Unit vector of y (dimensionless)
$\psi(\mathbf{r})$	Complex scattered phase at the object plane (dimensionless)
$\psi_R(\mathbf{r})$	Complex scattered phase in the first-order Rytov approximation (dimensionless)
$\psi_R^{im}(\mathbf{r}, \boldsymbol{\rho}')$	Complex scattered phase at the image plane in the first-order Rytov approximation due to off-axis illumination point $\boldsymbol{\rho}'$ (dimensionless)
$\psi_R^{im}(\boldsymbol{\rho}, \boldsymbol{\rho}')$	2D Fourier transform of $\psi_R^{im}(\mathbf{r}, \boldsymbol{\rho}')$ (μm^2)
$\psi_s(\mathbf{r})$	Complex scattered phase (dimensionless)
z	Spatial coordinate defining the optical axis of an imaging system (μm)
z_j	j^{th} defocus distance in POTF recovery (μm)
ζ	2D dummy variable used to define circ function (μm^{-1})
ζ	1D dummy variable used to define step function U (μm^{-1})

LIST OF ABBREVIATIONS

AOTF	Absorption Optical Transfer Function
BPM	Beam Propagation Method
CCD	Charge-Coupled Device
CMD	Coherent Mode Decomposition
CMT	Coupled Mode Theory
CO₂	Carbon Dioxide
CTF	Contrast Transfer Function
DIC	Differential Interference Contrast
DPM	Deconvolution Phase Microscopy
DPM	Diffraction Phase Microscopy
DPX	Distyrene, Plasticizer, and Xylene
DT	Diffraction Tomography
DT-OAI	Diffraction Tomography based on Off-Axis Interferometry
DT-PSI	Diffraction Tomography based on Phase-Shifting Interferometry
EDF	Erbium-Doped Fiber
EDFA	Erbium-Doped Fiber Amplifier
EDFL	Erbium-Doped Fiber Laser
HMC	Hoffman Modulation Contrast
FBA	Fiber-Based Amplifier
FBL	Fiber-Based Laser
FBPJ	Filtered Backprojection
FBPP	Filtered Backpropagation
FBPP	Filtered Backpropagation

FD-BPM	Finite-Difference Beam Propagation Method
FPM	Fourier Phase Microscopy
GIF	Green Interference Filter
IWFR	Iterative Wave-Front Reconstruction
LED	Light Emitting Diode
LMA	Large-Mode-Area
LPFG	Long-Period Fiber Grating
MFD	Mode Field Diameter
MFPI	Multifilter Phase Imaging
MFPI-PC	Multifilter Phase Imaging with Partially Coherent Light
MLA	Microlens Array
MTF	Modulation Transfer Function
NA	Numerical Aperture
NLM	Non-Local Means
NMSE	Normalized Mean Squared Error
OA-DHM	Off-Axis Digital Holographic Microscopy
OAI	Off-Axis Interferometry
ODT	Optical Diffraction Tomography
OF	Obliquity Factor
OFC	Optical Fiber Characterization
OFS	Optimal Frequency Selection
OPL	Optical Path Length
OTF	Optical Transfer Function
PC	Phase Contrast
PCF	Photonic-Crystal Fiber

POTF	Phase Optical Transfer Function
PMF	Polarization-Maintaining Fiber
PR	Phase Retrieval
PS-DHM	Phase-Shifting Digital Holographic Microscopy
PSI	Phase-Shifting Interferometry
PSF	Point Spread Function
PT	Projection Tomography
PTF	Phase Transfer Function
PT-OAI	Projection Tomography based on Off-Axis Interferometry
QPI	Quantitative Phase Imaging
QPM	Quantitative Phase Microscopy
QRI	Quantitative Retardation Imaging
RI	Refractive Index
RMSE	Root Mean Squared Error
RS	Residual Stress
SGDF	Savitzky-Golay Differentiation Filter
SLIM	Spatial Light Interference Microscopy
SM	Single-Mode
SMF	Single-Mode Fiber
SNR	Signal-to-Noise Ratio
SS-BPM	Split-Step Beam Propagation Method
TDPM	Tomographic Deconvolution Phase Microscopy
TEC	Thermal Expansion Coefficient
TIE	Transport-of-Intensity Equation
TIPI	Tomographic Incoherent Phase Imaging

TPM	Tomographic Phase Microscopy
WD	Weakly Defocused
wDPM	White Light Diffraction Phase Microscopy
WLDT	White Light Diffraction Tomography
WOTF	Weak Object Transfer Function
YDF	Ytterbium-Doped Fiber
YDFA	Ytterbium-Doped Fiber Amplifier
YDFL	Ytterbium-Doped Fiber Laser
2D	Two-Dimensional
3D	Three-Dimensional
3DD	Three-Dimensional Deconvolution
3DISD	Three-Dimensional Index-Stress Distribution

SUMMARY

Much of what is known about cell biology and physiology can be attributed to advances in optical microscopy. Fluorescence microscopy has been particularly transformative. There are, however, many advantages to using label-free imaging modalities, such as the ability to image living cells in their natural, unperturbed environment without phototoxicity or photobleaching. Quantitative phase imaging (QPI) has emerged as the leading label-free technology and is exploding with activity in both methods and applications. In taking a global view of QPI as a whole, however, one discovers that the conventional approach for QPI method design of optimizing both measurement (hardware) and interpretation (software) parameters simultaneously is not meeting the needs of QPI's primary end users in biology and medicine, who benefit greatly from combining multiple microscopy modalities into a single integrated system. Furthermore, there are many QPI applications, in addition to biomedical, which also benefit from the integrable nature of microscopy. One example is optical fiber characterization in which residual stress (RS), in addition to refractive index (RI), is fundamental to device performance and also measurable via microscopic methods.

In light of this growing need, the primary objective of the research presented in this thesis is to develop new QPI modalities which are compatible with standard microscope platforms utilizing Köhler illumination. This work derives novelty from the fact that, under Köhler illumination, the spatial coherence area of the detected wave field is typically much smaller than the field of view, leading many to the erroneous conclusion that QPI is impossible since phase is not well-defined. Specifically, the work presented herein aims to develop, verify, characterize, and apply three QPI modalities, including two interrelated two-dimensional methods, called multifilter phase imaging with partially coherent light (MFPI-PC) and phase optical transfer function (POTF) recovery, which

lead to a third three-dimensional method, called tomographic deconvolution phase microscopy (TDPM).

A secondary objective of the present thesis research is to apply microscopic QPI modalities to the characterization of optical fibers and fiber-based devices. This work is motivated by a growing need to understand fundamental mechanisms responsible for device operation, which ultimately depend on physical properties measurable via QPI. Specifically, the effects of manufacturing, cleaving, and fusion splicing large-mode-area erbium- and ytterbium-doped fibers are characterized using a joint-technique capable of measuring RI and RS in parallel, enabling their direct comparison.

In the concluding chapters of this thesis, the contributions associated with the aforementioned modalities are viewed in context of existing QPI methods, leading to the identification and discussion of future research areas. Similarly, future directions are provided for the application of QPI to the characterization and modeling of long-period fiber gratings. Since the modalities and applications are new and potentially transformative, multiple opportunities exist.

CHAPTER 1

INTRODUCTION

This introductory chapter provides a review of the background, motivation, and existing methods for quantitative phase imaging (QPI). Also reviewed are existing applications of QPI in the field of optical fiber and fiber-based device technology. By comparing methods directly, characteristics are identified which are essential to the growth of QPI and missing from existing implementations. Likewise, missing application areas of QPI-based optical fiber characterization (OFC) are also identified. In light of these observations, the objectives of the present thesis research are defined. Lastly, an overview is provided outlining the content and organization of the thesis.

1.1 Background

In optical microscopy, contrast may be either endogenous (intrinsic) or exogenous (extrinsic). The most common modality utilizing exogenous contrast is fluorescence microscopy, in which a specimen is labelled with a fluorescent molecule to provide targeted morphological information [1]. The relative importance of fluorescence microscopy has recently been made evident by the 2014 Nobel Prize in chemistry for “the development of super-resolved fluorescence microscopy”. Although fluorescence microscopy is continuously applied across a broad range of studies, there are a growing number of applications in biology for which methods employing endogenous contrast are required. This is because label-free methods are not subject to phototoxicity and/or photobleaching and therefore permit the observation of living cells in their natural environment over indefinite time periods with little or no sample preparation.

The primary challenge associated with endogenous contrast is that cells are transparent phase objects and produce very little contrast under normal illumination conditions. Historically, this problem has been solved optically using methods such as

phase contrast (PC) [2], differential interference contrast (DIC) [3], and Hoffmann modulation contrast (HMC) [4] microscopy. Although useful, these methods all suffer from one important drawback, which is that the measured intensity has a nonlinear, and thus non-invertible, relationship with the phase of the specimen. Without this information, extracting morphologically relevant quantities such as size, dry mass density [5], and refractive index (RI) is futile. This limitation, when combined with the advent of digital image sensors and advances in holography, has resulted in the burgeoning field of quantitative phase imaging (QPI), which combines innovations in optics, imaging theory, and computational methods to image phase variations quantitatively [6]. Two-dimensional (2D) QPI resolves the phase of a specimen integrated along the optical axis and three-dimensional (3D) QPI resolves the RI of a specimen in real space. Figure 1.1 illustrates the information which is typically available from 2- and 3D QPI experiments in the literature.

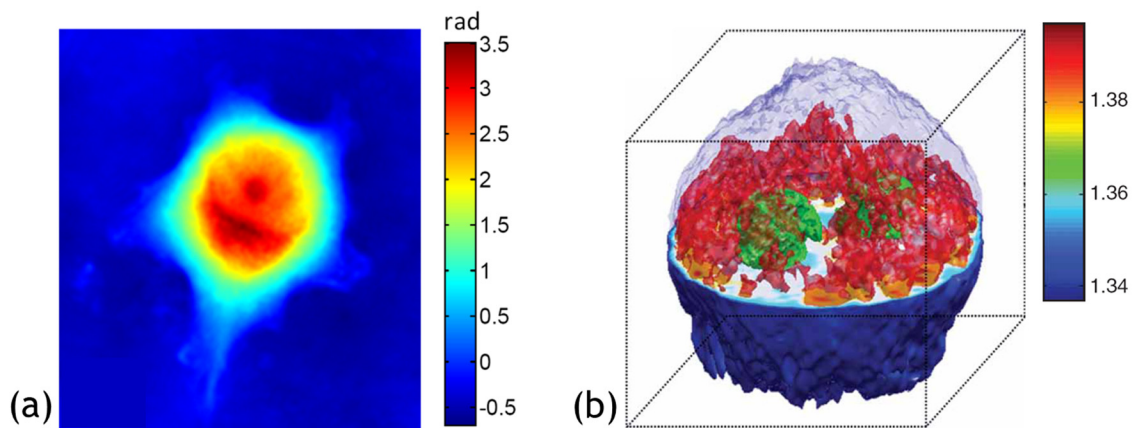


Figure 1.1: Representations of 2- and 3D QPI data. (a) 2D quantitative phase image of the total optical path delay through a breast cancer cell (MCF-7, Fig. 7 in [7], units-radians), (b) 3D RI image of a HeLa (extracted from Henrietta Lacks [8]) cell (Fig. 2 in [9], units-absolute RI).

1.2 Motivation and Impact

QPI has been used in a wide variety of biological investigations [10-14]. For example, QPI has recently measured cell cycle-dependent growth patterns by exploiting the fact

that phase images are proportional to dry mass density [11] and brought insight to the age-old question of how single cells regulate their growth. QPI has also enabled the monitoring of cytoskeletal/organelle interactions on short timescales due to its ability to image cytoskeletal structures in parallel [10], whereas fluorescence microscopy requires multiple fluorescent labels to image the same information. Likewise, QPI has been used to quantify intracellular mass transport [14], monitor the effects of ATP on red blood cell membrane dynamics [12], and measure chromosomal mass in living cells [13].

In addition to biology, QPI is making waves in the realm of clinical diagnostics [15-18], where it has recently manifested itself as a powerful tool for low-cost, high-throughput, and high-sensitivity red blood cell screening [17]. Another developing area for QPI is cancer diagnosis, where it has been used to differentiate cancerous cells in isolation [15], identify tissue self-affinity as a potential biomarker for precancer [16], detect calcium oxalate as a breast cancer screening tool [18], and correlate cancerous regions in prostate biopsies with high variance in the phase image [18].

As the number of biomedical QPI applications continues to climb, it is tempting but unwise to ignore the impact QPI is having in areas outside of optical microscopy such as semiconductor research, development, and manufacturing using electron microscopy [19], adaptive optics [20], and x-ray radiology [21]. In some regions of the hard x-ray regime, there is approximately 1,000 times more contrast in the phase of the soft biological tissues than in the attenuation or absorption [21]. Quantitative knowledge of phase could therefore dramatically increase signal-to-noise ratio (SNR) in soft tissue tomography.

Another critical application area of QPI is optical fiber characterization (OFC) [22]. As optical fibers and fiber-based device technologies continue to advance, the need to understand the fundamental mechanisms responsible for their operation increases. Previously, such mechanisms have been assumed based on empirical observations of transmission properties such as attenuation, dispersion, and spectral transmittance. One

example for which this approach has been insufficient is identifying the mechanisms responsible for RI modulation in long-period fiber gratings (LPGs) [23, 24], which have been attributed, without direct experimental verification, to a multitude of causes including residual stress (RS) modification [25], relaxation of frozen-in viscoelasticity (FIV) [26], RI densification [27], dopant diffusion [28], and geometrical deformation [29, 30], each of which results in differing device characteristics. Because these perturbations modify RI, which is measurable via QPI, and RS-induced birefringence, which is measurable via polarized light microscopy, the combination of QPI with quantitative retardation imaging (QRI) [31] enables the direct determination of mechanisms responsible for fiber-based device operation. The aforementioned combination has also proven useful in biological investigations [32] as local birefringence provides additional valuable information, which may even be a signature for the diagnosis and prognosis of cancer in tissues [33].

Overall, it is clear that QPI has developed and sustained enormous impact across a wide variety of disciplines. As a field of study, QPI is rapidly expanding, and with each new contribution it becomes increasingly difficult to maintain a global perspective, yet this is exactly what is necessary to propel QPI forward and realize its inherent potential. In the following section, an overview of QPI methods in the literature is provided and categorized according to inherent properties and performance characteristics. From this overview, research objectives are defined which address key issues facing QPI as a whole. Furthermore, recent contributions to QPI-based OFC are evaluated which motivate the applications detailed in this thesis.

1.3 Literature Review

1.3.1 Two-Dimensional Quantitative Phase Imaging Methods

2D QPI methods image the optical path length of a phase object integrated along the optical or z-axis. In the literature, there are numerous ways to do this [6]. In this thesis,

2D QPI is separated into three broad categories: phase-shifting interferometry (PSI), off-axis interferometry (OAI), and phase retrieval (PR). There are methods which do not fall under the umbrella of these categories such as wavefront sensing [34] and quantitative DIC microscopy [35]. For the purposes of this thesis, however, the above-mentioned categorization will be sufficient to understand the relative advantages and disadvantages of various methods and indicate which directions will be the most beneficial.

1.3.1.1 Phase-Shifting Interferometry

In PSI, a coherent laser beam is incident on an imaging system/interferometer. The beam is split into sample and reference arms, which are then recombined collinearly at the image plane. By modulating the phase of the reference arm, the resulting interferograms are also modulated where the bias of each pixel is determined by the phase of the sample. Conventionally, four interferograms are measured as the reference phase is modulated in equal increments around the unit circle such that the phase image is easily obtained using trigonometric relationships [6]. A block diagram representation is given in Fig. 1.2.

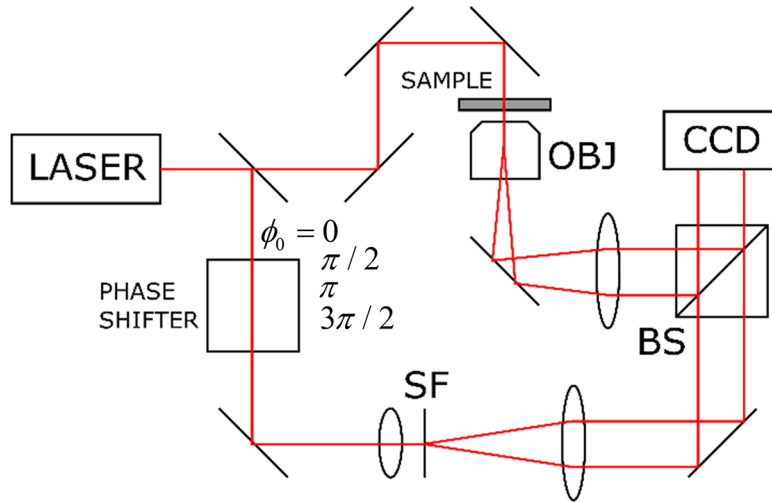


Figure 1.2: Block diagram representation of phase-shifting interferometry (PSI).

Because the interfering beams are collinear, PSI preserves the spatial resolution inherent in the sample arm's imaging optics, which may be diffraction-limited [6]. Phase sensitivity is determined by the SNR which is easily maximized by controlling the

relative powers of each beam. Furthermore, the method is computationally simple and requires no assumptions about the scattering properties of the sample. Disadvantages in PSI stem from the fact that multiple interferograms are required per phase image thereby limiting acquisition speed. Also, phase and speckle noise tend to reduce temporal and spatial phase stability in systems utilizing non-common-path geometries and monochromatic light. In recent years, researchers have mitigated some of these issues by sacrificing alignment tolerance for speed [36] and adapting PSI to common-path geometries [37] and white light illumination [38].

1.3.1.2 Off-Axis Interferometry

OAI is similar to PSI, except that spatial, rather than temporal, modulation is used in which the reference beam propagates at a known off-axis angle. The resulting interferograms are spatially modulated with a periodicity determined by this angle. The transmission function of the sample can be reconstructed in many ways; for example Fourier domain demodulation [39] or Hilbert transform methods [40] may be used. A block diagram representation is given in Fig. 1.3.

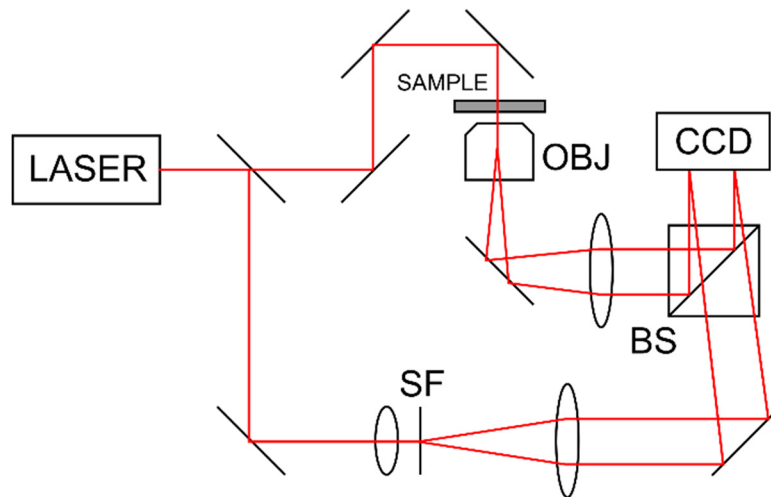


Figure 1.3: Block diagram representation of off-axis interferometry (OAI).

Because phase recovery is based on a single interferogram, temporal resolution is maximized and only limited by camera readout speed. Like PSI, OAI benefits from

controllable fringe visibility and doesn't require scattering assumptions. Unlike PSI, however, spatial resolution in OAI is often limited by the off-axis angle and not the imaging optics. OAI also suffers from reduced sensitivity associated with phase and speckle noise and reconstruction methods are often complicated by the need to unravel a highly wrapped phase function in the presence of noise [41]. As with PSI, OAI researchers have increased phase stability by adopting common-path geometries [42] and using white light [43].

1.3.1.3 Phase Retrieval

PR is a relatively broad term and includes methods which estimate phase using intensity images as the only input data. The Gerchberg-Saxton or error reduction algorithm is a well-known PR algorithm which operates on intensity images measured in both the focal and pupil planes [44]. The hybrid input-output algorithm improves the probability of convergence and is the industry standard for PR in astronomy [44]. Similar algorithms have been adopted for use with defocused images recorded in the near field [45]. The common theme among each of these methods is the iterative alternation between planes combined with the application of various constraints imposed by measured intensities and *a priori* knowledge of the object to converge towards solutions of the phase problem. Iterative PR algorithms preserve spatial resolution, make no scattering assumptions, and aren't plagued by the phase noise typical in interferometry because imaging is a common-path interference phenomenon. They also require multiple images, are sensitive to detector noise, and are more computationally expensive than their interferometric counterparts, thereby limiting application in situations where real-time processing is required.

Another significant, yet underutilized, subset of PR algorithms is based on linearizing the relationship between sample phase and defocused intensity in the near field. This makes phase calculations computationally simple and is accomplished by making

assumptions about either the defocus distance or the object's scattering properties. In the limit of small defocus, the transport-of-intensity equation (TIE) may be used to recover phase by measuring the axial derivative of intensity [46]. In practice, the intensity derivative must be approximated using finite difference methods resulting in a trade-off between sensitivity and spatial resolution [47]. It has been shown that multiple defocused images, as opposed to the conventional use of two images on either side of focus, can be used to circumvent this trade-off and obtain phase images with high resolution and sensitivity [48]. In the limit of slowly varying phase (SVP) modulation and weak absorption, a weak object transfer function (WOTF) method [49], which is also known as the contrast transfer function (CTF) in the field of propagation-based x-ray phase imaging [50], may be used to achieve high resolution and sensitivity using a smaller number of images [51]. Because deterministic PR algorithms are compatible with quasi-monochromatic light, spatial, in addition to temporal, phase stability is easily achieved. They also lend themselves to simple experimental configurations in which defocus is achieved by either moving the sample, the objective, or the imager (CCD) as depicted in Fig. 1.4.

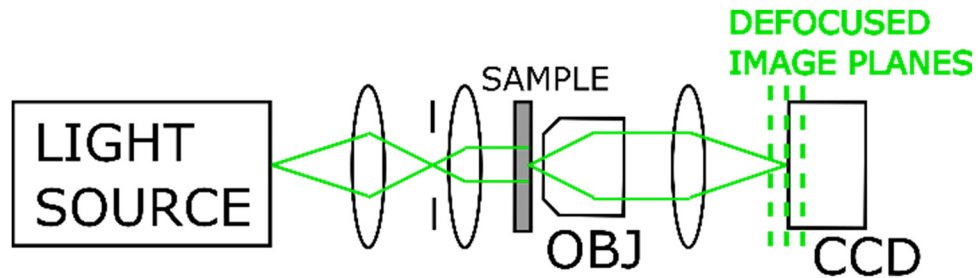










































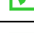




































Figure 1.4: Block diagram depicting experimental configuration for deterministic phase retrieval (PR).

1.3.1.4 Two-Dimensional Quantitative Phase Imaging Method Comparison

The overall characteristics of selected 2D QPI methods reported in the literature are summarized in Table 1.1. The configurations cited in Table 1.1 are not exhaustive and are meant to be representative of progress within each category. The table compares 2D QPI

methods using the following metrics: single-shot (enables high acquisition speed), high spatial resolution, sensitive (high SNR), common-path (eliminates phase noise), white light (eliminates speckle noise), no object scattering assumptions (strongly scattering 2D phase objects with sharp edges can be imaged without artifacts), and computationally simple (enables real-time processing).

Table 1.1: Characteristic summary for representative 2D QPI methods: (PS-DHM) phase-shifting digital holographic microscopy [52], (FPM) Fourier phase microscopy [37], (SLIM) spatial light interference microscopy [38], (OA-DHM) off-axis digital holographic microscopy [53], (DPM) diffraction phase microscopy [42], (wDPM) white light diffraction phase microscopy [43], (IWFR) iterative wave front reconstruction [45], (TIE) transport-of-intensity equation [54], (WOTF) weak object transfer function [49], (OFS) optimal frequency selection [48], and (CTF) contrast transfer function [50]. 's indicate presence of a desired trait, 's indicate absence of a desired trait, and 's indicate a trade-off between desired traits.

2D QPI Method	Published Configuration	Single-shot	High Resolution	Sensitive	Common-Path	White Light	No Object Assumptions	Comp. Simple
PSI	PS-DHM [52]							
	FPM [37]							
	SLIM [38]							
OAI	OA-DHM [53]							
	DPM [42]							
	wDPM [43]							
PR	IWFR [45]							
	TIE [54]							
	WOTF [49]							
	OFS [48]							
	CTF [50]							

1.3.2 Three-Dimensional Quantitative Phase Imaging Methods

3D QPI includes methods which resolve RI information in both lateral and axial dimensions. 3D QPI can be separated into three broad categories: projection tomography (PT), diffraction tomography (DT), and 3D deconvolution (3DD) methods. Although this is sufficient to motivate the present thesis research, there are 3D QPI methods which do

not fit within this categorization such as phase sensitive optical coherence tomography [55].

1.3.2.1 Projection Tomography

By the Fourier slice theorem, PT relates the 2D Fourier transform of a phase projection (measured using 2D QPI) to the 3D Fourier transform of the difference between the object RI and the surrounding medium RI along a slice perpendicular to the incident wave vector [56]. Rotating the angle of incidence provides frequency domain coverage and the object can be recovered using filtered backprojection (FBPJ) [56], for example. A block diagram representation is given in Fig. 1.5.

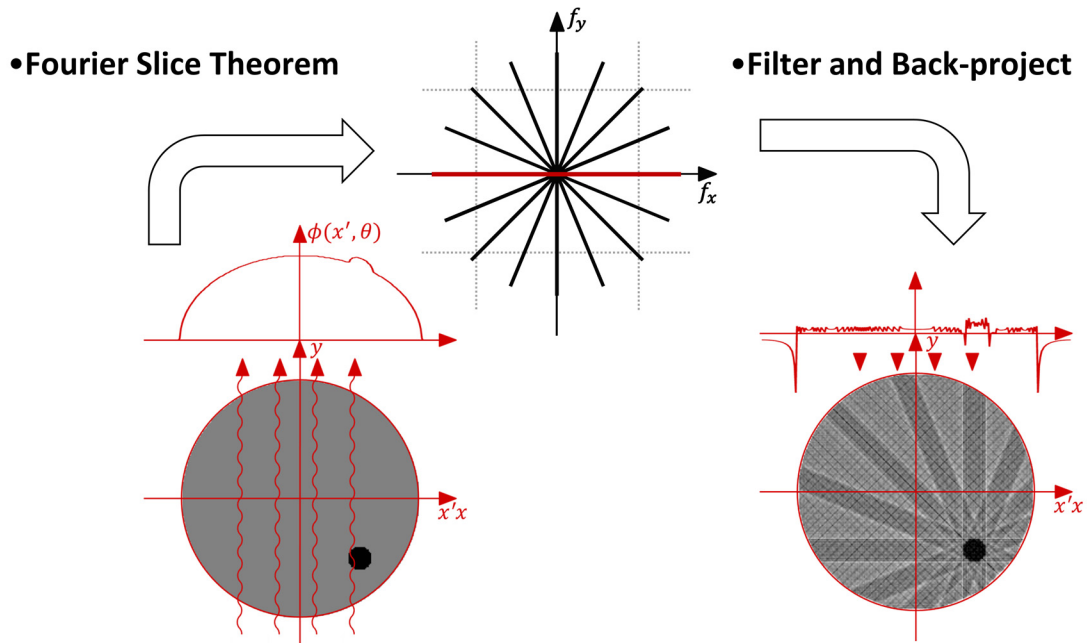


Figure 1.5: Diagram representation of projection tomography (PT).

The angle of incidence is usually altered by either rotating the specimen or the illuminating beam. Although rotating the specimen is prone to alignment error and limits acquisition speed, the reconstruction process is completely deterministic (computationally simple) and the resulting spatial resolution is isotropic (same in lateral and axial dimensions). If the illuminating beam is rotated then the reconstruction process

becomes complex if isotropic resolution is required. This is because there is a “missing cone” of unsampled frequencies in the 3D aperture of real systems due to the finite numerical apertures (NAs) of the illuminating and imaging optics [57]. It has been shown that these frequencies can be recovered, at the cost of increased computational complexity, using iterative methods and *a priori* knowledge of object domain constraints such as support and non-negativity [58]. Also, the projection approximation inherent in PT fails to consider diffractive effects, resulting in low spatial resolution and shallow depth of focus [56].

1.3.2.2 Diffraction Tomography

DT is the physical optics analog of PT, which assumes geometrical optics. The Fourier diffraction theorem relates the 2D Fourier transform of a complex scattered wave (again measured using a 2D QPI method) to the 3D Fourier transform of the complex scattering potential along a semicircular arc in the frequency domain [56]. Once again, rotating the angle of incidence enables object recovery. Conventional reconstruction methods include either frequency domain interpolation or filtered backpropagation which is the DT analog to FBPJ and accounts for the diffraction of light over the object domain [56, 59, 60].

Figure 1.6 shows a block diagram representation of DT.

The interpretation of the scattered wave depends on a linearizing object approximation, the most common of which are the first-order Born (weakly scattering) approximation and the first-order Rytov (small phase gradient) approximation [56]. It has been shown that the first Rytov approximation is well-suited for biological applications [61] in which RI contrast is weak but total phase delay may be large. Since PT is the short wavelength limit of DT in the first Rytov approximation [62], PT is also capable of imaging large phase objects. DT in the first Born approximation, however, limits object size since the total phase delay is required to be less than around $\pi/2$ radians [56].

Compared to PT, DT results in high spatial resolution over a large depth of focus. Lastly,

DT has a similar trade-off between acquisition speed and computational complexity in the choice of object versus beam rotation if isotropic resolution is needed.

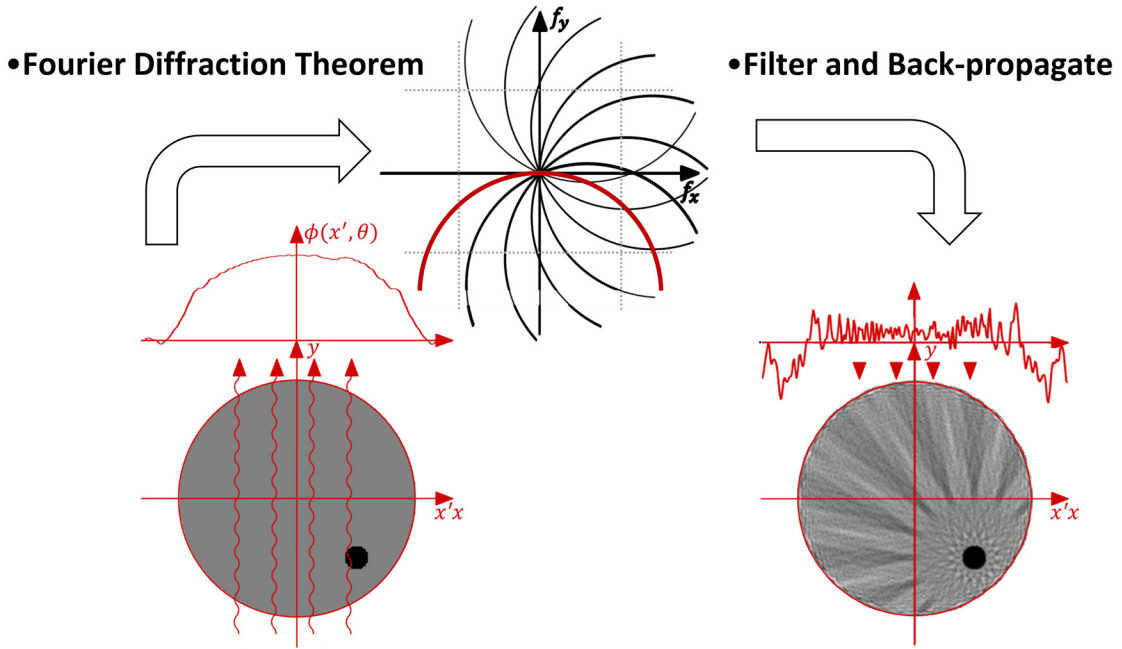


Figure 1.6: Diagram representation of diffraction tomography (DT).

1.3.2.1 Three-Dimensional Deconvolution

Another class of 3D QPI methods relies on wide-field 3DD. The unifying characteristic is the 3DD of some quantity which is resolved axially via acquisition of a through-focal series of 2D images. These depth-resolved measurements are in contrast with the angle-resolved measurements used in tomographic reconstructions. Figure 1.7 depicts the through-focal series acquisition used in 3DD methods.

The deconvolution is usually based on a 3D point spread function which has inherent optical sectioning capability. One approach for enhancing the optical sectioning capability in 3DD methods is exploiting the coherence gating effect in white light 2D QPI methods such as SLIM [63], which has the additional benefit of enhanced spatial sensitivity compared to PT and DT methods which generally utilize monochromatic light. The optical sectioning effect is enhanced further if spatial coherence is decreased as in

tomographic incoherent phase imaging (TIPI) [64, 65] because Bragg diffraction effectively widens the system 3D aperture in this case [66]. Another key benefit of 3DD methods is temporal stability due to the lack of separate reference and sample arms. Similar to DT, 3DD methods benefit from high spatial resolution over a large depth of focus by incorporating diffractive effects. Like PT and DT under beam rotation, most 3DD methods do not utilize object rotation. Although this results in increased speed and reduced mechanical error, it also implies that isotropic frequency domain coverage is not possible without using iterative constraint algorithms based on object assumptions known *a priori* [67].

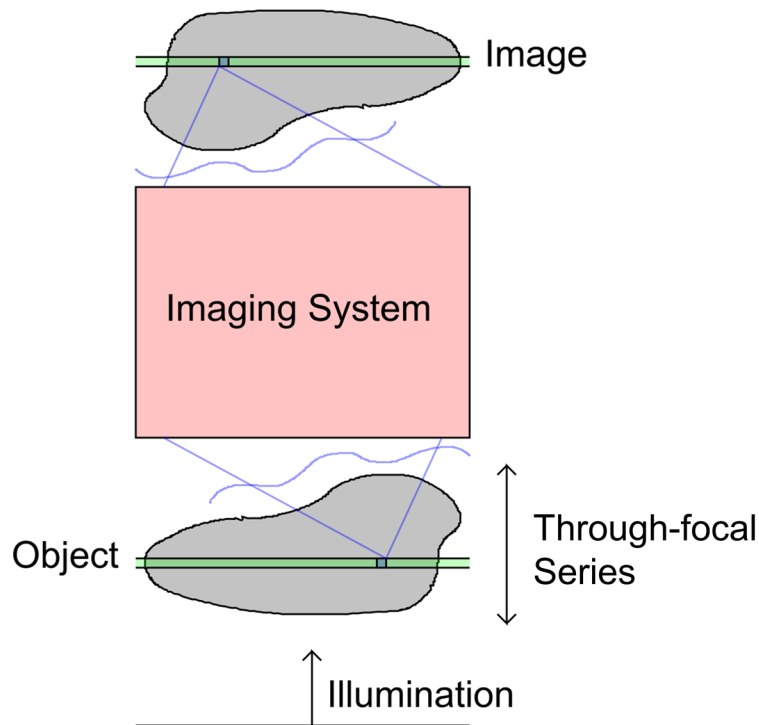


Figure 1.7: Diagram representation of 3D deconvolution (3DD).

1.3.2.1 Three-Dimensional Quantitative Phase Imaging Method Comparison

The overall characteristics of selected 3D QPI methods reported in the literature are summarized in Table 1.2. The list is not exhaustive and is meant to be representative of progress within each category. The following metrics are used: fixed object (enables high

acquisition speed), isotropic/high spatial resolution, common-path, white light, large phase objects (allowing for large total phase delays), and computationally simplicity.

Table 1.2: Characteristic summary for representative 3D QPI methods: (PT-OAI) projection tomography using off-axis interferometry [68], (TPM) tomographic phase microscopy [9], (DT-OAI) diffraction tomography using off-axis interferometry [69], (DT-PSI) diffraction tomography using phase-shifting interferometry [61], (WLDT) white light diffraction tomography [63], and (TIPI) tomographic incoherent phase imaging [64]. ✓'s indicate presence of a desired trait and ✗'s indicate absence of a desired trait.

3D QPI Method	Published Configuration	Fixed Object	Isotropic Resolution	High Resolution	Common-path	White Light	Large Phase Objects	Comp. Simple
PT	PT-OAI [68]	✗	✓	✗	✗	✗	✓	✓
	TPM [9]	✓	✓	✗	✗	✗	✓	✗
DT	DT-OAI [69]	✗	✓	✓	✗	✗	✓	✓
	DT-PSI [61]	✓	✓	✓	✗	✗	✓	✗
3DD	WLDT [63]	✓	✗	✓	✓	✓	✗	✓
	TIPI [64]	✓	✓	✓	✓	✓	✓	✗

1.3.3 Optical Fiber Characterization

As has already been mentioned, QPI, often in combination with QRI for the determination of RS in optical fibers, has the potential to be transformative in the field of fiber optics due to its ability to provide detailed information about the spatial distribution of fundamental physical properties of fibers, which ultimately determines device operation and performance. Since QPI and QRI are transverse fiber profiling techniques, meaning that they measure phase variation transversally through the fiber [70], such methods are capable of measuring axial variations along the fiber propagation axis. This is a key feature since many important devices have axial variation, such as fusion splices, gratings, tapers, lensed fibers, etc.

The diversity of fibers and fiber-based devices which are being characterized via QPI and QRI continues to grow, with examples including single-mode (SMF) [31, 71], multi-mode [71, 72], multi-core [73], photonic-crystal (PCF) [73-75], large-mode-area (LMA)

[76], rare-earth-doped [76, 77], and polarization-maintaining fibers [70, 78-80] as well as fiber Bragg gratings [81, 82], fiber-based lasers (FBL) and amplifiers (FBA) [70], femtosecond laser [76] and ion beam [81, 83] implanted waveguides, various fusion splices [84-87], and LPFGs [88-91]. In what follows, a brief review of the relevant literature in the specific areas of active LMA fiber, fusion splice, and LPFG characterization are provided which motivate both the present and future OFC research included in this thesis.

1.3.3.1 Active Large-Mode-Area Fiber Characterization

The development of high-power FBLs and FBAs over the past decade or so has provided motivation for new OFC technologies which are related to QPI and tomography [70]. This is at least partly because high-power FBLs often require single-mode guidance in extremely low NA fibers with correspondingly LMAs in order to avoid effects induced by fiber nonlinearity at high optical densities [92]. Because NA is determined primarily by the normalized index difference Δ between core and cladding, the effects of various RI and RS perturbations, including manufacturing induced effects like RS formation [93], dopant transport [94], and FIV strains [26, 95], are of primary importance since they represent a much larger relative deviation from the intended RI profile. The situation is complicated further by the need to optimize concurrently the spatial distribution of rare-earth dopants (typically erbium or ytterbium) within the fiber to achieve high gain.

For example, Schmidt *et al.* recently reported an ultra-LMA ytterbium-doped PCF with an active core diameter of 70 μm and a fundamental mode field area of 2,300 μm^2 requiring a normalized index difference of $\Delta = 7 \times 10^{-5}$ [96]. As common perturbations, such as draw-induced RS and FIV [95], produce RI changes greater than or equal to this order of magnitude [95], it is clear that such fibers (for more examples see [97, 98]) require an extensive and precise knowledge of all potential perturbations which may take effect during the fiber lifetime. For these reasons, joint RI/RS characterization methods,

such as the 3D index-stress distribution (3DISD) method recently proposed by Hutsel *et al.* [31], have the potential to be transformative in the field of ultra-LMA active fiber design and characterization intended for use with high-power FBLs and FBAs.

1.3.3.2 Fusion Splice Characterization

In addition to understanding the effects of fiber manufacture, the use of arc fusion splicing is used ubiquitously in fiber optic technology and development and warrants a complete characterization. For an excellent review of optical fiber fusion splicing and its current status please see [99]. One important topic of fusion splice characterization involves the use of RI profiling to measure dopant diffusion between dissimilar fibers. It is known that such diffusion, both parallel and perpendicular to the fiber axis, plays an important role in determining splice loss [99]. This is because the diffused region acts as a mode transformer making the transition between fundamental modes more gradual [100, 101]. Another key area is measuring RS distributions in the vicinity of a fusion splice [87], which, although of less optical significance than dopant diffusion [101], is critical in determining the mechanical strength of splices and may even be critical in determining optical properties, for instance when splicing low NA fibers together.

Lastly, another RI perturbation which may affect the operation of various fusion splices and is often overlooked is the relaxation of FIV [26, 95]. During fiber manufacture, FIV results in an isotropic decrease in cladding RI owing to the time dependent contraction induced in the viscoelastic silica as it cools rapidly from temperatures near or above its fictive temperature [26]. Such frozen-in changes are proportional to draw tension during manufacture and can be on the order of 1×10^{-3} RI units in SMF [26]. In the past, the cladding RI of silica optical fibers has been assumed to be a constant reference and independent of any fabrication parameter, which may explain why the effects of FIV have not been considered until the past decade. For fusion splices, relaxation of FIV theoretically results in a RI increase in the cladding near the splice,

however, their experimental confirmation, characterization, and modeling remain an area of active research.

1.3.3.3 Long-Period Fiber Grating Characterization

The last, and perhaps most interesting, application of QPI related methods to OFC lies in obtaining and using a more complete understanding of the physical mechanisms responsible for mode coupling in LPFGs fabricated via various methods including but not limited to CO₂ laser induction [102] and electric arc discharge [28]. Although many suggested mechanisms have been proposed in the literature [23, 24], such as mechanical RS relaxation, glass densification, diffusion of core dopants, relaxation of FIV, and geometric deformation, the source of modulation depends on the specifics involved in fabrication and more research is needed providing quantitative measurements concerning the origin and effect of various mechanisms, as is consistent with conflicting reports.

Recently, Hutsel *et al.* has provided a comprehensive characterization of both RI and RS effects in CO₂-laser-induced LPFGs [91] using the aforementioned 3DISD method [31]. This data provides insight on the effects of core RS relaxation and azimuthally asymmetric RI variations in the cladding induced via glass densification [91]. In addition to CO₂-laser-induced gratings, LPFGs fabricated via electric arc discharge represent a simple fabrication alternative as many configurations utilize commercially available fusion splicers [23] and will also benefit from quantitative measurements. In 2005, Durr *et al.* investigated the effects of arc discharge on the axial variation of RS, concluding that relaxation of mechanical RS are not likely to be primary source of RI modulation in arc-induced, as opposed to CO₂-laser-induced, LPFGs since the axial extent of RS relaxation is much longer than typical LPFG periods resulting in a washed-out effect [89]. Likewise, Abrishamian *et al.* have investigated the effects of differing arc discharge conditions on the LPFG RI profile measured via quantitative phase microscopy based on solving the TIE [88]. Results show a core reduction and cladding increase in RI as is

expected from RS and FIV relaxation respectively [88, 95]. Understanding, and potentially controlling, these effects is key to the realization of device repeatability. This is because, with typical splicing parameters, arc-induced LPFGs are thought to be dominated by geometric deformation, such as tapering [28], or microbending [30], which are less controllable in nature and induce larger insertion loss.

Lastly, an opportunity exists to use numerical optical modeling tools, such as a split-step beam propagation method (BPM) [103] or eigenmode expansion [104], to gain further intuition concerning the effects of various RI perturbations, including those which are measured directly and induced photoelastically from RS measurements. To date such investigations do not exist, as the modeling, fabrication, and RI/RS measurement capabilities often exist in separate laboratories and such a contribution would require a relatively broad, collaborative effort. However, it is likely that if such a capability were developed it would be transformative in the field of LPFG development as many authors currently rely on empirical methods based on observed transmission characteristics [105].

1.4 What is needed?

1.4.1 Quantitative Phase Imaging

In an effort to view QPI technology as a whole, a few key observations have been made which suggest a new paradigm for QPI development. QPI method design can be decomposed into innovations in measurement and interpretation as depicted in Table 3. Measurement innovations include what type of images/data are to be collected and how or with what hardware/experimental configuration. Interpretation innovations include the underlying mathematical models describing the physics of image formation as well as how the measured images/data are processed.

Table 1.3: Decomposition of QPI method design.

QPI Method Design	
Measurement (Hardware) Innovations	
<ul style="list-style-type: none"> • What is measured? <ul style="list-style-type: none"> - phase-shifting/off-axis/in-line interferograms/holograms, Hartmanngrams, PC/DIC/HMC images, bright-/dark-field images, etc. • How is it measured? <ul style="list-style-type: none"> - sources: lasers, light-emitting diodes, superluminescent diodes, lamps, etc. - optics: lenses, filters, beamsplitters, mirrors, gratings, light modulators, polarizers, etc. - detectors: charge-coupled devices, photodiodes, spectrometers, etc. - actuators: piezoelectric scanners, galvanometers, stepper motors, controllers, etc. 	
Interpretation (Software) Innovations	
<ul style="list-style-type: none"> • What is the underlying model for image formation? <ul style="list-style-type: none"> - linear/nonlinear, scalar/vector, geometric/physical, spatial/temporal coherence, diffraction model, etc. • How are the measured images processed? <ul style="list-style-type: none"> - Fourier transformation, demodulation, phase unwrapping, deconvolution, regularization, iteration, constrained optimization, differentiation, interpolation, backprojection, backpropagation, etc. 	

Until now, a majority QPI methods have been developed using an integrated approach, in which measurement and interpretation innovations are considered simultaneously to optimize performance. This approach is very reasonable as it provides the researcher with complete control over all aspects of method design and has resulted in a number of commercial 2D QPI products from companies such as Phase Holographic Imaging PHI AB, Lyncée Tec, Ovizio Imaging Systems, 4Deep, Phi Optics, Phasics, and Phase Focus Limited. These products are robust and have provided utility in a growing number of applications.

In spite of this progress, however, the integrated approach is not tailored to the needs of QPI's primary end users, namely microscopists in biology and biomedicine. One of the primary factors underlying the success of modern optical microscopy platforms is the ability to combine modalities into one universal product. Bright-field, dark-field, PC, DIC, HMC, and fluorescence imagery can all be recorded and automated in parallel using modern microscope systems and platforms which are highly developed for biological applications including live cell imaging. The integrated approach for QPI method design, however, commonly results in stand-alone systems which are expensive to acquire and

may be impractical additions to established laboratories. One of the primary reasons for this is the popular notion that coherent illumination is required for phase recovery [6], whereas microscopes are equipped with Köhler illumination from extended incoherent sources, which results in either partially coherent or incoherent imaging conditions [106]. Recent work, however, indicates that it is not only possible but in many ways desirable to recover sample phase information using partially spatially coherent illumination [107, 108].

Taken together, these observations suggest a new paradigm for QPI development in which a constrained approach is favored. In the constrained approach, measurement innovation parameters conform to hardware availability in commercial microscope platforms, such that resulting QPI methods are inherently compatible. Significant innovations in interpretation will be required to account for and exploit the favorable properties of partially coherent illumination. The resulting methods will be implemented as computer algorithms, which may at first be open-sourced and later bundled into commercial available microscopy software packages. It is believed that the constrained approach will lead to the wide-scale adoption of QPI among microscopists in biology and biomedicine, resulting in a dramatic increase of utility in these fields.

1.4.2 Optical Fiber Characterization

In Section 1.3.3, optical fiber application areas involving the use of QPI and relating imaging modalities, including QRI via polarimetric methods as well as polarized light microscopy, were reviewed. The thrust of this research is not necessarily in the development of new imaging methods so much as in the application of existing methods to develop a deeper understanding and advance fiber and fiber-based technology. A few key research areas, including FBL and FBA, fusion splice, and LPFG characterization were identified as ripe for application. In particular, as FBL and FBA applications involving the use of active LMA fibers is in growing demand, measurements detailing the

fundamental physical properties of these fibers as well as changes that occur during use, such as in fusion splicing, are needed especially. Likewise, conflicting reports in the literature outlining various grating formation mechanisms in LPFGs motivate the use of detailed measurements to clarify these issues. In order to push the field further, specific numerical methods adapted for use with measurable QPI data are needed, as predictions based on coupled-mode theory, although powerful, only provide meaningful interpretations in select cases which meet its theoretical assumptions [109, 110].

1.5 Research Objectives

In light of what is needed and consistent with the aforementioned constrained approach for QPI development, the primary objective of the research presented in this thesis is to develop new QPI modalities which are compatible with standard microscope platforms utilizing Köhler illumination. Specifically, the work presented herein aims to develop, verify, characterize, and apply three QPI modalities, including two interrelated 2D methods which lead to a third 3D method. The aim of the described QPI methods is to provide end users with QPI capability without extensive hardware modification or reduced performance relative to the current state-of-the-art.

A secondary objective of the present thesis research is to apply QPI and QRI to the characterization of RI and RS effects in LMA erbium- and ytterbium-doped fibers (EDFs and YDFs) in order to provide a basis for the future development of ultra-LMA devices requiring precise knowledge of and control over these perturbations, including the effects of fusion splicing. In addition to the OFC work detailed herein, future work concerning the optimization of parameters in arc-induced LPFGs based on commercial fusion splicers as well as the numerical modeling of measured LPFGs is suggested in the concluding chapter and mentioned here for relevance.

1.6 Thesis Overview

The research objectives described in the previous section are examined in detail in the following chapters which define the organization of content within this thesis. A natural subdivision between the aforementioned primary and secondary research objectives occurs with Chapters 2-4 centered on QPI development and Chapters 5 and 6 outlining the characterization of RI and RS effects in LMA EDFs and YDFs respectively.

In Chapter 2, a new 2D QPI method is developed for generalizing recently developed reconstruction techniques based on the TIE to the more relevant case of Köhler illuminated microscopy. The method is based on estimating the longitudinal intensity derivative in the TIE via convolution with multiple Savitzky–Golay differentiation filters. The resulting noise and resolution performance are evaluated via numerical simulation and demonstrated experimentally using a blazed transmission grating as well as a SMF as test phase objects.

In Chapter 3, the foundational work in Chapter 2 is generalized further to provide an optimal phase recovery algorithm based on a direct inversion of the phase optical transfer function under the assumptions of weak absorption and SVP. The method uses a small number of efficiently sampled defocus planes and as such is better-suited for mid-high speed QPI applications than the method described in Chapter 2. Simulation results are provided which compare the performance of similar algorithms and demonstrate compatibility with strong phase objects encountered in live cell imaging. Upon experimental validation using a microlens array as a test phase object, the method is then applied to both high-speed and time-lapse QPI experiments on live adherent cells.

Chapter 4 extends the theoretical foundations outlined for use with the novel 2D QPI methods of Chapters 2 and 3 to the more realistic and complex scenario of 3D QPI. This method is presented as an attractive alternative to ODT, which often requires the use of custom-built opto-mechanical configurations and laser illumination. Expressions analogous to the aforementioned weak absorption and SVP conditions are derived for 3D

imaging. By combining through-focal series acquisition with object rotation, 3D RI recovery with isotropic spatial resolution is made possible without requiring the use of *a priori* knowledge and iterative reconstruction. Lastly, simulated and experimental reconstructions are demonstrated using specialty optical fibers as well calibrated test phase objects.

Chapter 5 addresses the need for RS and RI measurements in LMA EDFs using the 3DISD method first described by Hutsel *et al.* [31]. The effects of fiber manufacturing, cleaving, and arc fusion splicing in a commercially available LMA EDF are all characterized, the primary results of which indicate the presence of strong perturbation strengths relative to the low normalized index differences required by current and future LMA and ultra-LMA EDFs.

Similar to the procedure used in Chapter 5, the effects of arc fusion splicing in LMA single-mode YDFs are characterized using the 3DISD method and described in Chapter 6. The results again indicate significant RI changes within a transformed region in the vicinity of the splice which is on the order of mm. Unlike LMA EDFs, however, these measurements identify the diffusion of core dopants to be a much stronger effect, increasing the overall mode-field-diameter by 39.6% and resulting in an additional splice loss of 20.8% as measured by a radially symmetric finite-difference BPM, which will be critical for the design and optimization of current high-power YDF FBLs and FBAs.

In Chapter 7, the results and accomplishments described in Chapters 2-6 are placed into context and briefly summarized. For the three QPI modalities presented in this thesis, a majority of the described research has centered on conceptual development and providing demonstrative “proof of concept” results. For this reason, future work is included in Chapter 8 which identifies fruitful research areas centered on the further development, verification, characterization, and application of these modalities.

Likewise, due to the need to characterize LPFGs, future work directions concerning the measurement of RI/RS perturbations in arc-induced LPFGs as well as the application of a

BPM towards modeling LPFGs based on measured profiles are also outlined in Chapter 8. Lastly, some concluding remarks are provided in Chapter 9.

CHAPTER 2

MULTIFILTER PHASE IMAGING WITH PARTIALLY COHERENT LIGHT

In Chapter 1, upon reviewing state-of-the-art quantitative phase imaging (QPI) methods, it was found that the current integrated approach of optimizing measurement and interpretation aspects simultaneously does not meet the needs of QPI's primary end users, who would benefit greatly from methods which are directly compatible with microscopy systems without modification. This chapter presents a novel phase reconstruction method, called multifilter phase imaging with partially coherent light (MFPI-PC), which provides this capability and is based on the application of the transport-of-intensity equation (TIE) to Köhler illuminated microscopy. The resulting noise and resolution performance are evaluated via numerical simulation and validated experimentally using a blazed transmission grating as well as a single-mode fiber as test phase objects. This chapter is based on the manuscript entitled "Multifilter phase imaging with partially coherent light," which was published in June of 2014 [111] and an associated provisional patent application [112].

2.1 Introduction

Phase imaging is critically important for a variety of biomedical and metrological applications because many objects of interest are not strongly absorbing but do induce significant phase shifts. A number of methods exist for both qualitative and quantitative phase imaging (QPI) [2, 3, 6]. Quantitative methods are attractive because of their ability to reveal structural information directly. For example, QPI has been used to study cell growth, motility, and membrane dynamics [38]. Most quantitative methods are based on interferometry and require explicit control over reference and object beams in order to

derive phase information from measured interferograms [6]. By contrast, propagation-based phase retrieval (PR) methods are experimentally simple since the only input data are images taken at varying propagation distances using traditional imaging hardware [46, 113]. More specifically, deterministic PR based on the transport of intensity equation (TIE) is especially useful due to its ability to recover the optical path length of an object when the illumination is partially (both temporally and spatially) coherent and the phase is not well-defined over the field of view [108]. This is to be contrasted with the strict spatial coherence requirements inherent in most phase imaging methods and is of significant practical importance for situations in which coherent sources are either unavailable or are not economically viable. Another important consequence of this compatibility is the potential for improved spatial resolution over coherent methods [1].

Derived from the paraxial scalar wave equation, the TIE as given by Eq. (2.1) specifies the relationship between phase ϕ and the derivative of intensity along the optical axis z , where λ is the wavelength and ∇_{\perp} is the gradient operator in the lateral dimensions (x, y) represented by the position vector $\mathbf{r} = x\hat{x} + y\hat{y}$ [46].

$$\frac{dI(\mathbf{r}, z)}{dz} = -\left(\frac{\lambda}{2\pi}\right) \nabla_{\perp} \cdot [I(\mathbf{r}, z)\nabla_{\perp}\phi(\mathbf{r}, z)]. \quad (2.1)$$

The intensity derivative cannot be measured directly and must be approximated typically using finite difference methods. Conventionally, the z derivative is approximated by subtracting two symmetrically defocused images [54]. One of the major reasons for which TIE phase imaging, despite its many desirable attributes, has not yet been widely adopted is an inherent trade-off between noise and spatial resolution in the choice of the defocus distance [47]. Choosing a small defocus distance improves resolution at the expense of dramatically increased noise sensitivity, while choosing a large defocus distance reduces noise sensitivity at the expense of degraded resolution.

In order to overcome this trade-off, there has recently been an increased effort to improve the intensity derivative estimate by utilizing information recorded in multiple

defocused planes [48, 114-116]. Among these, methods that decompose the problem in the lateral spatial frequency domain and estimate each Fourier component of the z derivative with an appropriately chosen finite difference approximation are particularly effective because they balance the effects of noise and diffraction induced nonlinearity over a wide range of length scales [47, 48]. Methods such as these may appropriately be termed multifilter phase imaging (MFPI) methods due to their use of multiple spatial frequency filters in post-measurement processing to produce a composite phase image. The appropriate choice for the finite difference approximation is determined by the dynamics of wave propagation between defocused planes and is therefore highly sensitive to the level of spatial coherence of the incident illumination.

Until now, MFPI methods have only been derived for the spatially coherent case, such the description given in [47] and the optimal frequency selection (OFS) algorithm described in [48] by Zuo *et al.*. These methods are not adapted to match the physics of partially coherent wave propagation, the regime for which the TIE method is particularly well-suited and is widely used. When the illumination is partially spatially coherent, two-dimensional (2D) wave propagation may be described by propagation of the four-dimensional mutual intensity function [107]. The additional mathematical complexity is simplified, however, if the source is assumed to be delta correlated, as in Köhler illuminated microscopy, for which the overall intensity upon propagation is the sum of intensities due to each off-axis point source [108]. Under this assumption, a new method is developed that enables the benefits of the multifilter approach for the important case of partially spatially coherent illumination for which conventional QPI methods are not applicable. This method was presented in [117], and a thorough treatment is now given here.

2.2 Principles of Multifiler Phase Imaging

2.2.1 Optimal Frequency Selection

The basic principles of MFPI were first introduced by Paganin *et al.* [47] and later adapted by Zuo *et al.* [48] to include derivatives estimated by higher-order finite difference methods. It was found that the previously developed finite difference methods [114-116] may be generalized in terms of a digital signal processing approach in which the z derivative is estimated via convolution with a Savitzky-Golay differentiation filter (SGDF) [48]. This convolution solution is equivalent to least squares polynomial fitting where the order of the polynomial fit corresponds to the order m of the SGDF [48]. Only odd orders m are considered because the SGDFs for each odd order are identical to the next highest even order, e.g., 1 and 2, 3 and 4, etc. [48].

Following the derivation of Pogany *et al.* [118], the three-dimensional (3D) image intensity distribution for a generic weakly scattering 2D object may be fully specified in terms of a combination of phase and amplitude optical transfer functions (POTF and AOTF), the combination of which has also been called the contrast transfer function (CTF) in the field of propagation-based x-ray phase imaging [50, 51, 119]. Since the AOTF is an even function of defocus and the POTF is an odd function of defocus, estimating the z derivative via convolution with a SGDF results in a decoupling of the phase and amplitude information because the SGDF is a Type III finite-impulse-response filter which is also odd-symmetric. Because of the fact that inversion of the TIE in the Fourier domain (for a pure phase object) amounts to the application of an inverse Laplacian filter, a simple change of variables then allows the TIE estimated phase to be described in terms of a low-pass filtered version of the actual phase as described in [48] and given by Eq. (25) in that reference. This phase transfer function (PTF) defines the relationship between the estimated phase and the actual object phase. Knowing the PTF associated with each SGDF allows the phase information to be combined in the spatial frequency domain, resulting in a composite phase which effectively increases signal-to-

noise ratio across a broad range of frequencies. This is the essence of the OFS method which was given by Zuo *et al.* [48], which may also be called MFPI, and is summarized by the block diagram shown in Fig. 2.1 which is similar to Fig. 3 in [48]. When the illumination is partially spatially coherent, the PTFs derived in [48] are no longer valid and need to be re-derived; however, the MFPI method may still be applied if the partially coherent PTFs are known.

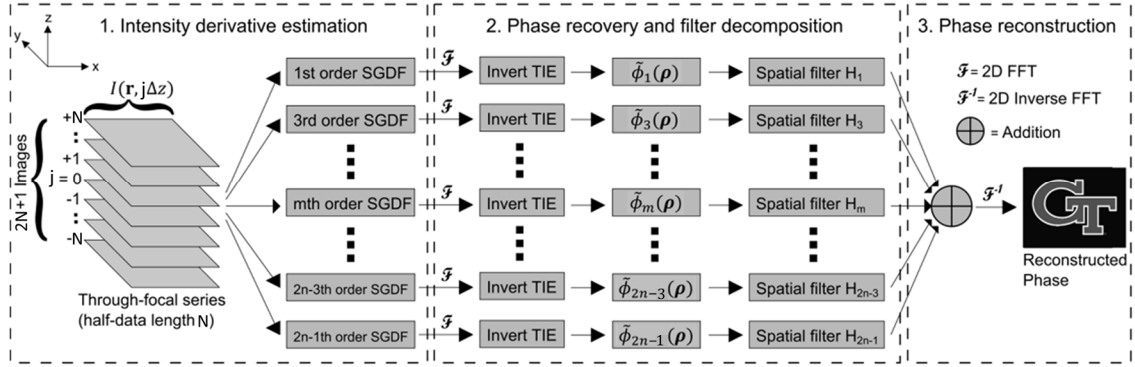


Figure 2.1: Block diagram representation of the multifilter phase imaging (MFPI) method.

2.2.2 Partially Coherent Multifilter Phase Imaging

In order to formulate the problem and adapt the PTFs, the model used in describing the 3D image intensity distribution must account for partial spatial coherence. For an ideal Köhler illuminated system, the image intensity distribution can be expressed in terms of a 2D [120] or 3D optical transfer function theory [66] which are related to each other via a one-dimensional Fourier transform along the optical axis (z direction) [120]. Both derivations rely on a weakly scattering or first-order Born approximation for which once-scattered light interferes only with unscattered light [66, 120], which has resulted in the use of weak object transfer function (WOTF) when referring to such methods throughout the literature [49, 120, 121]. Alternatively, one may also use a coherent mode decomposition (CMD) [122] to express the resulting intensities as the summation of appropriately apertured intensities due to each off-axis point of the extended source. In

this chapter the 3D WOTF formalism of Streibl will be used to derive the PTFs corresponding to SGDFs of various orders. The numerical simulations in Section 2.3 are based on a CMD model and the equivalence of these two approaches will be demonstrated in that section.

In [66], the image intensity spectrum for a telecentric imaging system is given by

$$I(\boldsymbol{\rho}, \rho_z) = B\delta(\boldsymbol{\rho}, \rho_z) + V_P(\boldsymbol{\rho}, \rho_z)H_P^{(3)}(\boldsymbol{\rho}, \rho_z) + V_A(\boldsymbol{\rho}, \rho_z)H_A^{(3)}(\boldsymbol{\rho}, \rho_z), \quad (2.2)$$

where B is the background intensity, $V_P(\boldsymbol{\rho}, \rho_z)$ and $V_A(\boldsymbol{\rho}, \rho_z)$ are 3D object phase and amplitude spectra corresponding to real and imaginary parts of the scattering potential $V(\mathbf{r}, z)$, and $H_P^{(3)}(\boldsymbol{\rho}, \rho_z)$ and $H_A^{(3)}(\boldsymbol{\rho}, \rho_z)$ are the 3D POTF and AOTF respectively, which together comprise the 3D WOTF. The variables $\boldsymbol{\rho}$ and ρ_z correspond to lateral and longitudinal spatial frequency coordinates, respectively, where $\boldsymbol{\rho} = \rho_x\widehat{\rho}_x + \rho_y\widehat{\rho}_y$ and ρ_x and ρ_y are conjugate to spatial variables x and y and ρ_z is conjugate to z . For 2D objects which are thinner than the Rayleigh depth of focus, the ρ_z dependence may be removed from $V_P(\boldsymbol{\rho}, \rho_z)$ and $V_A(\boldsymbol{\rho}, \rho_z)$ by inverse Fourier transformation. The WOTF for a paraxial system with a circular aperture is given by Eqs. (31) and (32) in [66] and depend on the sizes of the source and pupil. The resulting shape of the WOTF is primarily determined by the coherence parameter S of the incident illumination, Eq. (2.3), where NA_c and NA_o are the numerical apertures (NA) of the condenser and objective lenses respectively and $0 \leq S \leq 1$:

$$S = \frac{NA_c}{NA_o}. \quad (2.3)$$

The quantities $I(\boldsymbol{\rho}, \rho_z)$, $V_P(\boldsymbol{\rho}, \rho_z)$, and $V_A(\boldsymbol{\rho}, \rho_z)$ each possess Hermitian symmetry since $I(\mathbf{r}, z)$, $V_P(\mathbf{r}, z)$, and $V_A(\mathbf{r}, z)$ are each real valued functions. It then follows that $H_P^{(3)}(\boldsymbol{\rho}, \rho_z) = -H_P^{(3)*}(\boldsymbol{\rho}, \rho_z)$ and $H_A^{(3)}(\boldsymbol{\rho}, \rho_z) = H_A^{(3)*}(\boldsymbol{\rho}, \rho_z)$ so that phase information may be decoupled from amplitude information as in the coherent case. The in-focus intensity derivative is estimated by convolution with a SGDF with coefficients given by $h_{SG}[j] =$

$a_j/\Delta z$, as shown in Eq. (2.4), where N is the half-data length, j is the image number index, Δz is the distance between defocused planes, and $j = 0$ corresponds to the in-focus plane:

$$\frac{dI(\mathbf{r}, 0)}{dz} = \sum_{j=-N}^N \frac{a_j I(\mathbf{r}, j\Delta z)}{\Delta z}. \quad (2.4)$$

It then follows from the convolution and Fourier central slice theorems that the lateral Fourier spectrum of the derivative estimate may be represented by integrating the POTF multiplied by the SGDF frequency response, $H_{SG}(e^{i2\pi\rho_z\Delta z})$, along the axial spatial frequency coordinate, Eq. (2.5):

$$\frac{dI(\boldsymbol{\rho})}{dz} = \phi(\boldsymbol{\rho})H_P^{(2)}(\boldsymbol{\rho}), \quad (2.5a)$$

where

$$H_P^{(2)}(\boldsymbol{\rho}) = \frac{4\pi}{\lambda} \int H_{SG}(e^{i2\pi\rho_z\Delta z})H_P^{(3)}(\boldsymbol{\rho}, \rho_z)d\rho_z. \quad (2.5b)$$

$\phi(\boldsymbol{\rho})$ in Eq. (2.5a) corresponds to the 2D object phase spectrum and $i = \sqrt{-1}$. Equation (2.5b) defines the 2D POTF corresponding to the intensity derivative estimate under finite amounts of defocus. If the SGDF bandwidth is larger than the WOTF support, the axial frequency response in Eq. (2.5b) may be replaced by an ideal differentiation filter and the weakly defocused (WD) POTF derived in [8] is then recovered as

$$H_{P_w}^{(2)}(\boldsymbol{\rho}) = \frac{4\pi}{\lambda} \int i2\pi\rho_z H_P^{(3)}(\boldsymbol{\rho}, \rho_z)d\rho_z. \quad (2.6)$$

The POTF implied by the TIE (for a pure phase object) is easily identified by inspection of the TIE in the Fourier domain, [Eq. (2.7)], where $\bar{\lambda}$ is mean wavelength of the quasi-monochromatic illumination and $\rho = |\boldsymbol{\rho}|$. The use of a quasi-monochromatic approximation is justified if an interference filter is used in combination with broad band source such as mercury arc or halogen lamp. The background intensity B is given by Eq. (25) in [66]:

$$\frac{dI(\boldsymbol{\rho})}{dz} = \phi(\boldsymbol{\rho})2\pi\bar{\lambda}B\rho^2, \quad (2.7a)$$

$$H_{P_{TIE}}^{(2)}(\boldsymbol{\rho}) = 2\pi\bar{\lambda}B\rho^2. \quad (2.7b)$$

Figure 2.2 shows the normalized POTFs under finite defocus for a few SGDF orders m and coherence parameters S of 0.1, 0.5, and 0.9, where NA_o is 0.75 and $\bar{\lambda}$ is 546 nm. The half-data length N of the defocused image stack is 15 and the distance between symmetrically defocused planes Δz is 0.6 μm . For consistency, these same parameters will be used throughout the chapter. The WD and TIE POTFs are also plotted in Fig. 2.2 for reference.

As can be seen clearly by Fig. 1 in [123], regardless of S , the axial width of the 3D WOTF is greatest at the normalized frequency $\rho^N = 1$, even though this does not correspond to the maximum frequency transmitted. Consequently the spatial filters used in the decomposition phase of MFPI-PC take on a slightly different form. The form and cut-off frequencies of the spatial filters are defined by Eq. (2.8), where ρ_{co} is a lateral cut-off frequency for the spatial filter corresponding to a specific SGDF order m and χ is a constant that defines the cut-off ratio. Our experiments thus far have yielded good results with $\chi = 0.99$; however, its exact value represents another noise-resolution trade-off:

$$\chi = \frac{H_P^{(2)}(\rho_{co})}{H_{P_W}^{(2)}(\rho_{co})}. \quad (2.8)$$

For larger values of S there may be two cut-off frequencies, corresponding to a lower and upper cut-off, which define upper and lower bounds for the frequency range which can accurately be estimated with the corresponding SGDF. Each Fourier component of the resulting composite phase should be estimated using the lowest-order SGDF possible since noise is effectively suppressed by lower orders.

There is no simple relationship for the cut-off frequencies as they depend, in general, on N , m , Δz , S , NA_o , and $\bar{\lambda}$. Figure 2.3 depicts the normalized cut-off frequencies

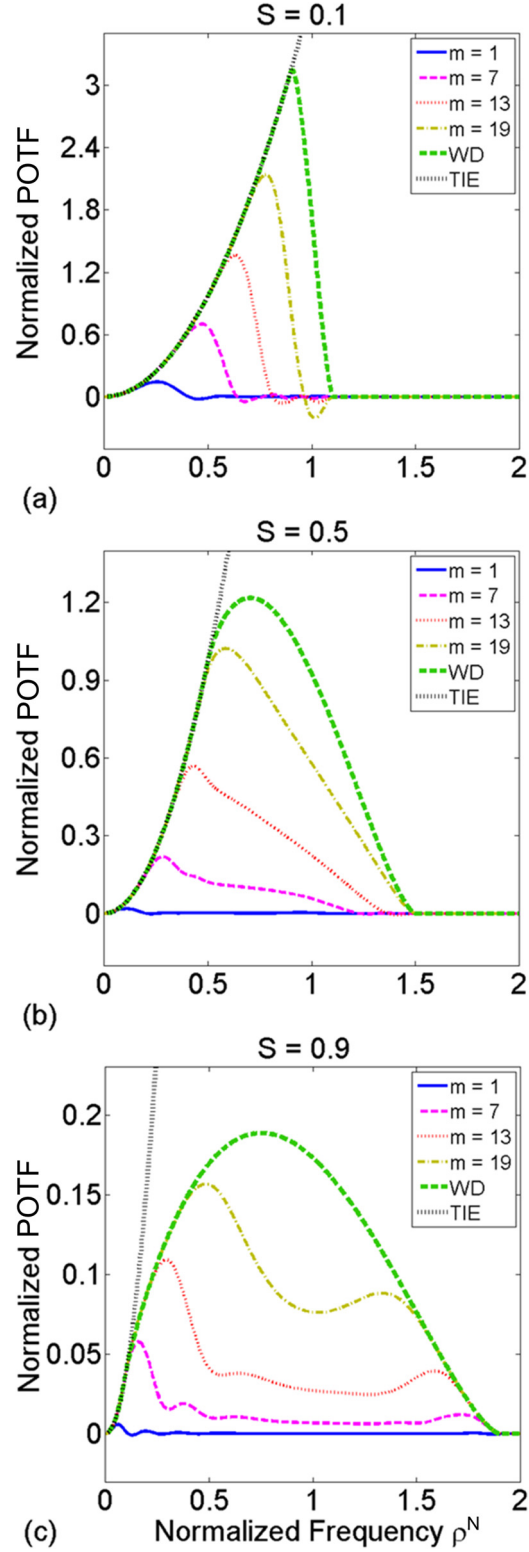


Figure 2.2: Normalized phase optical transfer functions (POTFs) $[H_p^{(2)} \Delta z / B, \rho^N = \bar{\lambda} \rho / NA_o]$ for orders $m = 1, 7, 13,$ and 19 and coherence parameters (a) $S = 0.1,$ (b) $S = 0.5,$ and (c) $S = 0.9.$ Weakly defocused (WD) and TIE POTFs are also plotted.

calculated using Eq. (2.8) for odd orders $m = 1$ through 25 and the same coherence parameters as in Fig. 2.2. As expected, the normalized lower and upper cut-offs converge to 1 as m is increased. The cut-off frequencies for the coherent case ($S = 0$) are also plotted in Fig. 2.3 for reference.

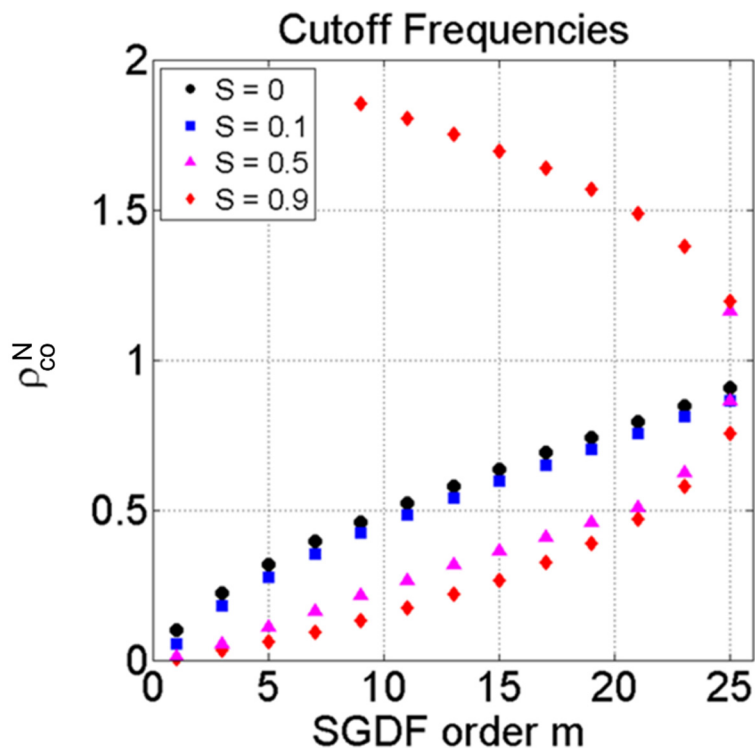


Figure 2.3: Normalized cut-off frequencies ($\rho_{co}^N = \bar{\lambda}\rho_{co}/NA_o$) for odd orders $m = 1$ through 25 and coherence parameters $S = 0, 0.1, 0.5,$ and 0.9 .

The partially coherent PTFs are given by dividing the estimated POTF by the implicit TIE POTF.

$$\text{PTF}(\boldsymbol{\rho}) = \frac{H_P^{(2)}(\boldsymbol{\rho})}{H_{PTIE}^{(2)}(\boldsymbol{\rho})}. \quad (2.9)$$

PTFs under finite defocus are plotted in Fig. 2.4 again for the same parameters as in Fig. 2.2. The WD PTFs are also included for reference. It can be seen that the theoretical resolution using this method is improved as S is increased at the cost of reduced contrast over a broad range of spatial frequencies due to aperture cut-off effects. When the MFPI-

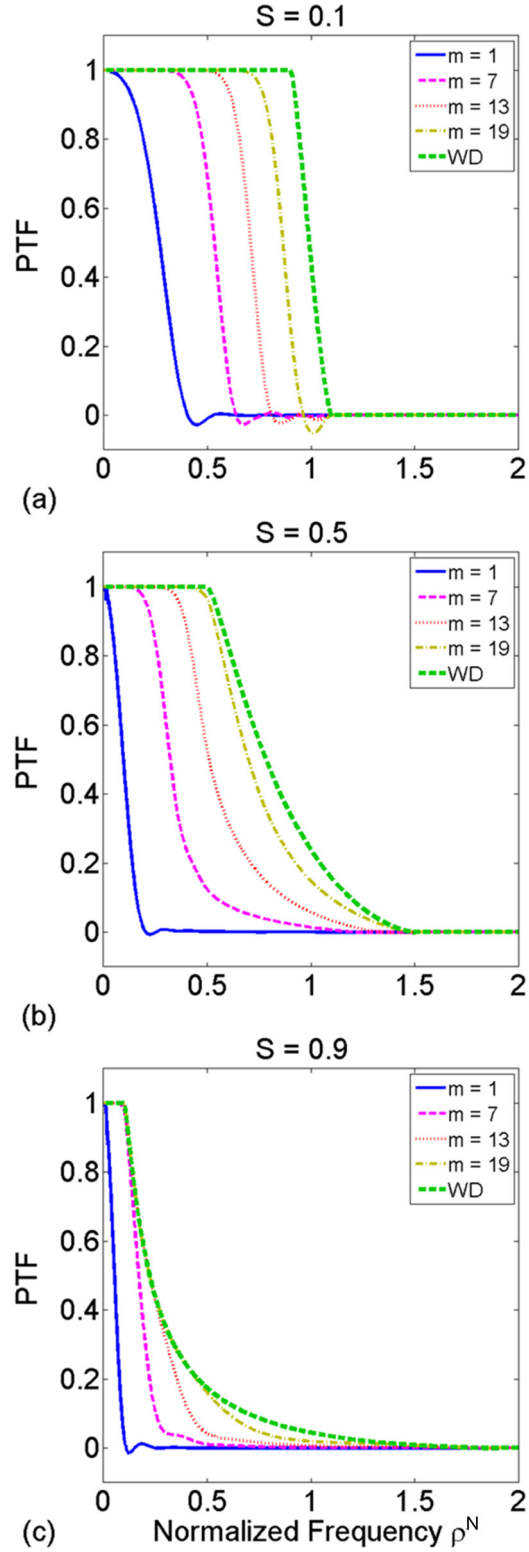


Figure 2.4: Phase transfer functions (PTFs) for orders $m = 1, 7, 13, 19$ and for coherence parameters (a) $S = 0.1$, (b) $S = 0.5$, and (c) $S = 0.9$ where $\rho^N = \bar{\lambda}\rho/NA_0$. Weakly defocused (WD) PTFs are also plotted.

PC method is used, the composite PTF approaches the WD PTF without increasing noise sensitivity, as will be verified numerically and experimentally in Sections 2.3 and 2.4.

2.3 Simulation Results

An alternative, and intuitive, description of a Köhler illuminated imaging system comes by way of a CMD. Using this method a partially coherent wave-field may be decomposed into statistically independent coherent modes with well-defined phases [122]. Because each mode is statistically independent, the resulting intensity pattern is the summation of intensities due to each mode [122]. For a delta-correlated source, the coherent modes correspond to individual plane waves propagating through the object with various inclination angles. Therefore, the intensity pattern resulting from an arbitrary object is easily modeled by summing together the intensities due to a large number of off-axis plane waves which have been apertured appropriately. The equivalence of the CMD formulation with the WOTF theory described in Section 2 can be demonstrated by a numerical example.

Using the CMD method, the intensities due to a weakly scattering phase object consisting of the letters “GT” as shown in Fig. 2.5 are simulated. The units of simulated phase object are radians. The simulation parameters match those in Section 2 and the grid dimensions are 1030×1300 with a square pixel size of $0.245 \mu\text{m} \times 0.245 \mu\text{m}$. In each simulation, the illuminating aperture was uniformly discretized into 40 intervals in each direction of the lateral spatial frequency domain resulting in around 1,256 individual plane waves. A Fresnel propagation kernel is used to mimic the paraxial approximation inherent in [66]. No noise was added in order to directly compare the simulated results to those predicted by WOTF theory. The PTFs are found by simply dividing the phase spectra estimated using a fixed order m by the simulated phase spectrum. In every case, the resulting radially averaged PTFs obtained from the simulation were indiscernible

from the PTFs obtained with WOTF theory as plotted in Fig. 2.4, indicating that the two formulations are equivalent.



Figure 2.5: Simulated phase object.

Lifting the paraxial approximation and using a spherical propagator instead results in error upon inversion of the TIE since it is based on a paraxial approximation. These errors are, in general, non-negligible for high-NA imaging systems and large coherence parameters especially. A detailed treatment of the errors associated with applying the TIE to such scenarios is beyond the scope of the present work. However, for all the cases highlighted here, the non-paraxial results show reasonable agreement with the paraxial theory and successfully demonstrate the anticipated characteristics. That is to say that the desired characteristics hold even though the remainder of simulation and experimental results presented in this chapter are based on non-paraxial light propagation.

Figure 2.6 displays the phases recovered after adding white Gaussian noise with normalized standard deviation $\sigma = 0.002$ to each simulated intensity image, where σ defines the ratio of the noise standard deviation to the mean image intensity level, meaning that the amount of noise added was 0.2% of the background intensity. If a first-order order SGDF is used, as in Fig. 2.6(a), 2.6(d), and 2.6(g), a blurry version of the original phase image is obtained along with the addition of a small amount of low spatial

frequency noise artifacts. Although the registered trademark symbol is not discernible in any case, the blurring is more severe as S is increased. This is because the longitudinal width of the 3D POTF dramatically increases with S for low to mid-range spatial frequencies [66].

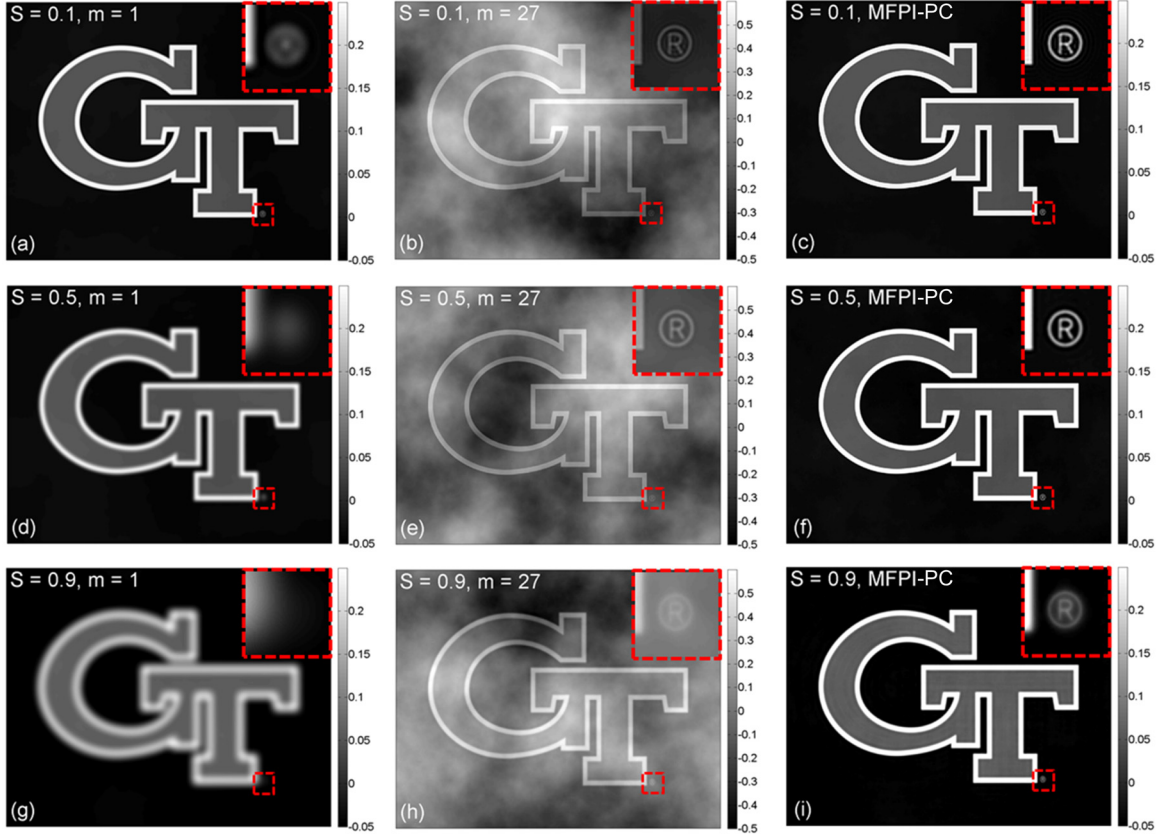


Figure 2.6: Recovered phases (colorbar units–radians) for (a) $S = 0.1$ and fixed-order $m = 1$, (b) $S = 0.1$ and fixed-order $m = 27$, (c) $S = 0.1$ and MFPI-PC including orders $m = 1$ to 27, (d) $S = 0.5$ and fixed-order $m = 1$, (e) $S = 0.5$ and fixed-order $m = 27$, (f) $S = 0.5$ and MFPI-PC including orders $m = 1$ to 27, (g) $S = 0.9$ and fixed-order $m = 1$, (h) $S = 0.9$ and fixed-order $m = 27$, and (i) $S = 0.9$ and MFPI-PC including orders $m = 1$ to 27. In all figures the registered trademark symbol is expanded in the top right with its associated location given by the dashed square outlines.

If a 27th-order SGDF is used, as in Fig. 2.6(b), 2.6(e), and 2.6(h), the resolution improves as the trademark symbol becomes discernible in each case. However, using a large-order m results in dramatically increased noise sensitivity due to overfitting. If the MFPI-PC method is applied, combining odd orders $m = 1$ through 27 and using the cut-off frequencies shown in Fig. 2.3, the resulting composite phase spectrum should

approximate the simulated phase spectrum multiplied by the corresponding WD PTF without adding severe noise. Careful inspection of Fig. 2.6(c), 2.6(f), and 2.6(i) verifies that this is true. The noise artifacts are of the same level as the first-order estimates, and the resolution features demonstrate the anticipated characteristics. In each case the registered trademark symbol is discernible; however its magnitude is reduced as S is increased due to aperture effects.

Figure 2.7 displays the phase recovered using the established OFS method [48] on partially coherent intensity data, $S = 0.5$, without taking partial spatial coherence into account. In this simulation the same level of Gaussian noise ($\sigma = 0.002$) was added and the cut-offs for $S = 0$ and $m = 1$ through 27 (also shown in Fig. 2.3) were used. Although the noise reduction is satisfactory because the first-order SGDF is used for most of the low spatial frequencies, it is plain to see that the overall reconstruction has been severely impacted by the improper placement of filter cut-off frequencies, resulting in the unnecessary attenuation of certain spatial frequencies.

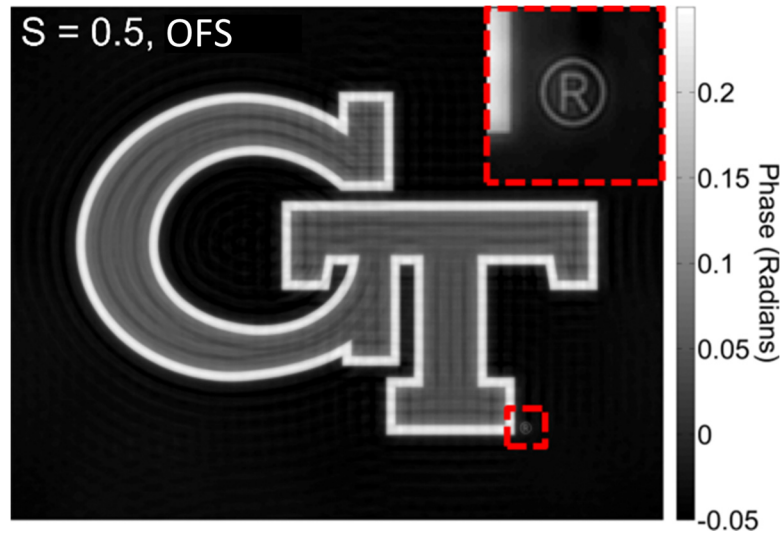


Figure 2.7: Recovered phase for $S = 0.5$ and optimal frequency selection (OFS) including orders $m = 1$ to 27. The registered trademark symbol is expanded in the top right with its associated location given by the dashed square outlines.

To demonstrate the robustness of the MFPI-PC method in the presence of severe noise, the phase root mean squared errors (RMSEs) as a function of simulated normalized

noise standard deviations from $\sigma = 0$ to 0.015 for the cases when $S = 0.1$, $S = 0.5$, and $S = 0.9$ are plotted in Fig. 2.8, where σ has the same meaning as before. The errors were calculated 10 times and averaged to reduce uncertainty. For all cases the same general behavior as given by Fig. 7 in [48] is observed in which the lower order estimates are more robust against noise but possess larger error with small noise levels due to lack of spatial resolution. In fact, for a given noise level, there is a fixed-order m which produces the lowest RMSE on average. However, with the MFPI-PC method, the full spatial resolution of the highest order is available and the RMSE is always lower because it judiciously stitches together the best portions from each phase estimate. The results also show that the MFPI-PC method is robust in the presence of high levels of noise as the slope of its RMSE with σ is only slightly larger than that of the first-order estimate for all cases. For comparison, the resulting RMSE for the OFS method is also plotted. When $S = 0.1$, the illumination is nearly coherent so that the MFPI-PC and OFS results are nearly indiscernible. This makes perfect sense because the MFPI-PC method is more general and converges to the OFS method with decreasing coherence parameters as can be seen by examining the cut-offs in Fig. 2.3 for $S = 0.1$ and $S = 0$. When $S = 0.5$, it can clearly be seen that the MFPI-PC results are better. This is because of the unnecessary attenuation of certain spatial frequency ranges due to improper placement of filter cut-off frequencies which produces the ringing artifacts evidenced by Fig. 2.7. Lastly, when $S = 0.9$, the OFS results approach the $m = 1$ results because the lower cut-off frequencies for each filter order are much higher than they should be resulting in severe attenuation for most frequency ranges. The MFPI-PC method correctly accounts for these effects and removes much of the blur typically present when attempting TIE phase recovery using relatively incoherent illumination.

It should be mentioned here that the optimal choice of distance between planes Δz was also investigated as a function of various parameters including σ , N , and S . The overall conclusion is that the result is ultimately object dependent, however, a general

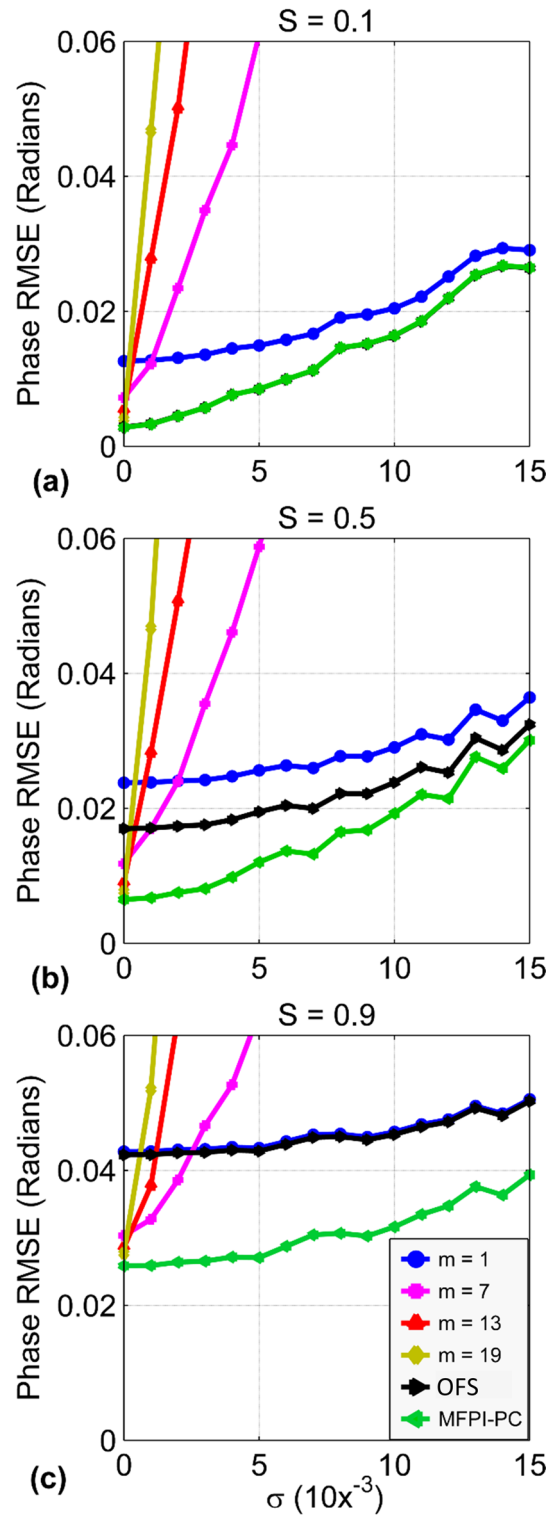


Figure 2.8: Phase root mean squared error (RMSE) as a function of normalized noise standard deviation σ (unitless) for (a) $S = 0.1$, (b) $S = 0.5$, and (c) $S = 0.9$ and fixed-orders $m = 1, 7, 13$, and 17 compared with the MFPI-PC result. The result for optimal frequency selection (OFS) is also plotted in each case.

rule of thumb is to select Δz such that the bandwidth of the highest-order SGDF used is equal to the longitudinal frequency support of the 3D WOTF. Choosing Δz to be larger than this value results in a loss of spatial resolution and choosing Δz to be smaller results in the unnecessary amplification of noise.

2.4 *Experimental Results*

To verify the theoretical predictions of this work, the phase shift induced by a visible blazed transmission grating (*Thorlabs GT13-03*, grating period $\Lambda = 3.33 \mu\text{m}$, blaze angle $\theta_B = 17.5^\circ$, Schott B270 glass $n_{\text{glass}} = 1.5251$) is measured using the proposed method with the same parameters as in Section 2.3. The imaging system is realized with an *Olympus BX60* microscope and a *UPlanFl 40 \times / 0.75* objective. The grating is mounted face up on a glass slide with refractive index (RI) matching oil (*Cargille Labs* $n_{\text{oil}} = 1.4620$) and a 0.17 mm coverslip. Applying the periodic boundary conditions inherent in the fast Fourier transform-based solution to the TIE to the periodic grating results in large low frequency phase shifts which are not related to image noise or background phase. To suppress this effect without rendering the result non-quantitative the composite phase images are high-pass filtered with a cut-off frequency defined by half of the first harmonic frequency of the grating, thereby also removing background effects and most of the noise. Because of this, the results presented here mostly demonstrate the resolution characteristics of MFPI-PC without much noise influence. The noise effects are demonstrated later using an optical fiber as a test object. It should be noted that although the periodic boundary conditions are an issue for this particular object it is not related to the MFPI processing and alternative solutions have been proposed in [124-126]. For a discussion on the effects of various boundary conditions on TIE solvers see [124].

The measured phase profiles for a 100×100 pixel square patch are represented in Fig. 2.9(a) and 2.9(b) as surface plots for $S = 0.1$ and 0.5. The results are interpolated for ease of viewing. Also plotted in Fig. 2.9(c) and 2.9(d) are a few periods of the associated

line profiles with no interpolation. Plotted for reference are the ideal profiles, assuming 90° groove angles, as well as the predicted results determined by filtering the ideal profiles with the appropriate WD PTF. In both cases there is excellent agreement between the measured profile and the predicted profile. The hard aperture effects are clearly visible in the measured profile for $S = 0.1$ as evidenced by the rapid oscillations. The soft aperture/extended resolution effects are clearly visible for $S = 0.5$ as evidenced by the smooth profile and slightly reduced amplitude. Results for $S = 0.9$ did not match the theory well because the measured intensities exhibited a high degree of asymmetry about the focal plane due to primary spherical aberration associated with the non-corrected thickness of the RI matching oil between the grating and the coverslip. In order to increase accuracy for large S , objective lenses with correction collars may be used to ensure symmetry in the microscope point spread function.

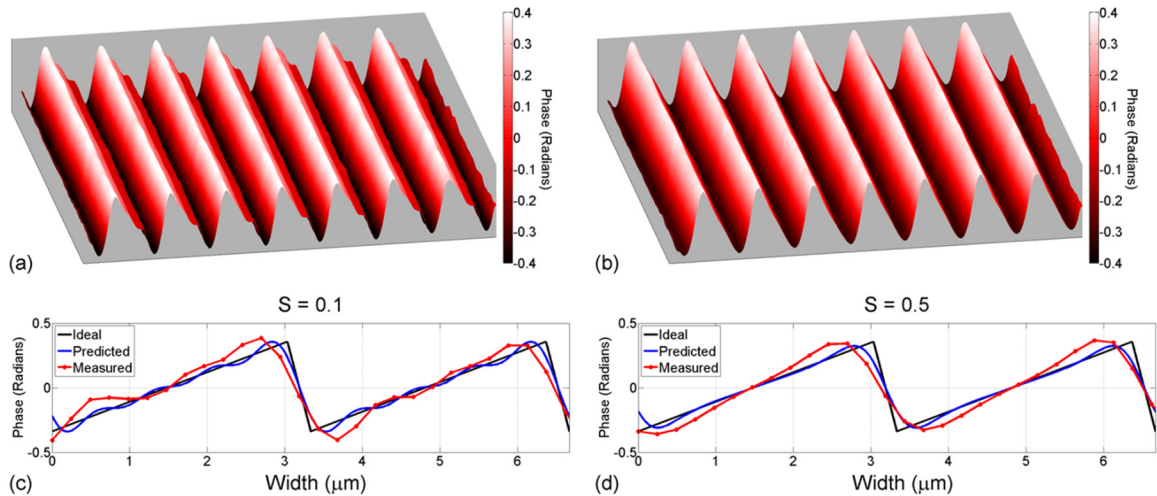


Figure 2.9: Visible transmission grating phase measurement results. Interpolated surface plots of the measured phase on a $24.5 \mu\text{m} \times 24.5 \mu\text{m}$ patch for (a) $S = 0.1$ and (b) $S = 0.5$. Measured line profiles for (c) $S = 0.1$ and (d) $S = 0.5$. Ideal (assuming 90° groove angles) and predicted [filtered using the associated weakly defocused phase transfer function (WD PTF)] line profiles are also plotted for reference.

To demonstrate the joint noise/resolution capability of MFPI-PC, the RI distribution of a single-mode optical fiber (*Corning SMF-28*) is reconstructed tomographically using filtered backprojection (FBPJ) [56]. As part of this reconstruction, phase profiles are

measured every 2° using the same parameters as in Section 2.3 for $S = 0.5$, which is solidly in the partially coherent regime. The fiber experiment was conducted using the same equipment and procedures outlined in Section 2 of [31] with the exception that the defocusing was achieved using a piezoelectric microscope objective scanner (*Physik Instrumente P-721.SL2*) and the same defocus parameters as in Section 2.3 were used. For all measurements, the fiber is suspended in RI matching oil between two coated fiber pieces and rotated about its axis, and the overall experimental setup is as shown in Fig. 1 in [31].

The resulting sinograms and tomograms are presented in Fig. 2.10. In this figure, four separate methods, including conventional TIE phase recovery using defocus distances (δz) of $9\ \mu\text{m}$ and $0.6\ \mu\text{m}$ as well as OFS and MFPI-PC (organized by row from top to bottom), were used to estimate the fiber phase shift. Organized by column are three separate representations of the data, including (from left to right) the phase sinogram, the Fourier spectrum of the phase sinogram (represented as the logarithm of the squared magnitude of the data), and lastly the resulting cross-sectional RI distribution. In Fig. 2.10(a) there is little variation in the recovered phase profiles versus projection angle because the fiber is radially symmetric and the noise performance is in direct proportion to the defocus distance, which is large. Likewise for Fig. 2.10(d) there are large variations (manifested as slowly varying features in the x direction) from angle to angle due to the small defocus distance used. However, in Fig. 2.10(b) we see that much of the high spatial frequency content (plotted along ρ_x) has been severely attenuated in the large defocus distance case when compared to the spectrum in Fig. 2.10(e). This results in a loss of radial spatial resolution which can be easily seen by comparing the cross-sectional tomograms in Fig. 2.10(c) and 2.10(f). The top-right insets in these figures display a zoomed-in version of the fiber core. Due to the fiber manufacturing process, it is well-known that there is a dip in RI which results in the center of the core and the reconstruction in the Fig. 2.10(f) is sharp enough to resolve this feature whereas the

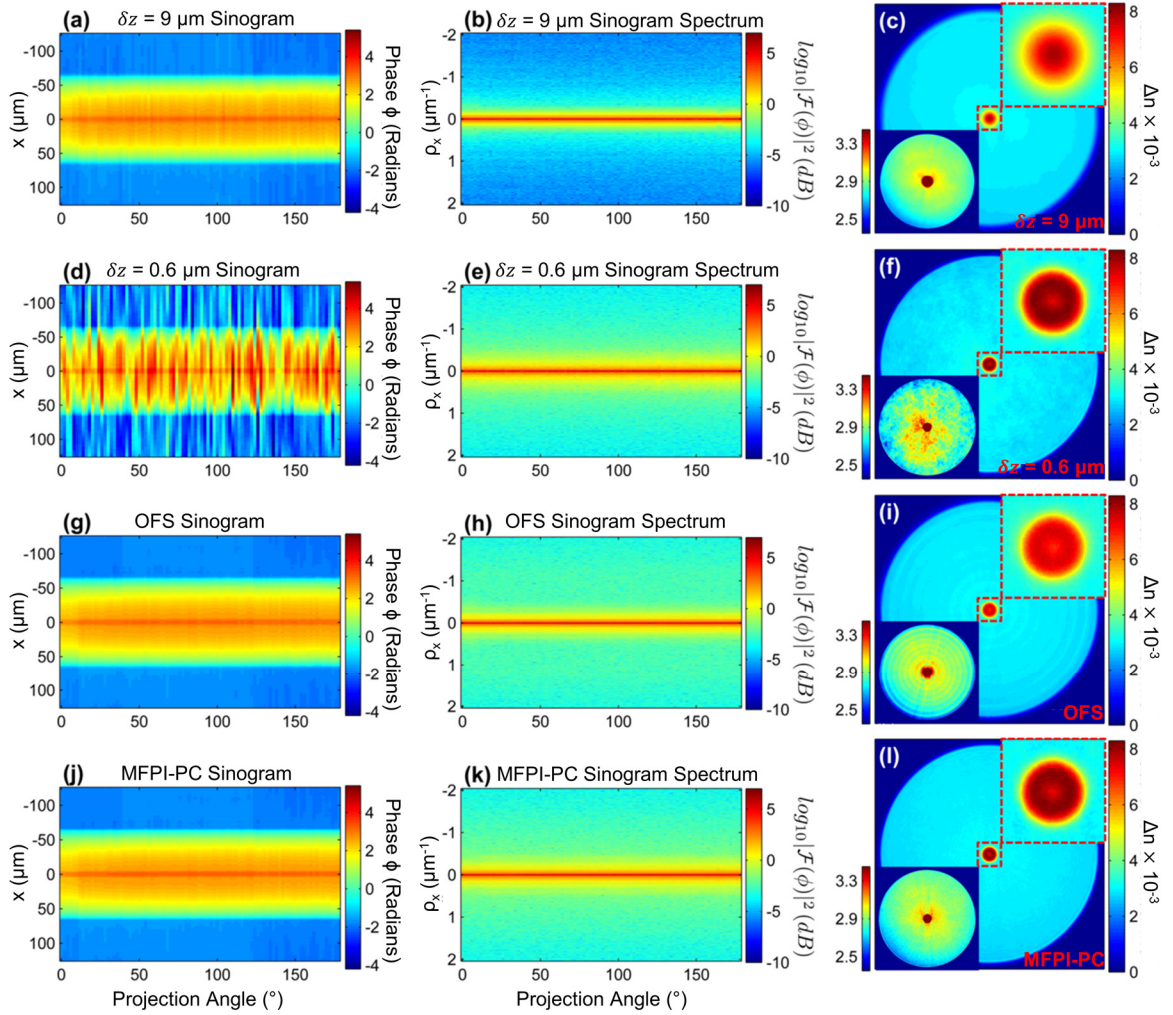


Figure 2.10: Various representations of optical fiber tomography experimental data processed using conventional TIE recovery with defocus distances of (a-c) $9\ \mu\text{m}$ and (d-f) $0.6\ \mu\text{m}$ as well as the established (g-i) OFS method and the proposed (j-l) MFPI-PC method. The phase sinogram data is represented in the first column [(a), (d), (g), and (j)]. The logarithm of the phase spectral density is represented in sinogram format in the second column [(b), (e), (h), and (k)]. The resulting tomograms, after applying filtered backprojection (FBPJ) using the data in the first column, are represented in the third column [(c), (f), (i), and (l)] as the relative difference in RI from the background $\Delta n(\mathbf{r}) = n(\mathbf{r}) - n_{\text{oil}}$ (RI units). Within the third column, the top-right insets are a zoomed-in image of the fiber core (region indicated by the dashed squares) and the bottom-left insets enhance contrast in the cladding using different colorbar limits. Partially coherent ($S = 0.5$) illumination was used to produce the intensity data for the measurement.

reconstruction in Fig. 2.10(c) displays a profile which is similar to a Gaussian in shape. The effects of noise are clearly seen by examining the variations in the cladding, which are displayed in the bottom-left insets where the colorbar limits have been altered to enhance contrast. In Fig. 2.10(f) the presence of noise is manifested as cladding variation and is much less uniform than in Fig. 2.10(c). As a side note, however, it should be mentioned here that projection tomography works well with TIE phase recovery to reduce noise overall because the phase noise features are proportional to $1/\rho_x^2$ and these same features are later processed with a filter proportional to ρ_x as part of the FBPJ algorithm resulting in tomogram noise which is proportional to $1/\rho_x$ only.

In Fig. 2.10(g)-2.10(i) the phase has been recovered using the established OFS method and in Fig. 2.10(j)-2.10(l) the phase has been recovered using the proposed MFPI-PC method. Although OFS appears to have resulted in excellent noise suppression and non-attenuated frequency content the cross-section in Fig. 2.10(i) has some artifacts which are not evident in the other tomograms. The core-cladding RI difference may be estimated by manual inspection of the tomogram data and is found to be $\sim 4.4 \times 10^{-3}$ for the OFS case and $\sim 5.1 \times 10^{-3}$ for the MFPI-PC case, a difference of $\sim 14\%$. The latter of these two approximations is in agreement with previously published data based on microinterferometry [22]. In addition to an inaccurate core index estimate, there are ringing artifacts manifested in the cladding which also result from the unnecessary attenuation of certain spatial frequency ranges. Lastly, the powerful capability of the MFPI-PC method to simultaneously suppress noise and enhance resolution without introducing measurement inaccuracy is manifested in Fig. 2.10(j)-2.10(l). In Fig. 2.10(j), there is little to no variation in phase across projection angles. In Fig. 2.10(k), significant attenuation of high spatial frequencies is not observed. In Fig. 2.10(l), both of these effects are manifested in the highly uniform cladding and the presence of a sharp center dip in RI. No ringing artifacts are observed and the measured core-cladding index

difference matches previously published data quite well [22]. All in all, the anticipated characteristics of the various processing methods are verified experimentally.

It should be mentioned here that MFPI-PC performs well in this scenario regardless of the fact that two assumptions inherent to its derivation are violated. The fiber is not a weak phase object as the maximum phase shift is approximately 3.6 radians [56]. Similarly, others have also found PR by means of direct inversion of the WOTF to be surprisingly robust with strong phase objects [49]. In principle, this is not surprising since the slowly varying phase approximation $|\phi(\mathbf{r}) - \phi(\mathbf{r} - \bar{\lambda}z\boldsymbol{\rho})| \ll 1$ used in coherent x-ray CTF phase recovery [127] is a relative condition dependent on wavelength, defocus, and spatial frequency and MFPI naturally tends to pair large spatial frequencies with small defocus distances and vice versa. This concept, as well as the relationship between the aforementioned condition and partial spatial coherence, will be explored further in Chapter 3.

Also, the fiber is clearly not a thin object as its diameter is much larger than the depth of focus. However, in [128] it was found that for simple geometries the WOTF theory produces accurate phase values if the object thickness along the optical axis is less than its lateral width. Providing a detailed error analysis is not the purpose of the present work, however, we note here the experimental observation of robustness with respect to these assumptions.

2.6 Summary

In this work, the basic principles of multi-filter phase imaging (MFPI) have been extended to the important practical case of partially spatially coherent illumination from an extended incoherent source (MFPI-PC). Results indicate that the MFPI-PC method can correctly account for a variety of coherence levels in the incident illumination. Results show that MFPI-PC is not only feasible but also desirable in the sense of enhanced lateral spatial resolution. Although MFPI-PC phase image theoretically shares

the same spatial resolution as optical microscopy, i.e. $1.22\bar{\lambda}/(NA_o + NA_c)$, the resolution corresponding to frequencies which are non-attenuated and therefore quantitative is actually $1.22\bar{\lambda}/(NA_o - NA_c)$ or $1.22 \times 546 \text{ nm} / (0.75 - 0.375) \approx 1.78 \mu\text{m}$ for the parameters used here, an issue which will be addressed and overcome in the next chapter. Using this method, highly sensitive QPI may be achieved in situations for which traditional interferometry is not practical and iterative methods are less effective. The sensitivity is dependent on a number of factors including image size, number of defocused images, defocus spacing, and level of coherence, however, for the parameters used here and $S = 0.5$, phase and optical path length resolutions approach ~ 0.02 radians or $\sim 1.74 \text{ nm}$ respectively. Although the method is based on assumptions of paraxial propagation through weakly scattering thin objects it is demonstrated here that considerable flexibility exists with regard to these assumptions. In summary, MFPI-PC appears to be a very powerful high-resolution/low-noise method for imaging a wide range of phase objects using readily available, realistic illumination sources.

CHAPTER 3

QUANTITATIVE PHASE MICROSCOPY VIA OPTIMIZED INVERSION OF THE PHASE OPTICAL TRANSFER FUNCTION

In Chapter 2, a novel phase reconstruction method, which is called multifilter phase imaging with partially coherent light (MFPI-PC) and enables quantitative phase imaging (QPI) using Köhler illuminated microscopy, was presented. In this chapter, another two-dimensional (2D) QPI method, called phase optical transfer function (POTF) recovery, is presented which, in addition to enabling quantitative phase microscopy (QPM) with no hardware modification, also overcomes many non-optimal aspects of MFPI-PC, including inefficient defocus sampling based on equally spaced planes, limited spatial resolution due to a reliance on the paraxial approximation, reduction of quantitative phase contrast due to finite numerical aperture (NA), and non-optimal noise suppression. POTF recovery is based on optimized inversion of the weak object transfer function (WOTF), which is shown here to be capable of imaging strong phase objects with large overall phase delay. POTF recovery is evaluated using numerical simulations and validated using a microlens array (MLA) as a test phase object. Once validated, the method is applied directly to time-lapse QPI of live adherent cell cultures to demonstrate its potential capability for biomedical applications. This chapter is based on a paper entitled “Quantitative phase microscopy via optimized inversion of the phase optical transfer function,” which was recently accepted for publication [129] and an associated provisional patent application [130].

3.1 Introduction

Quantitative phase imaging (QPI) is an emerging field in biomedical optics in which the optical path length (OPL) of phase objects, including biological specimens, is indirectly

imaged through interferometric analysis. Because it is label-free, QPI of live cells is possible without photo-toxicity or photo-bleaching as in fluorescence microscopy. QPI is capable of measuring the intrinsic properties of cells and tissues, as opposed to phase and differential interference contrast (DIC) microscopy which only provide qualitative information. The quantitative nature of the data also lends itself towards image processing, thereby improving the extractability of various physical, chemical, biological, and mechanical properties [131].

These quantitative measurements are likely to yield new understanding about the physiology/pathology of cells. For example, QPI was recently used to improve understanding of cell growth, a question which has long eluded biologists due to a lack of robust instrumentation for resolving the mass of individual adherent cells [11]. QPI data was used to measure exponential growth in *Escherichia coli* by relating integrated OPL to dry mass [11], implying the need for regulatory systems to maintain homeostasis. On the diagnostic front, machine learning algorithms based on QPI data have recently shown remarkable agreement with certified pathologists for the automated diagnosis of prostate cancer from tissue biopsies [132].

Because light detectors only measure intensity, phase information must be measured indirectly. Conventional approaches include interferometry and holography in which phase images are extracted from either temporally or spatially modulated interferograms or holograms detected in either in-focus or out-of-focus planes [6]. Typically, these methods require illumination to be coherent, which is known to reduce temporal and spatial phase sensitivity due to the presence of phase jitter and speckle interference [133, 134]. Mitigating coherent noise in QPI systems is expensive as it requires a high degree of mechanical isolation and parasitic reflection control.

Another approach, which has been highly effective, is to circumvent coherent noise by designing QPI systems based on common-path interferometry [42, 135] to be compatible with partially coherent or even incoherent illumination [34, 38, 43, 55, 136-

139], many of which such systems achieve nanoscale OPL sensitivity [34, 38, 43, 55, 136, 138]. A key advantage of these modifications is that they often lead to modular compatibility with commercial microscopes [34, 38, 42, 43, 135-137, 140, 141], the results of which have been transformative for the biomedical application of QPI [6, 10-12, 14, 18, 43, 132, 142-155]. Quantitative phase microscopy (QPM, or QPI via microscopy) has been enabling for many reasons, such as the ability to perform multi-modal investigations correlating QPI data with images from other microscopy modalities; for example fluorescence [156]. Another important, and perhaps primary, reason for the growth of biomedical applications based on QPM is the ubiquity of modern biological microscopy systems which are highly developed for live cell imaging with minimal invasion. Thus QPM methods are attractively seen as an integrable modality in addition to long established methods which are applied routinely, such as fluorescence, phase, or DIC.

Using the above observations, it may be argued that QPM methods based on phase retrieval (PR), which recover phase from light micrographs alone without explicit manipulation of reference or sample beams, are even more attractive to biomedical end users as they do not require any hardware modification. Within the context of PR from micrographs recorded under varying conditions, methods may be broadly categorized as iterative [44, 134, 157-162] or deterministic [7, 46, 49, 54, 108, 120, 121, 163, 164]. Iterative methods account for the inherent nonlinearity of the image formation process; however, since the problem is nonconvex [165], they cannot be proven to converge, thus adding additional complexity and constraints.

Deterministic PR is based on assumptions, concerning either the imaging parameters or the object, which linearize the image formation process. The most prominent examples of deterministic PR methods which have been applied to optical microscopy are solutions based on the transport-of-intensity equation (TIE) [46, 54] as well as the weak object transfer function (WOTF) [49, 120]. The TIE linearizes the relationship between phase

and the derivative of intensity along the axis of propagation [46] and the WOTF describes the frequency domain transfer of phase and absorption by expanding image intensity and ignoring bilinear terms originating from the self-interference of scattered light [66, 120]. The WOTF has also been called the contrast transfer function (CTF) in the field of propagation-based x-ray phase imaging [50, 51, 119].

Although methods based on the TIE assume weak defocus and paraxial imaging, the only object assumption in a widely used TIE solver [166] is that the gradients of phase and intensity are collinear [167], thus strong phase objects with sharp edges are theoretically recoverable. Another important feature in TIE recovery is that for quasi-monochromatic light (such that the coherence length is longer than the defocus distances used) and circularly symmetric illumination pupils in the Köhler geometry, the recovered solution is independent of the size of the extended incoherent source, making methods based on the TIE compatible with partial spatial coherence [108]. Such compatibility is not inherent in interferometric QPM methods, which result in halo artifacts [168] unless special measures, either optical [169] or computational [170], are taken to prevent or remove them. Recently, practical reconstruction methods based on the TIE have advanced considerably [48, 111, 114-116, 171-173], with efforts centered on circumventing the inherent trade-off between noise and spatial resolution in the choice of defocus distance(s) [47]. The optimal frequency selection (OFS) algorithm first proposed in [48] using spatially coherent light and later extended to the partially coherent case in [111] under the name of multifilter phase imaging (MFPI-PC) has shown great promise for the recovery of slowly varying objects [7]. However, the original descriptions are given for equally spaced planes whereas a recent study has shown exponentially spaced planes to be a more efficient sampling scheme [171]. In any case, partially coherent TIE methods result in high spatial frequency attenuation as the condenser numerical aperture (NA) is increased [111]. This results in blurry phase reconstructions with lower spatial resolution.

By contrast, reconstructions based on inverting the WOTF are capable of higher spatial resolution since they do not require a paraxial approximation and they directly compensate for attenuation at higher spatial frequencies [120]. Since phase contrast may be realized via any complex pupil transfer function [120], or by an asymmetric illumination pupil [121], defocus is not the only option for generating contrast. If defocus is used, however, the distances need not be small or equally spaced [174], resulting in improved sensitivity and sampling efficiency compared to TIE methods. Although, in the spatially coherent limit, WOTF phase reconstruction methods have a long history within the field of electron microscopy [175-177], foundational studies relating the theory of first-order diffracted intensity variations in both two-dimensional (2D) and three-dimensional (3D) optical microscopy have also been conducted by Streibl [66] and Sheppard [120, 178] which incorporate partial spatial coherence effects. More recently, microscopic WOTF phase reconstructions have been demonstrated using defocus under the paraxial approximation for both small [49] and large defocus [7]. In addition to defocus, WOTF phase recovery was achieved using differential phase contrast [121] realized via asymmetric illumination as well as Zernike phase contrast in the extreme ultraviolet [163]. One presumed drawback of methods based on the WOTF is reliance on the first-order Born approximation in which the magnitude of the scattered light is much smaller than the magnitude of the incident light [178], hence the use of “weak object” in WOTF. Interestingly, however, although each of the aforementioned authors acknowledge this approximation, the corresponding experimental results seem to indicate that recovery is possible even for objects in which the first Born approximation is not satisfied [7, 49, 121, 163].

In light of these findings, it is clear that further investigation concerning the range of applicability of the WOTF is warranted. In what follows, defocus-based WOTF phase recovery for spatially coherent light under the paraxial approximation is first reviewed and then generalized to incorporate partial coherence with arbitrary source/pupil

combinations. In the course of this development, it is recognized and shown that the WOTF may be linearized without assuming a weakly scattering object using conditions analogous to the weak absorption and slowly varying phase (SVP) conditions originally derived by Guigay [127]. Under these conditions, a new WOTF reconstruction method, which is based on an optimized inversion of the phase optical transfer function (POTF) portion of the WOTF and was briefly demonstrated in [179], is described which enables high spatial and phase resolution using defocused bright-field micrographs without any hardware modification. Due to experimental simplicity, this algorithm, referred to as POTF recovery, may appeal broadly to end users and practitioners, thus promoting a more widespread adoption of QPI in the biomedical community.

3.2 Quantitative Phase Microscopy via Inversion of the Weak Object Transfer Function

3.2.1 Coherent Phase Optical Transfer Function Recovery

In the limit of complete spatial coherence the WOTF is equivalent to the CTF referred to in the field of propagation-based x-ray phase imaging [50, 118]. It incorporates diffraction due to wave-object interactions which can be described by a transmittance function, Eq. (3.1), where $\mathbf{r} = x\hat{x} + y\hat{y}$ denotes spatial coordinates transverse to the propagation direction and $A(\mathbf{r})$ and $\phi(\mathbf{r})$ are the absorption (absorption coefficient integrated along the optical path) and phase distributions respectively and $i = \sqrt{-1}$:

$$T(\mathbf{r}) = \exp[-A(\mathbf{r}) + i\phi(\mathbf{r})]. \quad (3.1)$$

Guigay described the diffraction image spectrum due to paraxial wave propagation at distance z from the object plane as

$$I_z(\boldsymbol{\rho}) = \int T\left(\mathbf{r} - \frac{\lambda z \boldsymbol{\rho}}{2}\right) T^*\left(\mathbf{r} + \frac{\lambda z \boldsymbol{\rho}}{2}\right) \exp(-i2\pi \mathbf{r} \cdot \boldsymbol{\rho}) d^2 \mathbf{r}, \quad (3.2)$$

where $\boldsymbol{\rho} = \rho_x \hat{\rho}_x + \rho_y \hat{\rho}_y$ denotes spatial frequency coordinates conjugate to \mathbf{r} , λ is the illuminating wavelength, and x^* denotes the complex conjugation of x [127]. Equation (3.2) is an appropriate starting point for deriving both the TIE and WOTF [50]. Under the

assumptions of weak absorption, Eq. (3.3), and SVP, Eq. (3.4), we can reduce Eq. (3.2) to Eq. (3.5) by retaining only the first-order terms in the integral [50]. In Eq. (3.5), $\rho^2 = \boldsymbol{\rho} \cdot \boldsymbol{\rho}$ and a unit intensity normalization has been assumed.

$$\left| A\left(\mathbf{r} - \frac{\lambda z \boldsymbol{\rho}}{2}\right) + A\left(\mathbf{r} + \frac{\lambda z \boldsymbol{\rho}}{2}\right) \right| \ll 1. \quad (3.3)$$

$$\left| \phi\left(\mathbf{r} - \frac{\lambda z \boldsymbol{\rho}}{2}\right) - \phi\left(\mathbf{r} + \frac{\lambda z \boldsymbol{\rho}}{2}\right) \right| \ll 1. \quad (3.4)$$

$$I_z(\boldsymbol{\rho}) = \delta(\boldsymbol{\rho}) - 2 \cos(\pi \lambda z \rho^2) A(\boldsymbol{\rho}) + 2 \sin(\pi \lambda z \rho^2) \phi(\boldsymbol{\rho}). \quad (3.5)$$

Under this approximation, subtracting two symmetrically defocused micrographs recorded at positions $\pm z$ results in a directly invertible relationship between phase and intensity, Eq. (3.6):

$$\begin{aligned} \Delta I_z(\boldsymbol{\rho}) &= I_{+z}(\boldsymbol{\rho}) - I_{-z}(\boldsymbol{\rho}) \\ &= 4 \sin(\pi \lambda z \rho^2) \phi(\boldsymbol{\rho}) \\ &= H_z^C(\boldsymbol{\rho}) \phi(\boldsymbol{\rho}) \end{aligned} \quad (3.6)$$

In Eq. (3.6), $H_z^C(\boldsymbol{\rho})$ is the phase optical transfer function (POTF) for coherent illumination in the paraxial approximation corresponding to defocus distance z . In the limit of small z the POTF reduces to the transfer function implied by the TIE in the case of a pure phase object [47]. The sinusoidal function accounts for larger defocus but also introduces zeros into the POTF which establish the need for several distances to cover the whole Fourier domain [174]. The optimal spectral combination of N defocused image pairs ($2N$ total images) can be derived from the linear least squares formalism summarized by Eq. (3.7), where j is the index of defocused image pairs and α is a regularization parameter. Equation (3.7) can be solved to yield $\phi(\boldsymbol{\rho})$ as given by Eq. (3.8).

$$\min \epsilon = \sum_{j=1}^N \left| H_{z_j}^C(\boldsymbol{\rho}) \phi(\boldsymbol{\rho}) - \Delta I_{z_j}(\boldsymbol{\rho}) \right|^2 + \alpha |\phi(\boldsymbol{\rho})|^2. \quad (3.7)$$

$$\phi(\boldsymbol{\rho}) = \sum_{j=1}^N \xi_{z_j}(\boldsymbol{\rho}) \hat{\phi}_{z_j}(\boldsymbol{\rho}). \quad (3.8a)$$

$$\xi_{z_j}(\boldsymbol{\rho}) = \frac{|H_{z_j}^c(\boldsymbol{\rho})|^2}{\left[\sum_{j=1}^N |H_{z_j}^c(\boldsymbol{\rho})|^2 + \alpha \right]}. \quad (3.8b)$$

$$\hat{\phi}_{z_j}(\boldsymbol{\rho}) = \frac{\Delta I_{z_j}(\boldsymbol{\rho})}{H_{z_j}^c(\boldsymbol{\rho})}. \quad (3.8c)$$

In Eq. (3.8), $\xi_{z_j}(\boldsymbol{\rho})$ can be viewed as radially varying weighting functions which define the level of confidence that can be placed in a given phase estimate spectrum, $\hat{\phi}_{z_j}(\boldsymbol{\rho})$. The values of $\xi_{z_j}(\boldsymbol{\rho})$ range between 0 and 1 (when $\alpha = 0$) and depend on the relative power of each POTF, so that more weight is given to phase estimates with higher relative POTF power and thus higher signal-to-noise ratio (SNR). Equation (3.8) also summarizes POTF recovery from multiple defocus-plane pairs. The processing steps involved in implementing Eq. (3.8) are summarized in Fig. 3.1, where B is the background intensity used for normalization to match the aforementioned expressions.

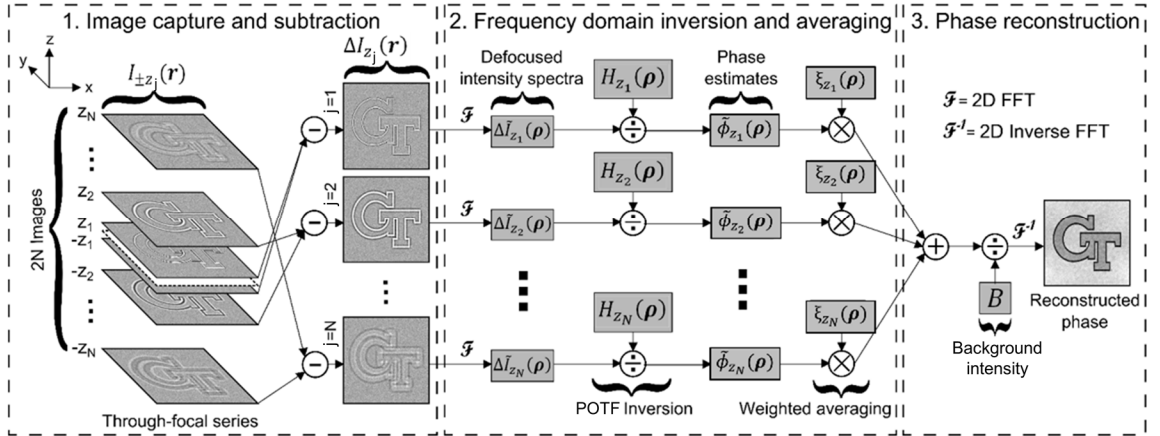


Figure 3.1: Block diagram representation of defocus-based phase optical transfer function (POTF) recovery.

3.2.2 Partially Coherent Phase Optical Transfer Function Recovery

Partially coherent POTF recovery is based on incorporating Köhler illumination into the phase recovery process described in Section 3.2.1. The effect of Köhler illumination is to induce partial spatial coherence in the illuminating wave field, the degree of which may be described via the Fourier transform of the extended incoherent source as given by the Van Cittert-Zernike theorem [180]. Implicit in this description is a quasi-monochromatic approximation, for which the spectral bandwidth of the illumination is presumed to be much less than the central wavelength, $\Delta\lambda \ll \bar{\lambda}$ [180], which may readily be realized in microscopy through the insertion of narrow-band interference filters into the illumination path. In this case the spatial coherence effects become dominant, as will be verified later in this section by comparing POTFs calculated both with and without the use of spectrally broadened sources.

Köhler illumination can also be described by a coherent mode decomposition in which the illuminating aperture contains a collection of point sources [122]. Each point source illuminates the sample with an off-axis plane wave and the resulting intensities are the incoherent summation of intensities due to each off-axis plane wave since the source is delta-correlated. Therefore, the overall WOTF can be formed by deriving the WOTF for each off-axis point source and integrating over the illumination aperture [66, 178].

The quantity $T(\boldsymbol{\rho} - \boldsymbol{\rho}')P(\boldsymbol{\rho})$ may be used to describe the spectrum of a complex object illuminated by an off-axis plane wave where $\boldsymbol{\rho}'$ defines the angle of oblique incidence and the spatial frequency coordinates of the source and $P(\boldsymbol{\rho})$ is the pupil function. The circular illumination pupil may be described by $S(\boldsymbol{\rho}') = \text{circ}(\boldsymbol{\rho}'/\rho_c)$, where $\rho_c = NA_c/\bar{\lambda}$, NA_c defines the NA of the illuminating condenser, and $\text{circ}(\boldsymbol{\zeta})$ is defined as

$$\text{circ}(\boldsymbol{\zeta}) = \begin{cases} 1, & |\boldsymbol{\zeta}| \leq 1 \\ 0, & |\boldsymbol{\zeta}| \geq 1 \end{cases} \quad (3.9)$$

Under the paraxial approximation, $P(\boldsymbol{\rho}) = \exp(-i\pi\bar{\lambda}z\rho^2) \text{circ}(\boldsymbol{\rho}/\rho_o)$ at propagation distance z where $\rho_o = NA_o/\bar{\lambda}$ and NA_o is the NA of the imaging objective.

Under these conditions the resulting spectrum for the defocused bright-field micrograph can be written in an expression analogous to Eq. (3.2) as

$$I_z(\boldsymbol{\rho}) = \int \text{circ}\left(\frac{\boldsymbol{\rho}'}{\rho_c}\right) I'_z(\boldsymbol{\rho}, \boldsymbol{\rho}') \exp(-i2\pi\bar{\lambda}z\boldsymbol{\rho} \cdot \boldsymbol{\rho}') d^2\boldsymbol{\rho}', \quad (3.10a)$$

$$\begin{aligned} I'_z(\boldsymbol{\rho}, \boldsymbol{\rho}') &= \int \left\{ \mathcal{F}^{-1} \left[\text{circ}\left(\frac{\boldsymbol{\rho} + \boldsymbol{\rho}'}{\rho_o}\right) \right] * T\left(\mathbf{r} - \frac{\bar{\lambda}z\boldsymbol{\rho}}{2}\right) \right\} \\ &\times \left\{ \mathcal{F}^{-1} \left[\text{circ}\left(\frac{\boldsymbol{\rho}' - \boldsymbol{\rho}}{\rho_o}\right) \right] * T^*\left(\mathbf{r} + \frac{\bar{\lambda}z\boldsymbol{\rho}}{2}\right) \right\} \\ &\times \exp(-i2\pi\mathbf{r} \cdot \boldsymbol{\rho}) d^2\mathbf{r} \end{aligned} \quad (3.10b)$$

where $\mathcal{F}^{-1}(x)$ denotes inverse Fourier transformation of x and $*$ denotes convolution.

From Eq. (3.10), it is seen that if the object is band-limited, i.e. $T(\boldsymbol{\rho}) = 0$ for $|\boldsymbol{\rho}| > \rho_o - \rho_c$, then $I'_z(\boldsymbol{\rho}, \boldsymbol{\rho}')$ is equivalent to the on-axis ($\boldsymbol{\rho}' = \mathbf{0}$) coherent intensity spectrum $I_z^C(\boldsymbol{\rho}, \mathbf{0})$ which does not vary with $\boldsymbol{\rho}'$, resulting in Eq. (3.10a) reducing to

$$I_z(\boldsymbol{\rho}) = BI_z^C(\boldsymbol{\rho}, \mathbf{0}) \frac{J_1(2\pi\bar{\lambda}z\rho_c\rho)}{\pi\bar{\lambda}z\rho_c\rho}, \quad (3.11)$$

where J_1 is the first-order Bessel function of the first kind, B is the background intensity level, and $\rho = |\boldsymbol{\rho}|$. Equation (3.11) implies that the resulting bright-field micrograph can be written in the spatial domain as

$$I_z(\mathbf{r}) = BI_z^C(\mathbf{r}, \mathbf{0}) * \frac{\text{circ}\left(\frac{\mathbf{r}}{\bar{\lambda}z\rho_c}\right)}{\pi(\bar{\lambda}z\rho_c)^2}, \quad (3.12)$$

so that image formation can be viewed as a simple convolution with a magnified replica of the source [108]. Although this relationship can and has been used as a means to model quickly image formation for use with defocus-based PR algorithms under Köhler illumination [134, 160], it is a special case of band-limited phase recovery under the paraxial approximation.

For a general description of partially coherent imaging using arbitrary pupils and delta-correlated sources Eq. (3.10) may be rewritten as

$$I(\boldsymbol{\rho}) = \int S(\boldsymbol{\rho}') \int \{\mathcal{F}^{-1}[P(\boldsymbol{\rho} + \boldsymbol{\rho}')] * T(\mathbf{r})\} \times \{\mathcal{F}^{-1}[P(\boldsymbol{\rho}' - \boldsymbol{\rho})] * T^*(\mathbf{r})\} \exp(-i2\pi\mathbf{r} \cdot \boldsymbol{\rho}) d^2\mathbf{r} d^2\boldsymbol{\rho}' \quad (3.13)$$

Normally, at this point, the first Born approximation is asserted such that $T(\mathbf{r}) \approx 1 - A(\mathbf{r}) + i\phi(\mathbf{r})$ [178], Eq. (3.13) is expanded, and the higher-order terms neglected so that Eq. (3.13) may be rewritten as

$$I(\boldsymbol{\rho}) = B\delta(\boldsymbol{\rho}) + H_A(\boldsymbol{\rho})A(\boldsymbol{\rho}) + H_\phi(\boldsymbol{\rho})\phi(\boldsymbol{\rho}). \quad (3.14)$$

in which $B = \int S(\boldsymbol{\rho}')|P(\boldsymbol{\rho}')|^2 d^2\boldsymbol{\rho}'$ is the background intensity level and the partially coherent absorption optical transfer function (AOTF) and POTF are given by Eqs. (3.15) and (3.16) respectively:

$$H_A(\boldsymbol{\rho}) = - \int S(\boldsymbol{\rho}') H_A^{OA}(\boldsymbol{\rho}, \boldsymbol{\rho}') d^2\boldsymbol{\rho}'. \quad (3.15)$$

$$H_\phi(\boldsymbol{\rho}) = i \int S(\boldsymbol{\rho}') H_\phi^{OA}(\boldsymbol{\rho}, \boldsymbol{\rho}') d^2\boldsymbol{\rho}'. \quad (3.16)$$

In Eqs. (3.15) and (3.16), $H_A^{OA}(\boldsymbol{\rho}, \boldsymbol{\rho}')$ and $H_\phi^{OA}(\boldsymbol{\rho}, \boldsymbol{\rho}')$ are elementary off-axis AOTFs and POTFs given by Eqs. (3.17) and (3.18) respectively:

$$H_A^{OA}(\boldsymbol{\rho}, \boldsymbol{\rho}') = P^*(\boldsymbol{\rho}')P(\boldsymbol{\rho} + \boldsymbol{\rho}') + P(\boldsymbol{\rho}')P^*(\boldsymbol{\rho}' - \boldsymbol{\rho}). \quad (3.17)$$

$$H_\phi^{OA}(\boldsymbol{\rho}, \boldsymbol{\rho}') = P^*(\boldsymbol{\rho}')P(\boldsymbol{\rho} + \boldsymbol{\rho}') - P(\boldsymbol{\rho}')P^*(\boldsymbol{\rho}' - \boldsymbol{\rho}). \quad (3.18)$$

Although weak scattering is a sufficient condition for validating the preceding expression, it is in fact not necessary. If we instead use the first-order Rytov approximation to express the complex wave field in the image plane, then Eq. (3.13) is given by Eq. (3.19) (see Appendix A) in which $\psi_R^{im}(\mathbf{r}, \boldsymbol{\rho}')$ is the first Rytov approximation for the complex scattered phase at the image plane and $\psi(\mathbf{r}) = -A(\mathbf{r}) + i\phi(\mathbf{r})$ is the scattered phase at the object plane.

$$I(\boldsymbol{\rho}) = \int S(\boldsymbol{\rho}') |P(\boldsymbol{\rho}')|^2 \times \int \exp\{2\text{Re}[\psi_R^{im}(\mathbf{r}, \boldsymbol{\rho}')] \} \exp(-i2\pi\mathbf{r} \cdot \boldsymbol{\rho}) d^2\mathbf{r} d^2\boldsymbol{\rho}' \quad (3.19a)$$

$$\psi_R^{im}(\mathbf{r}, \boldsymbol{\rho}') = \mathcal{F}^{-1} \left[\frac{P(\boldsymbol{\rho} + \boldsymbol{\rho}')}{P(\boldsymbol{\rho}')} \right] * \psi(\mathbf{r}). \quad (3.19b)$$

From Eq. (3.19) it is clear that if the following conditions hold $\forall \boldsymbol{\rho}' \in S(\boldsymbol{\rho}')$,

$$|\mathcal{F}^{-1}[H_A^{OA}(\boldsymbol{\rho}, \boldsymbol{\rho}')] * A(\mathbf{r})| \ll |P(\boldsymbol{\rho}')|^2, \quad (3.20)$$

$$|\mathcal{F}^{-1}[H_\phi^{OA}(\boldsymbol{\rho}, \boldsymbol{\rho}')] * \phi(\mathbf{r})| \ll |P(\boldsymbol{\rho}')|^2, \quad (3.21)$$

then Eq. (3.19) reduces to Eq. (3.14) (see Appendix A) which was established in the Born approximation. Equations (3.20) and (3.21) represent generalized linearization conditions for partially coherent imaging in the Köhler geometry analogous to the aforementioned weak absorption and SVP conditions first derived by Guigay [127]. Interestingly the conditions represented by Eqs. (3.20) and (3.21) do not always imply that the object must be weakly scattering. Intuitively, Eqs. (3.20) and (3.21) imply that for every point source in the back focal plane of the condenser, the contrast resulting from the first-order term in the series expansion for intensity must be a small fraction of the background, which depends in general on both the object and the imaging configuration and represents a trade-off between SNR and linearization validity. Thus the first Rytov approximation and the conditions defined by Eqs. (3.20) and (3.21) are, when taken together, also sufficient conditions for linearizing partially coherent imagery. Since the Rytov approximation is known to be sensitive to the phase gradient and not its magnitude, the “weak object” terminology in WOTF is perhaps a misnomer and the aforementioned successful reconstruction results [7, 49, 121, 163] are made plausible.

Since it is intensity contrast which matters, it follows that the magnitudes of $H_A^{OA}(\boldsymbol{\rho}, \boldsymbol{\rho}')$ and $H_\phi^{OA}(\boldsymbol{\rho}, \boldsymbol{\rho}')$ as $\boldsymbol{\rho}$ approaches $\mathbf{0}$ are of critical importance in determining the validity of linearization since the amplitudes of most naturally occurring objects are strongest for lower spatial frequencies. In most cases, $H_A^{OA}(\boldsymbol{\rho}, \boldsymbol{\rho}')$ takes on the form of a

low-pass filter implying the need to assume weak absorption. $H_{\phi}^{OA}(\boldsymbol{\rho}, \boldsymbol{\rho}')$, on the other hand, appears to be much more forgiving and often takes on the form of a high-pass filter, implying that phase does not necessarily need to be weak. This has positive and negative aspects because although it improves validity for linearization it also reduces phase contrast, making quantitative phase recovery either impossible or extremely noisy. For example, Fig. 3.2 plots off-axis POTF's for both Nomarski DIC and for simple defocus. For DIC, we calculated the off-axis POTF using the development provided in [181]. From Fig. 3.2 it is seen that in both cases the resulting contrast is diminished near the origin of frequency space, implying that phase will not necessarily need to be weak for linearization. For DIC [Fig. 3.2(a)], contrast is nearly linear near the origin implying stronger contrast and thus better SNR. For defocus [Fig. 3.2(b)], however, contrast is nearly parabolic near the origin implying improved validity for linearization at the expense of SNR. Another benefit of using defocus is that contrast is isotropic allowing phase recovery without needing to sample two orthogonal directions as in QPI methods based on DIC [35, 182] or differential phase contrast [121, 183].

If $S(\boldsymbol{\rho}')$ is axisymmetric, then $H_A(\boldsymbol{\rho})$ and $H_{\phi}(\boldsymbol{\rho})$ are symmetric and anti-symmetric with respect to defocus respectively. Thus subtracting two symmetrically defocused micrographs recorded at positions $\pm z$ results in a directly invertible relationship between phase and intensity [Eq. (3.22)] as in Eq. (3.6).

$$\begin{aligned}\Delta I_z(\boldsymbol{\rho}) &= I_{+z}(\boldsymbol{\rho}) - I_{-z}(\boldsymbol{\rho}) \\ &= H_z^{PC}(\boldsymbol{\rho})\phi(\boldsymbol{\rho})\end{aligned}\tag{3.22}$$

An additional benefit is that, for a pure phase object in this geometry, the second-order terms in the expanded intensity are also symmetric with respect to defocus, thus improving linearization conditions further upon subtraction of symmetrically defocused images.

In Eq. (3.22), the partially coherent POTF is $H_z^{PC}(\boldsymbol{\rho}) = 2H_{\phi}(\boldsymbol{\rho})/B$ where $H_{\phi}(\boldsymbol{\rho})$ is calculated using Eq. (3.16) with a circular illumination pupil $S(\boldsymbol{\rho}') = \text{circ}(\boldsymbol{\rho}'/\rho_c)$ as

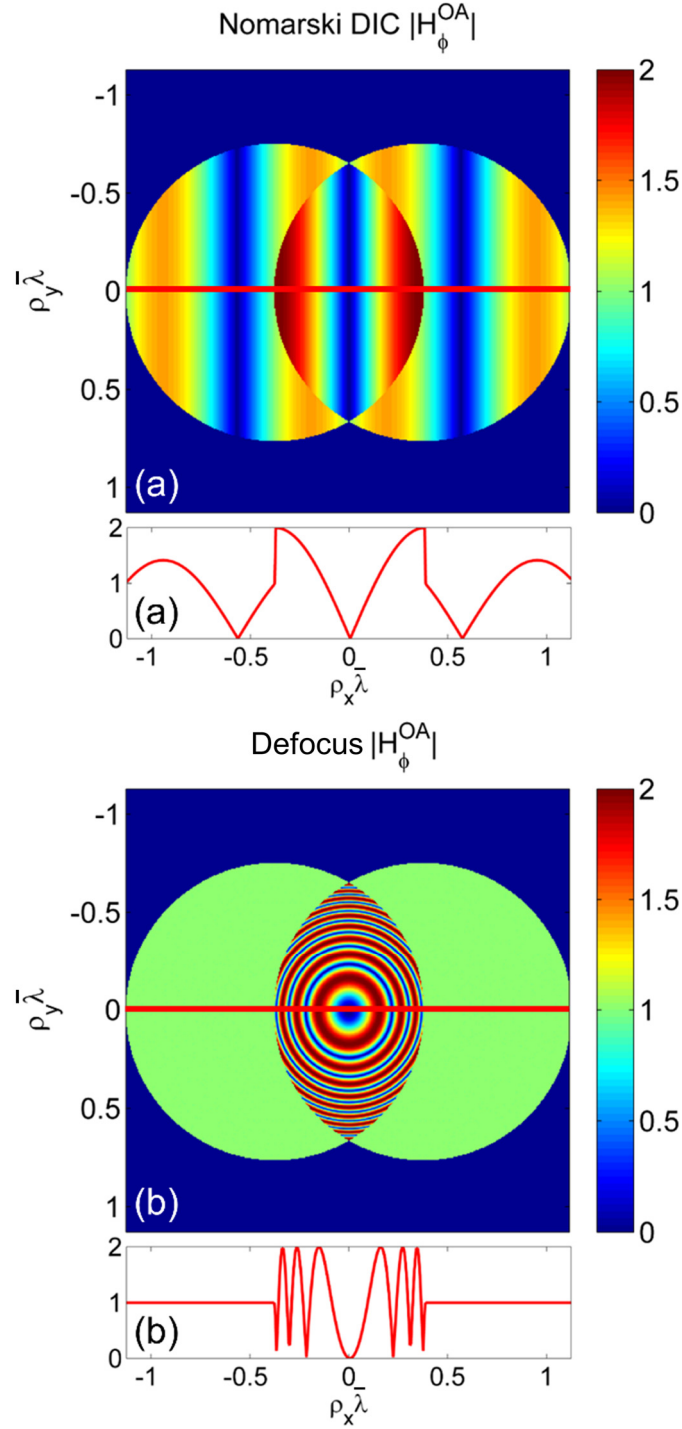


Figure 3.2: Magnitude of off-axis phase optical transfer functions (POTFs) [as given by Eq. (3.18)] for (a) Nomarski differential interference contrast (DIC) with a shear value of $\Delta_{DIC} = 1/2\rho_o$ in the x direction and a bias value of $\Phi = \pi/4$ and (b) defocus with a distance of $\delta z = 9 \mu\text{m}$. In both cases $NA_o = 0.75$ and the off-axis illumination is given by $\boldsymbol{\rho}' = (0.375/\bar{\lambda})\widehat{\rho}_x$.

before and a non-paraxial pupil $P(\boldsymbol{\rho}) = \exp\left(-ik_0\left\{1 - \left[1 - (\bar{\lambda}\rho)^2\right]^{1/2}\right\}z\right) \text{circ}(\boldsymbol{\rho}/\rho_o)$ (for which $k_0 = 2\pi/\bar{\lambda}$ is the free-space wave vector magnitude) as in the angular spectrum of plane waves method for field propagation [184]. Although not derived analytically, $H_z^{PC}(\boldsymbol{\rho})$ is easy to calculate numerically and can be used to optimize PR in a manner analogous to Eqs. (3.7), (3.8), and Fig. 3.1.

Thus POTF recovery based on defocus has been described for bright-field microscopy operating in transmission under linearization conditions of weak absorption and SVP. For imaging of live adherent cells, the authors have found that a good trade-off between total number of images, linearizability, and phase image quality is to set the total number of images to $2N = 4$ in which a small defocus distance z_1 is chosen to be close to the microscope depth of field and a larger defocus distance is chosen as $z_2 \approx 15z_1$. For the microscope utilized in the present work (*Olympus BX60* with a *UPlanFl 40 \times / 0.75 0.17 ∞* objective) $z_1 = 0.6 \mu\text{m}$ and $z_2 = 9 \mu\text{m}$ have been found to give favorable results. The illumination is provided by the green spectral line of a mercury arc lamp filtered using a green interference filter (GIF, $\bar{\lambda} = 546 \text{ nm}$, $\Delta\lambda = 10 \text{ nm FWHM}$). The level of partial spatial coherence is determined by $NA_c = 0.375$ which has been set using a condenser (*Olympus U-POC-2*) aperture diaphragm. Since we have not encountered any need for regularization, α is set to zero and the resulting radially varying partially coherent POTFs and optimized weighting functions are plotted in Fig. 3.3.

To model spectral broadening, the POTFs were also integrated in steps of 1 nm over the passband of the GIF, which was assumed to be Gaussian in shape. It was found that the resulting POTFs calculated using the central wavelength $\bar{\lambda}$ alone were visually indiscernible from the plots shown in Fig. 3.3, therefore, the quasi-monochromatic approximation is appropriate and calculations throughout the remainder of this chapter are based on a single wavelength only.

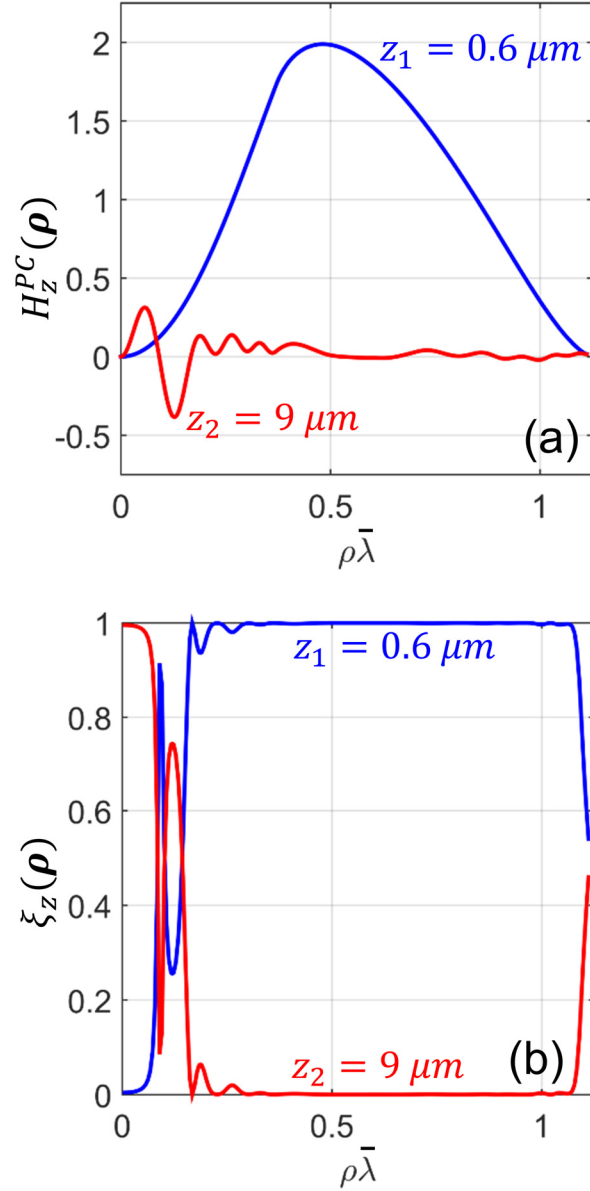


Figure 3.3: (a) Partially coherent phase optical transfer functions (POTFs) and (b) weighting functions used to define partially coherent POTF recovery for $NA_o = 0.75$, $NA_c = 0.375$, $\bar{\lambda} = 546 \text{ nm}$, $N = 2$, $z_1 = 0.6 \mu m$, and $z_2 = 9 \mu m$. For both figures, $\rho = |\boldsymbol{\rho}|$.

3.3 Simulation Results

In order to simulate and compare various forms of defocus-based deterministic PR we used the letters “GT” as shown in Fig. 3.4(a) as an example phase object. For simplicity, we used Abbe’s method for partially coherent image calculation [185, 186], which is similar to the coherent mode decomposition description provided in Chapter 2, in which

each defocused image was calculated as the sum of the intensities of the off-axis images corresponding to point sources in the back focal plane of the condenser. Propagation was modeled as the angular spectrum pupil function introduced earlier [184]. We simulated five images (four corresponding to $\pm z_1$ and $\pm z_2$ mentioned at the end of Section 3.2.2 and one in-focus image) to compare both TIE [48, 111] and coherent POTF recovery [50, 174] with the proposed partially coherent POTF recovery method. After all partially coherent images were calculated, additive white Gaussian noise with a realistic standard deviation of 1% of the background intensity ($\sigma = 0.01$) was added to simulate the noise process for shot-noise-limited bright-field imagery.

In Fig. 3.4(b), the OFS algorithm described in [48] was used and adapted to account for non-equally spaced planes. Previously, such algorithms have only been described for use with equally spaced planes [48, 111]. The development given in Chapter 2, however, is general enough to account for non-equally spaced planes if the Savitzky-Golay differentiation filter frequency response used in Eq. (2.5b) is replaced by a non-uniformly spaced equivalent. For a description of non-uniformly spaced data differentiation using Savitzky-Golay differentiation filters see [187]. From Fig. 3.4(b), we see that although noise suppression is quite good, as evidenced by the relatively low root mean squared error (RMSE) value of 0.028 radians, the reconstruction is also plagued with shadow-like or ringing artifacts resulting from modulation transfer function (MTF) attenuation of mid-range spatial frequencies due to the misplaced cut-off frequency between filters corresponding to the first and third differentiation orders [111]. By contrast, the recovery in Fig. 3.4(c) uses MFPI-PC which explicitly accounts for MTF roll-off due to partial coherence. Although this removes the aforementioned artifacts it also results in poorer noise suppression (RMSE = 0.035 radians) than the OFS result because more weight is given to the images spaced at $\pm z_1$.

Figure 3.4(d) utilizes coherent POTF recovery as described in Section 3.2.1 under assumptions of spatially coherent paraxial illumination. In this case, the errors resulting

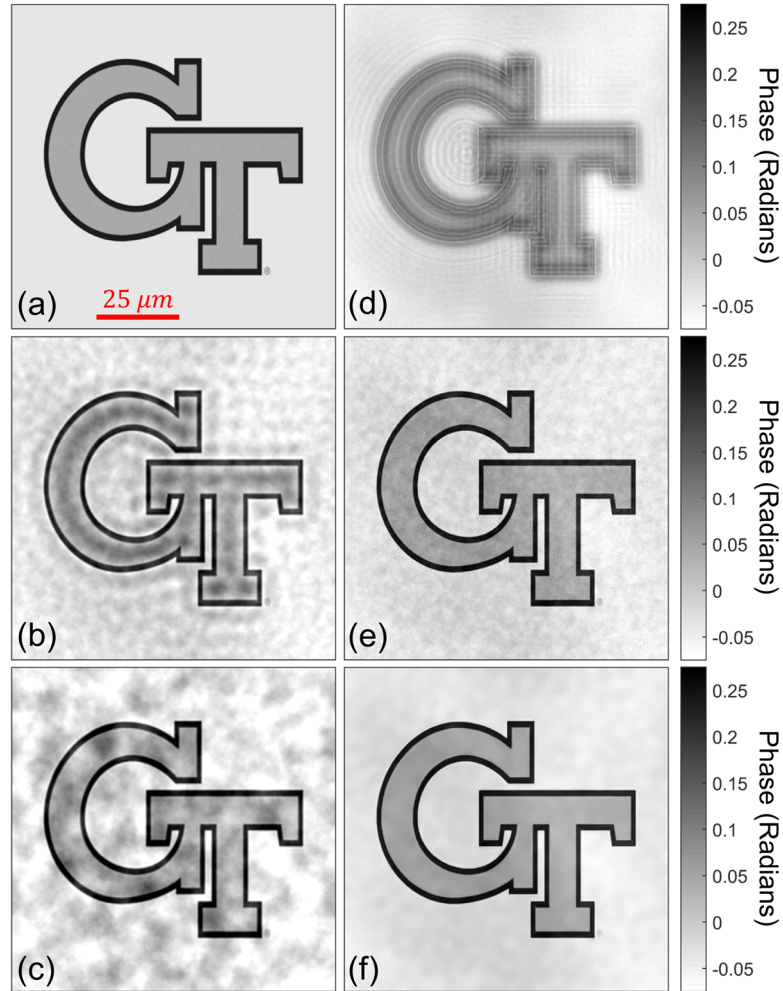


Figure 3.4: Partially coherent phase imaging simulation results based on the phase object shown in (a). (b-f) correspond to noisy phase recovery using various algorithms including (b) optimal frequency selection (OFS), (c) multifilter phase imaging with partially coherent light (MFPI-PC), (d) coherent phase optical transfer function (POTF) recovery, (e) partially coherent POTF recovery, and (f) partially coherent POTF recovery with post PR de-noising using non-local means (NLM) filtering. The corresponding root mean squared errors (RMSEs) are (b) 0.028, (c) 0.035, (d) 0.051, (e) 0.026, and (f) 0.014 radians respectively. All images are 400×400 square pixels with a sampling rate of $0.245 \mu\text{m}$.

from the assumption of coherence are more drastic when compared with the TIE-based methods. This results at least partially from the TIE being valid under partial spatial coherence [108] and because POTF methods are based on direct inversion and are thus more sensitive to model inaccuracies. By contrast, partially coherent POTF recovery [Fig. 3.4(e)] exhibits satisfactory results as it accurately accounts for partial coherence and

minimizes noise (RMSE = 0.026 radians). For this result, much of the error is due to low contrast at high spatial frequencies [as shown by Fig. 3.3(a)] in addition to the conventional low spatial frequency noise [111]. Fortunately, sophisticated algorithms, including non-local means (NLM) filtering, exist for removing uncorrelated noise at high spatial frequencies without smoothing or perturbing the underlying structure of the image [188]. Shown in Fig. 3.4(f) is the result of Fig. 3.4(e) after undergoing NLM filtering using a search window of 8×8 pixels, similarity window of 4×4 pixels, and filtering degree set to the RMSE of Fig. 3.4(e). It is observed that almost all the high spatial frequency noise present in Fig. 3.4(e) is removed without perturbing the resolution or structure of the underlying “GT” phase image, resulting in a dramatic reduction of error (RMSE = 0.014 radians).

Shown in Fig. 3.5 are the RMSEs of the PR algorithms highlighted in Fig. 3.4 as a function of the normalized standard deviation σ of white Gaussian noise added to the simulated imagery. To reduce uncertainty, each data point is represented by the average of ten measurements. At low noise levels, the MFPI-PC (red) curve is lower than the OFS (blue) curve because of the artifacts associated with uncompensated MTF attenuation in OFS. Although not quantitative, OFS does result in lower error than MFPI-PC at high noise levels due to greater emphasis on the first-order derivative. It is clear that coherent POTF recovery results in significant error due to model inaccuracy. For most levels, however, the RMSE of partially coherent POTF recovery both before and after NLM filtering are lower than the rest of the field, indicating that it is perhaps the best option currently available for enabling QPI of weakly absorbing objects from defocused bright-field imagery. For objects with absorption that is strong, but slowly varying, it is possible to establish linearity for the OFS algorithm [7] and likely possible for the MFPI-PC algorithm as well (see Chapter 8). Therefore, simulation studies comparing the performance of these algorithms for absorbing samples is warranted and a subject of future research.

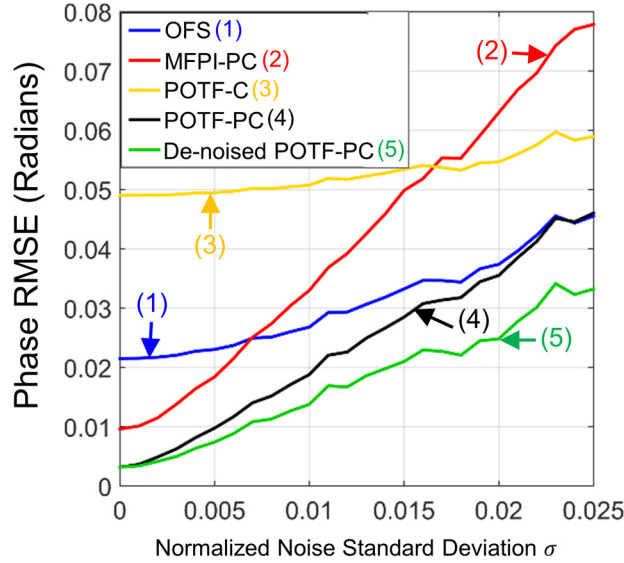


Figure 3.5: Root mean squared error (RMSE) of simulations corresponding to Fig. 3.4 under varying amounts of additive white Gaussian noise σ . In the legend, POTF-C indicates recovery based on the coherent POTF and likewise POTF-PC indicates recovery based on the partially coherent POTF.

In order to emulate the reconstruction of live adherent cells and simulate the effects of violating the SVP linearization conditions outlined in Section 3.2.2, we modelled an adherent HeLa cell (cell line obtained from Henrietta Lacks [8]) using a phantom consisting of a combination of projected phase values from oblate ellipsoids of revolution of varying refractive index (RI). Estimating cell volume using data from [189] and assuming an adherent cell diameter of $25 \mu\text{m}$ [189], an ellipsoidal thickness of $8 \mu\text{m}$ is deduced. Using the data from [190] to estimate nuclear volume and assuming the same ellipticity, the nucleus is modeled by a diameter of $6.5 \mu\text{m}$ and a thickness of $2.1 \mu\text{m}$. A spherical nucleolus is modeled inside the nucleus with a diameter of $2 \mu\text{m}$. The RI values assigned to the cytoplasm, nucleoplasm, and nucleolus were $n = 1.365$, $n = 1.355$, and $n = 1.38$ respectively, which are in reasonable accordance with RI values obtained in recent reports [9, 191].

Assuming the cell is imaged in water ($n = 1.33$), the projected phase profiles are calculated and shown in Fig. 3.6(a). Using these RI values, the object phase has a peak magnitude of about 3.5 radians and is in violation of the conventional first Born

approximation, which requires the total phase shift to be less than $\pi/2$ radians [56]. Shown in Fig. 3.6(b) is the partially coherent POTF reconstruction using the same parameters as in Figs. 3.4 and 3.5 with a high noise level of $\sigma = 0.03$ and a reduced field of view (FOV) of $30.6 \mu\text{m} \times 30.6 \mu\text{m}$. Figure 3.6(c) compares the simulated and recovered phase profiles along the blue and red lines indicated in Figs. 3.6(a) and 3.6(b) respectively. Excellent agreement is observed consistent with the linearization conditions outlined in Section 3.2.2 since the object is slowly varying. Because these dimensions and contrast levels are in rough agreement with adherent cell imaging we can expect that such specimens will be well approximated by the SVP approximation for the system parameters used here.

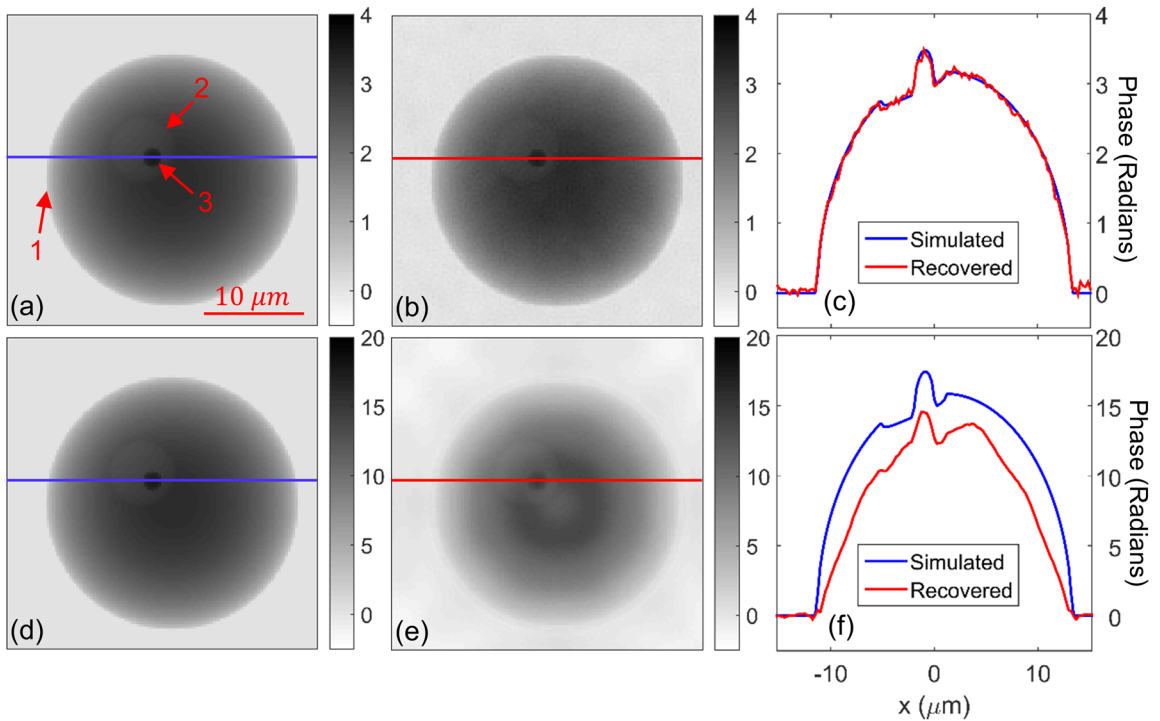


Figure 3.6: Simulation emulating reconstruction of adherent HeLa cell (a) Phase object consisting of integrated phase corresponding to three ellipsoids of revolution. (b) Partially coherent POTF reconstruction of (a). (c) Line profile comparison of (a) and (b). (d) Phase object with $5 \times$ larger contrast. (e) Partially coherent POTF reconstruction of (d). (f) Line profile comparison of (d) and (e). In (a), (1), (2), and (3) represents the cytoplasm, nucleus, and nucleolus respectively. All images are 125×125 square pixels with a sampling rate of $0.245 \mu\text{m}$.

In order to demonstrate the effect of violating these conditions, we simulated the same object assuming $5 \times$ larger RI contrast. The results are summarized in Figs. 3.6(d)-3.6(f) in which a noticeable departure from the simulated profile is observed due to non-linearity in the intensity formation process.

3.4 *Experimental Results*

In order to validate the accuracy of the proposed POTF recovery method a periodic microlens array (MLA, *Thorlabs MLA150-7AR*) was measured using the same parameters as in the simulation results shown in Section 3.3. The thickness of the unmounted array is specified as 1.19 mm, the radius of curvature of each lenslet as 3.063 mm, and the array pitch as 150 μm . During the measurement, the array was placed lenslet-side-up on top of a thin No. 0 coverslip and imaged directly in air without immersion oil using the aforementioned microscope objective, condenser, and GIF. In this arrangement, the array acts as a strong but slowly varying thin phase object which is ideal for verification. Shown in Fig. 3.7(a) is the raw intensity image difference between micrographs recorded at $\pm z_2 = 9 \mu\text{m}$ normalized by the average background intensity B . The camera (*QImaging Retiga 1300R*) full FOV is $252 \times 318.25 \mu\text{m}^2$ with 1030×1300 square pixels and a sampling rate of 0.245 μm .

Based on the recorded micrographs at $\pm z_1 = 0.6 \mu\text{m}$ and $\pm z_2$, the recovered phase of the region defined by the square inset in Fig. 3.7(a) is shown in Fig. 3.7(b). The reconstructed horizontal line profile through the center of a single lenslet [see the line inset in Fig. 3.7(b)] is shown as the solid green line in Fig. 3.7(c). Shown for validation and comparison is a profile of the MLA measured via profilometer (*KLA-Tencor P-15* with lateral scan resolution set to 0.1 μm) which has been scaled by the index difference between the MLA (fused silica, $n = 1.4601$ at $\bar{\lambda} = 546 \text{ nm}$ [192]) and air ($n = 1.0$) as well as the free-space wave vector magnitude k_0 to convert the measured surface profile into phase values [see the dashed black line in Fig. 3.7(c)].

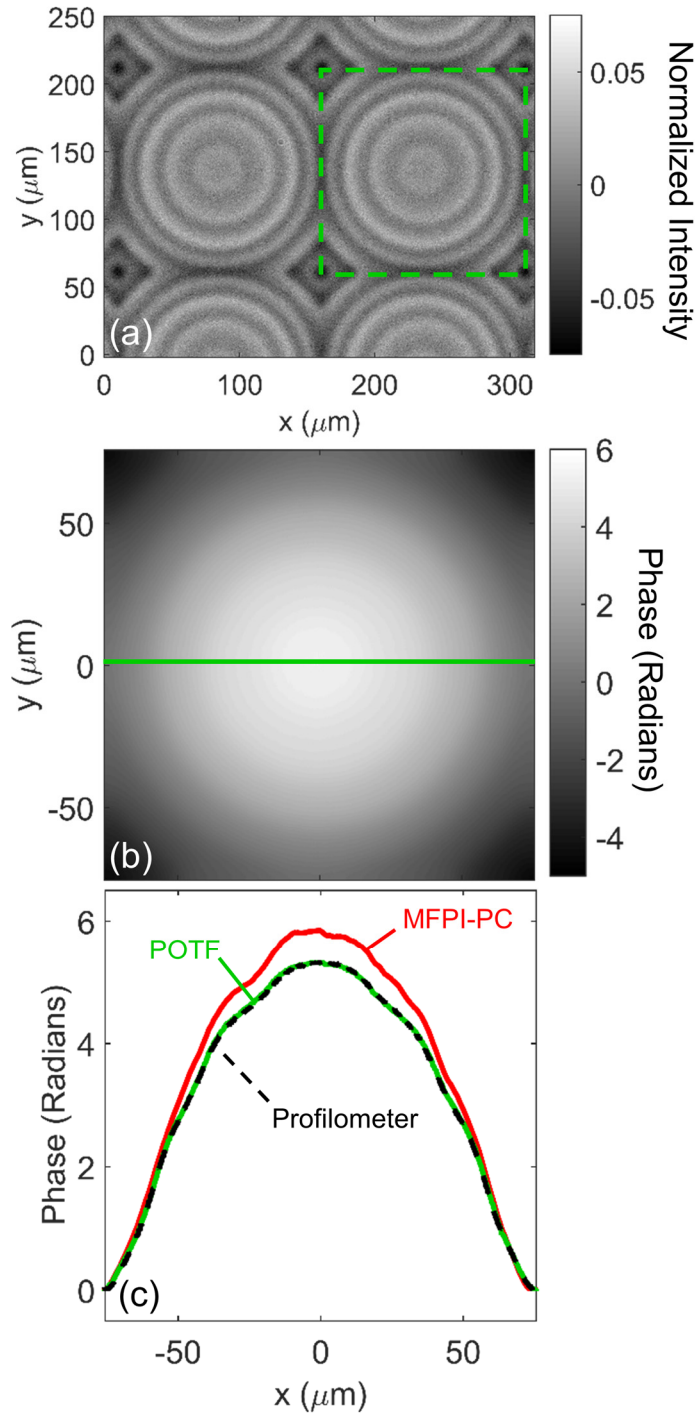


Figure 3.7: Experimental results for microlens array (MLA) validating the accuracy of POTF recovery. (a) Full field intensity difference image normalized by the background intensity level $\Delta I_{z_2}(\mathbf{r})/B$. (b) Single lenslet phase measured via partially coherent POTF recovery performed on the square inset region shown in (a). (c) Line profile comparison between POTF recovery [solid green line corresponding to inset in (b)], multifilter phase imaging with partially coherent light (MFPI-PC) (solid red line), and profilometry (dashed black line).

Of interest in these results is the excellent agreement between both the magnitude and shape of the compared lenslet profiles. Somewhat surprisingly, the shape is not completely circular, which is reflected in both POTF recovery and profilometry. Also shown for comparison is a profile reconstructed via MFPI-PC [see the solid red line in Fig. 3.7(c)] from the same defocused intensity data with the addition of an in-focus image for normalization. In addition to being slightly more noisy, the MFPI-PC result overestimates the profile magnitude by $\sim 9.5\%$. This overestimation is attributed to the paraxial approximation inherent in the TIE, since, in calculating the POTF using the non-paraxial pupil $P(\boldsymbol{\rho}) = \exp\left(-ik_0\left\{1 - \left[1 - (\bar{\lambda}\rho)^2\right]^{1/2}\right\}z\right) \text{circ}(\boldsymbol{\rho}/\rho_o)$, contributions arising from off-axis point sources increase contrast slightly for low spatial frequencies beyond the parabolic transfer assumed in the TIE. This scale factor increase in TIE-based phase reconstructions was also observed in producing the results shown in Section 2.3. The effect becomes more prominent as NA_c is increased and potential solutions are discussed in Chapter 8 on future work.

In order to characterize the sensitivity of the proposed method, the OPL error produced by fifty control measurements with no sample in place was analyzed in the Fourier domain. OPL is a more appropriate quantity since phase is wavelength dependent. Although an overall RMSE is often used to characterize the OPL sensitivity of QPI systems, more information is needed since sensitivity often depends on object characteristics including dimension, i.e. spatial frequency. Shown as the red curve in Fig. 3.8 is the square root of the average frequency resolved OPL error signal power (average power spectral density normalized by the pixel area) derived from the control measurements which provides a measure of the average RMSE corresponding to each radial spatial frequency. In these measurements, the system parameters were the same as in Section 3.3.

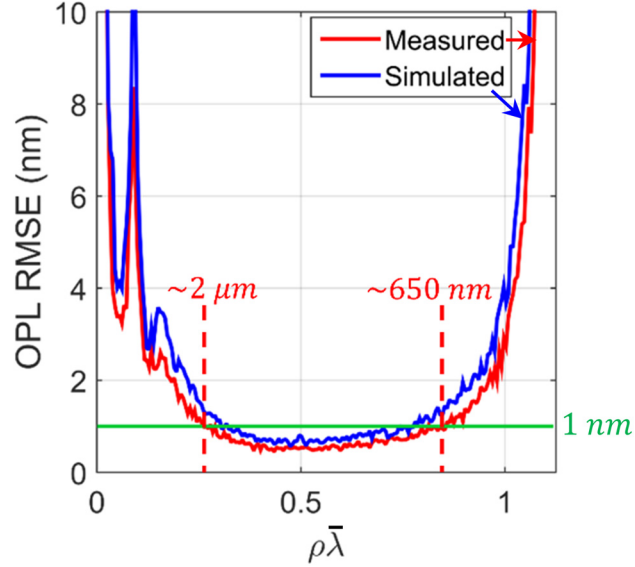


Figure 3.8: Simulated and measured optical path length (OPL) RMSE's resolved in the frequency domain. $\rho = |\rho|$.

In characterizing system sensitivity we also measured the normalized noise standard deviation for our setup as $\sigma = 0.011$. Using this value, we simulated the frequency resolved OPL RMSE and the result shows excellent agreement with measurement and is shown as the blue curve in Fig. 3.8. Also for reference, a green line is plotted at 1 nm indicating that phase objects having diameters D within the range of $\sim 650 \text{ nm} < D < \sim 2 \mu\text{m}$ are imaged with sub-nanometer OPL sensitivity, which is promising since sub-nanometer OPL sensitivity is considered quite good for interferometric/holographic QPI methods [6]. For both low and high spatial frequencies, the OPL error is large due to reduced phase contrast. Also of note are the peaks near $\rho\bar{\lambda} = 0.1$ in both cases, which result from the fact that the POTF corresponding to z_2 crosses zero before the POTF corresponding to z_1 obtains appreciable value. To resolve this issue a third mid-range distance might be added as has been done in the time-lapse results presented later in this section. If spatial frequencies are cut-off above $\rho\bar{\lambda} = 1$, as has been done in the reconstructions shown in Figs. 3.4-3.6, then the overall OPL RMSE is measured as 1.85 nm, which provides a measure of OPL resolution in the current implementation of POTF recovery and may be adequate for many applications including live adherent cell imaging

where OPL magnitudes are typically on the order of hundreds of nanometers. In order to improve sensitivity further, initial calculations show that annular illumination pupils, which are also readily available on most commercial microscopes, increase contrast for both low and high spatial frequencies and will be a subject of future work as outlined in Chapter 8.

In order to test the present reconstruction method in its intended application, high-speed QPI of live bovine mesenchymal stem cells using the aforementioned microscope and system parameters was performed. The defocusing was automated in NI LabVIEW using a piezo-electric objective scanner (*Physik Instrumente P-721.SL2* with *E-709.SR* controller) to achieve a total phase frame rate of 1.6 frames per second over a duration of 60 seconds. The cells were transported from the lab in which they were cultured in a phosphate buffered saline solution, which was also used to mount the cells onto a separate glass slide and coverslip. A snapshot of the results at $t = 27.5$ seconds are summarized in Fig. 3.9 with a full video accessible as Media 3.1.

Shown in Fig. 3.9 are the recovered phase image after NLM filtering using the aforementioned parameters [Fig. 3.9(a)] as well as a simplified DIC image approximated numerically as the central difference of Fig. 3.9(a) [Fig. 3.9(b)]. The resulting images appear to show a cluster of cells as no single nucleus is identifiable. Multiple blebs are observed indicating that the cells were not healthy during imaging. This is not surprising since the cells were imaged in a simple manner without regard to environmental factors such as pH and osmolality. The phase images appear to be relatively noise-free and sharp with the theoretical system spatial resolution defined as $\bar{\lambda}/[0.9(NA_o + NA_c)] = 546 \text{ nm}/[0.9(0.75+0.375)] = 539 \text{ nm}$, in which the factor of 0.9 is due a final low-pass filter applied to the phase images to prevent noise-amplification at spatial frequencies near the $\rho\bar{\lambda} = 1.125$ limit where contrast reduces to zero (see Fig. 3.3). No evidence of halo, shade-off, or other artifacts typically associated with partially coherent interferometric modalities [168, 169] are observed. In Media 3.1, movement in the outer blebs as well as

intracellular activity can be observed demonstrating the applicability of the proposed reconstruction method towards studying intracellular dynamics [10].

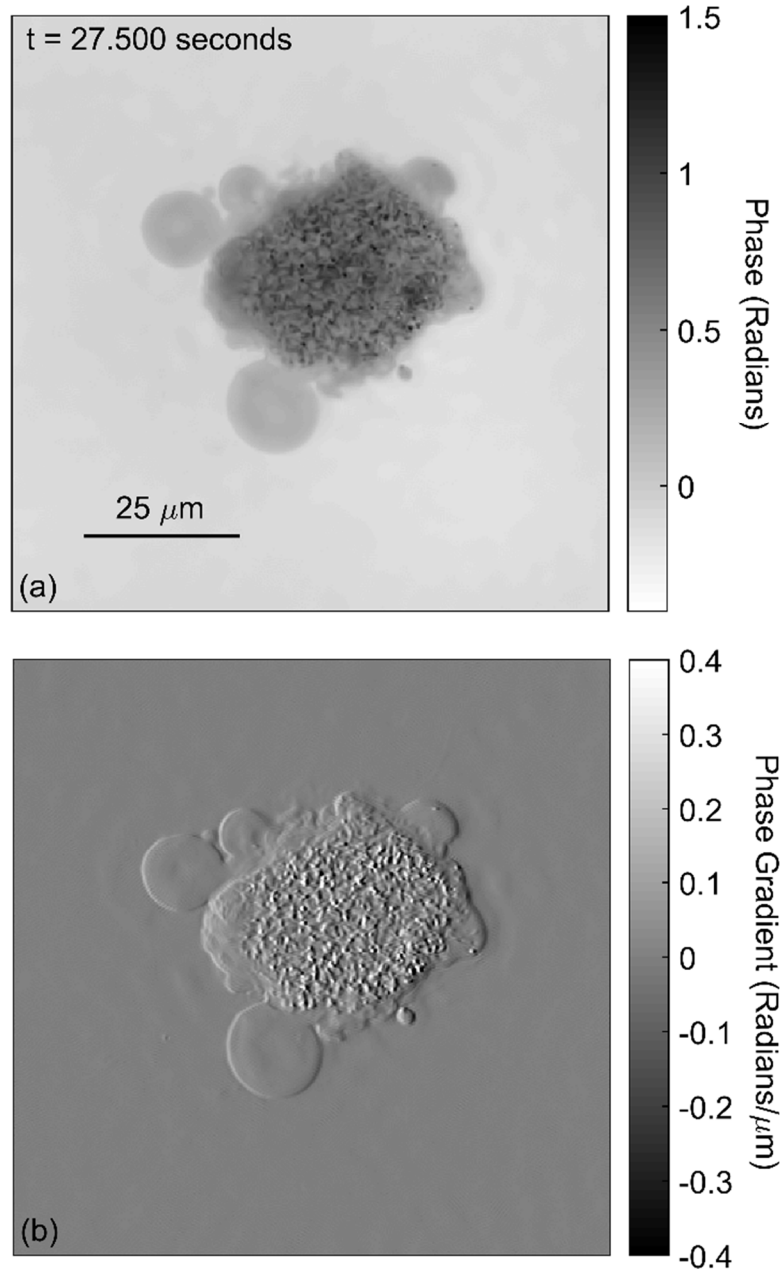


Figure 3.9: Snapshot of live bovine mesenchymal stem cell cluster taken from Media 3.1. (a) Quantitative phase image. (b) Simulated DIC image estimated by central-difference gradient approximation of (a).

In order to demonstrate the present method's potential for promoting the use of QPI within the biomedical community we performed time-lapse QPI of live endothelial cells

extracted from rat intestines using an off-the-shelf *Zeiss AxioObserver.A1* coupled with commercially available *AxioVision* microscopy software for data acquisition. These ubiquitous system elements are to be contrasted with expensive holographic microscopes and other customized QPI systems detailed throughout the literature. The *Zeiss Plan-Apochromat* objective had a NA of $NA_o = 0.3$ and again we used a coherence parameter $S = NA_c/NA_o = 0.5$ so that the condenser aperture was set to $NA_c = 0.15$ using an adjustable diaphragm. The illumination was provided by a tungsten halogen lamp and the wavelength was again set to $\bar{\lambda} = 546$ nm using a GIF ($\Delta\lambda = 10$ nm FWHM). For these optical parameters, the reconstruction parameters were selected to be $N = 3$ with $z_1 = 3$ μm , $z_2 = 15$ μm , and $z_3 = 45$ μm . *AxioVision* was programmed to image these distances every 10 minutes for 24 hours onto a *Zeiss AxioCam MRm* CCD with 1388×1040 pixels. With the $1.5\times$ Optovar lens in place, the FOV was $560 \mu\text{m} \times 419.25 \mu\text{m}$ with a sampling rate of $0.403 \mu\text{m}$. In order to maintain cellular health over the entire experiment, the *AxioObserver.A1* came with an incubator (*Incubators XL*) for warm air incubation and CO₂-control. Likewise the *AxioObserver.A1* comes with motorized defocus (step size 25 nm) and auto-focus capability which were utilized throughout the experiment to maintain a fixed focal reference to the petri dish on which the specimens were adhered.

Using these images, partially coherent POTF processing was performed over a square region of interest of 1000×1000 pixels. During the time-lapse, many cells migrated in and out of the FOV, resulting in well-known artifacts associated with the artificial periodic boundary conditions imposed by the fast Fourier transform-based processing [124, 126]. Although these artifacts remain an issue, for this study we observed their greatest effect to be near the image boundaries. We therefore found cropping 100 pixels off the recovered phase image boundaries and subtracting the mean to be an effective means of subduing these artifacts.

Shown in Fig. 3.10 are snapshots of the recovered phase image after NLM filtering [Fig. 3.10(a)] as well as the approximated phase gradient image [Fig. 3.10(b)].

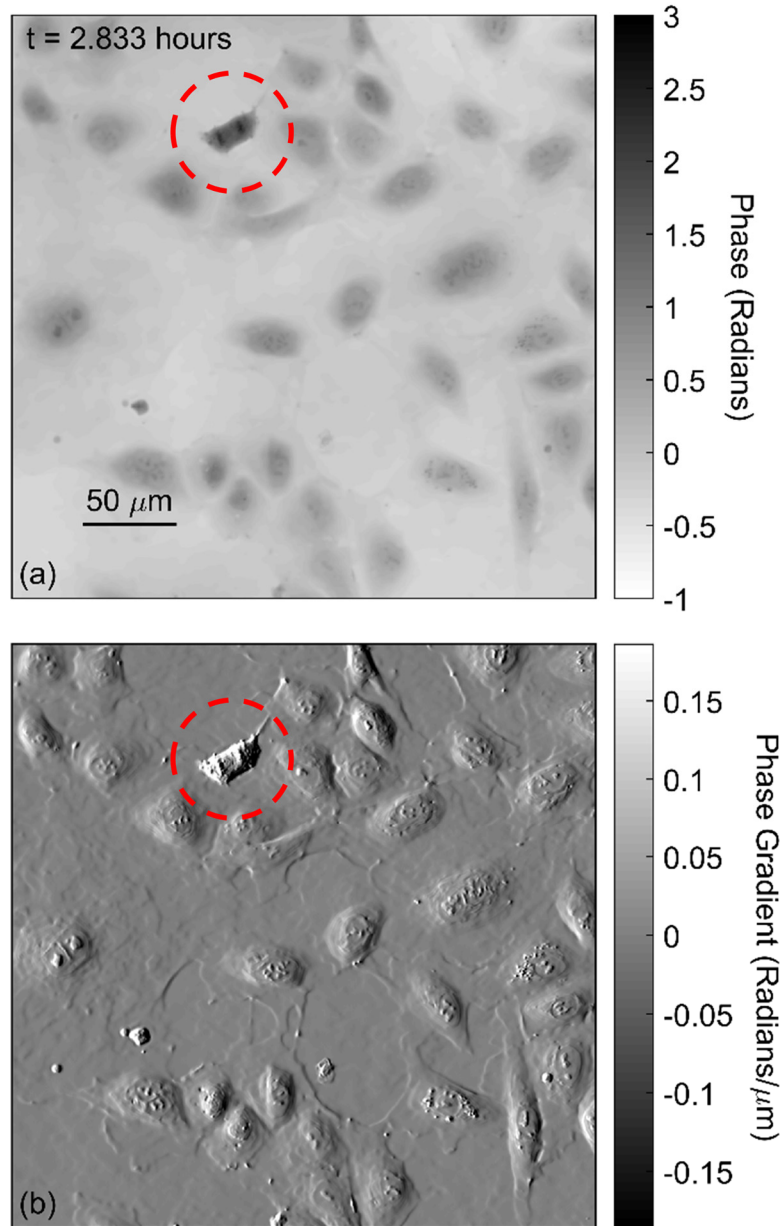


Figure 3.10: Snapshot of live endothelial cells taken from Media 3.2. (a) Quantitative phase image. (b) Simulated DIC image estimated by central-difference gradient approximation of (a).

The results are qualitatively similar to Fig. 3.9 except that many individual cells are included in the FOV. The cell highlighted by the red circle is clearly undergoing anaphase. The video accessible as Media 3.2 demonstrates the present method's

capability for time-lapse QPI studies with the processes of adherent cell migration, division, and differentiation all present and quantifiable. Throughout the video, various examples of mitosis are observed. In agreement with [131], the cells experience a significant reduction of surface area and increase in phase prior to dividing and then re-adhering. The phase/phase gradient combination is seen to be useful in that the gradient information allows for easy visualization while absolute phase yields quantitative structural information. Thus in order to demonstrate its applicability, future studies are concerned with the use of data recovered by the proposed method for cell segmentation and morphological analysis.

3.5 Conclusions

3.5.1 Discussion

In light of these results, it is appropriate to discuss the advantages and limitations associated with the proposed partially coherent POTF recovery method. Like all methods based on defocus, motorized scanners actuating either the stage plate, nosepiece, or objective are required in order for automation to be practical. Although this introduces significant costs and constraints in comparison to recently developed affordable QPM solutions such as the modular units proposed in [138] and [141], it should be noted that this limitation does not contradict the primary motivation for this work, which was to provide QPI capability using commercially available hardware without modification. As many potential users in biology and medicine already utilize modern live cell microscopy systems with motorized focus control, the work described herein represents an attractive approach for integrating QPI into their portfolio of imaging modalities. For this reason the proposed method should also have commercial appeal to manufactures of microscopy hardware and software, which could utilize such reconstruction algorithms to provided QPI capability via a software update only.

In addition to cost, the use of motorized focus control, including piezoelectric drivers, also limits the achievable acquisition speed of the present method. If objective scanners, as opposed to stage plate scanners, are used then the sample is not mechanically perturbed during imaging. In this case, rates in the range of 5-10 phase frames per second are achievable based on initial experimentation with custom software implementations using the objective scanner described herein. For high-speed investigations, for instance studying red blood cell membrane fluctuations [153], the proposed method is unsuitable and single-shot QPI methods should be used. The last point on defocus is that the proposed method may offer a cost effective solution in limited resource settings where low end microscopes are available and the lack of automated defocus is tolerable.

It is also noted that the simulation and experimental results presented herein highlight the advantages of partially coherent POTF recovery when the linearization conditions [represented by Eq. (20-21) indicating weak absorption and SVP] are valid. This is not always so, as many applications, perhaps industrial ones such as the measurement of phase in photolithography masks [163, 167], require compatibility with strongly absorbing objects. In such cases it is likely that QPM methods based on the TIE, such as the OFS and MFPI-PC algorithms, will offer better reconstructions as they have also been shown to be compatible with strong, but slowly varying, absorption [7]. Another approach, however, to handle violations of the linearization conditions is to use iterative methods from nonlinear optimization to converge to the correct phase result [163].

The last point of discussion is centered on the applicability of 2D phase imaging of thick phase objects under partially spatially coherent illumination. In general, partially coherent image formation for objects thicker than the microscope depth of field is highly complex and inherently nonlinear as each off-axis illuminating plane wave travels a different optical path with multiple scattering events possible, thus 2D phase results should always be viewed with scrutiny. If, however, image formation is well-described by the 3D WOTF, then phase recovery based on the 2D WOTF will converge to the

desired projected phase image if the object spectrum is uniform along the axial spatial frequency coordinate within the 3D aperture of the imaging system [128]. This will generally be the case for object which are much wider than they are thick [128], however, a more careful investigation of these 3D effects is a subject of future research, as outlined in Chapter 8.

3.5.2 Summary

In summary, it has been observed that despite its obvious biomedical applicability, many QPI methods lack sufficient appeal due to reliance on coherent light and specialized hardware. Among methods suitable to microscopy, deterministic PR is attractive due to its direct nature and lack of hardware modification. In response to these needs, we have developed and described a new deterministic PR algorithm based on the WOTF, referred to as POTF recovery, which is linearized using conditions less restrictive than the first Born approximation.

The results demonstrate the performance of the proposed method in comparison with other deterministic PR algorithms based on the TIE and WOTF. The capacity for reconstructing SVP phantoms with large overall phase delay such as might be encountered during adherent cell imaging has also been demonstrated. Experimentally, the POTF recovery has been validated using a MLA as a known test phase object. The capacity for both high-speed and time-lapse QPI of live adherent cells has also been demonstrated. The experimental images show no sign of halo or shade-off artifacts, and their theoretical spatial resolution is better than their coherent counterparts. The theoretical spatial resolution for the parameters used here is estimated as ~ 539 nm. The OPL resolution is also estimated as ~ 1.85 nm based on calibration measurements with no object in place. All in all, the proposed method is poised to promote the widespread adoption of QPI as it provides a simple processing platform by which one can obtain QPI

data of live adherent cells and other specimens which meet the linearization conditions using commercially available microscopy systems.

CHAPTER 4

THREE-DIMENSIONAL QUANTITATIVE PHASE IMAGING VIA TOMOGRAPHIC DECONVOLUTION PHASE MICROSCOPY

In Chapters 2 and 3, the problem of extending two-dimensional quantitative phase imaging (2D QPI) capability to commercial microscopy was addressed. In this chapter, another phase reconstruction method, called tomographic deconvolution phase microscopy (TDPM), is outlined which provides three-dimensional quantitative phase imaging (3D QPI) capability using commercial microscopes with only a slight modification for rotation of the sample. Like POTF recovery, TDPM is based on an optimized inversion of the weak object transfer function (WOTF), which is also shown here to be capable of reconstructing strong 3D phase objects. TDPM is analogous to similar methods utilized in 3D fluorescence microscopy which improve spatial resolution and location accuracy via deconvolution of multiple through-focal series obtained with varying angular orientations. In addition to its compatibility with microscopy, TDPM is unique in its ability to obtain isotropic spatial resolution without resorting to iterative reconstruction procedures for filling in the “missing cone” of spatial frequencies based on *a priori* knowledge of object characteristics, which commonly plagues 3D QPI methods based on optical diffraction tomography (ODT). The method is evaluated with numerical simulations and validated using optical fibers, including specialty fibers and azimuthally asymmetric long-period fiber gratings (LPFGs), as test 3D phase objects. This chapter is based on a manuscript entitled “Three-dimensional quantitative phase imaging via Tomographic Deconvolution Phase Microscopy (TDPM),” which is currently under review for publication [193] and an associated provisional patent application [194].

4.1 Introduction

Quantitative phase imaging (QPI) is an emerging field of biomedical optics in which the refractive index (RI) of phase objects is indirectly imaged through interferometric analysis [6]. QPI is preferred over alternative forms of biomedical imaging in that it is label-free, thus live cells can be imaged in their natural state without issues associated with photo-toxicity or photo-bleaching as in fluorescence microscopy. Another important benefit is that it is quantitative, enabling measurement of intrinsic properties, as opposed to modalities providing qualitative (non-linear) information such as phase and differential interference contrast microscopy. The data's quantitative nature also lends itself towards image processing, thereby improving the extractability of various features and properties [131]. In addition to biomedical applications, QPI techniques have been useful for a variety of other applications including adaptive optics, semiconductor defect inspection [195], and optical fiber characterization [82].

QPI can refer either to two-dimensional QPI (2D QPI), in which the 2D phase image is interpreted as the integrated optical path length (OPL) through the sample, or three-dimensional QPI (3D QPI), in which the real part of the object's complex RI is imaged in all three spatial dimensions [196]. In spite of the fact that most objects, including biological specimens, are essentially 3D phase objects, 2D QPI has found wide-spread biomedical applicability [6, 11, 12, 132, 196, 197]. For example, it is known that cellular dry mass is linearly related to OPL [197], therefore, QPI can be used to monitor cell growth as a function of cell-cycle [11]. Another example would be the study of red blood cell membrane dynamics [12], for which 2D QPI is appropriate since RI is essentially homogeneous.

In a general sense, however, single phase projections are insufficient for characterizing heterogeneous objects since, without approximation or special measures, it is impossible to differentiate OPL variations owing to changes in thickness versus RI. Thus for samples containing complex internal structure, such as eukaryotic cells, 3D QPI

is necessary for a complete morphological characterization. Current trends in QPI methods reflect this need as incorporating tomography and 3D microscopy is a major focus area for research [6]. Although most 3D QPI research has centered on methodology, applications areas, such as the biophysical characterization of malarial parasite exit from human erythrocytes [198] and the quantification of chromosomal dry mass values for human colon cancer cells [13], are being developed in parallel.

Conventionally, 3D QPI is realized via either tomographic [56] or deconvolution methods [5, 63, 64, 199]. In tomography, the object is illuminated over a range of incident angles via either object rotation, in which the sample itself is rotated relative to the imaging system (usually along a principal Cartesian axis), or beam rotation, in which the angle of incidence of the illuminating beam is changed relative to the object and the optical axis of the imaging system [61]. If beam rotation within a non-moving optical system is used, only a limited range of incident angles is possible due to the finite numerical apertures (NAs) of the illuminating and imaging optics, resulting in a missing conical region of the frequency domain support in which data is only recoverable using algorithmic approaches requiring *a priori* knowledge of the sample [67]. Without such recovery spatial resolution will be degraded along the optical axis. Alternatively, although object rotation enables isotropic spatial resolution, it also introduces technical challenges associated with a moving object and limits acquisition speed [61].

In order to recover RI, phase is measured at each angle of incidence. Once the phase is measured, the choice of tomographic reconstruction algorithm depends on how the interaction with the object is modeled [56]. In projection tomography, for example, the measured phase is interpreted as in 2D QPI, in which the light propagates straight through the object in an undeviated manner so that phase is simply the RI of the object integrated along the optical axis multiplied by the incident wave vector magnitude. In this case the object can be reconstructed using conventional algorithms such as filtered backprojection (FBPJ) [56]. This model, however, is usually inappropriate at optical

wavelengths since characteristic dimensions of the object are often on the same order as the illuminating wavelength, meaning that diffraction, in addition to refraction at object boundaries, contribute to image formation and degrade the line integral approximation.

For these reasons optical diffraction tomography (ODT) is usually employed in 3D QPI studies [61]. ODT accounts for diffraction of the incident light by the object and thus provides a more accurate model for image formation. In ODT, one of two approximations, namely the first-order Born or first-order Rytov approximations, are usually employed to linearize the relationship between the object's complex scattering potential and the angularly resolved complex image data, for which amplitude absorption and phase of each pixel are measured [56]. The choice of approximation once again depends on the image formation model. The first Born approximation is known to be appropriate for “weakly scattering” objects in which the total phase delay through the object is less than around $\pi/2$ radians [56]. For biomedical applications, the first Rytov approximation is usually a better choice as it allows for a large total phase delay as long as the gradient of the complex scattered phase isn't too large [200], as is usually the case for weak RI contrast [61]. In both cases, the complex image is related to the Fourier transform of the object along a semicircular arc in the spatial frequency domain and reconstruction algorithms using either spatial or frequency domain interpolation [60] can be utilized.

Although a significant portion of current 3D QPI research is centered on developing and applying ODT methods such as tomographic phase microscopy [9], ODT has some negative features which encourage the development of alternatives in parallel. In general, ODT requires the illumination to be coherent, both temporally and spatially, resulting in difficulties associated with coherent noise sources such as phase jitter and speckle interference [134]. Another factor which may prohibit the wide scale commercialization and adoption of ODT among biomedical users is the cost associated with such laser/opto-mechanical systems, as ODT must combine interferometric imaging with either object or

beam rotation. Most often, ODT employs beam rotation using either single [9] or dual axis [67] galvanometer-controller mirrors to change the angle of incidence. A recent approach combines two modular units to attach on to conventional microscopes providing beam rotation and single-shot 2D QPI respectively [140]. Object rotation has also been achieved on live cells via a hollow fiber capillary cell culture [191], patch-clamping with a micropipette [201], and via holographic tweezers [202].

To address these issues, 3D QPI solutions involving the deconvolution of 3D images (3DD) have been proposed [5, 63, 64, 199]. In such methods, a 3D image is constructed by collecting a through-focal series, after which RI is recovered via 3DD based on a linearized model. This approach is similar to fluorescence 3DD microscopy in which out-of-focus blur is removed numerically [203]. Partially coherent illumination is often employed, enabling compatibility with commercial microscopy, greatly reducing the anticipated cost of such systems. The optical sectioning capability of various methods is derived from differing mechanisms including coherence and high-NA gating [63] as well as extended optical transfer function (OTF) support using partially spatially coherent illumination [66, 199]. Thus it is possible to obtain similar spatial frequency domain support (ultimately limited by illuminating NA) to ODT under beam rotation using commercial microscopy hardware [66], as has been exploited in fluorescence 3DD microscopy [203, 204]. In spite of these benefits, 3DD methods, like tomography under beam rotation, result in degraded resolution along the optical axis, which may be limiting for samples possessing complex internal structure with rapidly varying features inconsistent with constraints imposed by iterative limited-angle tomographic recovery algorithms, such as known object support or piecewise constancy [67].

In what follows, we present a new numerical reconstruction method and approach for 3D QPI, called Tomographic Deconvolution Phase Microscopy (TDPM), which addresses the aforementioned issues by combining 3DD with object rotation to enable isotropic resolution using commercial microscopy hardware. TDPM is analogous to

similar methods used in 3D fluorescence microscopy [205-209], which are capable of 3D spatial resolution better than confocal microscopy. The extension to QPI was originally suggested by Cogswell *et al.* [206], although, to the authors' knowledge, this concept was never realized. Although the recovery model will be based on a 3D weak object transfer function (WOTF) theory [66, 178], we show that TDPM recovery is possible for “non-weak” phase objects with large total phase delay. Altogether, TDPM is an attractive alternative to ODT for both biomedical and industrial applications due to its compatibility with commercial microscopy, experimental simplicity, isotropic spatial resolution, and tolerance of large phase objects.

4.2 Principles of Tomographic Deconvolution Phase Microscopy

4.2.1 Relationship to First-Order Diffraction Tomography

First-order diffraction tomography is a scalar theory based on the inhomogeneous Helmholtz equation [Eq. (4.1)]:

$$[\nabla^2 + k^2(\mathbf{r})]u(\mathbf{r}) = 0. \quad (4.1)$$

In Eq. (4.1), $k(\mathbf{r}) = k_0 n(\mathbf{r})$ where $k_0 = 2\pi/\lambda$ is the free-space wave vector magnitude for the wavelength λ and $n(\mathbf{r}) = n_0 + \Delta n(\mathbf{r})$ in which n_0 is the average RI and $\Delta n(\mathbf{r})$ is the spatially varying component which defines the object, $u(\mathbf{r})$ is the total complex field amplitude (single polarization component for electromagnetic fields), and $\mathbf{r} = x\hat{x} + y\hat{y} + z\hat{z}$ denotes spatial coordinates. We may rewrite Eq. (4.1) as Eq. (4.2) to isolate the driving terms:

$$[\nabla^2 + (k_0 n_0)^2]u(\mathbf{r}) = -V(\mathbf{r})u(\mathbf{r}). \quad (4.2)$$

In Eq. (4.2), $V(\mathbf{r}) = k_0^2[n^2(\mathbf{r}) - n_0^2]$ is the complex scattering potential which is evidently zero outside the support of the object (given as V'). Using the method of Green's functions, we may write the solution for $u(\mathbf{r})$ as [56]

$$u(\mathbf{r}) = u_0(\mathbf{r}) + u_s(\mathbf{r}), \quad (4.3a)$$

$$\begin{aligned} u_s(\mathbf{r}) &= \int_{V'} V(\mathbf{r}') u(\mathbf{r}') g(|\mathbf{r} - \mathbf{r}'|) d^3\mathbf{r}' \\ &= [V(\mathbf{r})u(\mathbf{r})] * g(\mathbf{r}) \end{aligned}, \quad (4.3b)$$

where $u_0(\mathbf{r}) = U_0 \exp(i\pi \boldsymbol{\rho}' \cdot \mathbf{r})$ is an incident plane wave field with wave number $\boldsymbol{\rho}' = \hat{\boldsymbol{\rho}}' n_0 / \lambda$ in which $\hat{\boldsymbol{\rho}}'$ is a unit vector describing direction, $u_s(\mathbf{r})$ is the field scattered by the object, $g(\mathbf{r}) = \exp(ik_0 n_0 r) / (4\pi r)$ is the Green's function in three-space, $r = |\mathbf{r}|$, $*$ denotes convolution, and $i = \sqrt{-1}$. If $|u_s(\mathbf{r})| \ll U_0$ within V' we may rewrite Eq. (4.3b) as Eq. (4.4), which is the first Born approximation for the scattered field [56]:

$$u_B(\mathbf{r}) = [V(\mathbf{r})u_0(\mathbf{r})] * g(\mathbf{r}). \quad (4.4)$$

It has been shown that we may also write the solution to Eq. (4.2) as

$$u(\mathbf{r}) = u_0(\mathbf{r}) \exp[\psi_s(\mathbf{r})], \quad (4.5a)$$

$$\psi_s(\mathbf{r}) = \frac{1}{u_0(\mathbf{r})} \int \{V(\mathbf{r}') + [\nabla\psi_s(\mathbf{r}')]^2\} u_0(\mathbf{r}') g(|\mathbf{r} - \mathbf{r}'|) d^3\mathbf{r}', \quad (4.5b)$$

where $\psi_s(\mathbf{r})$ is the scattered component of the total field complex phase comprising both absorption and phase [56]. The first Rytov approximation for the complex scattered phase [Eq. (4.6)]:

$$\psi_R(\mathbf{r}) = \frac{u_B(\mathbf{r})}{u_0(\mathbf{r})}, \quad (4.6)$$

is recovered if we allow

$$V(\mathbf{r}) + [\nabla\psi_s(\mathbf{r})]^2 \cong V(\mathbf{r}), \quad (4.7)$$

in the integrand of Eq. (4.5b), even though the limits of integration technically extend over all space. Although there has been some controversy concerning the relative validity domains of the first Born and Rytov approximations [200], it is generally accepted that the first Rytov approximation for the scattered phase [Eq. (4.6)] may still be valid when $|u_s(\mathbf{r})| \ll U_0$ is invalid provided the change in scattered phase over one wavelength is

small [56]. Thus the Rytov approximation is usually employed in ODT since RI contrast is typically weak [61].

Let us now consider bright-field microscopy operating in transmission for which only forward propagating waves which fall within the system aperture exist in image space. Initially, the illumination is modelled as a spatially coherent quasi-monochromatic plane wave defined by $u_0(\mathbf{r}, \boldsymbol{\rho}') = \sqrt{S(\boldsymbol{\rho}')} \exp(i2\pi\boldsymbol{\rho}' \cdot \mathbf{r})$ where $\sqrt{S(\boldsymbol{\rho}')}$ is the normalized (with respect to unit amplitude/intensity) amplitude emanating from the source $S(\boldsymbol{\rho}')$. The quasi-monochromatic approximation, which implies that the illumination bandwidth is much smaller than the central wavelength, or $\Delta\lambda \ll \bar{\lambda}$, is easily obtained in microscopy through the use of interference filters and enables ignoring of partial temporal coherence from spectrally broadened sources [180]. Let us assume that the first Rytov approximation is valid, so that the scattered complex phase is well approximated by Eq. (4.6). Using Eq. (4.5a), we may write an expression for total normalized intensity, in which the $\boldsymbol{\rho}'$ dependence has been made explicit:

$$\begin{aligned} I(\mathbf{r}, \boldsymbol{\rho}') &= u(\mathbf{r}, \boldsymbol{\rho}') u^*(\mathbf{r}, \boldsymbol{\rho}') \\ &= S(\boldsymbol{\rho}') \exp\{2\text{Re}[\psi_R(\mathbf{r}, \boldsymbol{\rho}')]\} \end{aligned} \quad (4.8)$$

Expanding the exponent of Eq. (4.8) in a Taylor series reveals that if

$$|2\text{Re}[\psi_R(\mathbf{r}, \boldsymbol{\rho}')]| \ll 1, \quad (4.9)$$

Eq. (4.8) may be approximated as

$$I(\mathbf{r}, \boldsymbol{\rho}') = S(\boldsymbol{\rho}') \{1 + 2\text{Re}[\psi_R(\mathbf{r}, \boldsymbol{\rho}')]\}. \quad (4.10)$$

Expanding Eq. (4.10) using Eq. (4.6) and Eq. (4.4) results in

$$\begin{aligned} I(\mathbf{r}, \boldsymbol{\rho}') &= S(\boldsymbol{\rho}') \left\{ 1 \right. \\ &\quad \left. + 2\text{Re} \left[\frac{i}{u_0(\mathbf{r}, \boldsymbol{\rho}')} \{ [V_A(\mathbf{r}) u_0(\mathbf{r}, \boldsymbol{\rho}')] * g(\mathbf{r}) \} \right] \right. \\ &\quad \left. + 2\text{Re} \left[\frac{1}{u_0(\mathbf{r}, \boldsymbol{\rho}')} \{ [V_P(\mathbf{r}) u_0(\mathbf{r}, \boldsymbol{\rho}')] * g(\mathbf{r}) \} \right] \right\}, \end{aligned} \quad (4.11)$$

where $V(\mathbf{r})$ has been expanded into real and imaginary parts [Eq. (4.12)] corresponding to phase $V_p(\mathbf{r})$ and absorption $V_A(\mathbf{r})$ as in [26].

$$V(\mathbf{r}) = V_p(\mathbf{r}) + iV_A(\mathbf{r}). \quad (4.12)$$

The Fourier transform of Eq. (4.11) is given by Eq. (4.13), in which shifting property has been used.

$$\begin{aligned} I(\boldsymbol{\rho}, \boldsymbol{\rho}') = S(\boldsymbol{\rho}')\{ & \delta(\boldsymbol{\rho}) \\ & + iV_A(\boldsymbol{\rho})[G'(\boldsymbol{\rho} + \boldsymbol{\rho}') - G'^*(\boldsymbol{\rho}' - \boldsymbol{\rho})], \\ & + V_p(\boldsymbol{\rho})[G'(\boldsymbol{\rho} + \boldsymbol{\rho}') + G'^*(\boldsymbol{\rho}' - \boldsymbol{\rho})]\} \end{aligned} \quad (4.13)$$

In Eq. (4.13), $\boldsymbol{\rho} = \rho_x \widehat{\rho}_x + \rho_y \widehat{\rho}_y + \rho_z \widehat{\rho}_z$ denotes frequency coordinates conjugate to \mathbf{r} and $V_A(\boldsymbol{\rho})$ as well as $V_p(\boldsymbol{\rho})$ are the Fourier transforms of $V_A(\mathbf{r})$ and $V_p(\mathbf{r})$ respectively. Also used in Eq. (4.13), $G'(\boldsymbol{\rho})$ is the Fourier transform of the Green's function filtered to transmit forward propagating waves within the system pupil as defined by $P(\boldsymbol{\rho}_\perp)$ in Eq. (4.14):

$$G'(\boldsymbol{\rho}) = G(\boldsymbol{\rho})P(\boldsymbol{\rho}_\perp)U(\rho_z), \quad (4.14)$$

where $\boldsymbol{\rho}_\perp = \rho_x \widehat{\rho}_x + \rho_y \widehat{\rho}_y$. In Eq. (4.14), $P(\boldsymbol{\rho}_\perp)$ is usually given by $\text{circ}(\boldsymbol{\rho}_\perp/\rho_o)$ where $\rho_o = NA_o/\bar{\lambda}$ in which NA_o is the NA of the microscope objective lens, and $\text{circ}(\boldsymbol{\zeta})$ as well as the unit step function $U(\zeta)$ in Eq. (4.14) are defined as

$$\text{circ}(\boldsymbol{\zeta}) = \begin{cases} 1, & |\boldsymbol{\zeta}| \leq 1 \\ 0, & |\boldsymbol{\zeta}| \geq 1' \end{cases} \quad (4.15)$$

$$U(\zeta) = \begin{cases} 1, & \zeta \leq 0 \\ 0, & \zeta \geq 0. \end{cases} \quad (4.16)$$

Assuming an extended incoherent source, we may incorporate partial spatial coherence by integrating over the illumination pupil $S(\boldsymbol{\rho}')$ [66, 178], so that the final intensity spectrum may be written as

$$I(\boldsymbol{\rho}) = B\delta(\boldsymbol{\rho}) + V_A(\boldsymbol{\rho})H_A(\boldsymbol{\rho}) + V_P(\boldsymbol{\rho})H_P(\boldsymbol{\rho}): \quad (4.17a)$$

$$B = \int S(\boldsymbol{\rho}')d^2\boldsymbol{\rho}', \quad (4.17b)$$

$$H_A(\boldsymbol{\rho}) = i \int S(\boldsymbol{\rho}')[G'(\boldsymbol{\rho} + \boldsymbol{\rho}') - G'^*(\boldsymbol{\rho}' - \boldsymbol{\rho})]d^2\boldsymbol{\rho}', \quad (4.17c)$$

$$H_P(\boldsymbol{\rho}) = \int S(\boldsymbol{\rho}')[G'(\boldsymbol{\rho} + \boldsymbol{\rho}') + G'^*(\boldsymbol{\rho}' - \boldsymbol{\rho})]d^2\boldsymbol{\rho}', \quad (4.17d)$$

and the corresponding 3D intensity image is given by

$$I(\mathbf{r}) = B + V_A(\mathbf{r}) * h_A(\mathbf{r}) + V_P(\mathbf{r}) * h_P(\mathbf{r}), \quad (4.18)$$

in which $h_A(\mathbf{r})$ and $h_P(\mathbf{r})$ are real-valued point spread functions (PSFs) corresponding to the absorption and phase OTFs (AOTF and POTF respectively) defined by $H_A(\boldsymbol{\rho})$ and $H_P(\boldsymbol{\rho})$ and B is the background intensity. In Eq. (4.17) and (4.18), the unit intensity normalization has been accounted for by the integral over $\boldsymbol{\rho}'$. Equation (4.17) is the 3D WOTF first derived in [66] for circular illumination pupils under the paraxial approximation. Eq. (4.17) is usually derived by invoking the Born approximation [66, 178] implying that $\forall \boldsymbol{\rho}' \in S(\boldsymbol{\rho}'), |u_s(\mathbf{r}, \boldsymbol{\rho}')| \ll \sqrt{S(\boldsymbol{\rho}')}$ within V' . Here we have shown that the 3D WOTF is valid under the first Rytov approximation with an additional constraint defined by Eq. (4.9) $\forall \boldsymbol{\rho}' \in S(\boldsymbol{\rho}')$ and $\forall \mathbf{r} \in \Omega$ where Ω defines the measurement domain. The conditions imposed by Eq. (4.9) are similar to the weak absorption and slowly varying phase (SVP) conditions first derived by Guigay [127] for 2D imaging. Splitting up contributions arising from absorption and phase, we write Eq. (4.9) as

$$|V_A(\mathbf{r}) * 2i\text{Im}[g'(\mathbf{r}, \boldsymbol{\rho}')]| \ll 1, \quad (4.19a)$$

$$|V_P(\mathbf{r}) * 2\text{Re}[g'(\mathbf{r}, \boldsymbol{\rho}')]| \ll 1, \quad (4.19b)$$

where $g'(\mathbf{r}, \boldsymbol{\rho}') = \mathcal{F}^{-1}[G'(\boldsymbol{\rho} + \boldsymbol{\rho}')]$ is the effective coherent PSF and $\mathcal{F}^{-1}(x)$ denotes inverse Fourier transformation of x . Eq. (4.19a) requires weak absorption and Eq. (4.19b) requires SVP, increasing the likelihood that the first Rytov approximation is valid. In

essence, Eq. (4.19) implies that the magnitude of intensity variations caused by scattering from a coherent plane wave must be small in comparison to the background intensity, defining a trade-off between signal-to-noise ratio (SNR) and linearization validity. The aforementioned statement regarding scattered intensity must be valid for all illuminating waves independently and not their incoherent sum, in which contrast is usually reduced further. Additional intuition is gained by considering Eq. (4.19) in the frequency domain. In Fig. 4.1, the absolute values of simulated AOTF and POTF corresponding to the PSFs in Eq. (4.19) for on-axis coherent illumination are shown. In generating the PSFs, the parameters $\lambda = 546 \text{ nm}$, $n_o = 1.46$, and $NA_o = 0.75$ were used.

From Fig. 4.1(a) we see that the AOTF has a strong low-pass characteristic since the Ewald sphere cap and its conjugate overlap additively due to the fact that the imaginary part of $g'(\mathbf{r}, \boldsymbol{\rho}')$ is an even function of \mathbf{r} . This low-pass characteristic implies that the total absorption through the object must be small, as is consistent with our interpretation regarding scattered intensity. For the POTF, the opposite is true since the real part of $g'(\mathbf{r}, \boldsymbol{\rho}')$ is odd. Thus in Fig. 4.1(b) we observe the cancellation of contrast near the origin of frequency space. This implies that large but “slowly varying” phase objects with most of their energy residing in lower spatial frequencies are well approximated by the 3D WOTF theory, which further cements the Rytov approximation used in its derivation. In Section 4.3, examples demonstrating the validity of this observation are provided using a split-step beam propagation method (SS-BPM) validated against rigorous electromagnetic solutions to scattering from a homogeneous cylinder.

4.2.2 Tomographic Deconvolution Phase Microscopy Refractive Index Recovery

Assuming that the validity conditions [Eq. (4.19) and first Rytov approximation] are met, the 3D WOTF [Eq. (4.17)] becomes the basis for TDPM. Shown in Fig. 4.2 are the AOTF and POTF (shown in the $\rho_x - \rho_z$ plane with rotational symmetry implied) that are used through the remainder of this chapter which are calibrated to match the imaging properties of the microscope utilized (*Olympus BX60*).

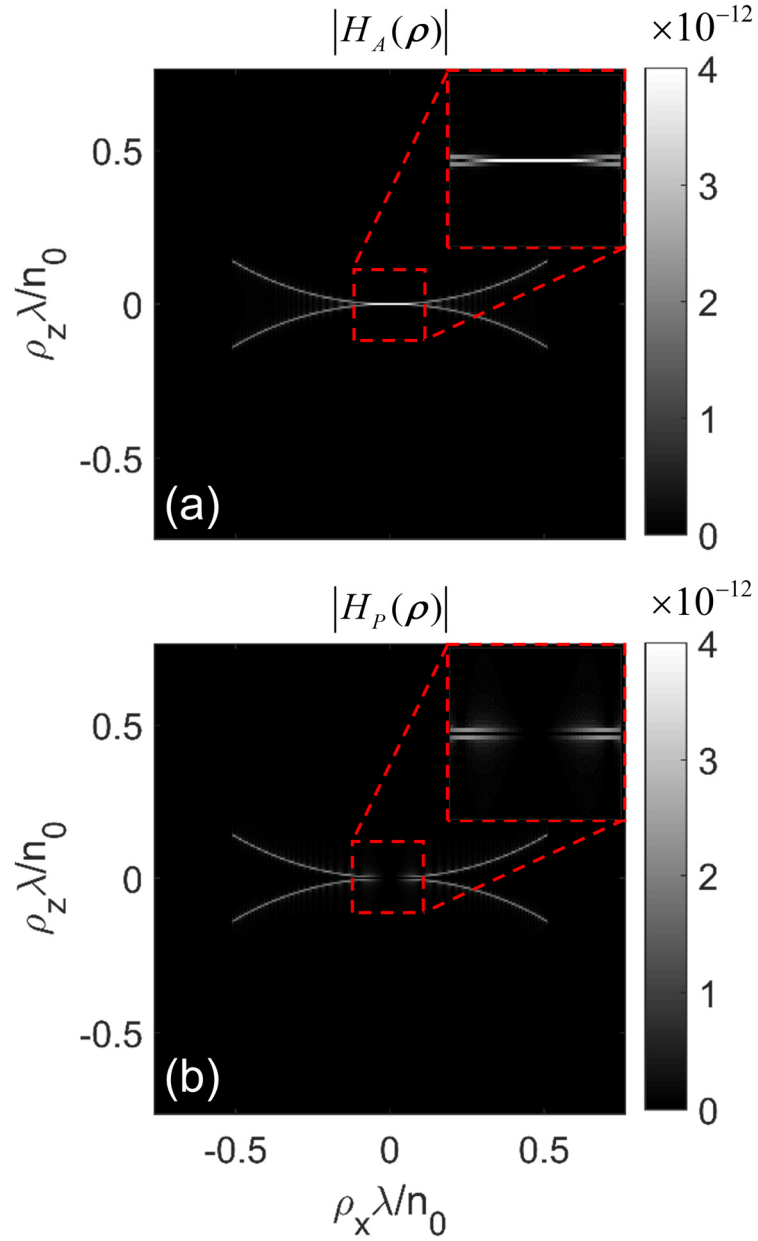


Figure 4.1: Magnitudes of the on-axis coherent 3D (a) absorption optical transfer function (AOTF) and (b) phase optical transfer function (POTF) derived from simulating the scattered complex field amplitude due to a point scatterer. All figures are plotted as a function of normalized frequency coordinates $\rho\lambda/n_0$, and have rotational symmetry about $\widehat{\rho}_z$.

The OTFs in Fig. 4.2(a) and 4.2(b) were calculated by simulating the scattering due to a line absorber, $V(\mathbf{r}) = i\delta(x)\delta(z)$, and a line scatterer, $V(\mathbf{r}) = \delta(x)\delta(z)$, respectively at $\bar{\lambda} = 546$ nm with $n_0 = 1.46$.

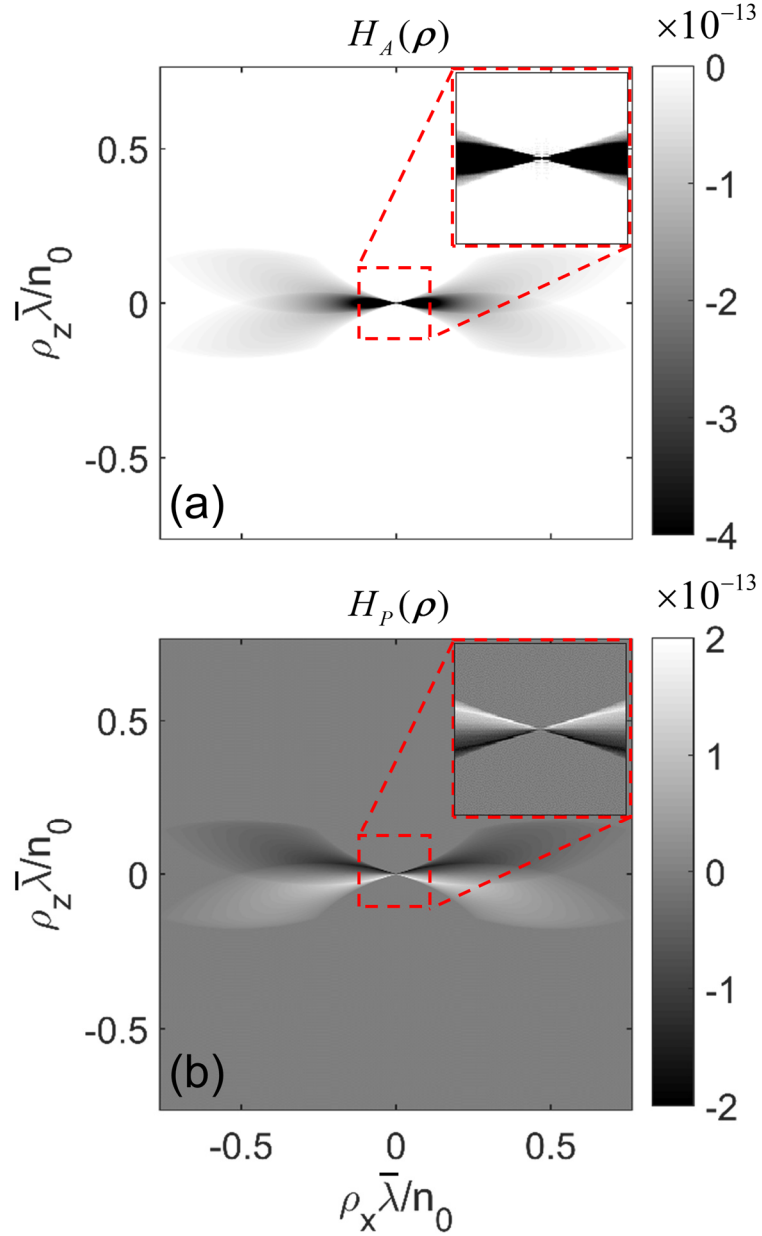


Figure 4.2: Partially coherent 3D (a) absorption optical transfer function (AOTF) and (b) phase optical transfer function (POTF) plotted as a function of normalized frequency coordinates $\rho \bar{\lambda}/n_0$.

In calculating the OTFs, the scattered intensity due to each coherent plane wave in the illumination pupil was summed incoherently as in Abbe's method for partially coherent image formation [210]. In order to increase accuracy, primary spherical aberration owing to focusing through uncompensated media was modeled by adding an extra term in the exponent of the defocusing pupil [180], for which the microscope was assumed to be

aberration free at $z = 0$. A circular illumination pupil with NA_c (NA of the illuminating condenser lens) was used to balance the trade-off between optical sectioning and image contrast. A Gaussian distribution for $S(\boldsymbol{\rho}')$ was assumed based on 2D curve fitting [Fig. 4.3(b)] to an image [Fig. 4.3(a)] of the back-focal-plane of the objective lens (*Olympus UPlanFl 40 \times / 0.75 0.17 ∞*) obtained by inserting a Bertrand lens into the optical train with no sample in place. Thus each point source was weighted by the curve-fitted estimate [Fig. 4.3(b)].

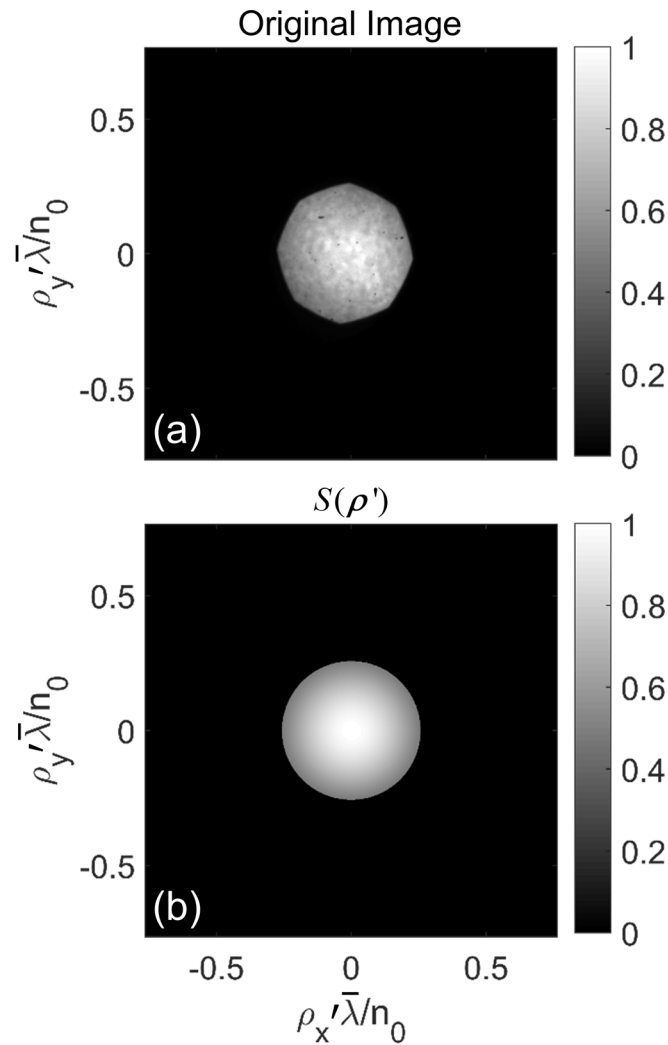


Figure 4.3: (a) Image of objective back-focal-plane with no sample in place. (b) Gaussian fit to (a) serving as the input source distribution in the calculation of optical transfer functions (OTFs) shown in Fig. 4.2. Both figures are plotted as a function of normalized frequency coordinates in the illumination pupil $\boldsymbol{\rho}' \bar{\lambda} / n_0$.

Since the linearization conditions depend only on the relative intensity contrast due to each point source, they are independent of $S(\boldsymbol{\rho}')$ and depend only on the choice of system pupil $P(\boldsymbol{\rho}_\perp)$. In order to remain compatible with commercial microscopy, the choices for $P(\boldsymbol{\rho}_\perp)$ are limited. Although it may seem advantageous to utilize Zernike phase contrast, in this case the real and imaginary parts of $V(\mathbf{r})$ effectively interchange roles in Eq. (4.19) thereby implying a weak phase condition. Differential interference contrast may be a much better option since contrast is related to lateral phase gradient rather than absolute value [181]. For bright-field microscopy, it may prove beneficial to optimize over the illumination pupil intensity distribution $S(\boldsymbol{\rho}')$. Although no such optimization has been attempted, it has been observed that pupils with monotonically decreasing intensity with illumination angle provide more uniform contrast in the frequency domain and lead to increased stability.

It can be seen from Fig. 4.2 that spatial frequency coverage under partial spatial coherence is similar to the coverage obtained in ODT under beam rotation [66] as well as widefield deconvolution microscopy [211]. This is because each plane wave in the illumination pupil samples the same Ewald sphere cap as in ODT plus its complex conjugate. Thus by measuring a through-focal series in a bright-field microscope one obtains similar information as in ODT with phase measurements over many angles. This is only true, however, in certain cases, such as imaging pure phase objects, in which a direct or regularized deconvolution between measured intensity and $V_p(\mathbf{r})$ can be achieved based on $H_p(\boldsymbol{\rho})$, as was first demonstrated by Noda *et al.* using annular illumination [199]. Another example would be when absorption is assumed to be proportional to phase, or $V_A(\mathbf{r}) = \varepsilon V_p(\mathbf{r})$, as in [212]. For a general object, with both weak absorption and phase, Streibl suggested that it should be possible to recover both components by measuring through-focal series under two different pupil functions [66].

In TDPM, this is realized via object rotation. If the sample is rotated by 180° , for example, the symmetries of $H_A(\boldsymbol{\rho})$ and $H_p(\boldsymbol{\rho})$ allow $V_p(\mathbf{r})$ to be recovered uniquely by

subtraction of their respective 3D image stacks relative to a single reference coordinate system because the absorption contrast is an even function about each scatterer. This is analogous to phase recovery using 2D WOTF theory based on subtraction of images on either side of focus, as demonstrated in Chapter 3 [129]. Another benefit of subtracting through-focal series obtained from opposing perspectives is the ability to recover stronger pure phase objects because the second-order term, as well as all even-ordered terms, in the Taylor series expansion of Eq. (4.8) produce even contrast. In spite of the benefits 360° coverage, for pure phase objects with weak RI contrast, complete object recovery is possible via object rotation over 180° and will be the basis of conventional TDPM RI recovery.

Assuming the addition of an experimental configuration for object rotation, which in practice will likely be a glass fiber or capillary coupled to a rotation stage/device [205, 208, 209], we are ready to devise a strategy for implementing TDPM. In order to sample the object spectrum in an isotropic fashion near the origin, the object must be rotated at least N times where $N \geq \lceil \pi/2\theta_c \rceil$, $\lceil x \rceil$ denotes rounding the decimal value x up to the nearest integer, and $\theta_c = \sin^{-1}(NA_c/n_0)$ is the marginal illumination angle in radians. In practice, however, it is often necessary to select $N \geq \lceil \pi/\theta_c \rceil$ in order to enable reasonable contrast across the entire spectrum. Assuming equiangular rotation, choosing N results in the rotational increment $\Delta\theta = \pi/N$. An optimal solution for the spectrum of the real part of the complex scattering potential, $V_p(\boldsymbol{\rho})$, is sought via the least squares formalism summarized by Eq. (4.20a), where j is an index associated with object rotation angle $\theta_j = j\Delta\theta$, $I_{\theta_j}(\boldsymbol{\rho})/B$ are the 3D intensity spectra normalized by the background intensity B , $H_p(\boldsymbol{\rho})$ are the normalized 3D POTFs given by Eq. (4.17d) assuming unit background intensity, $H_{p_j}(\boldsymbol{\rho})$ are the normalized 3D POTFs rotated at the angle θ_j , and α is a regularization parameter. Equation (4.20) can be solved directly to yield $V_p(\boldsymbol{\rho})$ as given by Eq. (4.20b):

$$\min \epsilon = \sum_{j=0}^{N-1} \left| V_P(\boldsymbol{\rho}) H_P(\boldsymbol{\rho}) - \frac{I_{\theta_j}(\boldsymbol{\rho})}{B} \right|^2 + \alpha |V_P(\boldsymbol{\rho})|^2, \quad (4.20a)$$

$$V_P(\boldsymbol{\rho}) = \sum_{j=0}^{N-1} \frac{\left[\frac{I_{\theta_j}(\boldsymbol{\rho})}{B} \right] H_P^*(\boldsymbol{\rho})}{\left[\sum_{j=0}^{N-1} |H_{P_j}(\boldsymbol{\rho})|^2 + \alpha \right]}. \quad (4.20b)$$

The numerical implementation of Eq. (4.20) is non-trivial. Also, as can be seen in the upper-right inset of Fig. 4.2(b), contrast for low spatial frequencies near the origin is reduced resulting in ill-posed recovery, which is a well-known problem in 2D phase retrieval (PR) [47]. In fact, if Ω is selected to be a rectangular prism which barely encompasses the object then the frequency domain is likely to be undersampled resulting in spatial aliasing artifacts. In this case there are likely to be low spatial frequencies which are never sampled and are thus unrecoverable via 3D Fourier inversion. TDPM solves these issues by using a hybrid algorithm with different processing steps for low versus high spatial frequencies. The high-frequency algorithm is based on Eq. (4.20) and is summarized in Fig. 4.4. The low-frequency algorithm is the partially coherent analogue to filtered backpropagation (FBPP) [59] and is summarized in Fig. 4.5. Although it has proven difficult to optimize the low-frequency algorithm as in Eq. (4.20), preliminary results indicate that such an optimization would only yield marginal improvement.

The high-frequency algorithm shown in Fig. 4.4 is divided into four stages. In the image capture and pre-processing stage, through-focal series of an object are first acquired over the measurement domain Ω as the object is rotated in equal increments of $\Delta\theta$ about the y -axis and then processed as inputs for RI recovery. The domain Ω should at least encompass the object, which is usually either known or easily estimated. If possible, Ω should also encompass the scattered intensity variations, thereby preventing errors associated with spatial aliasing and providing sufficient frequency domain resolution for a complete reconstruction via the optimized algorithm shown in Fig. 4.4. This will be difficult to achieve in practice, particularly for larger objects under increased

spatial coherence. Thus far, however, simulation and experimentation suggest that errors due to spatial aliasing do not inhibit quantitative interpretation of the data.

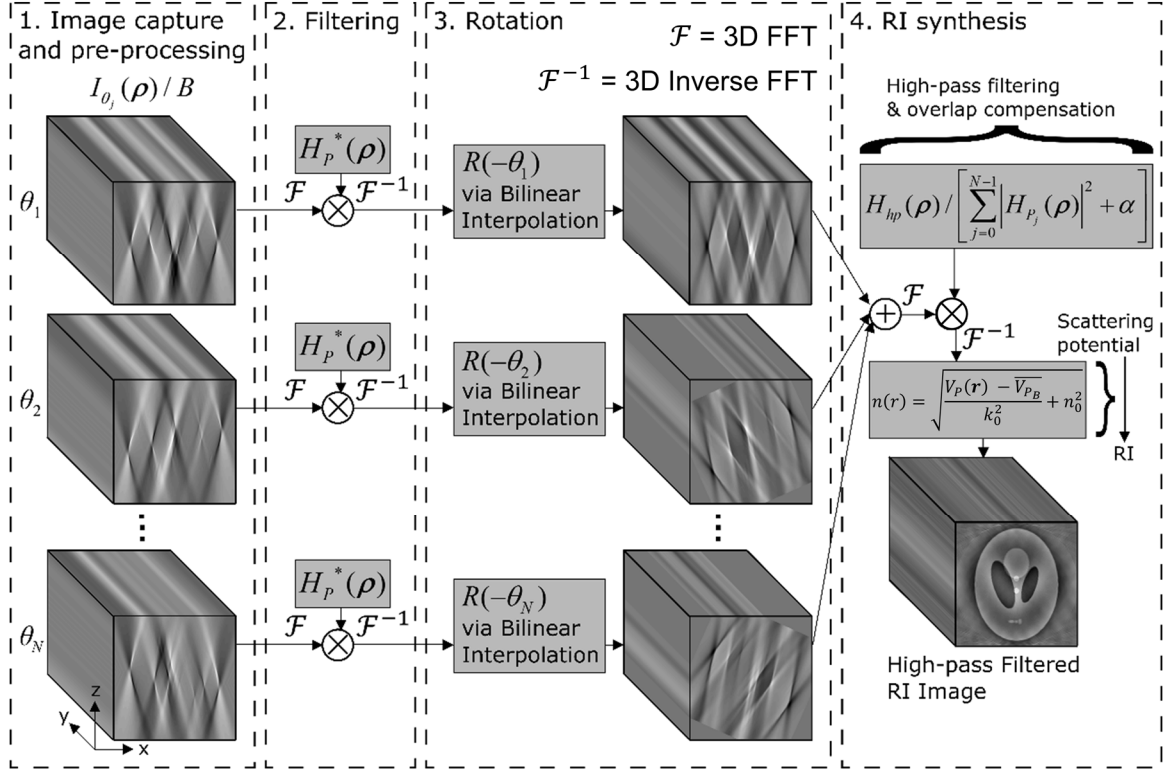


Figure 4.4: Block diagram representation of tomographic deconvolution phase microscopy (TDPM) refractive index (RI) recovery for high spatial frequencies.

Once the through-focal images are collected over all rotation angles, pre-processing steps include background intensity normalization and subtraction, z-slice registration, upsampling, and 3D image registration. Since background intensity B is a conserved quantity [66], each z-slice image is first normalized by its average. Following normalization, background intensity variations which are characteristic of the system and not of the sample are removed via subtraction with a background through-focal series measured over the same domain Ω . The next pre-processing step entails the registration of each z-slice to its nearest neighbors. This is only necessary in the event of object movement during 3D image measurement and has been successfully implemented via normalized cross-correlation between neighboring slices. Once the through-focal series is aligned internally, it is then usually upsampled along the z-axis. This is because the

microscope depth of field is usually larger than the lateral resolution $\Delta r = \Delta x = \Delta y$. An efficient sampling strategy, therefore, is to sample at the largest integer multiple of Δr which is less than or equal to the depth of field, so that $\Delta z = \Delta r$ after upsampling by the same integer. Note that care should be taken to ensure that defocus distances used in the measurement correspond to distances within object space, which may have a background RI n_0 greater than one, implying that the microscope should be defocused by $\Delta z/n_0$ to realize a distance of Δz within object space.

The final pre-processing step is 3D image registration which is usually necessary due to radial runout of the rotating cylinder. Although phase correlation has previously been used for this step [208], herein another normalized cross-correlation between the measured through-focal series and pre-simulated sub images which are characteristic of scattering from the cylindrical reference boundaries on a column by column basis along the axis of rotation (y -axis) was found to be sufficient. Once positions of maximum correlation are identified, each column is circularly shifted to the center ensuring a single rotational reference.

The next stage consists of filtering the spectrum of each through-focal series with the POTF conjugate, $H_p^*(\boldsymbol{\rho})$. Upon inverse Fourier transformation the images are ready for inverse rotation via bilinear interpolation to compensate for their physical rotation angle. In the final stage, the high spatial frequencies of RI are synthesized by summing over rotation angle, compensating for the frequency domain overlap between measurement angles via the denominator of Eq. (4.20b), filtering with a high-pass filter $H_{hp}(\boldsymbol{\rho})$, offsetting the result so that the scattering potential $V_p(\mathbf{r})$ is zero outside the object (by subtracting $\overline{V_{p_B}}$, or the mean of $V_p(\mathbf{r})$ in the background region, and conversion from scattering potential to RI. The denominator of Eq. (4.20b) is constructed by Fourier transforming (indicated by \mathcal{F}) the sum of rotated phase PSF autocorrelations [Eq. (4.21)].

The rotations are made in real space via bilinear interpolation, which is found to yield less reconstruction error than frequency domain interpolation.

$$\sum_{j=0}^{N-1} |H_{P_j}(\boldsymbol{\rho})|^2 = \mathcal{F} \left[\sum_{j=0}^{N-1} h_{P_j}(\mathbf{r}) * h_{P_j}^*(-\mathbf{r}) \right]. \quad (4.21)$$

Thus far a hard cut-off high-pass filter has been used [$H_{hp}(\rho) = U(\rho - \kappa)$, where $\rho = |\boldsymbol{\rho}|$] which retains all frequencies above a radial threshold $\kappa = 1/(\Omega_z \sin\theta_c)$ (Ω_z is the extent of Ω along to optical axis z), which defines the boundary between sampled frequencies and frequencies which are never sampled due to insufficient frequency resolution.

Because frequencies below κ are unrecoverable when Ω does not encompass the scattered intensity, the algorithm shown in Fig. 4.5 is necessary. The first stage of Fig. 4.5 is the same as the first stage of Fig. 4.4. The first stage shown in Fig. 4.5, which is the second stage in the low-frequency algorithm, consists of applying 2D PR to solve for phase at each z -slice through the object. Since it needs to operate on partially coherent intensity data, an algorithm is selected which can easily model partial coherence, such as TIE phase recovery [46] or methods based on inversion of the 2D WOTF [49]. In this work, a recent phase reconstruction method referred to as POTF recovery [129], and described in Chapter 3, was utilized. This method is the 2D analogue of TDPM and results in phase recovery from multiple defocused plane pairs which is optimal in the sense of minimizing noise in the final phase image.

Actually, the general use of depth-resolved phase recovery is unjustified in the case of partially coherent illumination of a 3D phase object because phase has no meaning in the out-of-focus planes from each slice [108]. Below the previously defined threshold $\rho < \kappa$, however, the projection approximation is actually rather good, justifying the use of depth-resolved PR for these frequencies since the phase contributed from each slice is roughly independent of the plane in which it is measured. Small phase variations do occur over

the same length scale as Ω_z , which is why the algorithm detailed in Fig. 4.5 is used, as opposed to conventional FBPJ [56].

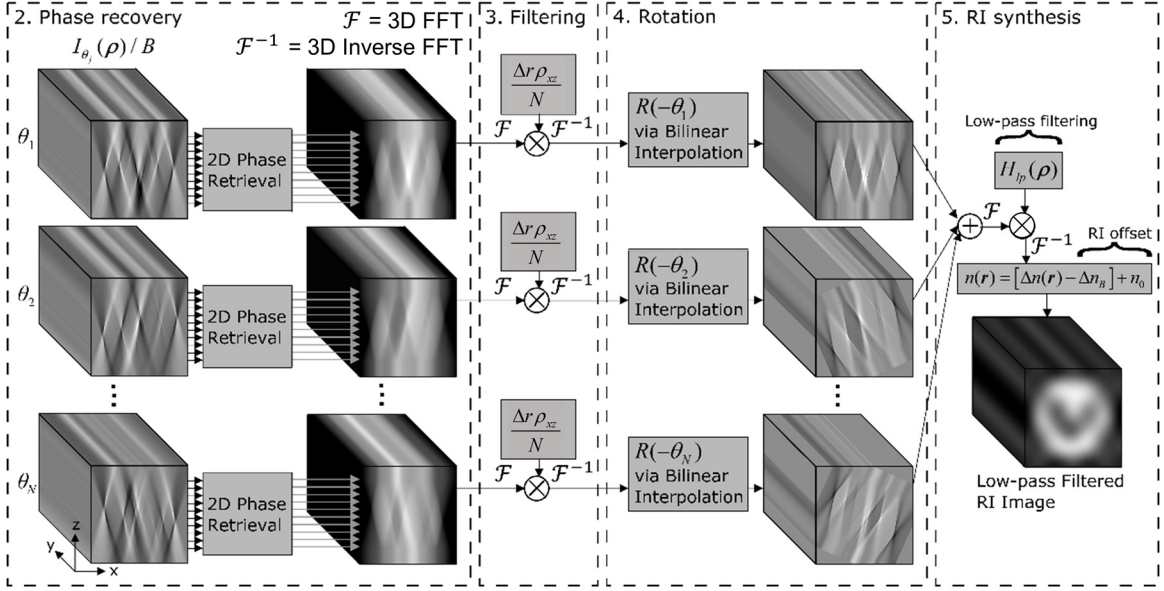


Figure 4.5: Block diagram representation of tomographic deconvolution phase microscopy (TDPM) RI recovery for low spatial frequencies.

In implementing depth-resolved PR a selected number of defocused intensity images on either side of focus are used as inputs to the POTF recovery algorithm. This number should be chosen so that phase can be reconstructed over the entire extent of the object without needing to use defocused images estimated via circular padding. Another good reason to select Ω to be as large as possible is that the eventual phase SNR is roughly proportional to the defocus range used. Planes near the top and bottom edges which are unrecoverable in this manner are estimated by extension of their nearest recoverable neighbor. The remaining stages shown in Fig. 4.5 correspond to the conventional FBPJ algorithm [59, 213]. In order to compensate for the increased sampling density near the spatial frequency origin, depth-resolved phases are filtered using normalized Ram-Lak filters with cylindrical symmetry about the y - or rotation-axis ($\Delta r \rho_{xz}/N$, $\rho_{xz} = \sqrt{\rho_x^2 + \rho_z^2}$), after which rotation is achieved via bilinear interpolation in the spatial domain [213]. In the synthesis stage, the filtered phases are summed over rotation angle,

low-pass filtered using $H_{lp}(\rho) = 1 - U(\rho - \kappa)$, and level shifted to compensate for the lack of absolute phase information. The final step in TDPM RI recovery is to add the results from Fig. 4.4 and Fig. 4.5 to obtain the overall 3D RI.

4.3 Simulation Results

4.3.1 Modified Split-Step Beam Propagation Method

In order to model the imaging of 3D phase objects using bright-field microscopy, a modified wide-angle SS-BPM is used. In this method, contributions arising from each point source in the illumination pupil are added incoherently to form the final 3D bright-field image. Each coherent simulation consists of implementing an off-axis wide-angle SS-BPM [103] which incorporates an obliquity factor (OF) given by Eq. (4.22) and which is associated with the local phase gradient magnitude [214], which compensates for additional phase delay associated with propagating through an effective thickness of $OF(\mathbf{r})\Delta z$, where Δz is the longitudinal resolution of the simulation. In Eq. (4.22), ∇_{\perp} is a gradient operating on lateral coordinates only and $\phi(\mathbf{r})$ is the phase of the total field $u(\mathbf{r})$.

$$OF(\mathbf{r}) = \frac{1}{\sqrt{1 - \left[\frac{|\nabla_{\perp} \phi(\mathbf{r})|}{k_0 n_0} \right]^2}}. \quad (4.22)$$

The SS-BPM is initialized with $u_z(\mathbf{r}) = u_0(\mathbf{r}, \rho')$ as given in Section 4.2.1. At each z-slice, the wave is first propagated by a half-step using the angular spectrum method in accordance with Eq. (4.23) [184], after which additional phase delay is added according to Eq. (4.24), and last of all Eq. (4.23) is applied once again, in which $\mathcal{F}(x)$ and $\mathcal{F}^{-1}(x)$ indicate 2D Fourier and inverse Fourier transformation of x in this instance.

$$u_{z+\frac{\Delta z}{2}}(\mathbf{r}) = \mathcal{F}^{-1} \left\{ \mathcal{F}[u_z(\mathbf{r})] \exp \left[ik_0 n_0 \sqrt{1 - \left(\frac{\lambda \rho}{n_0} \right)^2} \frac{\Delta z}{2} \right] \right\}. \quad (4.23)$$

$$u'_{z+\frac{\Delta z}{2}}(\mathbf{r}) = u_{z+\frac{\Delta z}{2}}(\mathbf{r}) \exp\{ik_0 [n(\mathbf{r}) - n_0] OF(\mathbf{r}) \Delta z\}. \quad (4.24)$$

For simplicity, the OFs are capped at $\sqrt{2}$ to avoid modeling the propagation between neighboring pixels in a given z -slice. At each z -slice, the phase gradient is estimated via a central difference approximation acting on the unwrapped phase values of the previous slice. Once the aforementioned algorithm has propagated through the entire structure, it is then filtered by NA_o and backpropagated through the simulation space. The squared magnitude is the incoherent intensity contribution associated with the source point $\boldsymbol{\rho}'$. Integrating over $S(\boldsymbol{\rho}')$ completes the partially coherent 3D image simulation.

In order to validate this model, its coherent outputs are compared with rigorous vectorial solutions to Maxwell's equations for plane waves polarized along the axis of cylinders with real homogeneous RI, as found in [215]. Simulations were conducted to compare plane wave scattering at both normal and marginal incidence for a range of RI values. In order to enable a direct comparison with forward scattered waves detectable in transmission, the complex electric field amplitudes from rigorous solutions which incorporate multiple scattering due to both forward and backward propagating waves was calculated at positions coincident with the last z -slice. Since the problem is now constrained to 2D, this 1D wave is then filtered by NA_o and backpropagated through the same simulation space, resulting in a solution for forward propagating waves only.

The SS-BPM simulation is then compared against this solution using normalized mean squared error of scattered intensity [NMSE, given by Eq. (4.25)] as a metric with results shown in Fig. 4.6. In Eq. (4.25), $I_S(\mathbf{r})$ is the simulated forward scattered intensity and $I_A(\mathbf{r})$ is the analytic solution with mean value \bar{I}_A .

$$\text{NMSE}[I_S(\mathbf{r})] = \frac{\sum [I_S(\mathbf{r}) - I_A(\mathbf{r})]^2}{\sum [I_A(\mathbf{r}) - \bar{I}_A]^2}. \quad (4.25)$$

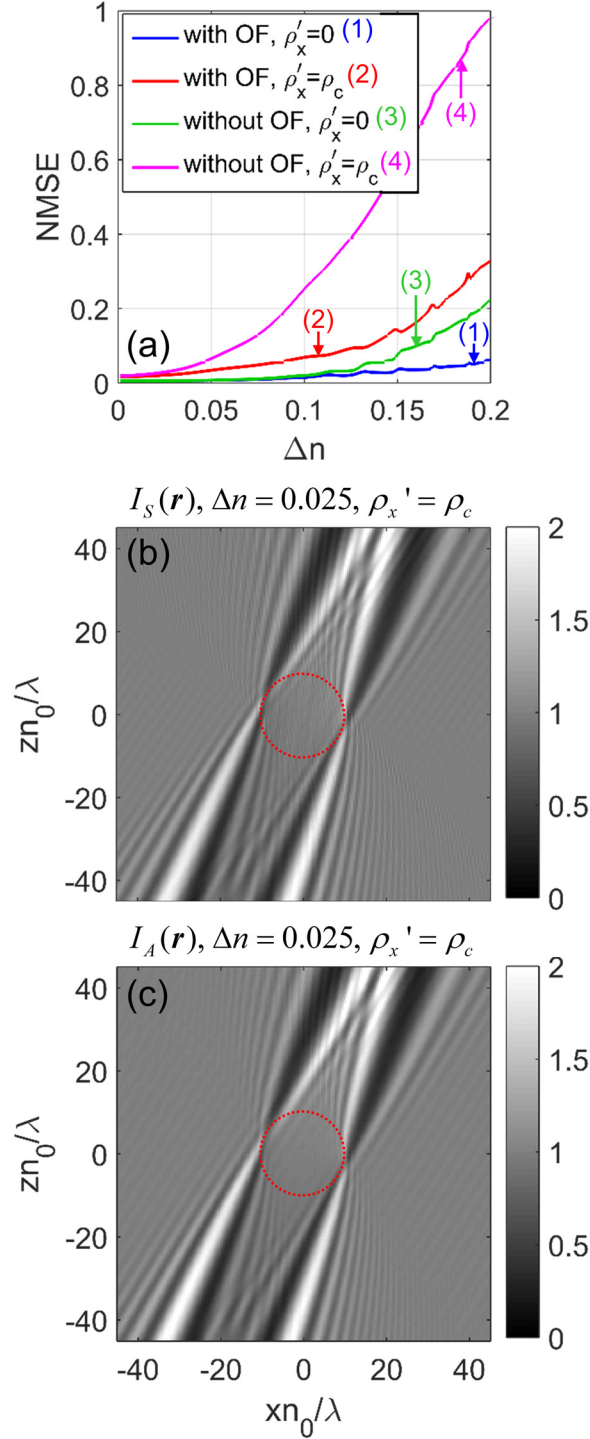


Figure 4.6: (a) Normalized mean squared errors (NMSEs) of various split-step beam propagation method (SS-BPM) simulations with and without obliquity factor (OF) correction [Eq. (4.22)] for normal ($\boldsymbol{\rho}' = (n_0/\lambda)\widehat{\rho}'_z$) and marginal [$\boldsymbol{\rho}' = (NA_c/\lambda)\widehat{\rho}'_x + \sqrt{(n_0/\lambda)^2 - (NA_c/\lambda)^2}\widehat{\rho}'_z$] incidence. (b) Simulated (with OF correction) and (c) analytic intensities with $\Delta n = n_{cyl} - n_0 = 0.025$ where n_{cyl} is the RI of the cylinder. Simulation parameters: $\lambda = 546$ nm, $n_0 = 1$, $\Delta x = \Delta z = 0.245$ μm , $NA_o = 0.75$, and $NA_c = 0.375$.

From Fig. 4.6(a) it is observed that correcting for the OF through each slice reduces error significantly, which is useful since SS-BPMs assume $\Delta n/n_0 \ll 1$ [103], yet the RI contrast for dehydrated cells in water is about $(1.55-1.33)/1.33 \approx 0.17$, where $n = 1.55$ for dehydrated cells [216] has been assumed. Also from Fig. 4.6, it is observed that NMSEs are less than 20% for $\Delta n/n_0 < 0.15$ with OF correction, validating the model and indicating its usefulness for simulating bright-field imagery from 3D phase objects. For the purposes of modeling TDPM reconstruction, this model is especially well-suited as the intensity contrast must satisfy Eq. (4.19), therefore Δn must be weak as in ODT under the first Rytov approximation [56], resulting in improved model accuracy. This can be seen qualitatively in Fig. 4.6(b) and 4.6(c) for which Eq. (4.19) begins to break down.

4.3.2 Simulated Tomographic Deconvolution Phase Microscopy Reconstructions

Due to memory and time constraints imposed by modeling 3D intensity distributions under partial coherence, the tomographic reconstructions presented in this section are, without loss of generality in 3D, based on a 2D cylindrical phantom (shown in Fig. 4.7). Even though the object is 2D, off-axis waves emanating from the entire illumination aperture [Fig. 4.3(b) in both ρ'_x and ρ'_y directions] have been incorporated in the partially coherent image calculation, so that the modelled intensities coincide with cylindrical scattering under Köhler illumination. The parameters used in the simulation are the same as in Fig. 4.6 except that $n_0 = 1.46$ as opposed to 1.

Fig. 4.7 shows a modified version of the Shepp-Logan phantom in which the outer skull material has been replaced by the surrounding head material. For such a phantom the surrounding head material may represent cytoplasm with internal ellipses representing organelles.

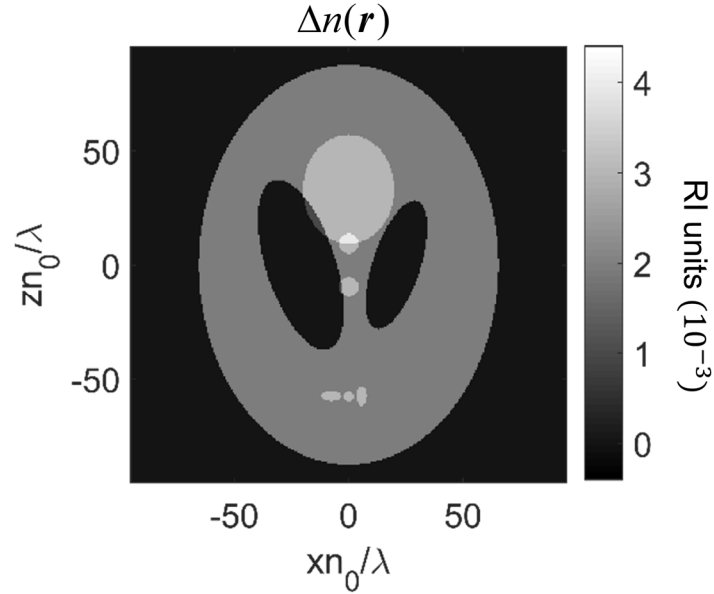


Figure 4.7: RI contrast $\Delta n(\mathbf{r})$ of modified Shepp-Logan phantom.

In Fig. 4.8, multiple tomographic reconstructions, including reconstructions obtained via ODT using FBPP under the first Born [Fig. 4.8(a), 4.8(d), and 4.8(g)] and Rytov [Fig. 4.8(b), 4.8(e), and 4.8(h)] approximations as well as the TDPM method [Fig. 4.8(c), 4.8(f), and 4.8(i)], are compared directly. The simulations are also differentiated by row according to maximum RI contrast Δn_{max} . In the results obtained via FBPP, the object was rotated 825 times about the y -axis so that the rotational increment corresponded roughly with the angular resolution (along the y -axis) used in the partially coherent image simulation. For each rotation angle, the aforementioned modified SS-BPM was used to calculate the total field, the scattered field was used in the first Born approximation, and the scattered phase was used in the first Rytov approximation. In calculating the scattered phase MATLAB's `unwrap` function was utilized. The TDPM reconstructions utilized the 2D analogue of the methods outlined in Figs. 4.4 and 4.5 using the POTF shown in Fig. 4.2. The TDPM reconstruction parameters were set to $N = 15$ and $\alpha = 0$.

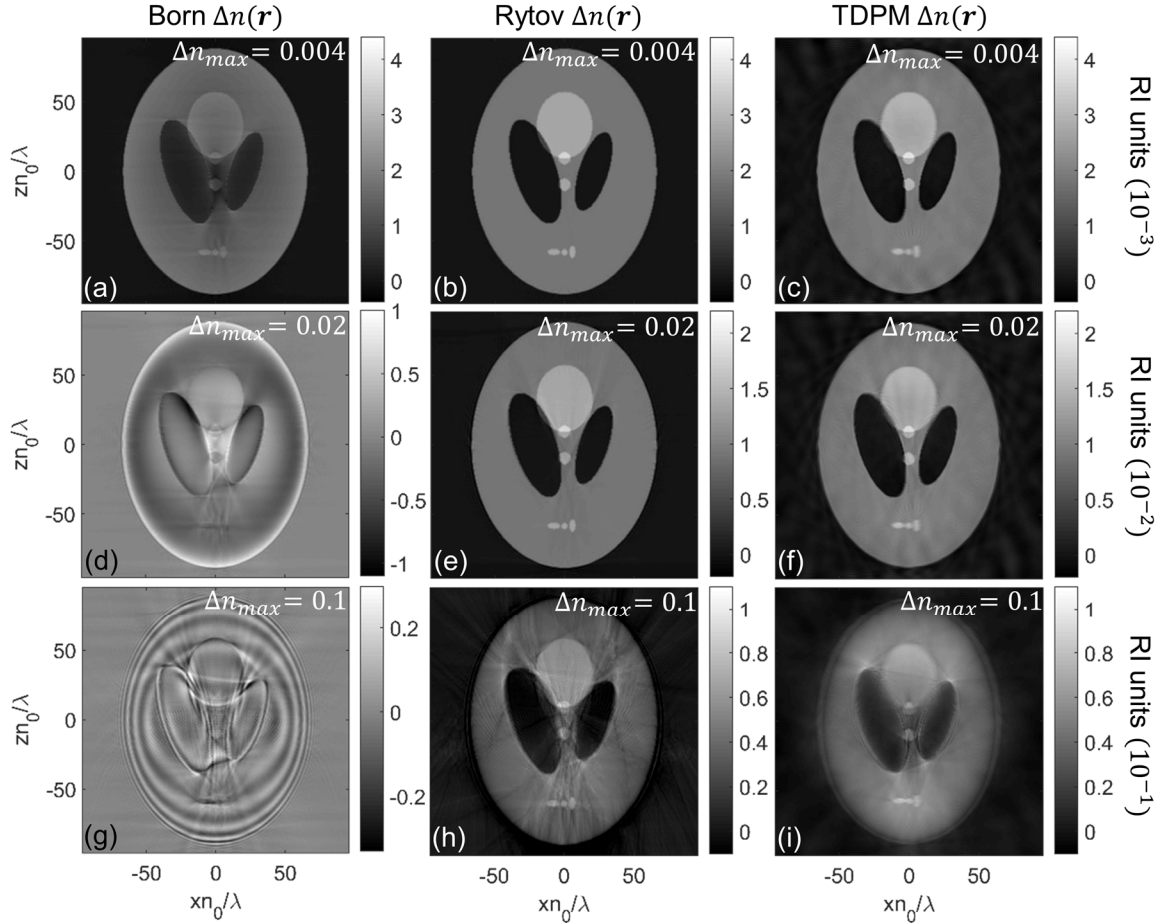


Figure 4.8: Reconstructions obtained using filtered backpropagation (FBPP) under the first Born (a), (d), and (g) and first Rytov (b), (e), and (h) approximations as well as tomographic denvolution phase microscopy (TDPM) (c), (f), and (i) for maximum RI contrast values of $\Delta n_{max} = 0.004$ (a), (b), and (c), $\Delta n_{max} = 0.02$ (d), (e), and (f), and $\Delta n_{max} = 0.1$ (g), (h), and (i). The resulting RMSEs are (a) 0.00042, (b) 0.00015, (c) 0.00017, (d) 0.00580, (e) 0.00088, (f) 0.00106, (g) 0.02681, (h) 0.01124, and (i) 0.01293.

Immediately it is seen that TDPM is not as restrictive as ODT in the first Born approximation in the size of objects which may be reconstructed, verifying that the object need not be “weak” as in the conventional interpretation of the first Born approximation [56], but must be “slowly varying” as given by Eq. (4.19). This is evident by comparing the reconstructions made under the first Born approximation [Fig. 4.8(a), 4.8(d), and 4.8(g)] with the TDPM reconstructions shown in Fig. 4.8(c), 4.8(f), and 4.8(i). Even when RI contrast is relatively weak, as in Fig. 4.8(a) in which the total phase delay through the object is approximately 1.1 radians propagating left to right, the first Born

approximation results in rotations in the complex plane which degrade the result [56]. Likewise, similar behavior is observed and is more pronounced in Fig. 4.8(d) and 4.8(g), in which the total phase delays are 5.6 and 28.2 radians respectively. By contrast, TDPM reconstructions shown in Fig. 4.8(c) and 4.8(f) display no such rotation effect, and the associated reconstruction RMSEs are comparable to reconstructions in the first Rytov approximation [Fig. 4.8(b) and 4.8(e)] without any visible degradation of resolution or image quality.

For the case of $\Delta n_{max} = 0.1$ the scattered phase is highly wrapped, leading to phase unwrapping errors and associated artifacts in the Rytov reconstruction shown in Fig. 4.8(h). In addition to errors due to phase unwrapping, deformation errors exist in Fig. 4.8(h), such as enlargement of the phantom's left eye ellipse, which are associated with the breakdown of the Rytov approximation. In TDPM, no phase unwrapping is necessary and thus the reconstruction shown in Fig. 4.8 (i) does not contain the same artifacts as in Fig. 4.8(h). The artifacts associated with TDPM appear to be predominant near object boundaries, resulting in a degradation of spatial resolution when RI contrast is too high. This results from an asymmetrical intensity distribution induced via multiple scattering events through the object which is especially pronounced near edges. It may be possible to counterbalance this asymmetry by illuminating from opposing angles over 360° as alluded to in Section 4.2.2. The application of this characteristic, however, will be the subject of future work. In spite of these errors, it is clear that TDPM, like ODT in the first Rytov approximation, will be useful over an appreciable range of RI contrast and will thus be relevant and applicable to biomedical studies.

In order to quantify the reconstruction error associated with noise in the bright-field imagery, white Gaussian noise with a normalized standard deviation set to 1% of the background intensity level ($\sigma = 0.01$) was added to the simulated intensity values. This value was selected to match the noise produced by the camera (*QImaging Retiga 1300R*, measured experimentally in Section 3.4) used in the experimental results shown in

Section 4.4 and is typical of many scientific imagers used for microscopy. The TDPM reconstruction results obtained with noise added are shown in Fig. 4.9 for (a) $\Delta n_{max} = 0.004$ and (b) $\Delta n_{max} = 0.04$.

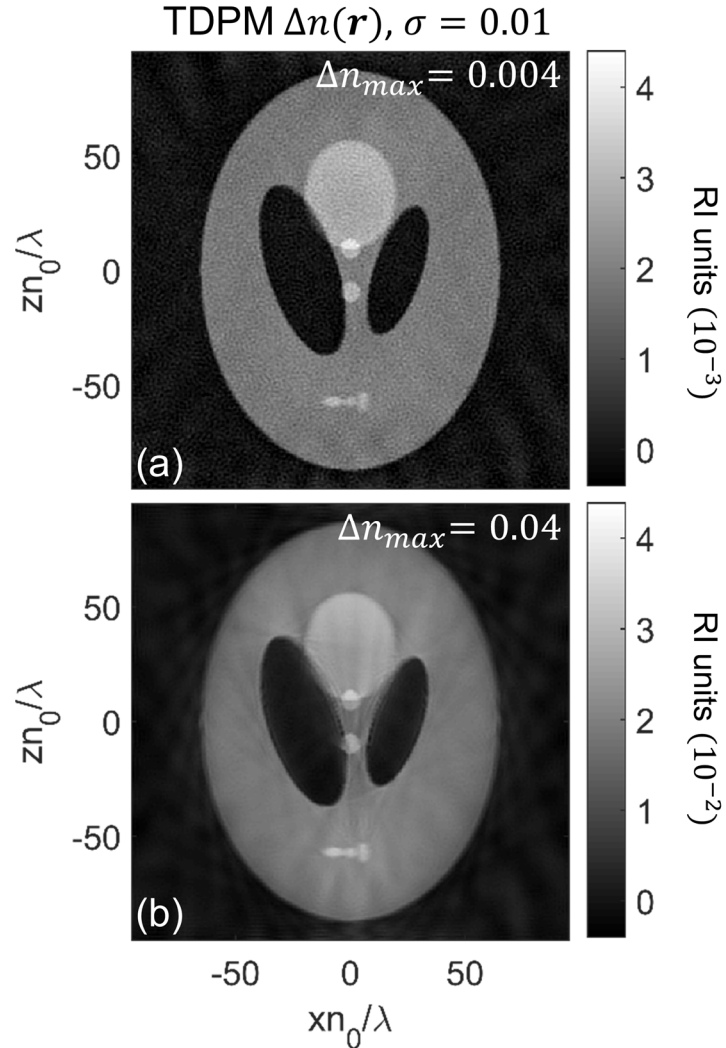


Figure 4.9: TDPM reconstructions obtained with additive noise with a normalized standard deviation of $\sigma = 0.01$ and (a) $\Delta n_{max} = 0.004$ and (b) $\Delta n_{max} = 0.04$. The resulting RMSEs are (a) 0.00026 and (b) 0.00294.

The reconstruction noise is visible primarily in Fig. 4.9(a) and dominated by the signal in the case of Fig. 4.9(b). In addition to demonstrating potential SNR, Fig. 4.9(b), for which the total phase delay through the object is approximately 11.3 radians, further supports the fact that TDPM does not require small total phase delay and can result in

good reconstruction quality for objects with wrapped phase. The RI contrast used in Fig. 4.9(b) is comparable to recently verified values for live cell imaging in water [9, 191]. Theoretically, the RI error associated with image noise will, at least for the high-frequency algorithm shown in Fig. 4.4, be spatial frequency dependent and inversely proportional to the square root of the denominator in Eq. (4.20b). Here the RI error associated with image noise is estimated by subtracting the reconstruction obtained without noise [Fig. 4.8(c)] from the reconstruction including noise [Fig. 4.9(a)] to yield a single-valued RI sensitivity of 2×10^{-4} RI units for these simulation parameters.

4.4 Experimental Results

In order to demonstrate TDPM experimentally, optical fibers are used as test 2D phase objects and a single exposure from a CO₂-laser-induced azimuthally asymmetric long-period fiber grating (LPFG) is used as a test 3D phase object. In order to implement TDPM, all that is required, in addition to a commercial microscope with automated defocus control, is an external stage for object rotation. The configuration utilized in the present work is designed to implement tomography on optical fibers using an upright microscope (*Olympus BX60*) and has been described elsewhere [31, 105]. In addition to this configuration, TDPM can immediately benefit from the groundwork laid for object rotation in similar fluorescent [205, 208, 209] and phase [191, 201, 202] methods. For the measurements presented here, the illuminating source was a mercury-arc lamp using a $\bar{\lambda} = 546$ nm green interference filter with a full-width at half-maximum bandwidth of $\Delta\lambda = 10$ nm. The imaging parameters and components are as outlined in Section 4.2.2 in order to match the calculated POTF. The microscope defocusing was automated using a piezoelectric microscope objective scanner (*Physik Instrumente P-721.SL2* with *E-709.SR* controller).

Figure 4.10 shows the results of implementing 2D TDPM, using the same reconstruction parameters outlined in Section 4.3 ($N = 15$ and $\alpha = 0$), with a (a) single-

mode fiber (SMF, *Corning SMF-28*), (b) polarization-maintaining fiber (PMF, *Thorlabs HB980T*), and (c) photonic-crystal fiber (PCF, *Blaze Photonics ESM-12-01*) used as test phase objects. For all cases, the defocused imagery were sampled at $\Delta z = 4\Delta x = 0.98 \mu\text{m}$, with 147 images per rotation angle for a total of 2,205 images. Since the objects are cylindrical, averaging along the fiber axis is possible to improve SNR and for the tomograms shown in Fig. 4.10, 51 columns were averaged.

In all cases, the fibers were surrounded by RI matching oil ($n_0 = 1.46$ at $\lambda = 589 \text{ nm}$, *Cargille Labs Series A*) to match the RI of the fused silica cladding ($n = 1.4601$ at $\lambda = 546 \text{ nm}$). Normal glass dispersion results in a slightly higher oil index $n_0 > 1.46$, however, for the results presented here, RI values are offset to n_0 , which was the background index used in calculating the POTF. In Fig. 4.10(a), the expected step profile between fiber core and cladding is observed. Also seen is the well-known “center dip” in RI in the fiber’s core associated with dopant burnoff effect. This effect is also clearly seen in Fig. 4.10(b), in which the RI of the PMF’s stress applying members is also clearly visible and well-resolved. Lastly, the reconstructed hexagonal lattice structure of the PCF shown in Fig. 4.10(c) highlights TDPM’s capability and the results may be compared directly with a recent published state-of-the-art optical fiber tomographic algorithm which is based on ODT in the first Rytov approximation [73]. In addition to the lattice structure, RI features resulting from the modification of residual stresses (RS) in the fiber, such as the ring surrounding the air-hole lattice, are visible in Fig. 4.10(c).

In order to demonstrate the 3D capability of TDPM, we have implemented the full 3D reconstruction procedure over a field of view of $293 \times 651 \times 293$ cubic voxels, each with a volume of $\Delta r = 0.49^3 \mu\text{m}^3$, corresponding to physical dimensions of $\sim 143 \mu\text{m} \times 318.5 \mu\text{m} \times 143 \mu\text{m}$. The resolution $\Delta r = 0.49 \mu\text{m}$ is a factor of two larger than previous cases to prevent excessive memory usage for 3D arrays. As in the 2D results, $N = 15$ angles were used with 147 images ($\Delta z = 2\Delta r = 0.98 \mu\text{m}$) taken at each angle. The reconstruction

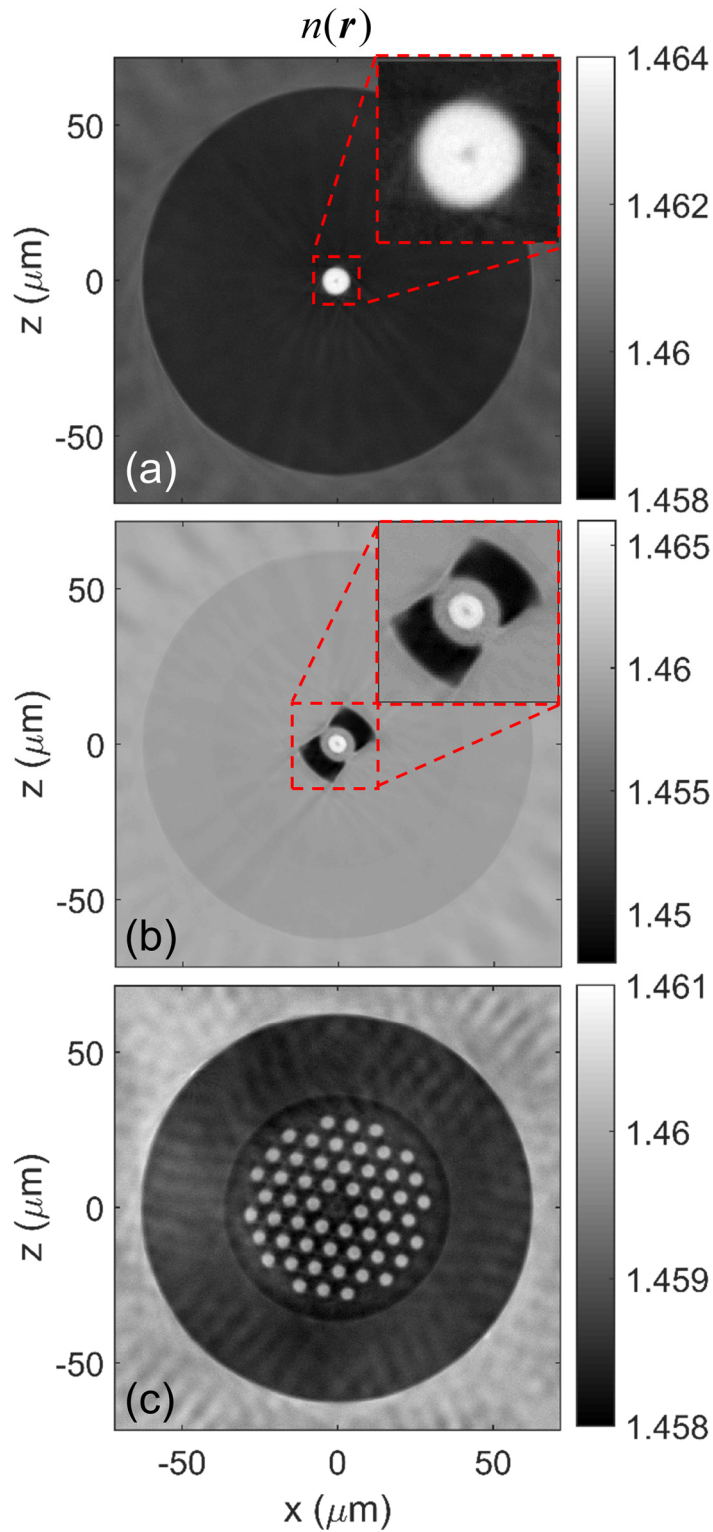


Figure 4.10: 2D TDPM cross-sectional tomograms obtained on (a) single-mode fiber (SMF), (b) polarization-maintaining fiber (PMF), and (c) photonic-crystal fiber (PCF). All colorbars indicate RI units.

procedure utilized the full 3D POTF as opposed to a column-by-column implementation of the 2D procedure used before.

The 3D sample consisted of a CO₂-laser-induced azimuthally asymmetric LPFG period ($\Lambda = 335 \mu\text{m}$ where Λ is the grating period) [91, 102]. In spite of the success of CO₂-laser-induced LPFGs [24] since their introduction by Davis *et al.* [102], the mechanisms for grating formation in these [24], as well as arc-induced LPFGs [23], have not yet been fully characterized. Different investigations suggest differing mechanisms, such as RS modification [25], cladding densification [217], or geometric deformation [29]. A recent report by Hutsel *et al.* presents 3D QPI data on a SMF exposed to focused CO₂-laser radiation of successive durations [91]. The LPFG period measured here was fabricated using the same experimental configuration with two pulses of 200 ms and 100 ms in duration respectively, which may be directly compared with the results in [91] for one 300 ms pulse. The results of TDPM applied to this sample are summarized in Figs. 4.11 and 4.12.

In Fig. 4.11(a), a cross-sectional RI tomogram reconstructed $\sim 150 \mu\text{m}$ away from the laser exposure is displayed and is similar to the result shown in Fig. 4.10(a) except that the RI difference between the matching oil and the fiber cladding is smaller. This most likely results from the temperature dependence of the oil ($\Delta n = -0.00038/^\circ\text{C}$) since the observed difference corresponds to a temperature difference of $\sim 2^\circ\text{C}$ and the measurements were performed on different days with different pre-stabilization periods (the microscope is normally turned on for ~ 3 hours prior to imaging in order to stabilize the oil temperature). In Fig. 4.11(b), another tomogram, reconstructed near the center of the CO₂-laser exposure, is shown and clearly demonstrates the expected azimuthal asymmetry (see the lower-left inset in which the exposure is clearly incident from the upper-right).

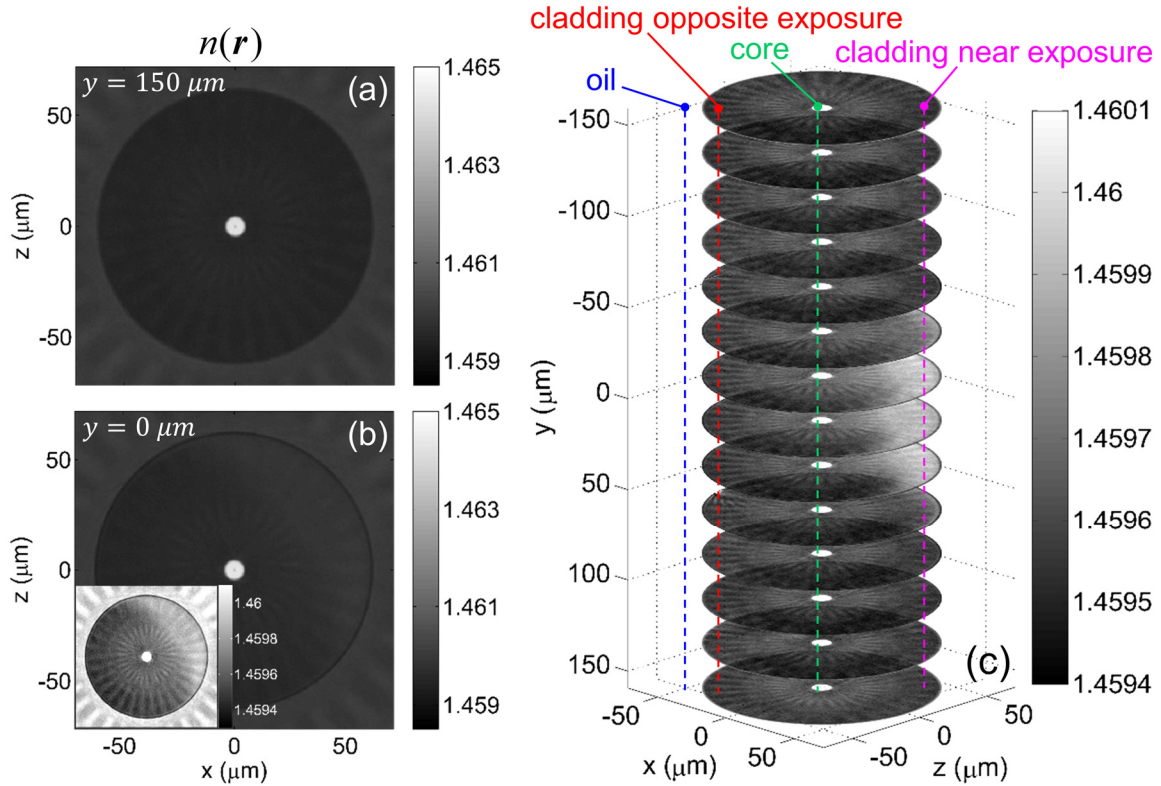


Figure 4.11: RI modification induced via CO₂-laser exposure. (a) Unperturbed SMF reconstructed $\sim 150 \mu\text{m}$ away from the center of the exposure. (b) Reconstruction near the center of the exposed region showing azimuthal variation. (c) Multiple slices showing the 3D nature of TDPM data plotted with a reduced colorbar range to highlight both azimuthal and axial changes in the fiber cladding facing the exposure. All colorbars indicate RI units.

The axial extent of this cladding index change can be easily visualized using Fig. 4.11(c) and Fig. 4.12. In Fig. 4.11(c), multiple tomograms throughout the volume are represented simultaneously and clearly show the asymmetric cladding perturbation and its axial variation. Selected line profiles, corresponding to the index matching oil, cladding on the opposite side of exposure [lower-left quadrant of Fig. 4.11(b)], cladding facing the exposure [upper-right quadrant of Fig. 4.11(b)], and core are overlaid on Fig. 4.11(c) and shown in Fig. 4.12. As expected, the RI of the oil remains constant throughout the extent of the sample. Similarly, the cladding side opposite the exposure appears to remain relatively unaffected. In contrast, the cladding side facing the exposure is clearly modulated and the magnitude and extent of RI change shown here ($\sim 5 \times 10^{-4}$

RI units and $\sim 100 \mu\text{m}$ respectively) is consistent with the results in [91], which adds validity to the proposed method since the results in [91] were based on a quantitative phase tomography technique [31], which has been used in a variety of fiber investigations [84]. The source of this cladding index modulation has been predicted to be glass densification caused by the relaxation of viscoelasticity frozen-in to the fiber during draw [26].

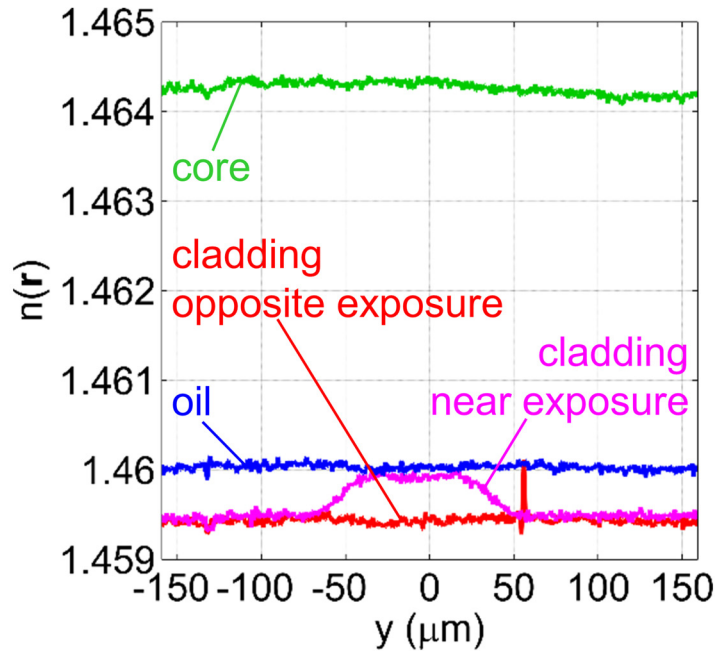


Figure 4.12: Line profiles showing axial variation of RI in selected regions of CO₂-exposed SMF.

Also shown in Fig. 4.12 is the core RI values which indicate a slight increase due to laser exposure, which is in contradiction to the lowering predicted by mechanical RS relaxation [25]. Such an increase may indicate that some form of densification occurs in the core as well, however, a complete characterization and study of grating formation mechanisms is a subject of future work.

To assess the spatial and RI resolution of the aforementioned measurements, the cladding-oil step response of the SMF shown in Fig. 4.10(a) as well as the standard deviation of RI in the oil region of the LPFG period shown in Fig. 4.11(c) are examined. The 10 – 90% rise distance determined by the cladding-oil step response was $\sim 735 \text{ nm}$

and provides a practical measure for spatial resolution in all three spatial dimensions. The standard deviation of RI in the oil region yielded a value of $\sim 7.7 \times 10^{-5}$ RI units, which provides an estimate of the RI resolution and sensitivity. Improved estimates of these specifications could be obtained by using polystyrene nanospheres to measure the system phase PSF and corresponding POTF, which is another subject of future work. Overall, the experiments presented here for both 2D and 3D reconstructions of optical fibers demonstrate the ability of TDPM to achieve 3D QPI in samples possessing RI variation in all three spatial dimensions.

4.5 Summary

In summary, a new method, called Tomographic Deconvolution Phase Microscopy (TDPM), is described which enables 3D QPI using commercial microscopy with minimal hardware modification. The linearization conditions for TDPM, comprising both weak absorption and SVP, have been elucidated and indicate applicability with large phase objects in which reconstructions based on a first Born approximation are known to fail. The spatial frequency domain support of TDPM is roughly isotropic and requires no *a priori* knowledge of the sample or phase unwrapping as in limited-angle ODT in the first Rytov approximation. The theoretical spatial resolution $(1.22\bar{\lambda})/(NA_o + NA_c)$ in the present implementation is estimated to be ~ 592 nm which agrees well with the ~ 735 nm 10 – 90% rise distance estimated by the cladding-oil step response. The RI resolution depends on a number of factors including the measurement domain Ω , the grid resolution Δr , and the level of coherence and is estimated here to be $\sim 7.7 \times 10^{-5}$ RI units based on the standard deviation in the oil of the LPFG measurement.

Due to its compatibility with commercial microscopy, TDPM is particularly well-suited to wide-scale application among biomedical users. Techniques associated with 3D cell fixation and culture using glass capillaries and other cylindrical housings are still a matter of research [191, 201, 202, 209], however, it is anticipated that such techniques

will be enabling in the application of TDPM to both fixed and living cells. Another important application area is in optical fiber characterization, such as the study of grating mechanisms in LPFGs, which was only briefly mentioned here.

For applications which preclude the use of object rotation, such as high-speed 3D QPI for imaging live cell dynamics [218], the modification of TDPM to incorporate algorithmic recovery of the “missing cone” of spatial frequencies from a single through-focal series should be possible and will be the subject of future work. In such an approach no hardware modification would be necessary, permitting 3D QPI with similar frequency domain coverage as limited-angle ODT with only a fraction of the complexity and associated costs.

CHAPTER 5

JOINT RESIDUAL STRESS/REFRACTIVE INDEX CHARACTERIZATION OF LARGE-MODE-AREA ERBIUM- DOPED FIBERS

In Chapters 2 through 4, the primary objective of the present thesis research of provided quantitative phase imaging (QPI) capability using commercial microscopy systems was addressed. In Chapters 5 and 6, the secondary objective of the present thesis research of applying existing QPI and quantitative retardation imaging (QRI) methods to the characterization of optical fibers and fiber-based devices is addressed. Specifically, in this chapter, the three-dimensional index-stress distribution (3DISD) method described in [Hutsel_2012] is applied to the characterization of large-mode-area (LMA) erbium-doped fiber (EDF). The effects of fiber manufacturing, cleaving, and fusion splicing are characterized. The formation of residual stresses (RS) induced during manufacturing can results in changes of refractive index (RI) by as much as 1.2×10^{-4} RI units via the photoelastic effect. Likewise, fusion splicing can results in a RS-induced RI change of 3.5×10^{-4} RI units over a fiber axial distance on the order of millimeters. The diffusion of core dopants during fusion splicing can reduce the core RI by as much as 21.7% over a transition length of $\sim 400 \mu\text{m}$. The measurements outlined herein indicate that RI/RS effects will play key roles in the design of future ultra-LMA EDFs in which the difference between core and cladding RI is reduced further. This chapter is based on the paper entitled “Joint residual stress/refractive index characterization of large-mode-area erbium-doped fibers,” which was published in July of 2013 [219].

5.1 Introduction

Using silica erbium-doped fiber (EDF) as the gain medium for erbium-doped fiber lasers (EDFLs) and erbium-doped fiber amplifiers (EDFAs) has been of considerable interest in the past few decades [220-231]. Many applications, such as extra-terrestrial free-space optical communications, laser surgery, and military weaponry require large optical powers (in the range of 100W–1kW), therefore large mode areas (LMAs) are needed to avoid non-linear effects, long-time-scale degradation of the fiber properties, such as photo-darkening, and in order to maintain good output beam quality [92]. LMA EDFs, like all optical fibers, are sensitive to unintended refractive index (RI) perturbations such as those induced via dopant transport during fiber manufacturing [94, 232, 233], residual stresses (RS) and inelastic strains formed during fiber manufacturing [95, 234-237], and stress relaxation near cleaved end-faces [238, 239]. Arc-fusion splicing also perturbs fiber RI distributions via dopant diffusion [101, 240] and RS relaxation [87].

Due to the plurality of perturbations, which may in general degrade or enhance the optical and mechanical properties of the fiber, it is a common goal to characterize these effects through measurement of their spatially resolved physical properties including their RS and RI distributions. From the inception of modern optical fiber technology in the early 1970's, researchers have been developing techniques for RI profiling, which is a form of 3D QPI, such as the refracted near field [71] and reflection methods [241]. Later, Chu *et al.* began probing RS in fibers using principles from photoelasticity [242], and this has been extended by others [238, 243-245]. More recently, Shin *et al.* reported the variation of RS along a fusion splice between dissimilar fibers including EDF to single-mode fiber (SMF) [87]. Dragomir *et al.* demonstrated the measurement of RI variation along a graded-index multi-mode fiber to SMF splice, highlighting the effects of potential imperfections in the arc-fusion process [84]. Although the fields of fiber RS and RI characterization have matured significantly, only recently were they combined into one

automated system for the joint residual stress/refractive index three-dimensional (3D) characterization of these properties [31].

In order to maintain single-mode operation with large mode-field diameters (MFDs), the numerical aperture (NA) in LMA EDFs must be kept low requiring small normalized index differences (Δ). Because Δ values must necessarily be suppressed, single-mode LMA EDFs are inherently more sensitive to perturbations in their RI and RS distributions due to the photoelastic effect [93]. Perturbations which have been neglected in the past will dramatically alter the optical properties of fibers such as the ultra LMA ytterbium-doped photonic-crystal fiber developed by Schmidt *et al.*, which has an effective index difference of $\sim 0.7 \times 10^{-4}$ [96]. LMA ytterbium-doped fibers with NAs of ~ 0.06 are already commercially available. In order for ultra LMA EDFs to be developed in the future, all of the perturbations in such fibers must be understood thoroughly and included in the fiber design. Therefore, accurate and detailed characterizations of RS and RI distributions for LMA EDFs are needed to develop future fibers with improved performance. As a starting point, in this chapter, a commercial *nLIGHT LIEKKITM Er80-8/125* LMA EDF is fully characterized for its RS and RI distributions in an unperturbed section, a cleaved end-face, and a section fusion spliced to a telecommunications fiber (*SMF-28*).

5.2 Experimental Methods

The measurements presented in this chapter are based on the high-resolution 3D index-stress distribution (3DISD) measurement method presented in [31]. Because both RS and RI measurements are performed within the same apparatus, there is no need to move the fiber between measurements and the stress and index can be compared directly. The RS is characterized tomographically by measuring the optical retardation due to stress-induced birefringence at multiple projection angles using a Brace-Köhler compensator technique in a polarization microscope [238, 246]. The RI is also characterized

tomographically by measuring the phase shift induced by the fiber RI profile at multiple projection angles using quantitative phase microscopy (QPM) based on the transport-of-intensity equation (TIE) [31]. For both measurements the fiber sample was surrounded by index matching oil (*Cargille Labs* $n = 1.456$) as light propagated transverse to the fiber axis. The accuracies associated with these techniques are 0.35 MPa and 2.34×10^{-5} RI units respectively [31]. Their lateral spatial resolutions depend on many factors including diffraction limits in microscopy, the number of projection angles used, the extent to which the straight ray assumptions are satisfied in projection tomography, and perhaps most importantly the effects of illuminating a 3D object with partial spatial coherence [128]. The resolutions have been shown to be sufficient for characterizing established RS and RI effects including hydroxyl impurities inducing large compressive stresses at the core-cladding interface and the center dip in RI induced during core preform fabrication [31].

5.3 Experimental Results

The experiments are based on a *LIEKKITM Er80-8/125* LMA EDF which has a core diameter of 8 μm and a cladding diameter of 125 μm . The erbium concentration is 4.7×10^{19} ions/cm³ and the absorption coefficient is ~ 80 dB/m at 1530 nm. The nominal cladding RI, NA, and MFD are 1.4573, 0.13, and 9.5 μm at 1550 nm respectively. Conventional EDF MFDs are typically ~ 5 -8 μm [247]. The fiber is designed to have a step index profile, and the RI difference between core and cladding ($\Delta n_{cc} \cong NA^2/2n_{clad}$) is approximately 6.0×10^{-3} .

The fiber is first characterized for its unperturbed RS and RI distributions to reveal effects of fiber manufacturing. Then, a cleaved end-face is characterized to investigate how RS and RI variations affect output coupling. Lastly, the fiber is fusion spliced to a *Corning SMF-28* fiber and characterized to predict optical coupling. A radially-

symmetric finite-difference beam-propagation method (FD-BPM) is employed to describe the propagation of the fundamental mode from the LMA EDF to the SMF.

5.3.1 Unperturbed Fiber Characterization

Fig. 5.1(a) and 5.1(b) shows the cross-sectional RS distribution and a RS profile (along the dashed line) of the unperturbed *LIEKKITM Er80-8/125* LMA EDF respectively. The off-horizontal solid and dotted lines in Fig. 5.1(a) correspond to the direction of maximum asymmetry and the associated profiles will be displayed later in Fig. 5.4(b). For comparison, a *Corning SMF-28* RS profile is also plotted using the dotted curve in Fig. 5.1(b). Generally, there is a thermal component and a mechanical component of the RS in optical fibers [95, 99, 238]. Thermal stresses result from the difference in thermal expansion coefficients (TECs) of doped and un-doped silica glasses. When a fiber cools after being heated beyond its fictive temperature, regions with large TECs seek to contract more than regions with low TECs and are met with resistance from the solidified glass. The result is tensile stress in regions with a high TEC, typically the core, and compressive stress in regions with a low TEC, typically the cladding. Mechanical stresses result from variations of viscosity during the fiber drawing processes. As the fiber cools, regions with higher viscosity, usually the cladding, bear the brunt of draw tension and modify RS in other areas after mechanical equilibrium is established, resulting in compressive stress in the core. Typically, these two components oppose each other due to large TECs and low viscosities in the doped core compared to the pure silica cladding. The influence of mechanical, or draw-induced, stress is usually greater than thermal stress when the draw tension is sufficiently high, and the resulting stresses are tensile in the cladding and compressive in the core as shown in Fig. 5.1.

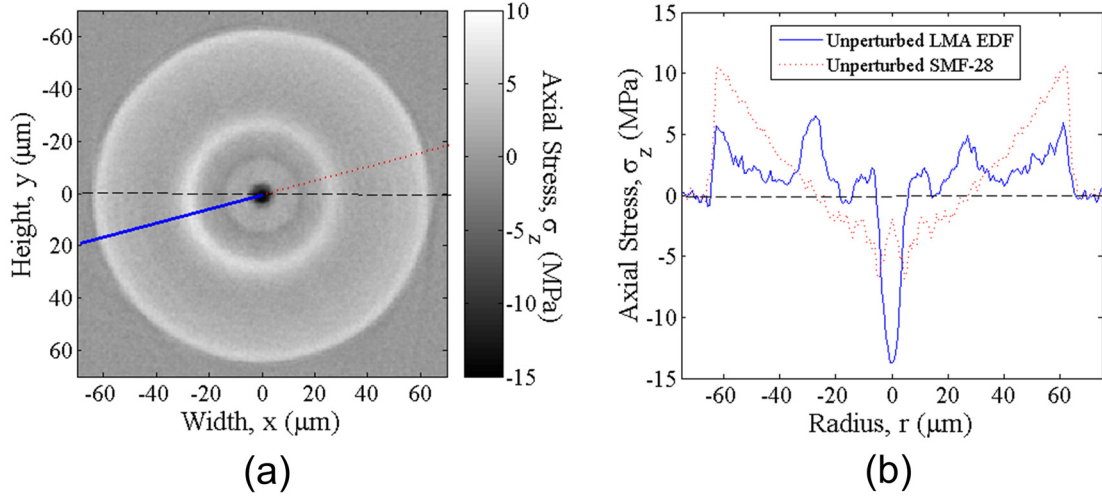


Figure 5.1: (a) Cross-sectional residual stress (RS) distribution and (b) RS profile along the dashed center line in (a) of the unperturbed large-mode-area erbium-doped fiber (LMA EDF).

This fiber was fabricated using a direct nanoparticle deposition (DND) method, which enables highly uniform and controllable layers in the soot deposition process [248]. In order to obtain the correct core-to-cladding ratio, the core preform must sometimes be sleeved more than once. Also, it is possible that the preform may need to be drawn prior to the second sleeving process [249]. In general, these processes will perturb the RS. For example, impurities, which lower the viscosity of silica glass and result in localized compressive stress, may form when sleeving a core preform [250]. Compared to *SMF-28* fiber, this LMA EDF contains more radial stress variation in the pure silica cladding, which may be due to additional sleeving and drawing steps.

As seen in Fig. 5.1, the RS in the outer cladding is less than that of *SMF-28* fiber. This is to be expected because the high volume production of *SMF-28* requires a high draw tension/speed. Also as an indicator of draw speed, the mean axial stress, $\overline{\sigma_z}$, as calculated using Eq. (8) in [238], over a cross-section of the LMA EDF, which should be zero in the absence of external forces, is approximately 2.50 MPa compared to 4.71 MPa for *SMF-28* fiber [238]. This anomaly has been reported by many authors [236, 251] and

is due to the viscoelastic properties of silica [26]. The mean axial stress is an indicator of inelastic strain birefringence in the fiber and is in proportion to draw tension.

The RS distribution in and around the core region of the LMA EDF is highly compressive, indicating less thermal expansion and a reduced viscosity compared to the *SMF-28* fiber core. The RS induced during fiber manufacturing perturbs the RI distribution according to the photoelastic effect, see Eq. (5.1), where n_0 is the isotropic RI and $C_1 = -0.65 \times 10^{-6} \text{ MPa}^{-1}$ and $C_2 = -4.22 \times 10^{-6} \text{ MPa}^{-1}$ for fused silica [252]. For weakly-guiding fibers, the radial RI, n_r , is the most significant principal index of refraction.

$$n_r = n_0 + C_1 \sigma_r + C_2 (\sigma_\theta + \sigma_z). \quad (5.1)$$

The axial RS, σ_z , is the measured RS distribution minus the mean axial stress, $\bar{\sigma}_z$, to ensure mechanical equilibrium is satisfied. The radial and circumferential components, σ_r and σ_θ , can be calculated using Eq. (5.2a) and (5.2b) from the theory of linear elasticity assuming radial symmetry [253], in which $r = \sqrt{x^2 + y^2}$:

$$\sigma_r = \frac{1}{r^2} \int_0^r \sigma_z r dr, \quad (5.2a)$$

$$\sigma_\theta = \sigma_z - \sigma_r. \quad (5.2b)$$

Fig. 5.2 shows the change in radial RI, Δn_r , which results from the manufacturing induced RS distribution calculated using Eq. (5.1) and (5.2). This level of stress results in a positive RI change of $\sim 1.2 \times 10^{-4}$ RI units in the core, which represents a significant change for ultra LMA fibers. The magnitude of RS in this fiber is relatively moderate, as stresses can easily reach values of several hundred MPa in optical fibers [253]. Therefore, it is anticipated that even larger stress-induced RI changes may form in some LMA EDFs. Also, because the inelastic strain birefringence is not necessarily uniform and localized in regions of high viscosity [26], the cladding RI may also be lowered by values on the order of 10^{-5} RI units corresponding the observed mean axial stress. If not taken

into account beforehand, these index changes may dramatically affect waveguiding characteristics for ultra low NA fibers and may even result in multi-mode operation. Therefore, it is critical to understand the RS distributions in LMA EDFs currently being researched. These measurements represent an initial effort towards characterizing these effects. More measurements are needed to understand completely how various dopants affect the RS and to achieve the precise balance of RS and RI necessary in ultra LMA EDFs.

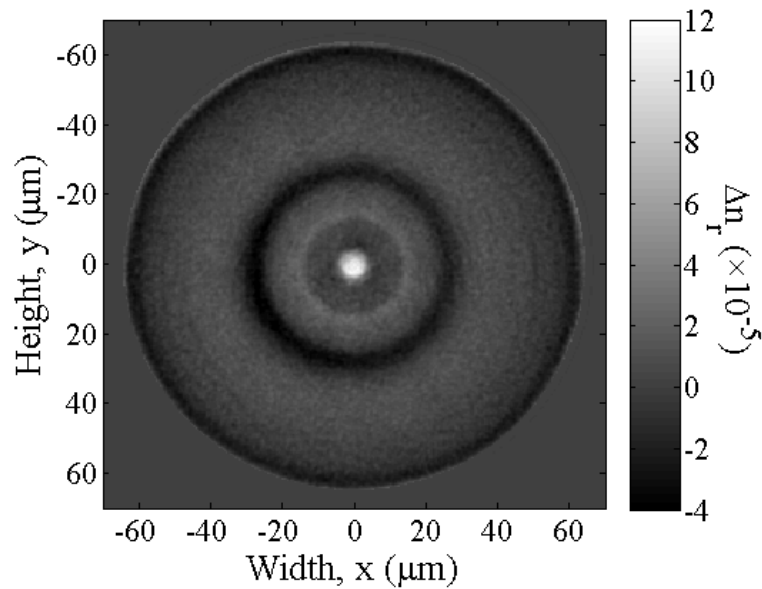


Figure 5.2: Cross-sectional changes in radial refractive index (RI), Δn_r , resulting from manufacturing induces RS.

The cross-sectional RI distribution of the unperturbed LMA EDF and RI profile along the dashed line are shown in Fig. 5.3(a) and 5.3(b) respectively. As before, the off-horizontal solid and dotted lines in Fig. 5.3(a) correspond to the direction of maximum RS asymmetry. This direction was chosen arbitrarily because no apparent asymmetry could be detected in the RI cross-sections, indicating a high level of radial symmetry as is evidenced by Fig. 5.4(d). A very uniform cladding is observed and a sharp step-index profile can easily be seen in Fig. 5.3(b). In the center of the core region, a RI dip, commonly known as the “center-dip” or “burnoff dip” [31], is seen. The RI difference

between the core and cladding, Δn_{cc} , is approximately 6.34×10^{-3} . According to the cladding RI of 1.4573, the NA of this fiber is calculated ($NA \cong \sqrt{2\Delta n_{cc}n_{clad}}$) as 0.1359, which is consistent with the nominal value supplied by the manufacturer of this fiber, NA = 0.13. Due to its relatively large core size, severe spreading due to dopant diffusion during fiber drawing [232] is not observed in spite of a large erbium concentration.

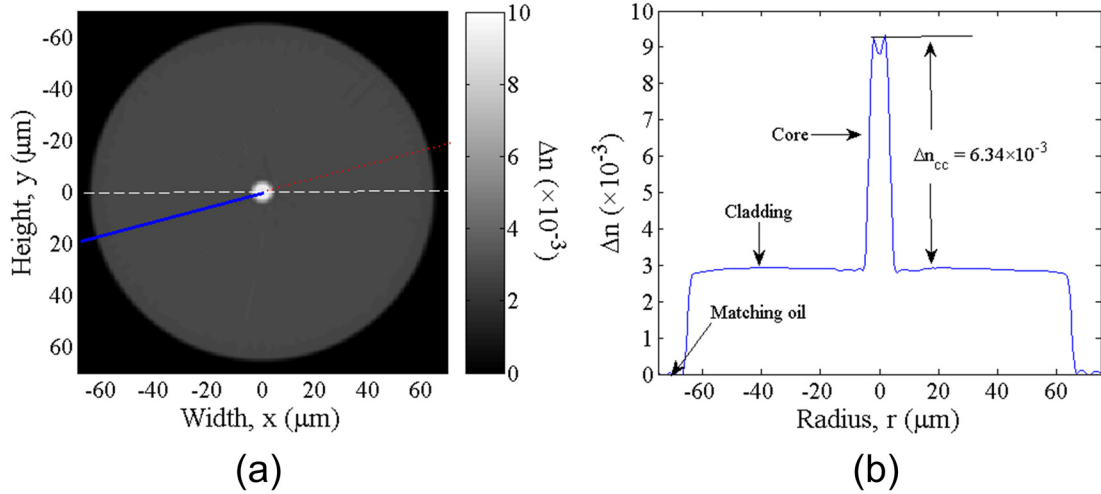


Figure 5.3: (a) Cross-sectional RI distribution and (b) RI profile (along the dashed center line) of the unperturbed LMA EDF. Δn denotes the relative RI compared to the RI of the index matching oil.

Fig. 5.4(a) and 5.4(c) display radial RS and RI profiles averaged from 90,000 profiles (180 angular orientations \times 500 cross sections) taken from a single tomographic measurement. Each cross section was taken at an axial spacing of $0.49 \mu\text{m}$ and corresponds to 1 pixel column of a CCD image. The error bars represent radially resolved standard deviations. These deviations include actual non-uniformities in the fiber as well as measurement variations across one tomographic field of view. Fig. 5.4(b) and 5.4(d) display radial profiles, averaged over the same 500 axial cross-sections, taken along the directions of maximum RS asymmetry, or along the solid and dotted lines of Fig. 5.1(a) and Fig. 5.3(a) respectively. Fig. 5.4(b) reveals a true asymmetry at $r \approx 28 \mu\text{m}$ induced via imperfections in fiber manufacturing, perhaps during a drawing stage. The asymmetry is most likely due to mechanical stresses because thermal stresses originate from radially

symmetric TEC profiles. Also, the error bars on Fig. 5.4(a) are larger in the corresponding location due to this asymmetry. Altogether, Fig. 5.4 demonstrates the capability of this characterization method to detect small RS and RI non-uniformities in the fiber sample.

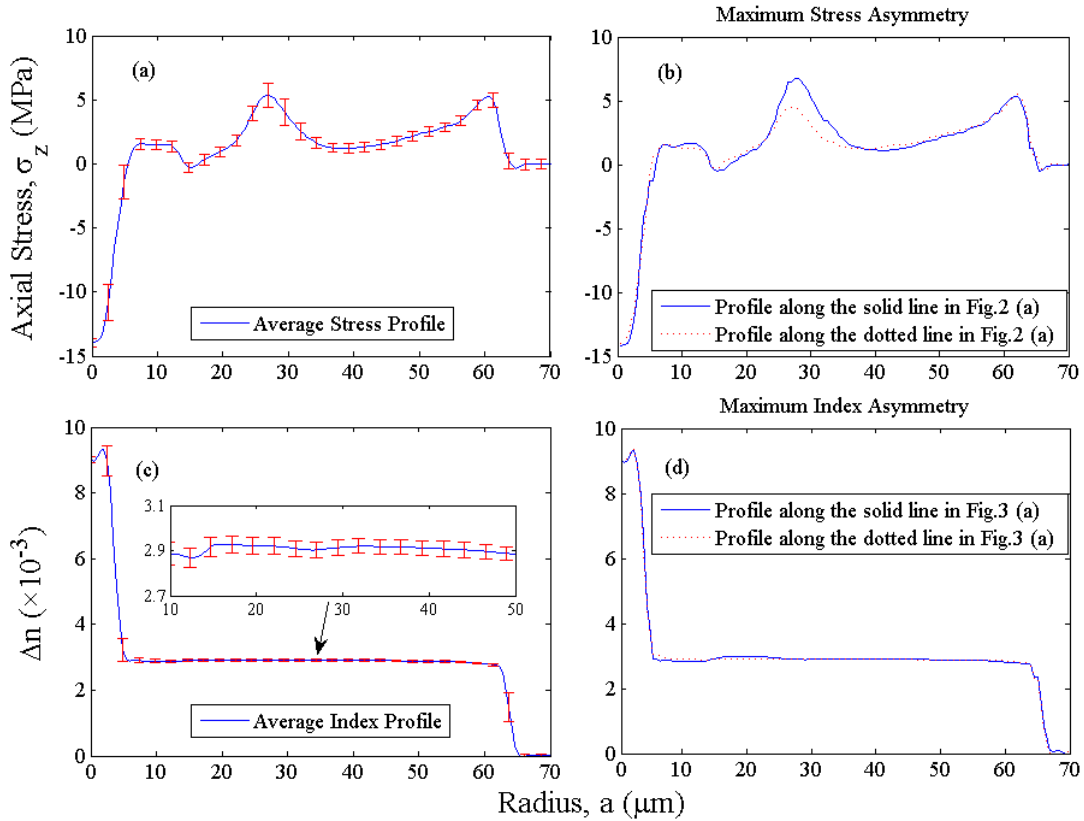


Figure 5.4: Average stress and index profiles, with associated non-uniformities, of unperturbed LMA EDF are shown in (a) and (c) respectively. Error bars indicate radially resolved standard deviations of the axial RS and RI. Maximum stress asymmetry is shown in (b) along the direction indicated by the off-horizontal lines in Fig. 5.1(a). The lack of index asymmetry is illustrated in (d) along the same direction.

5.3.2 Cleaved end-face Characterization

In order to characterize the effects of cleaving, a *Fujikura GT-04B* high precision fiber cleaver was used and variations along the fiber axis were measured. Fig. 5.5(a) and 5.5(b) show the cross-sectional RS distribution and profile at $5 \mu\text{m}$ from the fiber end-face. For comparison, Fig. 5.5(a) uses the same scale as Fig. 5.1(a) and the unperturbed fiber profile is plotted with a dotted line in Fig. 5.5(b). Diffraction and scattering from the end-

face degrade the stress measurement and cross-sections closer than 5 μm from the end were heavily distorted. From Fig. 5.5(b), it is obvious that elastic stresses have relaxed when compared to the unperturbed RS profile, similar to the results obtained in [239]. The cladding stresses have become less tensile and the core stresses have become less compressive, indicating a gradual change towards zero elastic stresses at the cleaved end-face. The transition region for these changes is on the order of tens of μm , and the resulting stress-induced index change will be on the same order as that induced via manufacturing. In spite of this, any LMA EDF with a NA low enough to be sensitive to these changes will also have a large MFD and will not experience significant mode transformation over this characteristic length.

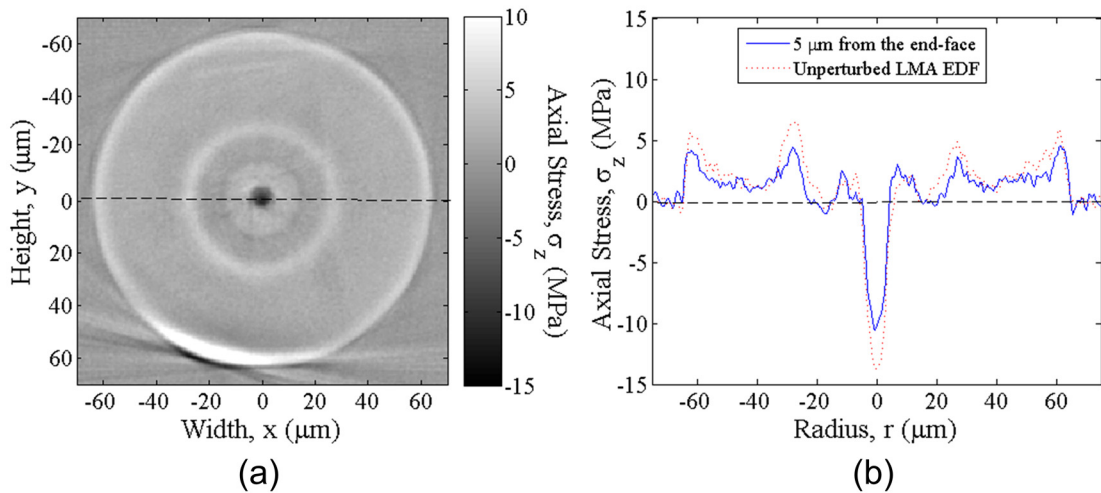


Figure 5.5: (a) Cross-sectional RS distribution and (b) profile along the dashed line in (a) 5 μm from the end-face of the LMA EDF. For comparison, the unperturbed RS profile is also shown (dotted line).

To investigate further the effects of cleaving, mean axial stresses were calculated near the cleaved end-face. The mean axial stress, $\overline{\sigma_z}$, is shown in Fig. 5.6 over a length of 50 μm . For comparison, the unperturbed fiber mean axial stress is also shown in the figure as a dotted line. An obvious trend from the fiber's unperturbed value to 1.90 MPa at the end-face is observed. The characteristic length associated with this transition is approximately 30 μm . The mean axial stress in this LMA EDF decreases by 0.6 MPa,

which is much less than the corresponding value for *SMF-28* fiber, 3.59 MPa [238]. Shin *et al.* also observed this decrease in inelastic strain birefringence near a cleaved end-face [239]. The physical reason for this observation is not well understood, because for most applications the associated index change is negligible. Similar to the relaxation of elastic RS, changes of this magnitude will also be insignificant over the observed length scales ($\sim 30 \mu\text{m}$). Overall, RS perturbations induced by fiber cleaving will not significantly affect the optical characteristics of LMA EDFs.

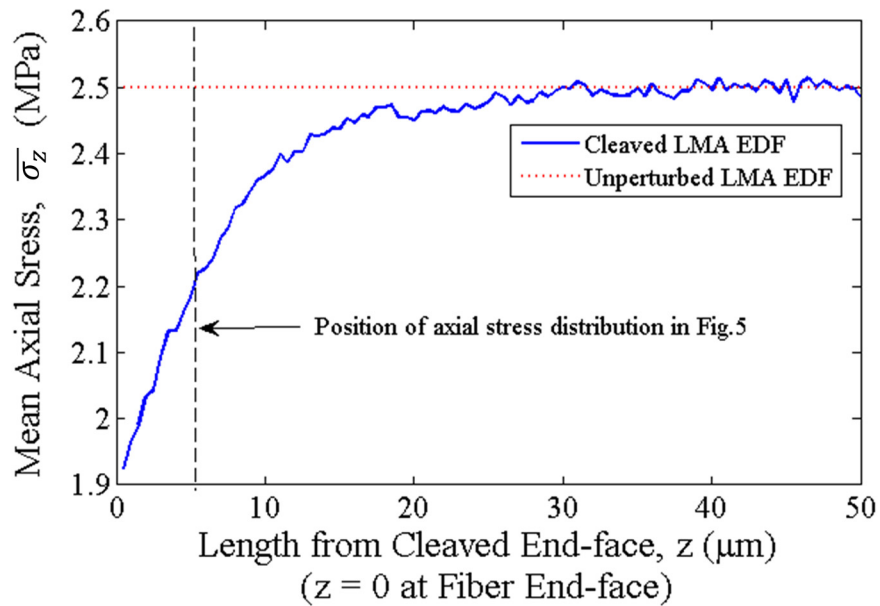


Figure 5.6: Mean axial stress inside the LMA EDF at various lengths from the cleaved end-face (solid curve). For comparison, the unperturbed mean axial stress is also shown (dotted line).

The cross-sectional RI distribution and profile $5 \mu\text{m}$ from the end-face are shown in Fig. 5.7. Like the RS, measurements closer to the end-face are distorted by diffraction and scattering. For comparison, the RI profile of the unperturbed LMA EDF is plotted in Fig. 5.7(b) using a dotted curve. Although the relaxation of RS is detected as shown in Fig. 5.5, the associated RI changes are smaller than the RI accuracy and no additional perturbations are observed. This is to be expected because the fiber has not been altered in any way aside from the relaxation of RS.

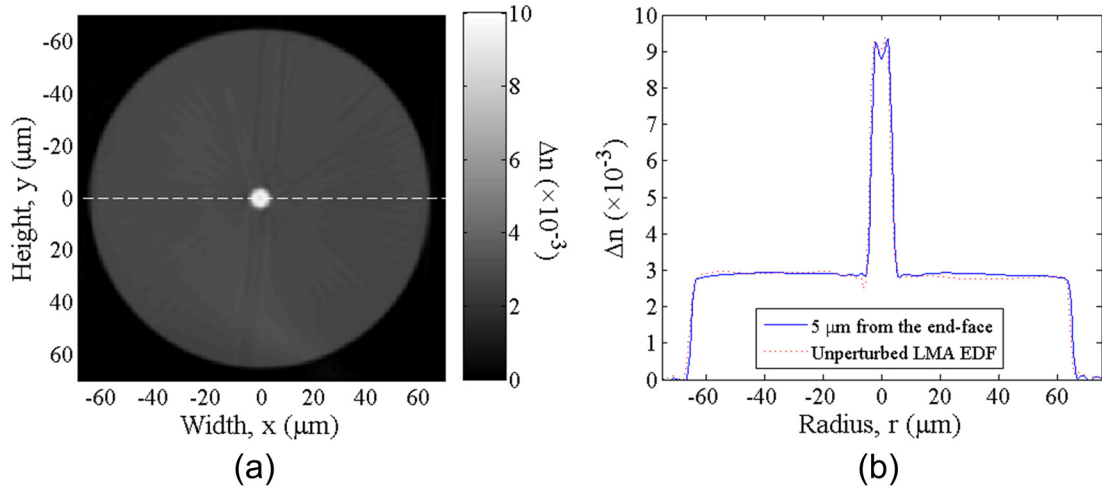


Figure 5.7: (a) Cross-sectional RI distribution and (b) RI profile along the dashed center line in (a) 5 μm from the end-face of the LMA EDF.

5.3.3 Fusion Splice Characterization

In order to interconnect with existing fiber-based systems and networks, it is often necessary to perform an arc fusion splice between dissimilar fibers. The success of many fibers and fiber-based devices depends on optimizing fusion splices. In general, fusion splicing induces optical loss due to mode-field mismatch between dissimilar fibers [99]. The high temperatures associated with fusion splicing can cause diffusion of dopants such as erbium and fluorine which affect RI distributions [247]. In addition, fusion splicing also perturbs RS distributions [254] which may also have significant consequences for LMA EDFs. In order to characterize all of these effects, the *LIEKKITM Er80-8/125* was arc fusion spliced to an *SMF-28* fiber using the normal SMF-SMF P.01 program of an *Ericsson FSU 975* fusion splicer. The fusion splicer estimated a splice loss of 0.01 dB indicating excellent lateral alignment between these two fibers.

Fig. 5.8(a) shows the LMA EDF cross-sectional RS distribution at 100 μm from the splicing point. When compared to the unperturbed profile in Fig. 5.8(b), significant changes are seen in the RS profile, taken from the dashed line in Fig. 5.8(a). The core stresses become tensile and the cladding stresses become slightly compressive. During

the arc fusion splice process, the electrical discharge heats the fibers beyond their fictive temperatures, relaxing both thermal and mechanical stresses. Because the fibers are not held under tension, mechanical stresses do not form upon cooling and only thermal stresses remain. Also, the mean axial stress should be zero, as will later be verified in Fig. 5.9, because inelastic strain birefringence is proportional to draw tension and the fibers are heated beyond their fictive temperature and cooled under no tension. The resulting thermal stresses, as well as the mean axial stress, can be subtracted from the unperturbed RS distribution to calculate the mechanical stresses. For this reason, fusion splicing provides an excellent method for isolating thermal and draw-induced stress components as well as inelastic strain birefringence in optical fibers. Also note that the stress asymmetry mentioned in Section 5.3.1 is not observed in the spliced profile, again suggesting that it is a draw-induced effect.

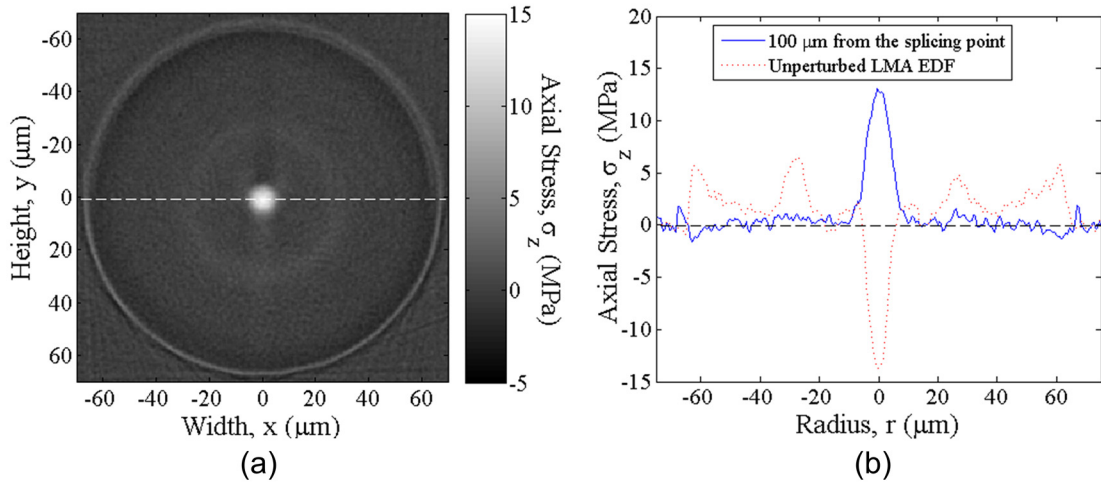


Figure 5.8: (a) Cross-sectional RS distribution and (b) RS profile along the dashed center line in (a) of the LMA EDF 100 μm from the splicing point.

Fig. 5.9 shows the RS profiles located within 1.6 mm of the splicing point on either side. The fiber axial resolution (horizontal axis in the figure) is $0.49 \mu\text{m}$ so there are 6,530 profiles displayed in the figure. For this measurement, the RS distributions were assumed to be axisymmetric, and tomograms were reconstructed from only one retardation projection.

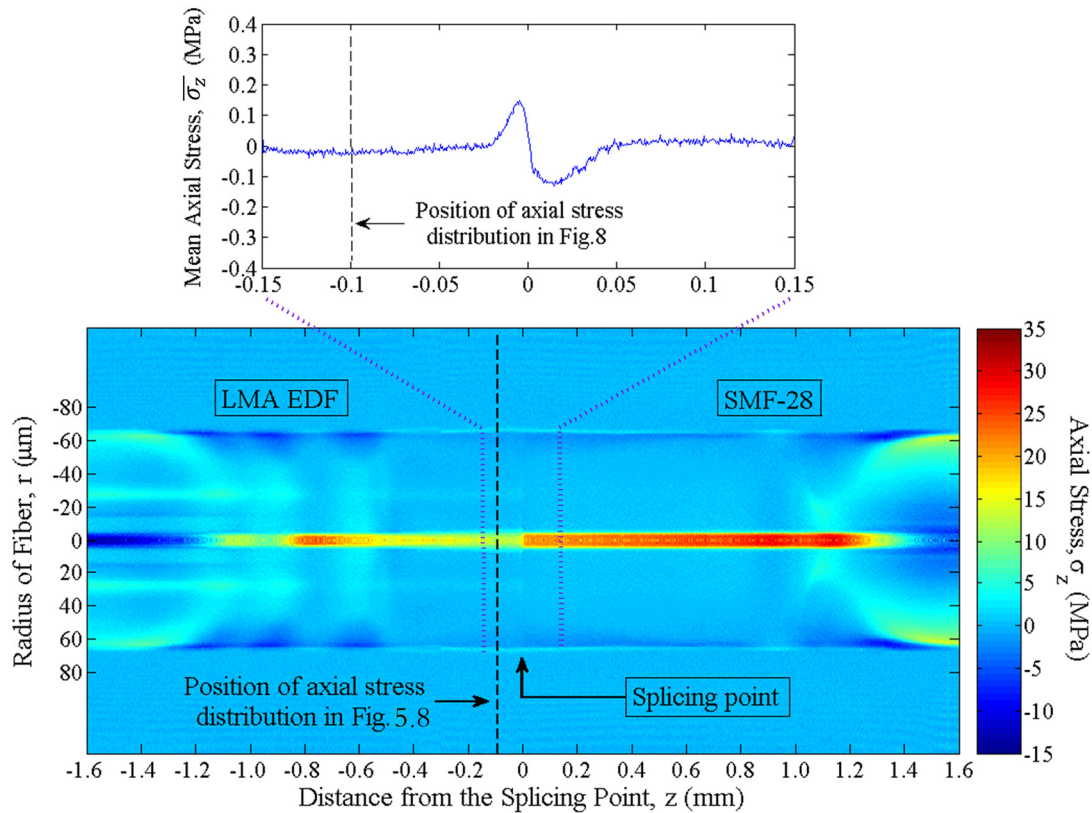


Figure 5.9: Arc fusion splicing induced RS distribution along the LMA EDF (left) and the *SMF-28* fiber (right). Splicing point at $z = 0$; left fiber is LMA EDF and right fiber is *SMF-28*. The inserted figure (top) shows the mean axial stress near the splicing point.

From this figure, it can be readily seen that the mechanical stresses near the splicing point for both the LMA EDF (left) and the *SMF-28* fiber (right) have been relaxed. The inserted figure (top) also verifies the prediction of zero mean axial stress, confirming that inelastic strain birefringence is in proportion to draw tension. For each fiber, a different transition pattern is observed. The transition patterns are influenced by the functional forms of RS in the two fibers as well as the spatio-temporal distribution of heat within the fusion splicer and the fiber itself. There is an obvious stress discontinuity in the core region at the splicing point, owing primarily to different doping conditions between the two fibers. The thermal stresses in the LMA EDF core are less tensile than the *SMF-28* fiber core, which is consistent with the observation of larger compressive stresses in the

unperturbed LMA EDF core. Another reason for reduced thermal expansion in the core is the radial diffusion of dopants, which increases the effective core diameter.

Using the data from Fig. 5.9, the change in radial RI, Δn_r , can be calculated from Eq. (5.1) and (5.2), and is shown in Fig. 5.10. These data are calculated using the change in axial, radial, and circumferential elastic stresses from their unperturbed values rather than the RS shown in Fig. 5.9. The mean axial stresses must be subtracted from the measured RS before calculating these changes. The RI changes near the splicing point are discontinuous because they are proportional to the unperturbed mechanical stresses within each fiber.

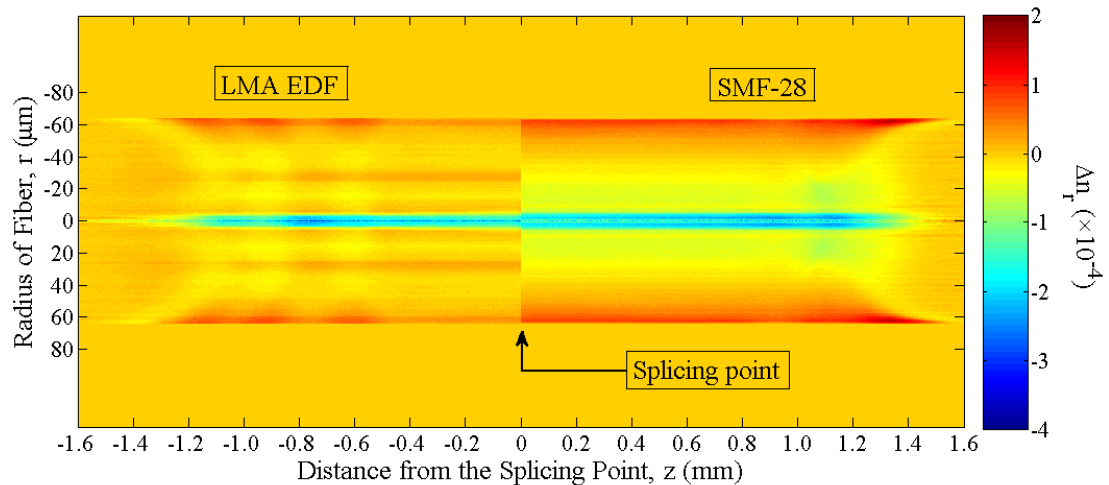


Figure 5.10: Change of radial RI, Δn_r , induced by the RS change along the fusion splice between the LMA EDF (left) and the *SMF-28* fiber (right). Splicing point at $z = 0$; left fiber is LMA EDF and right fiber is *SMF-28*.

From Fig. 5.10, it is obvious that the magnitudes of stress-induced index changes due to fusion splicing are larger than those induced via manufacturing or cleaving for this LMA EDF. In the cores, the RI can be decreased by as much as 3.5×10^{-4} . Although this may be insignificant for some fibers, these levels of stress-induced RI changes cannot be overlooked in ultra LMA EDFs. For some ultra-low NA fibers, changes of this magnitude will reduce the core RI below the cladding RI, eliminating any possibility of waveguiding over a long optical length of ~ 1 mm. Unlike the cleaved end-face, perturbations of this

magnitude and length scale are large enough for significant mode transformation and may degrade coupling efficiency. Because these changes are primarily due to relaxation of draw-induced stresses, they will be exacerbated as draw speeds increase for high volume fiber production. Also, the disappearance of inelastic strain birefringence near the splicing point corresponds to a cladding RI increase on the order of 10^{-5} RI units.

Fig. 5.11 shows the RI distribution inside the LMA EDF and *SMF-28* fiber near the splicing point. For this measurement, the RI distributions were assumed to be axisymmetric, and tomograms were reconstructed from only one phase projection.

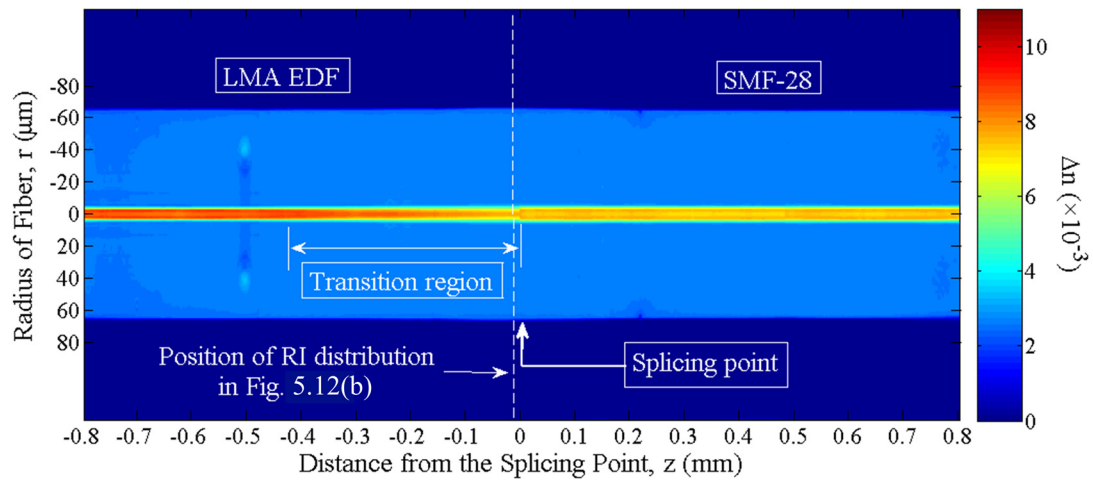


Figure 5.10: RI distribution along the LMA EDF (left) and the *SMF-28* fiber (right). Splicing point at $z = 0$.

Unlike the unperturbed fiber and cleaved end-face, significant changes in RI are observed directly in the RI measurement. These changes are attributed primarily to the heat-induced radial diffusion of core dopants and are usually much larger in magnitude than stress-induced RI changes. In some cases dopant diffusion can be exploited to improve splicing loss by forming a transition region of RI to act as a mode transformer between dissimilar fibers [100, 101, 240]. This is often true when splicing conventional EDF to *SMF-28* fiber because erbium diffuses much more readily than germanium,

allowing the small EDF core to expand up to the size of an *SMF-28* fiber core over a distance of hundreds of μm [99].

In Fig. 5.11, from around -0.43 to 0 mm, a transition from the LMA EDF's unperturbed profile to a radially diffused profile is observed whereas no such transition region is found in the *SMF-28* fiber. The transition region length is found to be around 400 μm . This length is much shorter than the perturbed region in the RS distribution because stresses are relaxed above the fictive temperature whereas higher temperatures are required for significant diffusion to take place [99]. Also, though not easily seen in the figure, axial diffusion across the splicing point over a small region (a few μm) is observed and this effect is known to reduce splice reflectivity [99].

Fig. 5.12(a) displays the evolution of the core RI profile in the transition region marked in Fig. 5.11 and Fig. 5.12(b) shows the cross section at the dashed line.

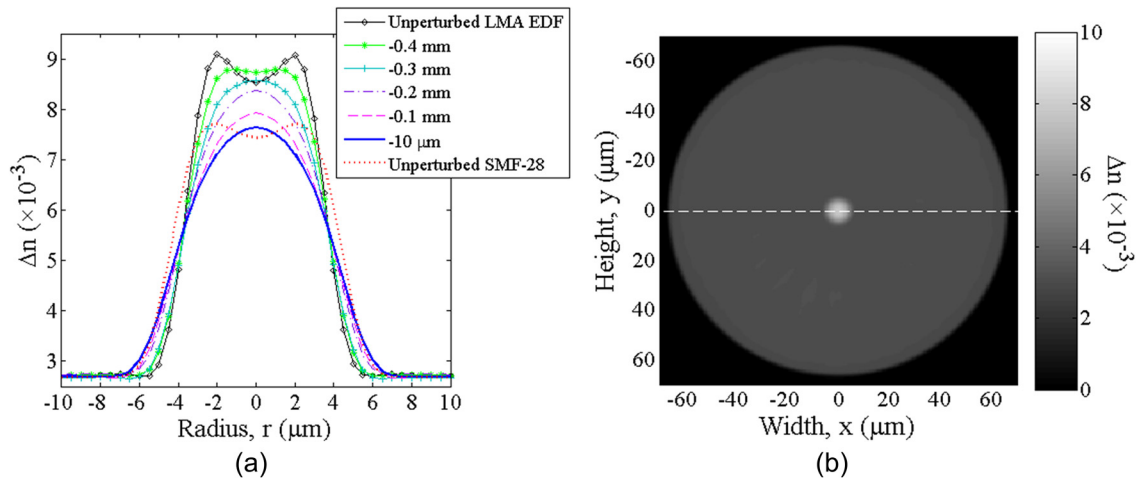


Figure 5.12: (a) RI profiles at various lengths along the transition region from the fusion splicing point. For comparison, RI profiles of the unperturbed LMA EDF and *SMF-28* are also shown. The cross-sectional RI distribution of the LMA EDF 10 μm from the splicing point is shown in (b).

The RI profile near the splicing point is very different from the unperturbed profile. The center dip disappears near the splicing point and the transition between core and cladding becomes more gradual. The RI difference between core and cladding, Δn_{cc} , changes from $\sim 6.34 \times 10^{-3}$ in the unperturbed profile to $\sim 4.96 \times 10^{-3}$ near the splicing point as

measured from the maximum core value to the cladding, representing a 21.7% change. Because the LMA EDF RI profile at the splicing point is similar to the *SMF-28* fiber profile, coupling loss due to mode-field mismatch should be reduced below what it would have been in the absence of diffusion. Although there will be additional losses induced by the transition region, it is expected that the relatively long transition length ($\sim 400 \mu\text{m}$) should subdue this effect [240].

To model the effects of diffusion and to highlight the usefulness of the measured RI data, a radially symmetric FD-BPM [255] was employed to simulate the propagation of the fundamental mode of the unperturbed *LIEKKITM Er80-8/125* across the fusion splice from -0.8 mm to 0.8 mm. A radially symmetric BPM was selected over the split-step BPM used in Chapters 2 through 4 because the radial symmetry condenses a 3D problem to a 2D one, thereby reducing complexity and increasing speed. The data from Fig. 5.11 was used directly and the *SMF-28* fiber RI profiles ($z > 0$) were assumed to be invariant along the z -axis and were therefore replaced by the mean profile to reduce the effects of noise. The radial node spacing, Δr , was $0.2 \mu\text{m}$ and the axial node spacing, Δz , was $1 \mu\text{m}$. Fig. 5.13 shows the resulting normalized electric field amplitude squared, $|E(r, z)|^2$, as it propagates through the fusion splice. As expected, the intensity profile expands monotonically in the thermally diffused transition region and a small discontinuity is observed at the splicing point ($z = 0$).

The simulated fusion splice loss is calculated using an overlap integral technique [99]. Using this method, the splice loss is calculated to be 0.013 dB. In the limit of no diffusion, the splice loss is calculated to be 0.061 dB, demonstrating that the effect of dopant diffusion is to reduce the splice loss by 0.048 dB in this case. However, this result is not anticipated for LMA EDFs in general. Because diffusion tends to increase MFD, LMA EDFs with MFDs larger than in *SMF-28* fiber will not experience a decrease in splice loss. It may be necessary to design tapered fibers or other mode transformers to improve coupling efficiency for such fibers. Generally, the time required for substantial

diffusion scales with the square of the characteristic length [99]. Therefore, LMA EDFs with larger cores may not diffuse as much as in this example. Even still, large inherent doping concentrations require the radial diffusion of dopants to be a key consideration when designing LMA EDFs and should not be overlooked. Also, LMA EDFs with fine annular structure in their doping profile [247] may be extremely susceptible to diffusion.

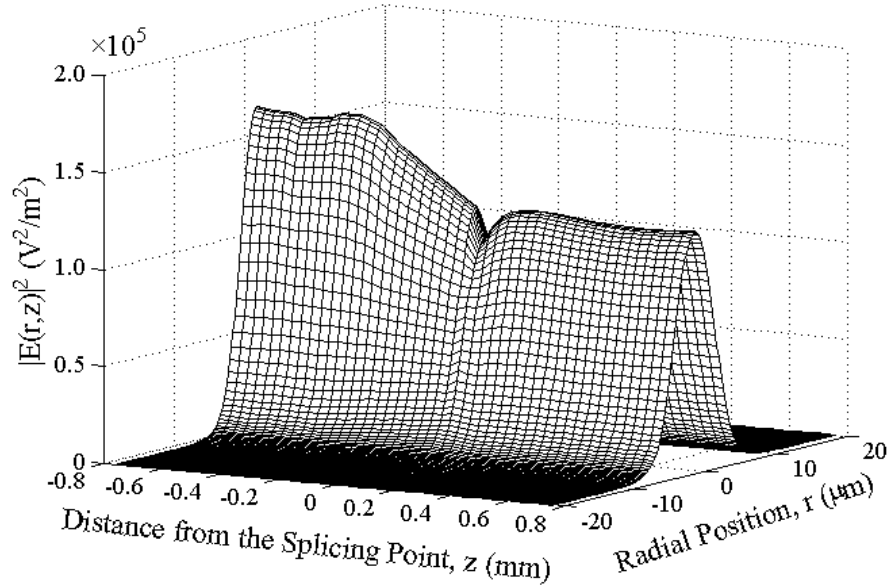


Figure 5.13: Finite-difference beam propagation method (FD-BPM) simulation of the fusion splice between the LMA EDF and the *SMF-28* fiber. A fundamental guided mode of the LMA EDF is used as the input at $z = -0.8$ mm.

5.4 Summary

In summary, the effects of fiber manufacturing, cleaving, and fusion splicing on the RS and RI distributions for a commercial LMA EDF (*LIEKKITM Er80-8/125*) were characterized using a novel high-resolution 3DISD measurement method. The results indicate that there are many potential perturbations to be considered when designing LMA EDFs with relatively low NAs. Fiber manufacturing can easily create stress-induced index changes of RI units and therefore cannot be overlooked and must be accounted for in the design process as the core/cladding RI difference becomes comparable to these changes. The relaxation of RS and inelastic strain birefringence near

a cleaved end-face is not found to be significant due to the relatively short length scales of these effects and the large transverse mode dimensions of LMA EDFs. RS distributions are perturbed significantly in the vicinity of an arc fusion splice and can lead to index changes of RI units over an axial distance on the order of mm, which is large enough for significant mode transformation. These effects will be exacerbated as draw speeds increase for high-volume production. Also, it is found that the creation and alteration of inelastic strain birefringence via fiber drawing and splicing may be significant for some applications. Although isotropic RI perturbations associated with frozen-in viscoelasticity were not observed in this study, it has been shown that changes on the order of 10^{-3} RI units can occur in fibers drawn at high tension [26] and cannot be overlooked when designing LMA EDFs.

The diffusion of core dopants can lead to dramatic changes in the RI profile of EDFs near a fusion splice. In order to measure this effect in an LMA EDF, we spliced the *LIEKKITM Er80-8/125* to an *SMF-28* fiber and found a diffused transition region in RI leading up to the splicing point. The maximum core RI changed by 21.7% over a distance of around 400 μm . A FD-BPM was used to simulate the effects of this transition region and highlights the usefulness of the measured RI data. Although this transition region is found to improve splice loss for this fiber, diffusion will in general degrade splice loss for fibers with MFDs larger than *SMF-28* fibers. Although the diffusion time scales with the square of the characteristic length, the radial diffusion of dopants should still be a key consideration for LMA EDF fusion splice optimization due to the dopant concentrations necessary for high gain and the common use of fine annular structure in the doping profile [247]. Considering all of these factors, effective design of LMA EDFs requires the careful consideration of all of the perturbations which have been described in this chapter.

CHAPTER 6

ARC FUSION SPLICING EFFECTS IN LARGE-MODE-AREA YTTERBIUM-DOPED FIBERS

In Chapter 5 it was found that the effects of fiber manufacturing and fusion splicing could affect the operation of large-mode-area (LMA) erbium-doped fiber (EDF) and fiber-based devices. In this chapter, the same approach, involving the application of the three-dimensional index-stress distribution (3DISD) method, is taken in order to characterize the effects of fusion splicing in LMA ytterbium-doped fibers (YDFs). The results indicate that the effects of fusion splicing can be much stronger in LMA YDFs than in LMA EDFs and will accordingly affect the performance and operation of splices involving current LMA YDF technology. Specifically, it is shown that the diffusion of core dopants can reduce the core refractive index (RI) in LMA YDFs by as much as 1.74×10^{-3} RI units over a fiber axial length corresponding to many hundreds of wavelengths, which is shown herein to result in an additional splice loss of 20.8% via a simulation based on a finite-difference beam propagation method (FD-BPM). This chapter is based on the paper entitled “Arc fusion splicing effects in large-mode area single-mode ytterbium-doped fibers,” which was published in November of 2013 [256].

6.1 Introduction

Silica ytterbium-doped fibers (YDFs) have been widely used in space optical communications, medicine, industrial processing, national defense, etc. as the gain medium for high power fiber lasers and amplifiers due to their simple energy level systems, broad gain-bandwidths, high light-to-light conversion coefficients, and good beam quality [257-260]. Additionally, because of the absence of excited state absorption and concentration quenching, compact high power ytterbium-doped fiber lasers (YDFs)

and amplifiers (YDFAs) are enabled by using short fiber lengths [258]. To avoid non-linear effects and long-time-scale degradation of the fiber properties, high power (in the range of 100W-1kW) YDFs need large-mode-areas (LMAs) in order to decrease the power density. To obtain optimal beam quality, LMA YDFs must operate in the single-mode (SM) regime, which requires low numerical apertures (NAs) and small normalized index differences. Thus, LMA-SM-YDFs are sensitive to unintended refractive index (RI) perturbations such as the relaxation of residual stress (RS) and frozen-in viscoelasticity (FIV), dopant diffusion, etc. [26, 87, 94, 95, 101, 235, 239].

Many researchers have characterized the RS and RI distributions in optical fibers using various techniques [84, 238, 243-245]. Recently, Feng *et al.* used a state-of-the-art three-dimensional index-stress distribution (3DISD) measurement method [31] to provide a detailed characterization of RS and RI perturbations in LMA erbium-doped fibers (EDFs) resulting from manufacturing, cleaving, and arc fusion splicing [219], which was the basis of Chapter 5. Results indicate that LMA EDFs are sensitive to the aforementioned perturbations, especially in the case of arc fusion splicing. During fusion splicing, high temperatures from the arc discharge can result in the relaxation of RS and FIV and induce dopant diffusion, which will perturb the RI distribution significantly. Due to higher power requirements for YDFs and YDFAs, LMA-SM-YDFs have even lower NAs than LMA-EDFs and are therefore more sensitive to RS and RI perturbations. For example, LMA-SM-YDFs with NAs as low as ~ 0.08 are already commercially available.

Arc fusion splicing is a preferred process for the interconnection of optical systems and the fabrication of fiber-based devices. Generally, there are several fusion splicing points in high power all-fiber YDFs and YDFAs. Fusion splice quality can directly affect many properties in YDFs and YDFAs, such as pump threshold, output power level, and beam quality. Researchers have recently investigated the effects of splice and return loss on power distribution in YDF systems [261] as well as splice shift and tilt on beam quality in YDFs [262]. None of these investigations have considered the effects of

the aforementioned perturbations on YDFL performance, even though there is considerable evidence suggesting that they may have a significant impact [219]. Therefore, it is important to understand the characteristics of RS and RI perturbations in fusion spliced LMA-SM-YDFs. Investigating such physical properties allows researchers to predict their effect on YDFL and YDFA system performance as well as improve LMA-SM-YDF design and fabrication.

In this chapter we employed the same measurement 3DISD technique as in [219] to study the characteristics of RS and RI in fusion spliced LMA-SM-YDFs. The measurements are based on a commercial LMA-SM-YDF (*LIEKKITM Yb1200- 10/125-DC*), generally used in medium to high power YDFs and YDFAs, spliced to a *Corning SMF-28* fiber. Using the experimental data, a finite-difference beam propagation method (FD-BPM) [255] is employed to describe the propagation of the fundamental mode from the LMA-SM-YDF to the *SMF-28*. The splice coupling coefficient and the mode transformation effect are predicted based on the simulated results.

6.2 Experimental Methods

The experiments performed in this chapter are based on the state-of-the-art 3DISD measurement method presented in [31]. In the RS measurement, the NA of the microscope condenser lens was $NA_c = 0.15$. In the RI measurement, the condenser NA and defocus distance were 0.1 and 8 μm respectively. The fiber sample was surrounded by index matching oil (*Cargille Labs*, $n = 1.460$, temperature coefficient of $-3.89 \times 10^{-4} / ^\circ\text{C}$). Using this technique, the associated RS and RI accuracies are 0.35 MPa and 2.34×10^{-5} RI units respectively [31]. In this chapter, σ_z and Δn denote the axial component of RS and the RI relative to the index matching oil as in [219].

In this measurement, the SMF-SMF P.01 program of an *Ericsson FSU 975* arc fusion splicer was used. The *LIEKKITM Yb1200-10/125-DC* has a core diameter of $\sim 10 \mu\text{m}$ and a cladding diameter of $\sim 125 \mu\text{m}$. The nominal cladding RI, core NA, and mode-field

diameter (MFD) are 1.4573, 0.08, and 11.1 μm respectively. The ytterbium concentration is $\sim 9 \times 10^{19}$ ions/ cm^3 . The fiber is designed to have a step-index profile, and the core/cladding RI difference, Δn_{cc} , is $\sim 2.3 \times 10^{-3}$. The outer edge of the cladding is octagonal as shown in Fig. 6.1.

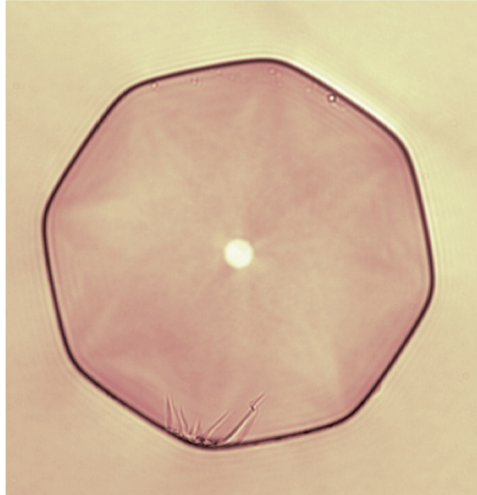


Figure 6.1: Cross-section of *LIEKKITM Yb1200-10/125-DC* as observed in a bright-field microscope.

For the results presented in Fig. 6.2 and Fig. 6.5 and later simulated in Fig. 6.7, RS/RI cross-sections were reconstructed under an assumption of axial symmetry, in which one projection angle was assumed to be representative of all projection angles. This assumption was made due to the impracticality of gathering full tomographic data over an axial length of ~ 3 mm (due to a limited camera field-of-view) and also because the primary focus of our investigation is on the effects associated with the fundamental mode, which is located in the vicinity of the core region where the assumption is most valid. In addition, Fig. 6.3 and Fig. 6.6 were reconstructed using all projection angles and their lack of axial asymmetry indicate that this assumption is reasonable.

6.3 Experimental Results

Fig. 6.2(a) shows the RS profiles within 1.5 mm on the *LIEKKITM Yb1200-10/125-DC* side and within 0.3 mm on the *SMF-28* side, where the splicing point is located at $z = 0$ mm.

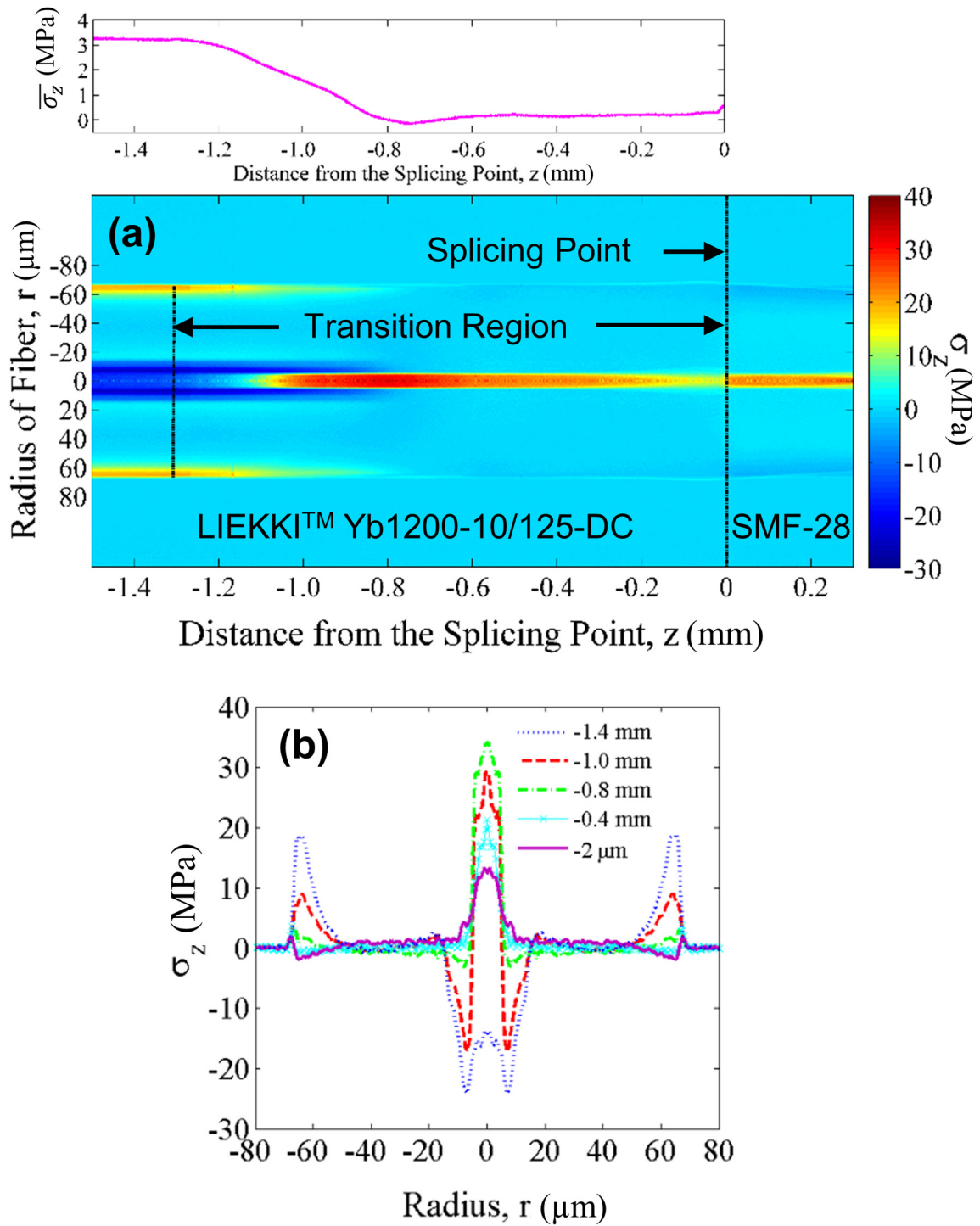


Figure 6.2: (a) The residual stress (RS) distribution along the *LIEKKI*TM Yb1200-10/125-DC (left) and the SMF-28 (right) after arc fusion splicing. The inserted figure (top) shows the mean axial stress $\bar{\sigma}_z$ near the splicing point. (b) RI profiles at indicated positions along the transition region from the splicing point.

The fiber axial resolution is 0.49 μm and there are 3,674 profiles utilized in the figure. The RS contains both mechanical and thermal components [238]. During the splicing process, the arc discharge heats the *LIEKKITM Yb1200-10/125-DC* beyond its fictive temperature, relaxing both thermal and mechanical stress. Because the fiber is not held under tension, mechanical stress does not form upon cooling and only thermal stress remains. In Fig. 6.2(a), a stress transition region is observed in the *LIEKKITM Yb1200-10/125-DC* over an axial length of ~ 1.3 mm, where the RS gradually changes from having thermal and mechanical components to thermal only. In this region, from left to right, the tensile stress in the outer cladding has become slightly compressive while the compressive stress in the core has become tensile. At approximately $z = -0.8$ mm the tensile stress in the core has reached a maximum, after which it gradually decreases to the splicing point. This is due to the diffusion of ytterbium ions which reduces the thermal expansion in the core. To visualize this effect more clearly, Fig. 6.2(b) displays RS profiles at indicated positions along the transition region.

Fig. 6.3 shows the cross-sectional RS distribution (reconstructed using all projection angles) in the *LIEKKITM Yb1200-10/125-DC* 20 μm from the splicing point, and is consistent with the profiles given in Fig. 6.2. Also, after splicing, the outer edge of the cladding has become round instead of octagonal due to the effects of surface tension as the fiber cools down from its liquid state. In general, this rounding phenomenon may have some effect on the pump modes in the cladding. However, this is beyond the scope of the present work.

The inserted figure on top of Fig. 6.2(a) shows the cross-sectional mean axial stress, $\bar{\sigma}_z$, along the *LIEKKITM Yb1200-10/125-DC* from the far-zone, $z < -1.3$ mm, to the splicing point. $\bar{\sigma}_z$ is calculated using Eq. (6.1) [239],

$$\bar{\sigma}_z = \frac{\int_0^{a_2} \sigma_z r dr}{\int_0^{a_2} r dr}, \quad (6.1)$$

where a_2 is the radius of the cladding. As described in [219], $\bar{\sigma}_z$ is an indicator of inelastic strain birefringence and is in proportion to draw tension. The inelastic strain birefringence is induced by the anisotropic component of FIV formed via fiber manufacturing [26, 95]. From the figure, it is observed that the splicing process completely relaxes the anisotropic component of FIV, which induces a RI change of $\sim 2 \times 10^{-5}$.

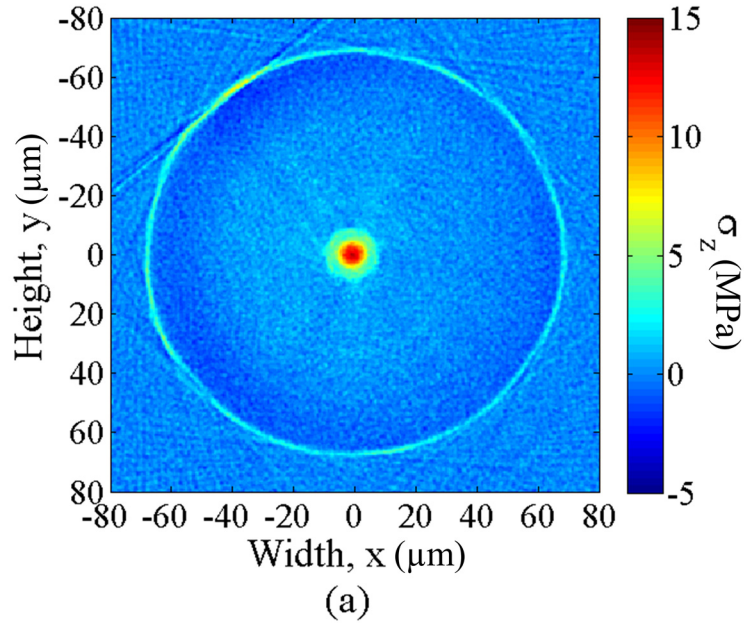


Figure 6.3: Cross-sectional RS distribution (reconstructed using all projection angles) in *LIEKKI™ Yb1200-10/125-DC* 20 μm from the splicing point.

Employing the same method presented in [219], using the RS data from Fig. 6.2(a), the radial RI change, Δn_r , is calculated and shown in Fig. 6.4. From this figure, it is seen that the core RI is decreased by as much as 4×10^{-4} , which represents a 17.4% change compared to the unperturbed core/cladding index difference, $\Delta n_{cc} \approx 2.3 \times 10^{-3}$. Furthermore, the affected fiber length is on the order of mm, or many hundreds of wavelengths within the core. Changes of this magnitude cannot be ignored when considering fusion splice characteristics for current LMA-SM-YDFs and their effect on YDFL and YDFA system performance will be appreciable. Still further, in future LMA-SM-YDFs with even lower NAs this effect will become more pronounced. Lastly,

because these RI changes are mainly induced via relaxation of draw-induced stress, they will be exacerbated as draw speeds increase for high volume production.

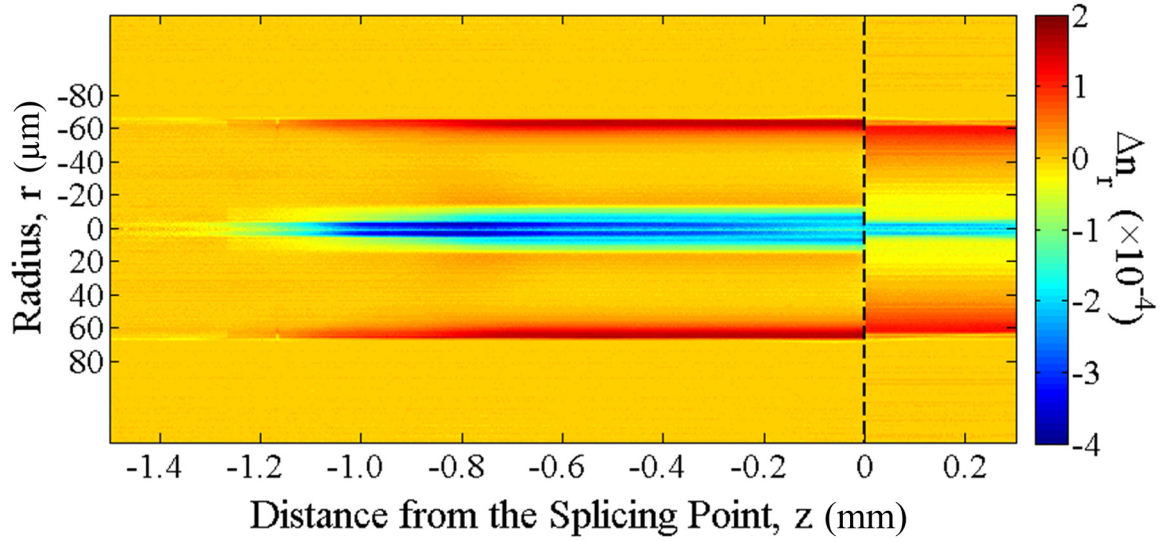


Figure 6.4: Change of radial refractive index (RI), Δn_r , induced by the RS change along the fusion splice between the *LIEKKITM Yb1200-10/125-DC* (left) and the *SMF-28* (right).

Fig. 6.5(a) shows the RI profiles within 1.5 mm on the *LIEKKITM Yb1200-10/125-DC* side and within 0.3 mm on the *SMF-28* side, where the splicing point is located at $z = 0$ mm. The fiber axial resolution is the same as Fig. 6.2(a). In Fig. 6.5(a), a transition region with a length of ~ 0.8 mm is observed in the *LIEKKITM Yb1200-10/125-DC*. In the transition region, there are RI changes in both core and cladding regions. The cladding RI is uniformly increased due primarily to the relaxation of the isotropic component of FIV formed via fiber manufacturing, however, the outer cladding RI is also increased due to the relaxation of tensile mechanical stress as shown in Fig. 6.4. The core RI is decreased due primarily to the diffusion of ytterbium ions which results in a spreading out of RI, however, the core RI is also decreased due to the relaxation of compressive mechanical stress as shown in Fig. 6.4. Fig. 6.6 shows the cross-sectional RI distribution (reconstructed using all projection angles) in the *LIEKKITM Yb1200-10/125-DC* $20 \mu\text{m}$ from the splicing point, and is consistent with the profiles given in Fig. 6.5(a).

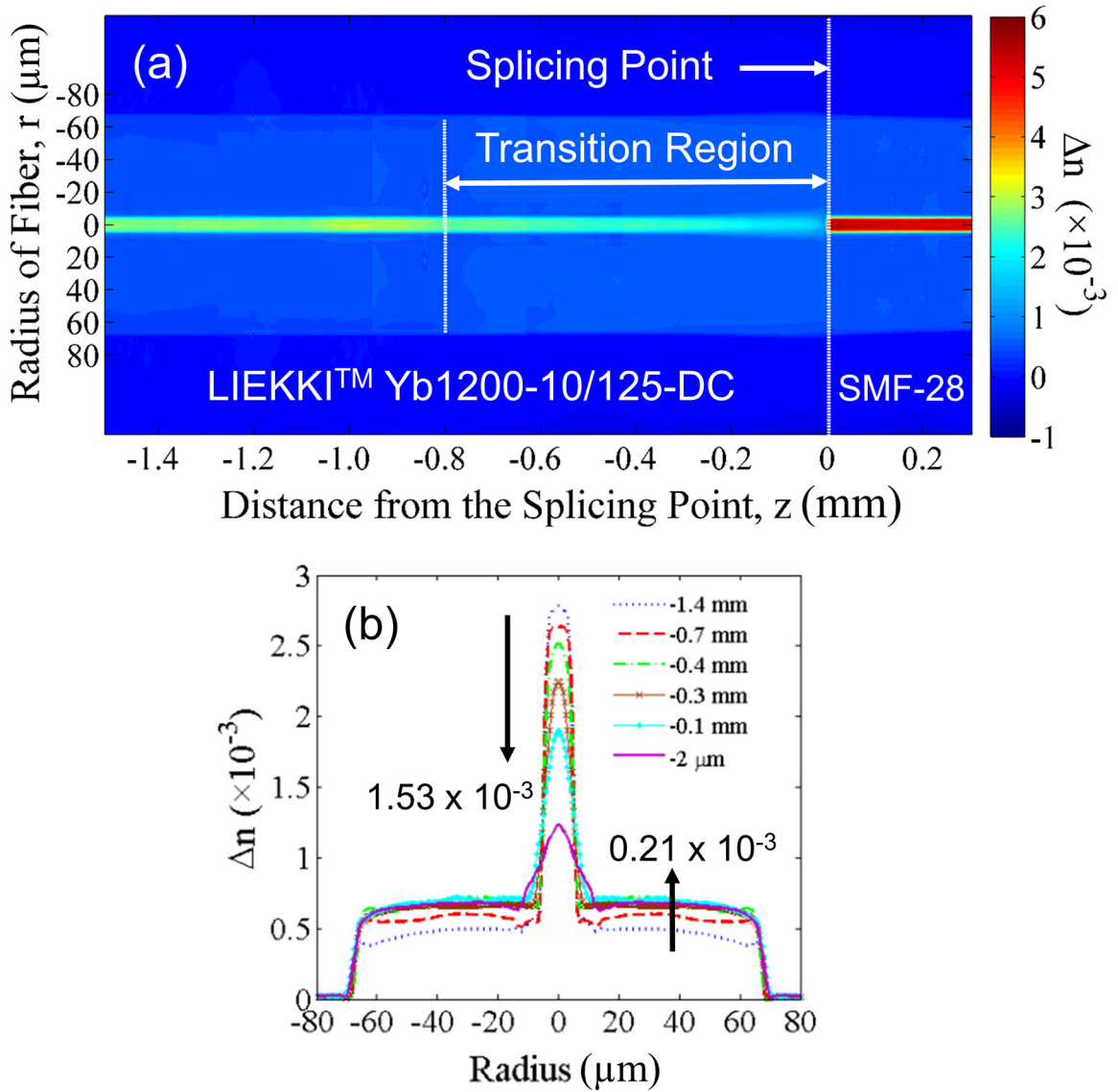


Figure 6.5: (a) The RI distribution along the *LIEKKI™ Yb1200-10/125-DC* (left) and the *SMF-28* (right) after arc fusion splicing. (b) RI profiles at indicated positions along the transition region from the splicing point.

To visualize these effects more clearly, Fig. 6.5(b) displays RI profiles at indicated positions along the transition region. From this figure, we obtain the mean increase in cladding RI as 0.21×10^{-3} and the maximum decrease in core RI as 1.53×10^{-3} . The core shape has become graded near the splicing point. Compared to the unperturbed value of $\sim 2.3 \times 10^{-3}$, Δn_{cc} is decreased by as much as 1.74×10^{-3} , representing a 75.8% change. Once again, such RI changes over axial distances on the order of hundreds of

wavelengths should not be ignored when analyzing the optical characteristics of fusion splices involving fibers of this type. In order to emphasize this point, the effects of the measured RI data will be investigated in the following simulation.

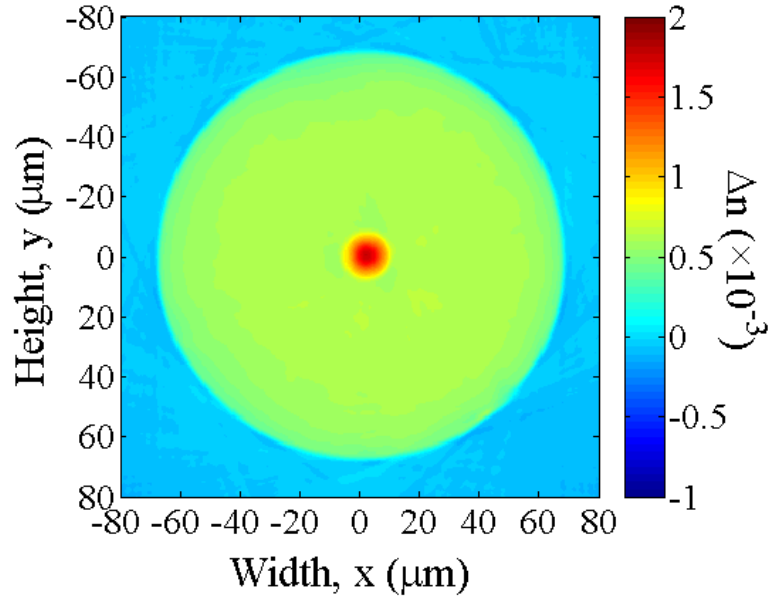


Figure 6.6: Cross-sectional RI distribution (reconstructed using all projection angles) in *LIEKKI™ Yb1200-10/125-DC* 20 μm from the splicing point.

Using the measured RI data within 1.5 mm on the *LIEKKI™ Yb1200-10/125-DC* side and within 1.4 mm on the *SMF-28* side and employing a FD-BPM [255], the propagation of the *LIEKKI™ Yb1200-10/125-DC* fundamental mode across the fusion splice is simulated at an operating wavelength of $\lambda = 1060$ nm. The resulting electric field amplitude, $|E(r, z)|$, is shown in Fig. 6.7(a). For comparison, we performed an identical simulation using ideal RI data taken from unperturbed measurements of the *LIEKKI™ Yb1200-10/125-DC* and the *SMF-28* and the result is presented in Fig. 6.7(b). In both simulations, the radial node spacing, Δr , is 0.2 μm and the axial node spacing, Δz , is 1 μm. It is apparent that a larger percentage of fundamental mode energy is lost to radiation modes in Fig. 6.7(a) compared to Fig. 6.7(b). Also, in Fig. 6.7(a), significant mode transformation is observed in the RI transition region as marked in Fig. 6.5(a).

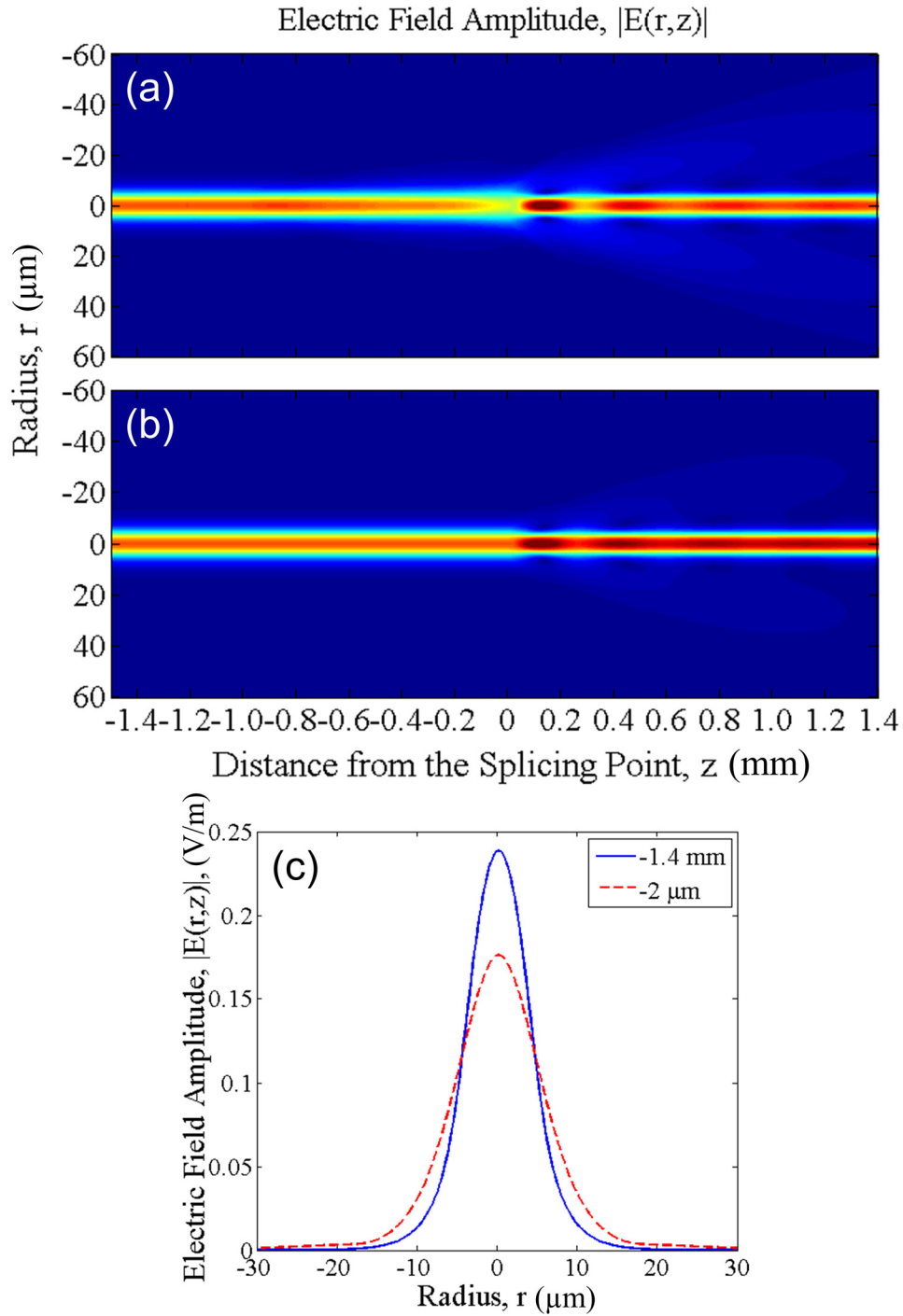


Figure 6.7: Finite-difference beam propagation method (FD-BPM) simulation of a fusion splice between the LIEKKI™ Yb1200-10/125-DC (left) and the SMF-28 (right) (a) using the measured RI data and (b) using the ideal RI data without any perturbations. The splicing point is at $z = 0$ mm. A fundamental guided mode of the LIEKKI™ Yb1200-10/125-DC core is used as the input at $z = -1.5$ mm. (c) Electric field amplitudes from (a) at the indicated positions.

Based on these results, the splice loss for the cases in Fig. 6.7(a) and 6.7(b) are calculated to be 1.37 dB (72.9% transmission, 27.1% loss) and 0.28 dB (93.7% transmission, 6.3% loss) respectively using an overlap integral technique [99]. This indicates that an extra 20.8% of incident power is lost when RS/RI effects are considered for this example. Fig. 6.7(c) illustrates the mode transformation associated with the RS/RI transition regions created by the splice process. From this figure, and assuming that both fields are reasonably described by a Gaussian function, the MFDs can be obtained by locating the radial positions where the field is $1/e$ times its maximum value. The MFD before the transition region is $\sim 10.6 \mu\text{m}$, which matches well with the nominal value supplied by the manufacturer of $11.1 \mu\text{m}$, and $\sim 14.8 \mu\text{m}$ after the transition region. Therefore the RS/RI transition region results in a 39.6% change in MFD which in most cases cannot be ignored, especially for applications involving high power all-fiber YDFs and YDFAs. Regardless of which fiber the *LIEKKITM Yb1200-10/125-DC* is spliced to, this RS/RI induced mode transformation effect will be present.

6.4 Summary

Recently, a state-of-the-art 3DISD measurement method was used to investigate RS and RI perturbations in LMA EDFs resulting from manufacturing, cleaving, and arc fusion splicing [219], as outlined in Chapter 5. The method was found to be especially well-suited to investigations of this type and the results indicated that the effects of fusion splicing are significant for LMA EDFs [219]. The results of the current investigation indicate that the effects of fusion splicing are even more prominent in LMA-SM-YDFs. The experiments are based on a commercial LMA-SM-YDF (*LIEKKITM Yb1200-10/125-DC*) spliced to *Corning SMF-28*. Arc fusion splicing can relax both the anisotropic and isotropic components of FIV as well as the mechanical component of RS. High splicing temperatures also result in heavy diffusion of core dopants. Together, these perturbations decrease the core/cladding RI difference by as much as 1.74×10^{-3} ,

representing a 75.8% change from the unperturbed fiber, over an axial distance of many hundreds of wavelengths.

Using a FD-BPM as a numerical tool, the optical effects of the aforementioned perturbations were simulated. For the measured sample, an extra 20.8% of incident power is lost when RS/RI effects are considered compared to the ideal situation without any perturbations. The transition region created by the RS/RI perturbations results in an expansion of the MFD by 39.6%. If not considered beforehand, this expansion will result in significant error in terms of expected splice loss. Because the performance of high power all-fiber YDFs and YDFAs depend heavily on this value, the results presented here are critically important for the design and optimization of such devices.

CHAPTER 7

RESEARCH SUMMARY


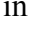
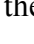
The primary objective of this research was to develop new quantitative phase imaging (QPI) modalities which are compatible with standard microscope platforms utilizing Köhler illumination. This was accomplished by (1) developing the recent concept of multifilter phase imaging (MFPI) based on the transport-of-intensity equation (TIE) to incorporate the effects of partially coherent light (MFPI-PC) from extended incoherent sources, (2) developing phase optical transfer function (POTF) recovery for two-dimensional (2D) QPI based on commercial microscopy while deriving improved linearization conditions which confirm the extension of previously developed imaging theory to large, but slowly varying, phase objects and (3) developing tomographic deconvolution phase microscopy (TDPM) which enables, for the first time, microscopy-based three-dimensional (3D) QPI based on a physical optics theory without making a projective approximation.

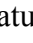


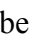


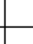

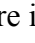
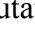






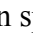

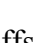
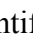
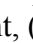



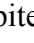
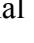

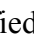




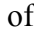

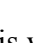





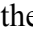

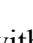

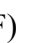



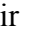

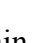





A secondary objective of this research was to apply established QPI and quantitative retardation imaging (QRI) methods to the characterization of refractive index (RI) and residual stress (RS) effects in large-mode-area erbium- and ytterbium-doped fibers (LMA EDFs and YDFs). This was accomplished by utilizing the recently developed 3D index-stress distribution (3DISD) method [31] to (4) characterize the effects of manufacturing, cleaving, and fusion splicing in commercially available LMA EDFs and (5) demonstrate the criticality of such effects when fusion splicing LMA YDFs. In this chapter, the main results and accomplishments associated with each of these works are summarized.

7.1 Summary of Results and Accomplishments

7.1.1 New Two-Dimensional Quantitative Phase Imaging Methods

In light of the literature review of state-of-the-art 2D QPI technologies conducted in Section 1.3.1, it was found that propagation-based phase retrieval algorithms possessed significant experimental advantages in comparison with more conventional interferometric approaches such as phase-shift and off-axis interferometry. Deterministic phase retrieval algorithms, such as those based on the TIE and the weak object transfer function (WOTF), have received relatively little attention in the literature in spite of their potential value associated with extending QPI capability to modern commercial microscopy systems without additional hardware modification or computational complexity. Such methods are attractive for biomedical applications and derive compatibility with microscopy by incorporating partial spatial coherence. They are also practical in the sense that they address the inherent noise/resolution trade-offs. It is within this context that the present research accomplishments associated with the development of two 2D QPI methods, namely MFPI-PC and POTF recovery, can be identified.

Table 7.1: Characteristic review for representative PR methods: (IWFR) iterative wave front reconstruction, (TIE) transport-of-intensity equation, (OFS) optimal frequency selection, (MFPI-PC) multifilter phase imaging with partially coherent light, (WOTF) weak object transfer function, (CTF) contrast transfer function, and (POTF) phase optical transfer function. 's indicate presence of a desired trait, 's indicate absence of a desired trait, and 's indicate a trade-off between desired traits.

PR Method	Single-Shot	High Resolution	Sensitive	Common-Path	White Light	No Object Assumptions	Comp. Simple	No Hardware Modification
IWFR [45]								
TIE [54]								
OFS [48]								
MFPI-PC [111]								
WOTF [49]								
CTF [50]								
POTF [129]								

Shown in Table 7.1 is a characteristic summary of existing PR methods in comparison to the two 2D QPI modalities outlined in this thesis using the same characteristics as Table 1.1 with the addition of “No Hardware Modification” indicating that standard microscope platforms may be used. Prior to the present thesis research, the only 2D QPI methods which did not require any hardware modification were the most basic implementations of the TIE and WOTF involving only two defocused planes [7, 49, 54], which are impractical due to the inherent trade-offs between sensitivity and spatial resolution in each case. The solutions to these problems [48, 50, 51, 174] were only described for the spatially coherent case, which is incompatible with commercial microscopy. In addition, the specific accomplishments associated with these two methods are outlined below:

1. The extension of both multi-plane TIE and multi-plane WOTF reconstruction methods to incorporate partially coherent imaging theory.
2. The proof and derivation of less restrictive linearization conditions for the validity of said reconstruction methods enabling application to strong phase objects.
3. The verification of said reconstruction methods for quantitative phase recovery of both simulated and well-known experimental test phase objects.
4. The analysis of said reconstruction methods in terms of phase/optical path length sensitivity.
5. The application of MFPI-PC to projection tomography.
6. The application of POTF recovery to both high-speed and time-lapse QPI of live adherent cells.

7.1.2 New Three-Dimensional Quantitative Phase Imaging Method

Similar to 2D QPI, the literature review of 3D QPI conducted in Section 1.3.2 indicated that methods based on the deconvolution of some 3D-resolved quantity, usually complex wave field amplitude [63, 64], possess experimental advantages compared to methods

based on either projection of diffraction tomography because images are scanned in z (defocus) as opposed to illumination angle. In addition to experimental simplicity, such methods derive inherent stability, both temporal and spatial, due to the use of partial coherence [5, 63, 64, 199], in contrast with diffraction tomography which relies on coherent light in general [263]. In spite of these benefits, the level of coverage in the literature concerning these topics is small in comparison to conventional tomographic approaches, perhaps owing to their conceptual simplicity. Furthermore, although the enhanced optical sectioning effect associated with increasing the illumination aperture in microscopy is well-known [66, 178], the application of this theory to 3D QPI is even less extensive [128, 199]. Such application is of great worth to the biomedical community as, similar to the aforementioned 2D QPI methods, it enables the addition of 3D QPI capability to ubiquitous microscopy systems with minimal hardware modification. It is within this context that the research accomplishments associated with the development of TDPM become clear.

Table 7.2: Characteristic review for representative 3DD methods: (WLDT) white light diffraction tomography, (TIPI) tomographic incoherent phase imaging, and (TDPM) tomographic deconvolution phase microscopy. ✓’s indicate presence of a desired trait and ✗’s indicate absence of a desired trait.

3D QPI Method	Fixed Object	Isotropic Resolution	High Resolution	Common-Path	White Light	Large Phase Objects	Comp. Simple	Microscopy Compatible
WLDT [63]	✓	✗	✓	✓	✓	✗	✓	✓
TIPI [64]	✓	✓	✓	✓	✓	✓	✗	✓
TDPM [193]	✗	✓	✓	✓	✓	✓	✓	✓

Shown in Table 7.2 is a characteristic summary of existing 3DD methods in comparison to TDPM using the same characteristics as Table 1.2 with the addition of “Microscopy Compatible” modular capability with standard microscope platforms. By their nature, 3DD methods are usually compatible with microscopy as they rely on various optical sectioning effects. A trade-off, however, is now observed between the ability to fix the object versus enabling computational simplicity and robust object

recovery. For example, in TIPI [65], the object may remain fixed enabling higher acquisition speed, however, doing so relies on iterative algorithms to improve resolution along the optical or z-axis. TDPM, by contrast, measured the entire object spectrum directly thereby enabling robust object recovery with computational simplicity at the cost of reduced acquisition speed. In addition to this new option for microscopy-based 3D RI recovery, the specific accomplishments associated with TDPM are as follows:

1. The extension of tomographic deconvolution methods, which have previously been developed for fluorescence microscopy, to QPI.
2. The derivation of generalized linearization conditions for the validity of reconstructions based on the 3D WOTF which demonstrates compatibility with strong, but slowly varying, phase objects.
3. The development of a modified split-step beam propagation method (BPM) for the accurate modeling of 3D partially coherent imagery.
4. The verification of said BPM against rigorous solutions based on Maxwell's equations for canonical objects.
7. The verification of TDPM for quantitative phase recovery of both simulated and well-known experimental test phase objects.
8. The demonstration of isotropic spatial resolution with high RI sensitivity in optical fibers over a large depth of focus.
9. The preliminary application of TDPM to long-period fiber grating (LPFG) characterization.

7.1.3 Large-Mode-Area Erbium- and Ytterbium-Doped Fiber Characterization

In Section 1.3.3, three key areas of optical fiber characterization were identified, including: fiber-based lasers and amplifiers, fusion splicing, and long-period fiber gratings (LPFGs). In the course of this thesis the first two have, at least to some extent, been addressed through the measurement of RI/RS perturbations in LMA EDFs and

YDFs, though further characterizations are still possible. The overall results of the investigations indicate the presence of strong variations, relative to current and future normalized index differences in LMA and ultra-LMA fibers. These perturbations need to be addressed in order to enable more robust implementations of extremely weak guidance, such as has been demonstrated recently in [97] and [96]. A list of associated accomplishments of the work described herein is provided here:

1. The first concurrent characterization of RI and RS in LMA EDFs.
2. The first measurement of RI and RS changes in the vicinity of a fusion splice for LMA EDFs and YDFs.
3. The application of a radially-symmetric BPM [255] for predicting the overall performance of LMA EDF and YDF splices using measured RI profile changes originating mostly from the diffusion of core dopants.

CHAPTER 8

FUTURE WORK

The research results presented in this thesis, especially those associated with the newly developed quantitative phase imaging (QPI) modalities, are novel and potentially transformative. Therefore, in this chapter, detail is provided on potential areas for future research. For future work related to QPI methods, suggested directions are categorized according to development, verification, characterization, and application. For future work centered on utilizing QPI data in long-period fiber grating (LPFG) research, suggested directions are provided for the measurement and modeling of LPFGs.

8.1 Multifilter Phase Imaging with Partially Coherent Light

8.1.1 Development

Although phase optical transfer function (POTF) recovery is better than multifilter phase imaging with partially coherent light (MFPI-PC) for objects which satisfy the generalized linearization conditions [Eqs. (3.20) and (3.21)], there may be applications, particularly those involving objects with strong absorption, for which MFPI-PC is needed. For example, in [167] it is observed that if the intensity and phase gradients are collinear [i.e. if $\nabla_{\perp}\phi(\mathbf{r}) = c(\mathbf{r})\nabla_{\perp}I(\mathbf{r})$ in which $\mathbf{r} = x\hat{x} + y\hat{y}$, ∇_{\perp} is the gradient operator acting in the lateral coordinates only, $\phi(\mathbf{r})$ is phase, $I(\mathbf{r})$ is intensity, and $c(\mathbf{r})$ is any scalar function], then the conventional solution to the transport-of-intensity equation (TIE) is exact provided the boundary conditions are satisfied. Implicit in this assumption is the absence of curl in the power flow vector $I(\mathbf{r})\nabla_{\perp}\phi(\mathbf{r})$.

This is the case in Lambert-Beer's law for homogeneous transmissive objects [264] where $c(\mathbf{r}) = \varepsilon I^{-1}(\mathbf{r})$ and absorption is proportional to phase via a constant ε , i.e. $\phi(\mathbf{r}) = \varepsilon A(\mathbf{r})$ in which $A(\mathbf{r})$ is absorption [265]. However, POTF recovery would also

be applicable in this case since an effective POTF could be modelled as $H_\phi'(\boldsymbol{\rho}) = H_\phi(\boldsymbol{\rho}) + \varepsilon H_A(\boldsymbol{\rho})$ as in [266]. There may be applications, however, in which the absorption and phase of inhomogeneous objects are correlated, though not proportional, resulting in collinear intensity and phase gradients. In this case the conventional TIE solution can be quite good even though the object may be strongly scattering, as is shown in the simulated example shown below.

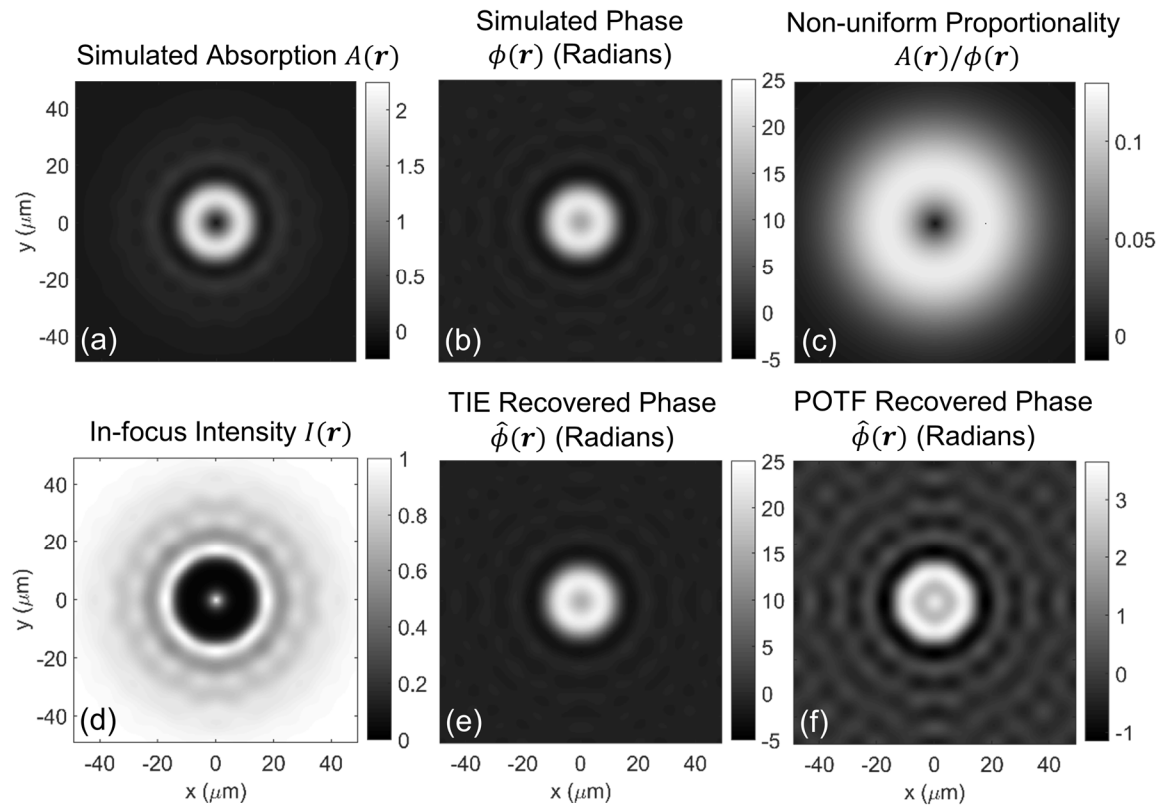


Figure 8.1: Simulation showing the power of transport-of-intensity equation (TIE) phase recovery for strong objects with correlated phase and absorption. (a) Simulated absorption. (b) Simulated phase. (c) Non-uniform proportionality between absorption and phase. (d) In-focus intensity distribution. (e) Phase recovered via conventional TIE solver. (f) Phase recovered via inversion of the phase optical transfer function (POTF).

Figure 8.1 illustrates the aforementioned characteristics using a synthetic complex object which consists of the strong absorption shown in Fig. 8.1(a) and the large phase delay shown in Fig. 8.1(b). In this case the intensity and phase gradients are collinear although the proportionality between the two distributions, which is shown in Fig. 8.1(c),

is non-uniform. In the simulation, coherent illumination with $\lambda = 546$ nm was assumed and the complex wave field was propagated via the angular plane wave spectrum method in the paraxial approximation [184]. Simulated intensities were generated at defocus distances of $z = \pm 3$ μm as well as in-focus as shown in Fig. 8.1(d). Fig. 8.1(d) demonstrates the extent of absorption with minimum values close to 0.02. The advantage of using a TIE-based solution in this case is clearly demonstrated by the recovered solutions shown in Fig. 8.1(e) for the conventional TIE solver and Fig. 8.1(f) for POTF recovery. If careful attention is given to the scale bars, it is observed that POTF recovery underestimates significantly the highly wrapped phase distribution which is recovered well by the TIE. For this class of objects, the TIE solution is in general required with a small defocus distance δz for linearization, however, if the object can be assumed to be slowly varying, the optimal frequency selection (OFS) algorithm, and thereby MFPI-PC, should also be applicable [7], as will be shown in Section 8.1.2.

In addition to objects with collinear phase and intensity gradients, however, there exist a range of applications for which the conventional TIE solution is insufficient as has recently been shown by Zuo *et al.* [265] and Shanker *et al.* [167]. For example, a simple and cost effective solution is sought for mask characterization in photolithography [167], in which masks have both strong absorption and phase features which are uncorrelated. Since the conventional TIE solver does not account for rotational power flow caused by perpendicular phase and absorption features, the recovered phase solution is corrupted by rotational artifacts [167, 265]. It has been shown that these artifacts may be eliminated using an iterative error reduction algorithm [167], however, such methods have not been demonstrated under partially coherent imaging conditions or in concert with the OFS or MFPI-PC algorithms in the presence of severe noise or in applications requiring high accuracy. Therefore, to develop MFPI-PC further, ***it is proposed to incorporate iterative error reduction algorithms for generic object recovery.***

Another potential shortcoming of MFPI-PC and TIE methods in general is a reliance on the paraxial approximation [46], making the interpretation of high numerical aperture (NA) results questionable. For example, Fig. 8.2 elucidates the importance of correcting for these errors in high-NA phase imaging, in which a high resolution phase structure (sharp circles spaced 810 nm apart) is shown to produce as much as ~15% error due to the paraxial approximation. This overestimation of phase occurs because the parabolic shape of the POTF inherent in the TIE [111] underestimates contrast at high spatial frequencies, the effects of which were seen in Chapters 2 and 3. Although POTF recovery can model and invert the increased contrast at high spatial frequencies by utilizing non-paraxial pupils in the POTF calculation [Eq. (3.16)], it also requires the use of a weak absorption approximation, which may be limiting for many applications.

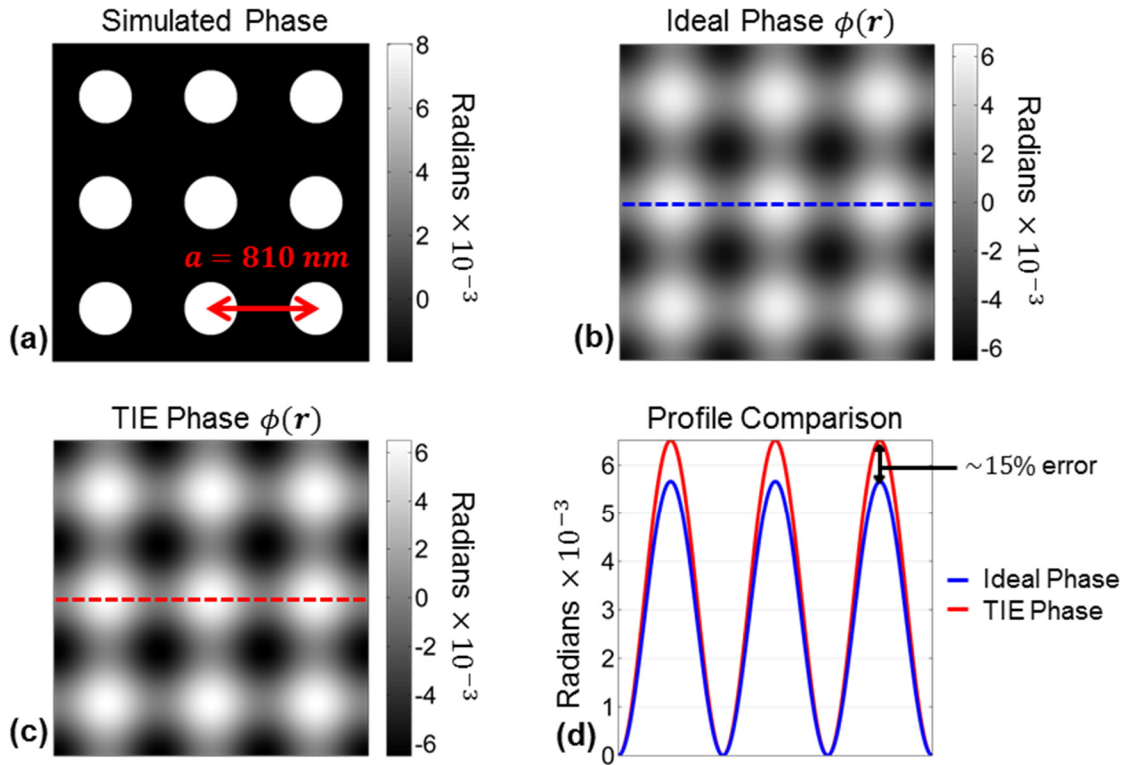


Figure 8.2: (a) Simulated phase object, (b) phase after filtration by $NA_o = 0.75$ with $\lambda = 546$ nm, (c) transport-of-intensity equation (TIE) recovered phase based on ideal intensity derivative assuming spatially coherent light, and (d) profile comparison of (b) and (c) showing ~15% error in TIE reconstruction.

For strongly scattering samples with fine structural detail, however, it may be possible to utilize a non-paraxial variant of the TIE which is described herein. The spectrum of a defocused (at distance z) scalar wave field $T_z(\boldsymbol{\rho})$ diffracted from a thin transparency $T(\mathbf{r}) = \exp[-A(\mathbf{r}) + i\phi(\mathbf{r})]$ located in the $z = 0$ plane may be described in the paraxial approximation by Eq. (8.1a). Modeling propagation as in the angular plane wave spectrum method [184], we may replace Eq. (8.1a) by Eq. (8.1b) in which the parabolic pupil function has been replaced by a spherical function as in Chapter 3. Eq. (8.1b) may then be expanded to the infinite series shown in Eq. (8.1c).

$$T_z(\boldsymbol{\rho}) = T(\boldsymbol{\rho})\exp[-i\pi\lambda z\rho^2], \quad (8.1a)$$

$$T_z(\boldsymbol{\rho}) = T(\boldsymbol{\rho})\exp\left\{i\frac{2\pi}{\lambda}z\left[\sqrt{1-(\lambda\rho)^2}-1\right]\right\}, \quad (8.1b)$$

$$T_z(\boldsymbol{\rho}) = T(\boldsymbol{\rho})\exp\left\{-i\pi\lambda z\left[\frac{2}{\lambda^2}\sum_{n=1}^{\infty}\frac{(2n)!}{(2n-1)(n!)^2(4^n)}(\lambda\rho)^{2n}\right]\right\}. \quad (8.1c)$$

Using the preceding expression and the shifting and complex conjugation properties of Fourier transforms we arrive at the following intensity spectrum for the diffracted field, which is in the same form as Guigay's expression [127].

$$\begin{aligned} I_z(\boldsymbol{\rho}) = & \int T\left\{\mathbf{r}-\left[\frac{1}{\lambda\rho^2}\sum_{n=1}^{\infty}\frac{(2n)!}{(2n-1)(n!)^2(4^n)}(\lambda\rho)^{2n}\right]\mathbf{z}\boldsymbol{\rho},0\right\} \\ & \times T^*\left\{\mathbf{r}+\left[\frac{1}{\lambda\rho^2}\sum_{n=1}^{\infty}\frac{(2n)!}{(2n-1)(n!)^2(4^n)}(\lambda\rho)^{2n}\right]\mathbf{z}\boldsymbol{\rho},0\right\} \\ & \times \exp(-i2\pi\mathbf{r}\cdot\boldsymbol{\rho})d^2\mathbf{r} \end{aligned} \quad (8.2)$$

Expanding each term in the integrand to first order in z , retaining only first-order terms in the product, transforming the frequency domain factors of $\boldsymbol{\rho}\cdot$ and ρ^2 into $\nabla_{\perp}\cdot/2\pi i$ and $\nabla_{\perp}^2/-4\pi^2$ respectively, and expanding $\nabla_{\perp}T(\mathbf{r})$ as in [50] results in a non-paraxial TIE [Eq. (8.3)] which is valid for high spatial frequencies and compatible with spatially coherent quasi-monochromatic illumination. In Eq. (8.3b), $\hat{\Gamma}$ is an operator involving successive orders of ∇_{\perp}^2 , i.e. $1, \nabla_{\perp}^2, \nabla_{\perp}^4$, etc. The first term of $\hat{\Gamma}$ equals 1 so that the first

term on the right hand side (RHS) of Eq. (8.3a) represents the paraxial TIE [Eq. (2.1)] and the remaining terms represent higher order corrections.

$$-\left(\frac{2\pi}{\lambda}\right)\frac{\partial I(\mathbf{r})}{\partial z} = \hat{\Gamma}\{\nabla_{\perp} \cdot [I(\mathbf{r})\nabla_{\perp}\phi(\mathbf{r})]\}, \quad (8.3a)$$

$$\hat{\Gamma} = \left[2 \sum_{n=1}^{\infty} \frac{(-1)^{n-1}(2n)!}{(2n-1)(n!)^2(4^n)} \left(\frac{\bar{\lambda}\nabla_{\perp}}{2\pi}\right)^{2(n-1)} \right]. \quad (8.3b)$$

Eq. (8.3) is a nice result because it is still linear in $\phi(\mathbf{r})$ and thus solvable using the popular Fourier method [166]. For example, Eq. (8.3) can be solved in the usual way by making Teague's approximation, i.e. $I(\mathbf{r})\nabla_{\perp}\phi(\mathbf{r}) = \nabla_{\perp}\varphi(\mathbf{r})$ [Teague_1983], and first solving for $\varphi(\boldsymbol{\rho})$ in the Fourier domain using Eq. (8.4), in which the conventional parabolic term in the denominator has been replaced by the spherical function corresponding to the angular spectrum method. Once $\varphi(\boldsymbol{\rho})$ is found, the process for obtaining $\phi(\mathbf{r})$ is the same as before [166], which is a Fourier domain solution to Poisson's equation.

$$\begin{aligned} \varphi(\boldsymbol{\rho}) &= \frac{\frac{\partial I(\boldsymbol{\rho})}{\partial z}}{\left[\left(\frac{4\pi}{\lambda}\right) \sum_{n=1}^{\infty} \frac{(2n)!}{(2n-1)(n!)^2(4^n)} (\bar{\lambda}\boldsymbol{\rho})^{2n} \right]} \\ &= \frac{\frac{\partial I(\boldsymbol{\rho})}{\partial z}}{\left(\frac{4\pi}{\lambda}\right) \left[1 - \sqrt{1 - (\bar{\lambda}\boldsymbol{\rho})^2} \right]} \end{aligned} \quad (8.4)$$

In deriving the non-paraxial TIE shown in Eq. (8.3), an assumption of spatial coherence is required, thus limiting the potential range of applicability. However, in many situations, spatially coherent, or close to spatially coherent, illumination can be used when compatibility with microscopy is not necessary. For example, applications in industrial metrology, photomask characterization [167], surface topography, or optical fiber characterization [73] may be categorized as such. ***It is therefore proposed to develop the non-paraxial TIE, Eq. (8.3), further for applications involving absorbing***

samples which require both high spatial resolution and the simplicity afforded by propagation-based phase retrieval.

8.1.2 Verification

In Chapter 2, the development of MFPI-PC was based on the weak object transfer function (WOTF) theory originally described by Streibl [66]. Therefore the applicability of MFPI-PC depends on the applicability of the two-dimensional (2D) WOTF which was shown in Chapter 3 (see Appendix A) to be linearizable under conditions of weak absorption and slowly varying phase (SVP). In [7], however, it was shown that the OFS algorithm, whose partially coherent analogue is MFPI-PC, requires only an assumption of a slowly varying object in which absorption does not need to be weak [7]. Here we generalize this observation to MFPI-PC, after which *it is proposed to be verified both experimentally and using simulation studies.*

In [50], it was shown that for on-axis coherent illumination under the paraxial approximation, the assumptions of SVP, i.e. $|\phi(\mathbf{r}) - \phi(\mathbf{r} - \bar{\lambda}z\boldsymbol{\rho})| \ll 1$, and slowly varying amplitude, i.e. $\beta(\mathbf{r} - \bar{\lambda}z\boldsymbol{\rho}) = \beta(\mathbf{r}) - \bar{\lambda}z\boldsymbol{\rho} \cdot \nabla_{\perp}\beta(\mathbf{r})$ where $\beta(\mathbf{r}) = \exp[-A(\mathbf{r})]$, imply that the Fourier spectrum of the diffracted intensity pattern recorded at a defocus distance z may be written as

$$I_z(\boldsymbol{\rho}) = I_0(\boldsymbol{\rho}) + 2[\sin(\pi\bar{\lambda}z\rho^2) - \pi\bar{\lambda}z\rho^2 \cos(\pi\bar{\lambda}z\rho^2)]\mathcal{F}\{I_0(\mathbf{r})\phi(\mathbf{r})\} - \frac{\bar{\lambda}z}{2\pi} \cos(\pi\bar{\lambda}z\rho^2) \mathcal{F}\{\nabla_{\perp} \cdot [I_0(\mathbf{r})\nabla_{\perp}\phi(\mathbf{r})]\}, \quad (8.5)$$

where $I_0(\mathbf{r})$ is the in-focus intensity distribution. In Section 3.2, it was also shown that if the object is band-limited [i.e. $T(\boldsymbol{\rho}) = 0$ for $|\boldsymbol{\rho}| > \rho_o(1 - S)$, where $\rho_o = NA_o/\bar{\lambda}$ and $S = NA_c/NA_o$ is the coherence parameter defining the NA ratio between the condenser and the objective], then the corresponding intensity Fourier spectrum under partial coherence may be written as

$$I_z(\boldsymbol{\rho}) = B \frac{J_1(2\pi\rho_c\bar{\lambda}z|\boldsymbol{\rho}|)}{\pi\rho_c\bar{\lambda}z|\boldsymbol{\rho}|} I_z^c(\boldsymbol{\rho}), \quad (8.6)$$

where B is the non-diffracted background intensity level, $I_z^C(\boldsymbol{\rho})$ is the intensity spectra resulting from on-axis coherent light which in this case is given by Eq. (8.5), J_1 is the first-order Bessel function of the first kind, and $\rho_c = NA_c/\bar{\lambda}$. Given Eq. (8.5) and Eq. (8.6), we may write an expression for the lateral Fourier spectrum of the intensity derivative estimates utilized in MFPI-PC as

$$\begin{aligned}
\frac{dI(\boldsymbol{\rho})}{dz} &= \sum_{j=-n}^n h_{SG}[j] I_{z_j}(\boldsymbol{\rho}) \\
&= B \sum_{j=-n}^n h_{SG}[j] \frac{J_1(2\pi\rho_c\bar{\lambda}z_j|\boldsymbol{\rho}|)}{\pi\rho_c\bar{\lambda}z_j|\boldsymbol{\rho}|} I_0(\boldsymbol{\rho}) \\
&\quad + 2B \sum_{j=-n}^n h_{SG}[j] \frac{J_1(2\pi\rho_c\bar{\lambda}z_j|\boldsymbol{\rho}|)}{\pi\rho_c\bar{\lambda}z_j|\boldsymbol{\rho}|} \sin(\pi\bar{\lambda}z_j\rho^2) \mathcal{F}[I_0(\mathbf{r})\phi(\mathbf{r})] \\
&\quad - 2B \sum_{j=-n}^n h_{SG}[j] \frac{J_1(2\pi\rho_c\bar{\lambda}z_j|\boldsymbol{\rho}|)}{\pi\rho_c\bar{\lambda}z_j|\boldsymbol{\rho}|} \pi\bar{\lambda}z_j\rho^2 \cos(\pi\bar{\lambda}z_j\rho^2) \mathcal{F}[I_0(\mathbf{r})\phi(\mathbf{r})] \\
&\quad - \frac{\bar{\lambda}B}{2\pi} \sum_{j=-n}^n h_{SG}[j] \frac{J_1(2\pi\rho_c\bar{\lambda}z_j|\boldsymbol{\rho}|)}{\pi\rho_c\bar{\lambda}z_j|\boldsymbol{\rho}|} z_j \cos(\pi\bar{\lambda}z_j\rho^2) \mathcal{F}\{\nabla_{\perp} \cdot [I_0(\mathbf{r})\nabla_{\perp}\phi(\mathbf{r})]\}
\end{aligned} \tag{8.7}$$

where $h_{SG}[j]$ are the Savitzky-Golay differentiation filter (SGDF) coefficients of a particular odd order m up through $2n - 1$ in which $2n + 1$ is the odd number of defocused images recorded which may be equally [111] or unequally [129] spaced at the symmetric defocus distances specified by z_j . In Chapter 2, the SGDF coefficients were $h_{SG}[j] = a_j/\Delta z$ at a uniform spacing of Δz , but in this treatment non-uniformly spaced data may also be used in which Δz has no meaning and the coefficients $h_{SG}[j]$ are calculated as in [187].

Since the SGDF coefficients are odd-symmetric with a central weight $z_0 = 0$ then the first term on the right hand side of Eq. (8.7) vanishes. In order to show that the intensity derivatives estimated in MFPI-PC correspond to the intensity derivatives predicted by the TIE and thus demonstrate its validity for slowly varying objects we require the following condition,

$$\sum_{j=-n}^n h_{SG}[j] \frac{J_1(2\pi\rho_c\bar{\lambda}z_j|\boldsymbol{\rho}|)}{\pi\rho_c\bar{\lambda}z_j|\boldsymbol{\rho}|} \sin(\pi\bar{\lambda}z_j\rho^2) = \pi\bar{\lambda}\rho^2, \quad (8.8)$$

to be valid since Eq. (8.7) would then reduce to the TIE given by

$$\frac{dI(\boldsymbol{\rho})}{dz} = -\frac{\bar{\lambda}}{2\pi} \mathcal{F}\{\nabla_{\perp} \cdot [BI_0(\mathbf{r})\nabla_{\perp}\phi(\mathbf{r})]\}, \quad (8.9)$$

Since the primary concept of MFPI-PC is to, for each lateral Fourier component, select the lowest SGDF order which does not result in phase attenuation due to either nonlinearity of the intensity derivative or partial coherence effects, MFPI-PC inherently selects SGDF orders m for which Eq. (8.8) is valid within the passband defined by $\rho_o(1 - S)$. Therefore, for a slowly varying band-limited object, MFPI-PC extends the TIE solution beyond the small-defocus limit enabling good noise suppression without sacrificing the benefits of using the TIE in cases of strong absorption and phase. In order to verify this claim, ***it is proposed to conduct both simulation and experimental studies to test the performance characteristics for a diversity of objects that fall into this category.*** A potential object to be used for verification in this regard is shown in Fig. 8.3.

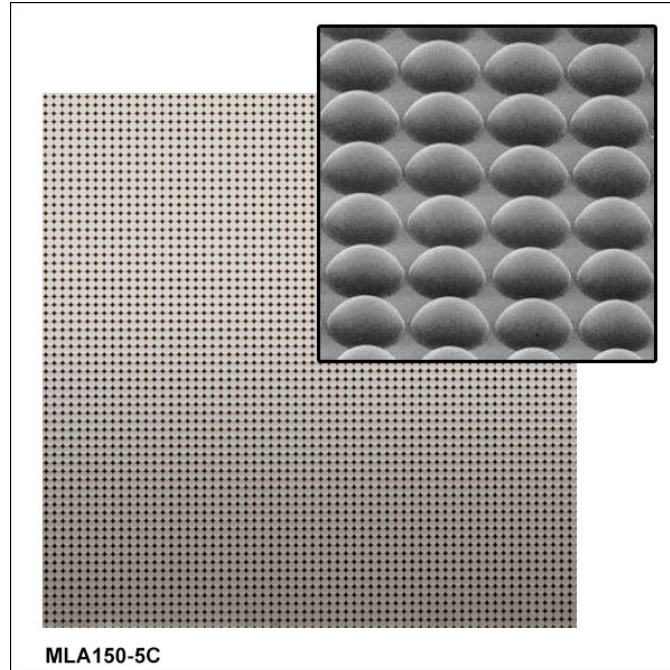


Figure 8.3: Commercial microlens array (*Thorlabs, MLA150-5C*) with chrome in the interstitial regions.

8.1.3 Characterization

In the theoretical development for both MFPI-PC and POTF recovery presented in Chapters 2 and 3 respectively, the object was considered to be infinitely thin, i.e. thinner than the microscope depth of field $d = \lambda/NA_0^2$, such that it can be completely characterized as a transparency of the form $T(\mathbf{r}) = \exp[-A(\mathbf{r}) + i\phi(\mathbf{r})]$ in which $A(\mathbf{r})$ and $\phi(\mathbf{r})$ are the projected absorption and phase respectively. In practice, most objects are not infinitely thin, but also possess some finite thickness and variation along the optical or z-axis, e.g. the thickness parameters used to emulate adherent cell imaging in Chapter 3 were $\sim 8 \mu\text{m}$ when $d = \lambda/NA_0^2 = 546 / 0.75^2 \approx 971 \text{ nm}$.

Bellair *et al.* studied the effects of applying 2D phase recovery to three-dimensional (3D) objects thicker than d under partial spatial coherence [128] by utilizing the 3D WOTF theory of Streibl [66]. This approach, however, requires the assumption of single-scattering and thus fails to analyze the inherent non-linear nature of 3D image formation when multiple elastic scattering events are incorporated. For this reasons, it is proposed to utilize the modified split-step beam propagation method (SS-BPM) described in Chapter 4, which models the effects of multiple forward elastic scattering events through a transmissive 3D object and is shown there to produce excellent agreement with rigorous solutions over a wide range of normalized index contrast values ($0 < \Delta n/n_0 < 0.15$) [193]. Utilizing this numerical tool, ***it is proposed to identify necessary conditions for the appropriateness of the projective approximation and also determine what is measured when such conditions are not met.***

Another important topic in the area of TIE-based phase recovery is the use and assumptions of various numerical boundary conditions employed in the solution. The TIE itself is an second-order elliptic partial differential equation for the phase $\phi(\mathbf{r})$ and as such its solution depends heavily on the specified boundary conditions [124]. In spite of its popularity, the numerical boundary conditions inherent in the most common solution

to the TIE, as given by Eq. (21) in [166], are often not satisfied in practice as the use of fast-Fourier transforms implies a periodic object. This implementation is known to work well for situations in which the phase object is isolated within the field of view (FOV) [126]. When objects are located on the image borders, however, severe artifacts appear which impair the accuracy of phase reconstruction [124].

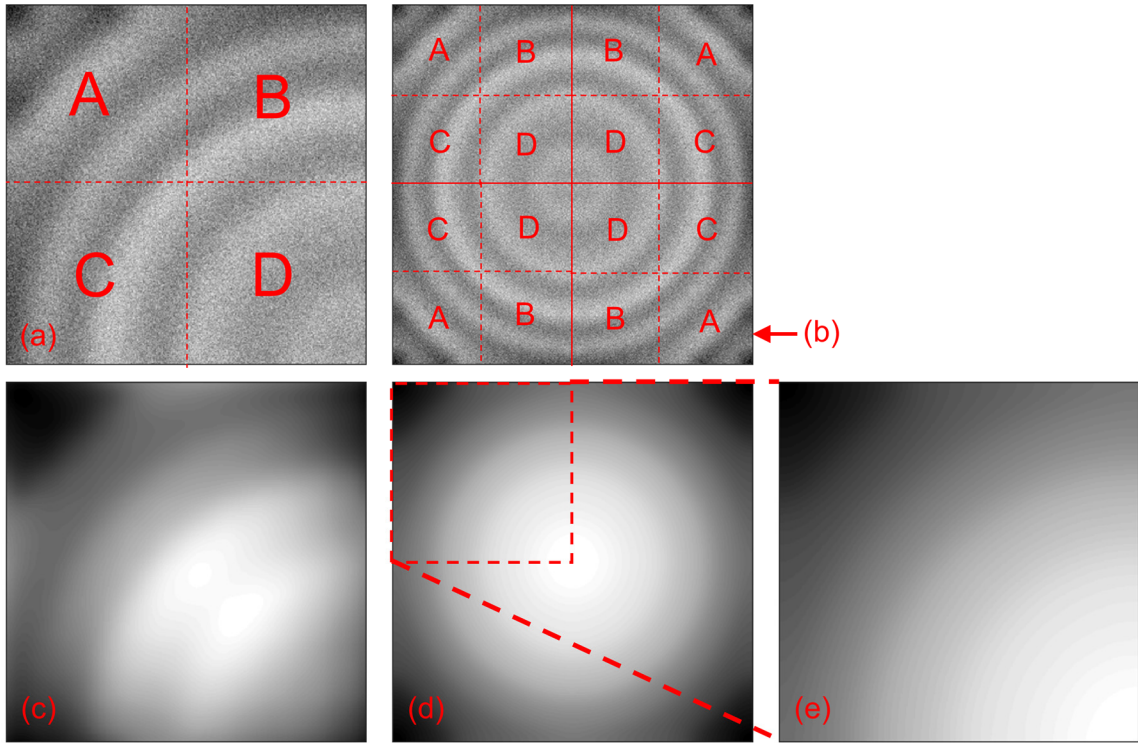


Figure 8.4: (a) Intensity difference image ($\Delta I_z = I_{+z} - I_{-z}$) used as input to TIE phase recovery. (b) Mirrored-extension of (a) in which the four quadrants have been padded symmetrically. (c) Phase reconstruction of (a) showing artifacts near the image boundaries associated with non-periodic field of view (FOV). (d) Phase reconstruction of (b) showing the reduction of edge artifacts evident by comparing (e) with (c), where (e) is a magnified view of the top-left corner.

In the general case, the boundary conditions can be satisfied explicitly by the use of a hard rectangular aperture and a slight alteration of the numerical implementation as shown by Zuo *et al.* [126]. This approach, however, requires the use of an add-on module with a physical aperture placed in a plane conjugate to the object and therefore violates the approach taken in this thesis in which numerical solutions are sought without the addition of hardware. Another approach, which has been outlined by Volkov *et al.* [125],

is based on mirror padding schemes which can be viewed as special cases of either Dirichlet or Neumann boundary conditions [124]. Such an approach requires no additional hardware and has been shown to reduce edge artifacts [125]. ***It is proposed, therefore, to characterize the use of such a mirror padding scheme to reduce reconstruction error in both MFPI-PC and POTF recovery.*** An example demonstrating the potential improvement is shown in Fig. 8.4, in which the mirror padding scheme defined by Fig. 8.4(a) and 8.4(b) is shown to reduce errors associated with sampling the microlens array imaged in Chapter 3 in a non-periodic fashion.

8.1.4 Application

As mentioned in Section 8.1.1, one major strength of MFPI-PC lies in its ability to recover phase in objects also possessing strong absorption features [167]. ***We therefore propose to demonstrate the utility of MFPI-PC by applying it in cases with strong absorption which is not correlated with the phase,*** such as photomask characterization for photolithography [167] in which the aforementioned iterative error reduction algorithm will be necessary. Such an application could enable a cost-effective solution for phase defect inspection in extreme ultraviolet photomasks where the use of partial coherence improves both light throughput and spatial resolution [163].

Another important feature of TIE- and other propagation-based phase reconstruction methods are their compatibility with various forms of radiation. For example, the TIE has been used to recover phase in both optical [54] and electron [267] microscopy as well as using x-rays [268] and even matter waves [269]. ***It is therefore proposed to apply the MFPI-PC algorithm to phase recovery outside of the optical regime,*** e.g. in high-resolution transmission electron microscopy in which the finite size of the electron source results in partial spatial coherence [45].

8.2 Phase Optical Transfer Function Recovery

8.2.1 Development

Although sub-second temporal resolution has been achieved for POTF recovery as shown in Media 3.1, single-shot methods [42] are still much faster as they are only limited by camera frame rate and require no mechanical movement. Many dynamics, such as the influence of ATP on red blood cell membrane fluctuations [153], occur on millisecond timescales for which single-shot methods become critically important. For these reasons, *it is proposed to develop a version of POTF recovery which uses only a single defocused image as input data.* Although it is technically possible to recover the phase of a pure phase object with a single defocused image using POTF recovery, in practice the solution is much more stable if at least two images of opposite defocus are subtracted. This is evident in Fig. 8.5, in which significant error is induced from single image phase recovery [Fig. 8.5(b)] as opposed to two images of opposite defocus [Fig. 8.5(c)].

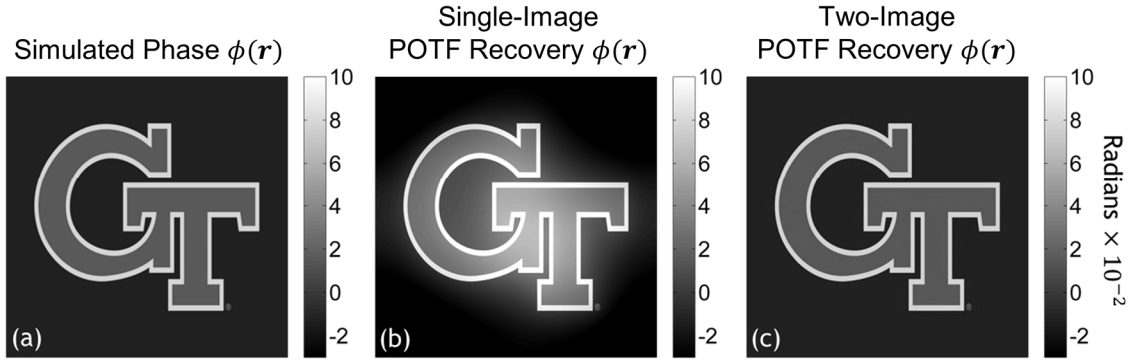


Figure 8.5: (a) Simulated phase object, (b) phase recovered with one defocused image [found by filtering with one-half the inverse of $H_{0.6}^{PC}(\rho)$, Eq. (3.22)], (c) phase recovered using two images of opposite defocus [filtered with the inverse of $H_{0.6}^{PC}(\rho)$]. $\delta z = 0.6 \mu\text{m}$ in both (b) and (c).

This error is likely due to image formation nonlinearities which are symmetric, as opposed to anti-symmetric, about $z = 0$. This effect becomes more pronounced as the overall phase magnitude, and its associated nonlinearity, increases. To address this issue, *it is proposed to reduce these errors by utilizing iterative error reduction methods*, such

as that which was recently proposed by Claus *et al.* [163], which is conceptually similar to the aforementioned TIE error reduction algorithm [167]. If successful, such computational reconstructions could enable the application of POTF recovery when single-shot acquisition times are required at the expense of increased computational complexity. Another approach for a single-shot QPI system based on POTF recovery in a provisional patent application [270] in which the defocused images are acquired in parallel on a single imager using diffraction gratings.

If single-shot acquisition speeds are not required, however, it will still be beneficial to maximize the phase frame rate and provide real-time phase visualization. Real-time visualization of the phase will be useful in applications requiring feedback, e.g. in studying the effects of various treatments in live cell culture time-lapse imaging or in CO₂-laser-induced LPFG fabrication. In order to enable higher frame rates and real-time visualization, ***it is proposed to implement a customized software package which can interface with system hardware components including the camera and piezoelectric objective scanner in an automated fashion.*** In addition to automating the steps of image capture and defocus, the proposed software should also perform POTF recovery processing in the background to display a live phase image in real-time. Figure 8.6 offers a block diagram representation of how this might be achieved. In Fig. 8.6, the hardware control and phase computation aspects are handled in separate threads so that the most recent phase image can be computed and displayed while the intensity images corresponding to the next iteration are recorded. Thus far, in preliminary implementations, the bottleneck appears to be in image transfer from the camera to the computer. Even with this limitation phase frame rates on the order of ~6 frames per second have been achieved in which 5 intensity images were used for POTF recovery over a 400 × 400 pixel region of interest. Real-time visualization of differential interference contrast (DIC) images corresponding to the phase images has also been

demonstrated in parallel without additional processing delay due to the threaded implementation.

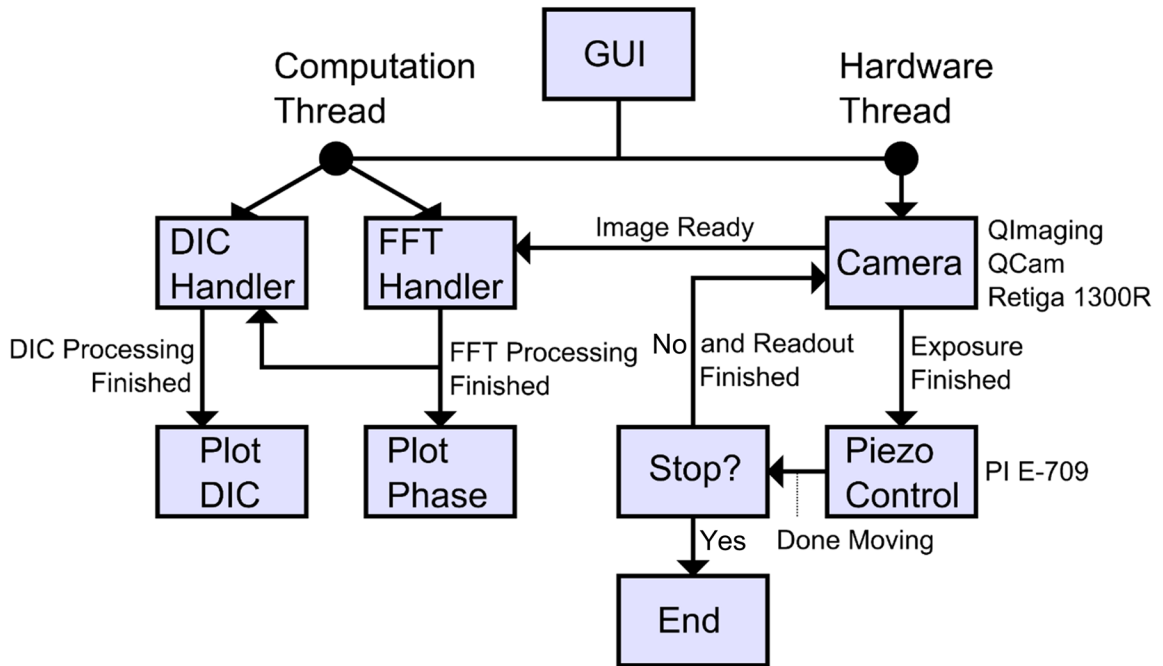


Figure 8.6: Block diagram representation of real-time high-speed phase optical transfer function (POTF) recovery software implementation.

8.2.2 Verification

The theory outlined in Chapter 3 for POTF recovery under partial spatial coherence is general enough to account for arbitrary source and pupil functions. It is therefore of interest to verify the ability to recover phase information using contrast mechanisms other than defocus. Recently, POTF recovery has been demonstrated using differential phase contrast in which the source function is created synthetically by subtracting two images recorded with equal and opposite hemispherical source functions generated via an LED array [121]. Similarly, POTF recovery has also been shown to converge to the same result using a through-focal series of both bright-field and phase contrast images in extreme ultraviolet microscopy [163]. In both cases, successful phase recovery was demonstrated when the first Born approximation appears to be violated, highlighting the importance of the generalized linearization conditions derived in Chapters 3 and 4.

In general, the primary benefit of using defocus is experimental simplicity. There may, however, be applications for which the use of alternative contrast modalities in microscopy is desirable. In any case, the pros and cons associated with POTF recovery based on various forms of contrast is not well-studied in the literature. *Therefore, it is proposed to verify the applicability of POTF recovery to various contrast modalities in microscopy and characterize their strengths and weaknesses via both simulation studies and experimental measurements.*

An example simulating quantitative phase recovery from differential interference contrast (DIC) micrographs is shown in Fig. 8.7.

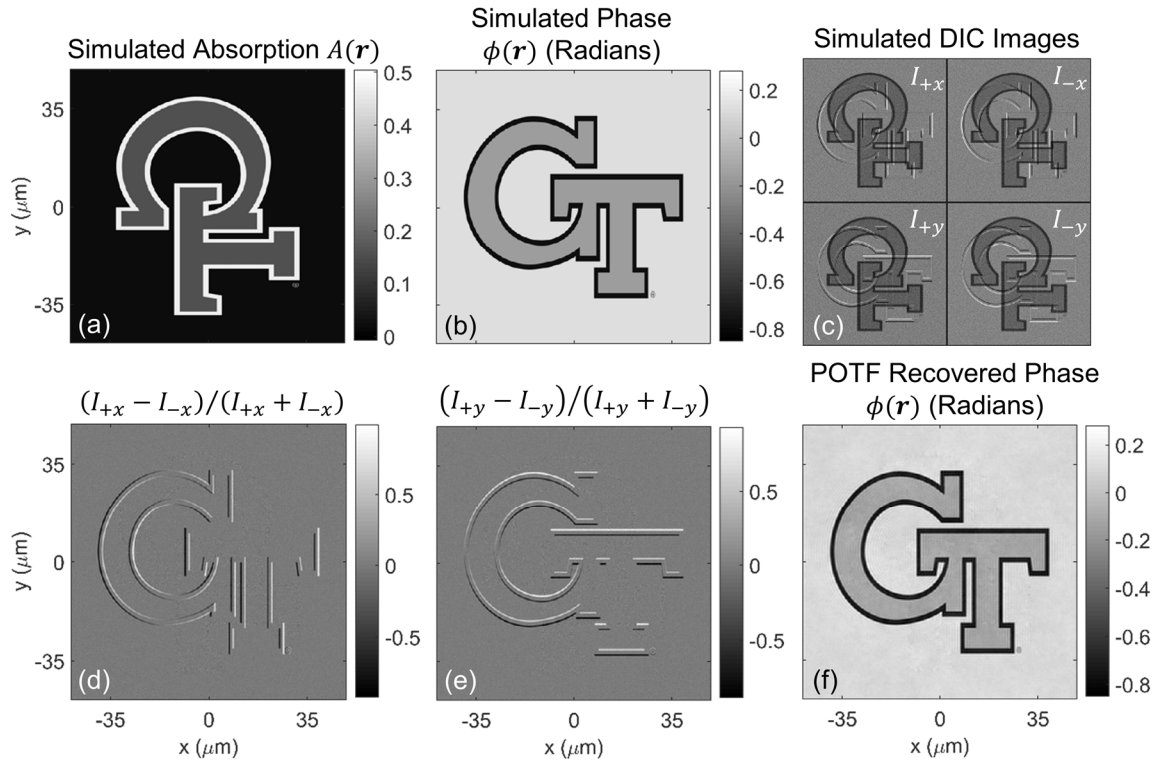


Figure 8.7: Simulation demonstrating phase optical transfer function (POTF) recovery based on differential interference contrast (DIC) microscopy. (a) Simulated absorption. (b) Simulated phase. (c) Resulting DIC images for a shear value of $2\Delta_{DIC} = 0.49 \mu\text{m}$ and bias value of $\Phi = \pi/4$, where shear was calculated in $+x$ (top-left), $-x$ (top-right), $+y$ (bottom-left), and $-y$ (bottom-right) directions. (d,e) Normalized images designed to be roughly proportional to the phase gradient in the (d) x as well as (e) y directions. (f) POTF recovered phase image showing good agreement with (b). In all images, $NA_c = 0.2$, $NA_o = 0.75$, and $\bar{\lambda} = 546 \text{ nm}$. A relatively large amount of image noise, $\sigma = 0.04$, was added to (c) prior to phase recovery.

The complex object defined by the absorption shown in Fig. 8.7(a) and the phase defined in Fig. 8.7(b) produces the four intensity images shown for $\pm x$ and $\pm y$ shear ($2\Delta_{DIC} = 0.49 \mu\text{m}$, Δ_{DIC} is the shear magnitude) and a DIC bias value of $\Phi = \pi/4$ in Fig. 8.7(c). In the images shown in Fig. 8.7(c), partially coherent image calculations have been performed via the Abbe method as in Chapter 3 [185]. Following the approach given in [121], phase contrast can be isolated in each orthogonal direction by subtracting images recorded with opposite shear directions (in [121] opposing source hemispheres are used) and normalizing the result with the in-focus bright-field image estimated by their respective addition. The resulting images are shown in Figs. 8.7(d) and 8.7(e). In this case effective POTFs, which are approximately linear and imaginary near the spatial frequency origin, are formed corresponding to quantitative phase gradient measurements in both x and y directions. Estimating phase via optimized inversion of these POTFs results in the phase shown in Fig. 8.7(f).

In the simulations, additive white Gaussian noise with a standard deviation of 4% of the background intensity ($\sigma = 0.04$, as opposed to $\sigma = 0.01$ used in Chapter 3) was added to emphasize the potential noise suppression in this form of phase recovery. In addition to enhanced noise suppression, the result of direct POTF recovery based on DIC appears to be more resilient to object absorption than defocus-based POTF recovery. Although the results indicate that POTF recovery based on DIC has desirable characteristics in comparison with defocus, it should also be recognized that the precise calibration and manipulation of DIC shear is non-trivial [271]. Also, this form of recovery would require the addition of specialized hardware for automated shear rotation such as the solutions offered by other quantitative DIC approaches in the literature [272].

8.2.3 Characterization

Another potential area for improvement of defocus-based POTF recovery is in the method for selecting the defocus distances, which in Chapter 3 is simply done via trial

and error/inspection of the POTFs. Jingshan *et al.* showed in [171] an efficient exponentially spaced defocus sampling scheme based on the assumption of spatial coherence. Falaggis *et al.* demonstrated an optimum plane selection method in which the distances form a geometric series that maximizes the range of spatial frequencies using a minimum number of planes in POTF recovery also assuming spatial coherence [174]. What is missing is a defocus sampling scheme which is optimized in consideration of the level of partial spatial coherence used. The problem is to select the optimum defocus distances given a finite number of planes and extended source distribution which minimizes mean squared error in the recovered phase. ***It is therefore proposed to characterize the effects of various defocus sampling schemes in the literature and provide an optimization in consideration of Köhler illuminated microscopy.***

In x-ray phase contrast imaging [212], spatially coherent POTF recovery (referred to as CTF phase recovery in this field) is used in which only forward scattered defocus planes are available, as opposed to the symmetrically defocused planes utilized in Chapter 3. For this case, it is possible to show that the optimal phase spectrum is given by Eq. (15) in the development given by Zabler *et al.* [273]. Of interest here is the performance of this inversion when the POTFs and AOTFs in Eq. 15 of [273] are replaced by their partially coherent equivalents. Figure 8.8 shows an example of simulated phase recovery in such a scenario, where three forward defocused distances were used ($z = \pm 0.6, 3, \text{ and } 9 \mu\text{m}$) and Gaussian noise at 1% of the background intensity ($\sigma = 0.01$) was added. Although slightly more sensitive to noise than recovery based on symmetric defocus planes, phase recovery from forward scattered planes only with partially coherent illumination appears to be viable. This is of great importance in x-ray phase contrast imaging, since spatial coherence is generally thought to be a required [118]. However, in the x-ray regime, spatially coherent sources are a great deal more expensive and bulky than partially coherent tabletop tube sources [274]. Using forward scattered planes only may also help to reduce the total number of defocused images

required, thereby increasing measurement speed. For these reasons, *it is proposed to characterize the retrieval of phase from single-sided defocus under partially coherent illumination.*

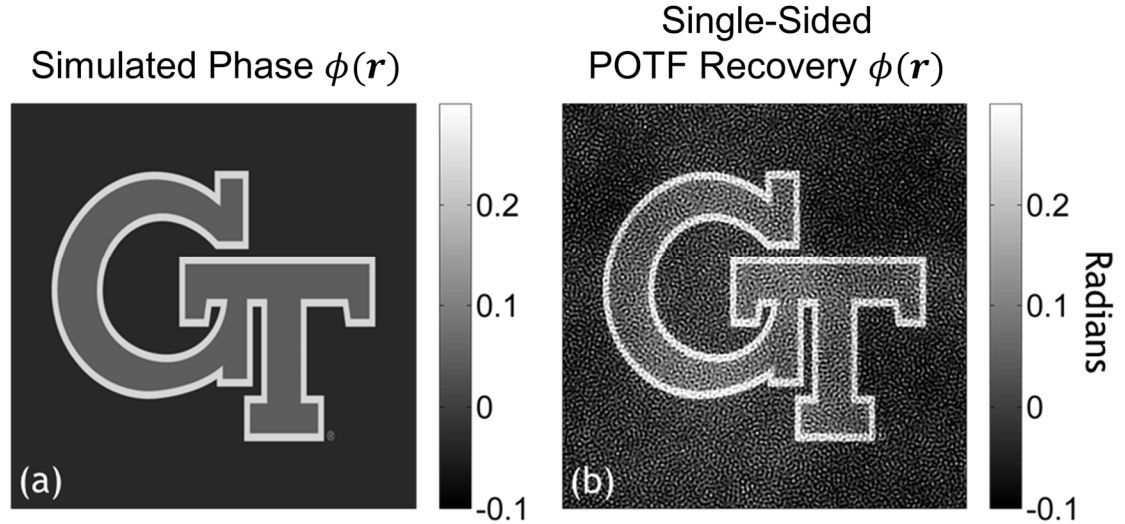


Figure 8.8: (a) Simulated phase object, (b) POTF recovered phase from three forward defocus planes ($z = \pm 0.6, 3, \text{ and } 9 \mu\text{m}$) with 1% additive noise ($\sigma = 0.01$). ($\bar{\lambda} = 546 \text{ nm}$, $NA_c = 0.375$, $NA_o = 0.75$).

8.2.4 Application

One of the most prominent application areas for 2D QPI is the automated extraction of quantitative metrics (i.e. dry mass content, area, thickness, volume etc.) from time-lapse phase imagery of live adherent cell cultures [131, 148]. It is well-known that cellular dry mass content can be obtained [197] via integration of the projected phase image according to

$$\text{Dry Mass} = \int \frac{\bar{\lambda}\phi}{2\pi\gamma} dx dy, \quad (8.10)$$

in which $\gamma \sim 0.2 \text{ ml/g}$ to within $\pm 10\%$ [197] and the distances $\bar{\lambda}$, dx , and dy are given in cm. In order to extract these metrics it is necessary to perform cell segmentation in order to determine the projected area of each cell in the FOV. Since the quantitative phase image is roughly proportional to the actual cell thickness, it provides a better basis for

image segmentation algorithms than qualitative methods such as phase contrast or DIC [131]. *It is therefore proposed to apply POTF recovered phase data to the automated extraction of quantitative metrics from live cell cultures by developing image segmentation procedures which are tailored specifically.* This application/demonstration will be critical for establishing POTF recovery using commercial microscopy as a simple path towards automated morphological data from live cell cultures within the biomedical community without any additional hardware.

8.3 Tomographic Deconvolution Phase Microscopy

8.3.1 Development

The development given in Chapter 4 describes tomographic deconvolution phase microscopy (TDPM) as the analogue to similar methods which have been developed for 3D fluorescence microscopy which rely on the fusion of data extracted from multiple through-focal series acquired over equiangular object orientations [206]. In addition to TDPM with explicit object rotation, it should also be possible to recover the “missing cone” of spatial frequencies using iterative constraint algorithms developed for regularized solutions to the limited-angle tomography problem [61]. Within such, error is reduced by enforcing positivity and support constraints as well as congruency with measured data.

In Fig. 8.9, preliminary simulation results of this algorithm are shown. Diffracted intensities due to eight spheres of varying refractive index [Fig. 8.9(a)] are generated using the angular spectrum method [184] and a coherent mode representation of partial coherence [122]. Deconvolution by the system point spread function, i.e. the inverse Fourier transfer of the 3D POTF, is followed by the aforementioned iterative constraint algorithm requiring positivity and known object support. Figures 8.9(b) through 8.9(e) show simulated and recovered indices along planes perpendicular, 8.9(b) and 8.9(c), and parallel, 8.9(d) and 8.9(e), to the optic or z-axis.

As expected, recovery is much better perpendicular to the z -axis where there is less missing frequency information. Currently, recovery is quite poor parallel to the z -axis indicating the need for stronger constraints and a more sophisticated implementation, which may potentially include regularized edge preservation or total variation minimization [67]. *Therefore, it is proposed to develop and improve the application of iterative recovery algorithms to TDPM for thick objects under a single illumination angle.* Such an algorithm might appropriately be called deconvolution phase microscopy (DPM) since the meaning of “tomographic” in (TDPM) would no longer be applicable. Such improvements would enable high-speed 3D QPI using commercial microscopy without any additional hardware or modification and are thus of high interest for widespread biomedical application.

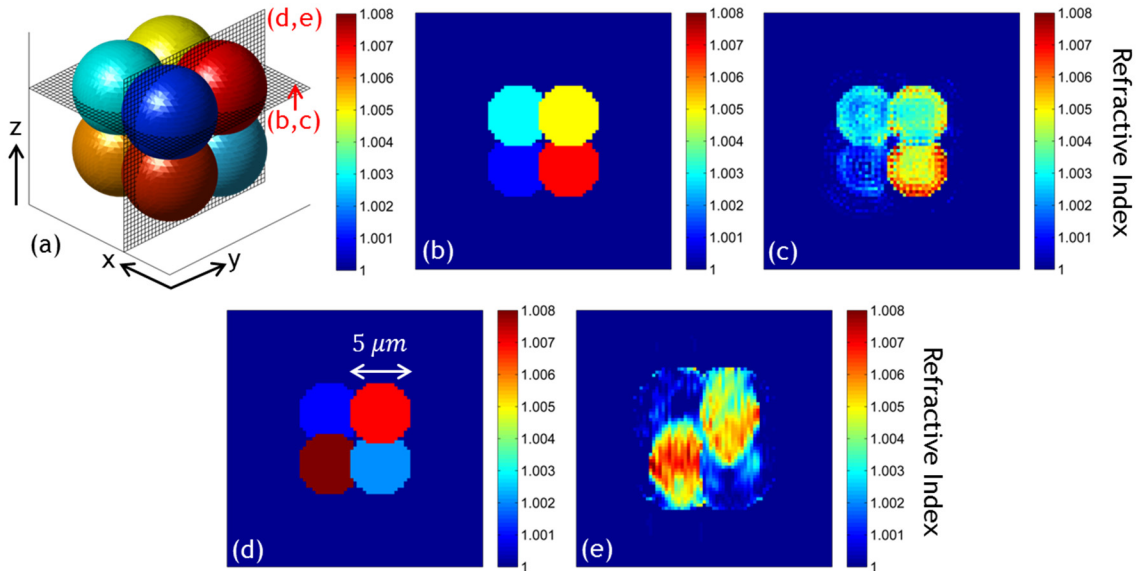


Figure 8.9: The effect of iterative constraint algorithms [Sung_2009] on tomographic deconvolution phase microscopy (TDPM) refractive index (RI) data. (a) Eight spheres ($5 \mu\text{m}$ diameter) of indices $1.001:0.001:1.008$ in vacuum, (b) Top-view slice of simulated RI, (c) Top-view slice recovered RI, (d) Side-view slice of simulated RI, (e) Side-view slice recovered RI.

Another potential area of great interest in TDPM is the application of nonlinear error reduction algorithms similar to those proposed for both MFPI-PC and POTF recovery.

The central idea is to estimate and remove the nonlinear portion of the measured

intensities based on a prior estimate of the object [265]. In the case of TDPM, 3D refractive index (RI) is first estimated using the approach provided in Chapter 4, and then the nonlinear portion of the measured intensities are estimated via the modified SS-BPM outlined in the same chapter [193]. Such an algorithm could enable 3D QPI for objects with RI contrast too high for satisfactory recovery in the direct solution alone. *It is therefore proposed to develop a nonlinear error reduction algorithm for use with TDPM.*

8.3.2 Verification

In Section 4.4, TDPM is demonstrated using a variety of optical fibers as control samples for the purpose of verification. In order to test TDPM for applications in biology, *it is proposed to implement TDPM on cells fixed within a glass capillary as an initial demonstration.* Such capillaries are commercially available with similar dimensions as optical fibers and thus the procedure outlined in Chapter 4 can be duplicated with little variation. Figure 8.10 shows the proposed sample configuration with the rotatable glass capillary used for sample fixation under Köhler illumination.

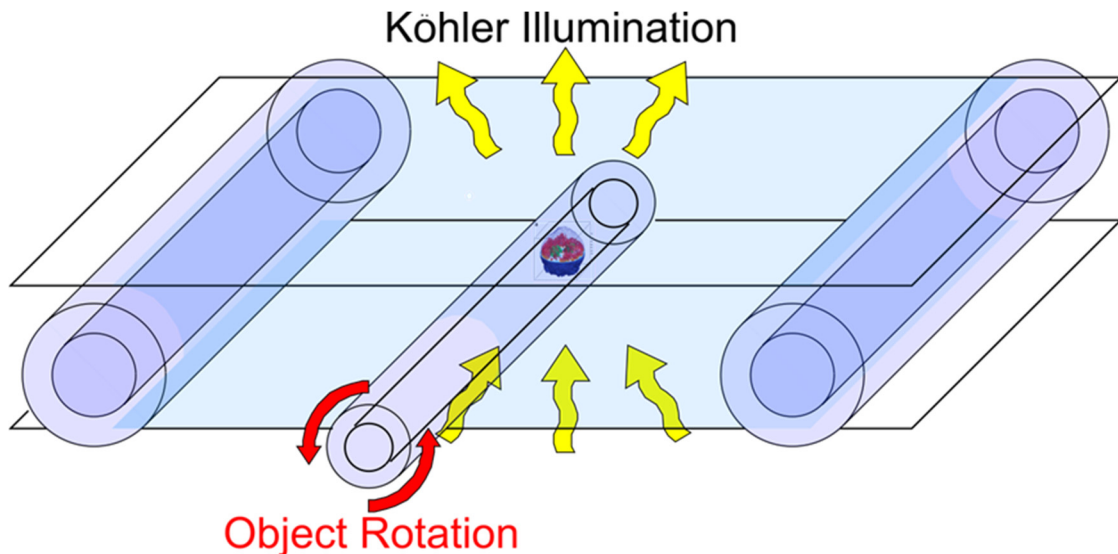


Figure 8.10: Sample configuration for fixed cell tomographic deconvolution phase microscopy (TDPM) measurement. A biological sample is fixed inside a hollow glass capillary using a synthetic resin mounting media (DPX), which is then illuminated and rotated between microscope slide and coverslip separated by two coated optical fibers.

During cell fixation via dehydration in an organic solvent, the cells die and dehydrate, leaving only proteins and lipids behind. Such material should have a RI of ~ 1.55 [216] and thus it is suggested to utilize capillaries made soda-lime or borosilicate glass to minimize capillary-induced aberrations. To fix the cell inside the capillary, a synthetic resin mounting media, such as DPX (distyrene, plasticizer, and xylene), could be used to match the refractive index of the dehydrated cells.

Another important area in which TDPM needs to be verified is its applicability to reconstructing phase in weakly absorbing objects as all of the results presented in Chapter 4 assume a pure phase object. In the case of a general object with both phase and absorption components, Streibl predicted that both should be recoverable if measurements from two different pupil functions are combined [66]. In the case of TDPM, this could be realized by subtracting measurements from equal and opposite illumination directions since absorption and phase contrast are symmetric and anti-symmetric respectively. Ultimately the performance of such an approach will depend on a variety of factors, many of which will only be verifiable via experiment. *It is therefore proposed to investigate the reconstruction of complex objects via simulation and experimentation.* Potential test objects may include doped fibers or red blood cells illuminated near their respective absorption bands.

8.3.3 Characterization

One undeveloped degree of freedom in all three QPI methods outlined in this thesis is the shape of the illumination pupil function $S(\rho')$. In particular, microscopes condensers are often outfitted with annular diaphragms designed for use with phase contrast objectives. If used in bright-field, however, annular illumination may be advantageous compared to circular diaphragms.

Figure 8.11 highlights differences in imaging properties for 2D and 3D QPI using circular vs. annular illumination. In Fig. 8.11(a), it is seen that the 2D overall contrast

spectrum, given by the square root of the sum of the squares of the POTFs, differs between the two forms of illumination, with annular illumination having more contrast in both mid- and upper-range spatial frequencies. Likewise, Fig. 8.11(b) and 8.11(c) show the overall contrast available as a function of 3D spatial frequency and indicate that annular illumination may provide improved contrast for use with TDPM. In order to exploit these favorable properties, *it is proposed to characterize the use of annular illumination in all three QPI methods using simulation and experiment.*

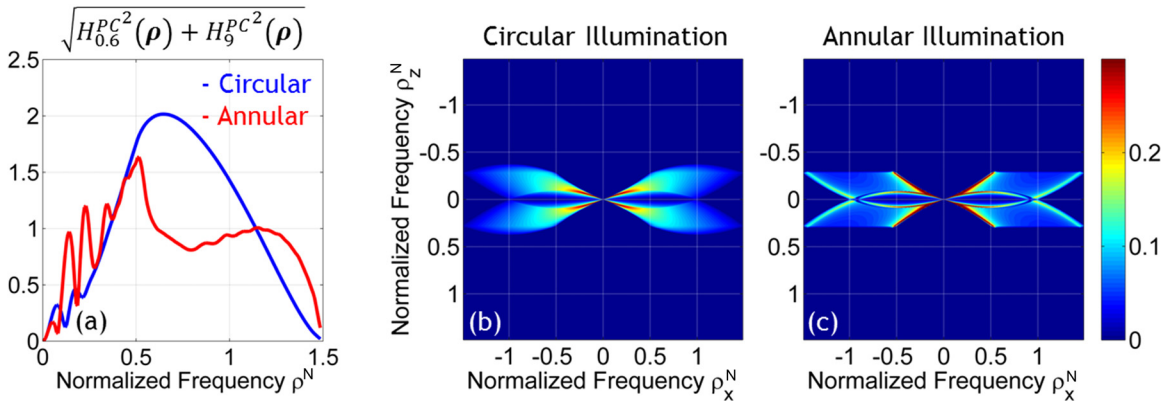


Figure 8.11: (a) Overall POTF recovery contrast spectrum for circular ($NA_c = 0.375$) and annular (outer radius $NA_c^{out} = 0.375$, inner radius $NA_c^{in} = 0.3375$) illumination with two defocus distances ($z = \pm 0.6 \mu\text{m}$ and $\pm 9 \mu\text{m}$). The overall 3D TDPM contrast spectrum, i.e. the absolute value of the 3D POTF, for (b) circular and (c) annular illumination [same radii as in (a)] are also shown. In all figures, $NA_o = 0.75$ and $\bar{\lambda} = 546 \text{ nm}$. In all figures, $\rho^N = \rho\bar{\lambda}/NA_o$.

8.3.4 Application

Pending the successful verification of TDPM on fixed cells, the next logical step for biological application is time-lapse 3D QPI of live cells cultured in glass capillaries [191]. In [191], it was shown that object-rotation-based tomography on living cell cultures is possible via a fiber capillary which was also used for cell cultivation in addition to its primary mechanical function of uniaxial rotation. Utilizing the results of such groundbreaking studies, *it is proposed to apply the improvements offered by TDPM*, i.e. experimental simplicity and improved spatial resolution, *to 3D QPI of live*

cell cultures, in which TDPM measurements may be acquired every 30 minutes or so in a time-lapse series.

Another biological application involves high-speed 3D QPI, which has remained challenging for even the most sophisticated approaches and has only recently been enabled [218]. In [218], for example, a 3D RI image update rate of 1.3 seconds was achieved over a $96 \times 96 \times 96$ voxel FOV. Experimentally, deconvolution phase microscopy (DPM), which is the single-angled version of TDPM proposed in Section 8.3.1, may possess speed advantages over optical diffraction tomography (ODT) since focus, rather than the illuminating beam angle, is the scanned quantity. *It is therefore proposed to develop software, similar to the proposed improvements for real-time POTF recovery proposed in Section 8.2.1, for automating the acquisition of through-focal series in parallel with the DPM reconstruction associated with the previous iteration for real-time display.* Such a system would undoubtedly find application in biology and biomedicine, where real-time 3D QPI is still in its infancy at the forefront of research.

8.4 Long-Period Fiber Grating Applications

As alluded to in the introduction, the application of QPI and quantitative retardation imaging (QRI) to LPFG characterization and modeling are perhaps the most interesting and useful among the fiber characterization applications mentioned in this thesis. This is in part because: (1) the primary causes for grating formation in certain LPFGs are not well understood, and (2) LPFG research has been largely conducted in an empirical manner based on observed changes in the transmission spectra owing to the trial and error of various fabrication methods and parameters.

The field would therefore benefit greatly from the development of numerical modeling tools which can predict LPFG transmission spectra based on arbitrary 3D RI variations within a single LPFG period. Such tools may be utilized for design or

modeling of real device performance based on measured RI and residual stress (RS) data. Therefore, *it is proposed to characterize RI/RS effects in arc-induced LPFGs* (predictions of which have been controversial in the literature [23]) *and to develop modeling tools with the aforementioned capabilities.*

8.4.1 Characterization of Arc-Induced Long-Period Fiber Gratings

Preliminary measurements of RI and RS in single-mode fibers which have been exposed to weak electric arc discharges (parameterized by arc current and discharge duration) in commercial fusion splicers indicate two potential sources for RI modulation in arc-induced LPFGs, namely the relaxation of mechanical stresses in the core and frozen-in viscoelasticity (FIV) in the cladding. When the electric arc discharge parameters approach and exceed those used in conventional single-mode fiber splicing (~ 18 mA for ~ 1 second), both of these effects approach saturation in which no additional modulation is obtained with higher currents/durations. The axial extent of these perturbations, which may e.g. be characterized by full width at half maximum, has been measured to be on the order of mm and is therefore thought to preclude the possibility of LPFG formation, whose periods are typically less than ~ 700 μm .

These measurements, however, have been conducted on fusion splices and, to our knowledge, the magnitude and axial extent of these perturbations at less than saturation has not been published. Shown in Fig. 8.12 are preliminary measurements demonstrating the possibility of LPFG formation based on the relaxation of mechanical stresses within the core. The RS profile reconstructions are based on an assumption of axial symmetry.

In Fig. 8.12(a) the progression of RS changes from unperturbed to an arc current of 24 mA at an arc duration of 0.1 seconds is measured. Corresponding curves for 2-10 mA are not shown because there was no observable change. In Fig. 8.12(b), the axial variation of core stress between two adjacent arc discharges (15 mA, 0.1 seconds) which are separated by ~ 544 μm is shown. The results provide evidence that core RS modification could play a major role in weak arc-induced LPFGs as the axial stress

modulation magnitude of $\Delta\sigma_z \sim 7.5$ MPa corresponds approximately to a RI modulation magnitude of $\Delta n \sim 3.2 \times 10^{-5}$ assuming a stress-optic constant of $C_2 = -4.22 \times 10^{-6}$, which is only slightly less than the range normally used for modeling LPFG transmission spectra using coupled mode theory (CMT) [110].

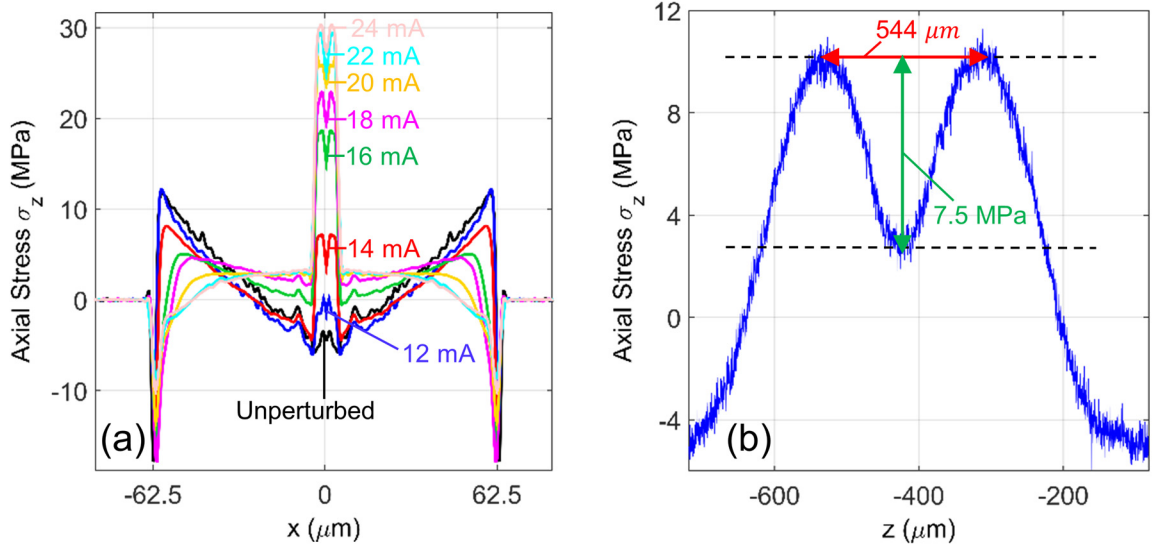


Figure 8.12: (a) Progression of axial residual stress (RS) modification in *Corning SMF-28* fiber exposed to electric arc currents ranging from 0 to 24 mA for 0.1 seconds. (b) Axial variation of mean core RS between two electric arc discharges written with a current of 15 mA for 0.1 seconds.

Until now, measuring the RI index changes in the cladding due to the relaxation of FIV using quantitative phase microscopy (QPM) based on the TIE [31] has been difficult, although possible as evidenced by the results in Fig. 6.5, because the phase images measured via QPM are extremely sensitive to noise. While random image noise can be offset by using a larger defocus distance, non-random noise sources, such as non-repeatability in the background phase subtraction from measurement to measurement, have been especially limiting in quantifying axial RI variations on the order of 1×10^{-4} . TDPM, on the other hand, is based on the 3D deconvolution of through-focal series and registration over many angular views. Although the RI resolution of $\sim 7.7 \times 10^{-5}$ specified in Chapter 4 is higher the value of 2.34×10^{-5} specified by Hutsel *et al.* [31], it has been observed that the measurements are much more repeatable, which has been the limiting

factor thus far. *Therefore, it is proposed to use the joint combination of TDPM and the Brace-Köhler compensator technique to characterize RI/RS effects in weak arc-induced LPFGs. It is also proposed to use CMT to model and optimize future LPFGs based on these mechanisms*, assuming that the RI modulations measured in the core (due to RS changes) and cladding (due to FIV) can be approximated as uniform in cross section and sinusoidal along the fiber axis.

8.4.2 Modeling of Measured Refractive Index/Residual Stress Data

Once RI is measured over a single LPFG period, it would be invaluable to have an accurate numerical modeling tool which could estimate the transmission spectrum based on the measurements. One might naïvely assume that a SS-BPM [103] would be sufficient. While this may be true in some cases, in many others, e.g. when the RI difference between the cladding and the surrounding material is large, the discrepancies between the outputs of CMT and SS-BPM will be significant, as is shown in Fig. 8.13.

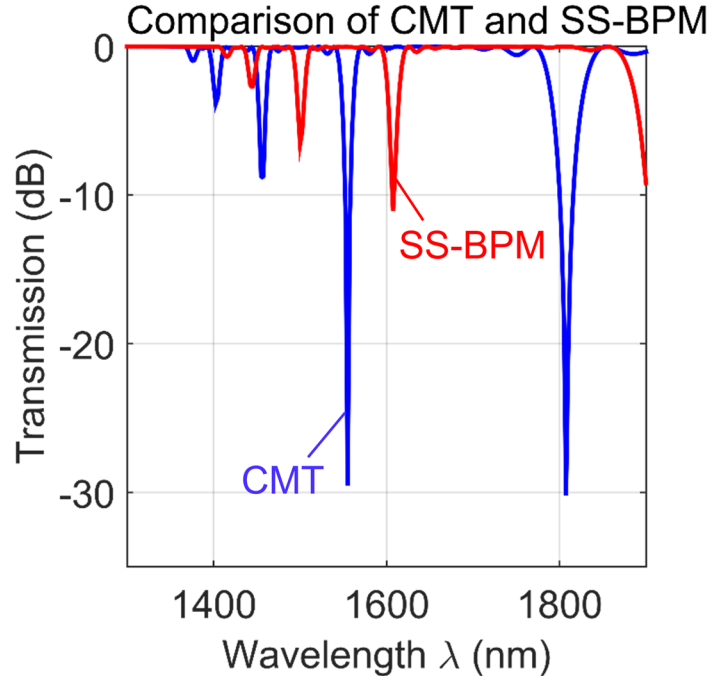


Figure 8.13: Transmission spectra modeled using coupled mode theory (CMT) (blue) and a split-step beam propagation method (SS-BPM) (red). It is believed that the discrepancy, which manifests here as a red-shift and a reduction of transmission depth, is due to inaccuracy of the weak RI contrast assumption in the SS-BPM.

In Fig. 8.13, the spectrum plotted in Fig. 10(b) of [110] is reproduced in blue using CMT and the LPFG parameters outlined therein. Also plotted in Fig. 8.13 is a spectrum modelled using a wide-angle SS-BPM [103] (shown in red) and based on the same uniform LPFG structure outlined in [110]. In the case of the SS-BPM, the simulation was initialized with the fundamental core mode in the unperturbed fiber and allowed to propagate through entire LPFG structure, after which the overlap integral [99] was used to calculate the energy percentage remaining in the fundamental mode. It is believed that the discrepancies between the two curves owes primarily to assumption of weak RI contrast inherent in the SS-BPM [103], which is inaccurate for this particular device since the LPFG is surrounded by air.

It is therefore proposed to develop the modified SS-BPM outlined in Chapter 4, which is there shown to produce better agreement with rigorous solutions due to its accounting for the obliquity factor in the refractive step, *for this application*. Although the use of a SS-BPM is more straightforward, it may be necessary to develop more rigorous modeling tools, such as those based on eigenmode expansion [104], for application with LPFGs as has been recently shown in [275].

CHAPTER 9

CONCLUDING REMARKS

The methods presented in this thesis directly enable quantitative phase imaging (QPI) using standard microscope platforms which are ubiquitous in biomedical laboratories. This brings QPI, as a technology, much closer to its primary end user and potentially allows QPI to be added as another modality in microscopy, like fluorescence or phase contrast, thereby diversifying the imaging portfolio of the biologist or practitioner, who are generally non-experts in optics.

In addition to their enabling features, the methods described herein have desirable traits not possessed by their conventional interferometric/holographic counterparts, such as enhanced spatial resolution due to the use of partial spatial coherence and inherent stability due to the use of white light sources and common-path imaging inherent in microscopy. The use commercial microscopes also implies good imaging quality benefitting from centuries of optical engineering as opposed to stand-alone custom QPI configurations.

In applying QPI and related methods to the characterization of refractive index and residual stress in large-mode-area erbium- and ytterbium-doped fibers (LMA EDFs and YDFs) it has been observed that the effects of manufacturing, cleaving, and splicing play significant roles in device operation, both mechanical and optical. In designing future LMA EDFs and YDFs for use with fiber-based lasers and amplifiers, consideration of the effects characterized in Chapters 5 and 6 will become critical to achieving LMAs larger than the current state-of-the-art.

All in all, the results presented herein have the potential to be transformative in the fields of QPI and optical fiber characterization. The future directions outlined in Chapter 8 will therefore be critical towards their eventual success and adoption.

APPENDIX A

DERIVATION OF GENERALIZED LINEARIZATION CONDITIONS FOR PHASE OPTICAL TRANSFER FUNCTION RECOVERY

In what follows the generalized linearization conditions [Eqs. (3.20) and (3.21)] for direct object recovery from the two-dimensional weak object transfer function (2D WOTF) [Eq. (3.14)] are derived.

Let us write an expression for the total normalized complex wave field at the image plane as

$$u^{im}(\mathbf{r}, \boldsymbol{\rho}') = h(\mathbf{r}) * \{u_0(\mathbf{r}, \boldsymbol{\rho}') \exp[\psi(\mathbf{r})]\}, \quad (\text{A.1})$$

in which $u^{im}(\mathbf{r}, \boldsymbol{\rho}')$ is the wave field at the image plane normalized to unit amplitude/intensity, $h(\mathbf{r}) = \mathcal{F}^{-1}[P(\boldsymbol{\rho})]$ is the coherent point spread function describing the transfer from object to image plane, $u_0(\mathbf{r}, \boldsymbol{\rho}') = \sqrt{S(\boldsymbol{\rho}')} \exp(i2\pi\boldsymbol{\rho}' \cdot \mathbf{r})$ is the normalized incident field at the object plane corresponding to the off-axis point source $\boldsymbol{\rho}'$, and $\psi(\mathbf{r})$ is the complex scattered phase comprised of both absorption and phase as given in Section 3.2.2. If the first-order Rytov approximation is assumed to be valid, Eq. (A.1) may be approximated as

$$u_R^{im}(\mathbf{r}, \boldsymbol{\rho}') = u_0^{im}(\mathbf{r}, \boldsymbol{\rho}') \exp[\psi_R^{im}(\mathbf{r}, \boldsymbol{\rho}')], \quad (\text{A.2})$$

in which $u_R^{im}(\mathbf{r}, \boldsymbol{\rho}')$ is the first-order Rytov approximation for the normalized wave field at the image plane, $u_0^{im}(\mathbf{r}, \boldsymbol{\rho}') = h(\mathbf{r}) * u_0(\mathbf{r}, \boldsymbol{\rho}')$ is the normalized incident field at the image plane, and $\psi_R^{im}(\mathbf{r}, \boldsymbol{\rho}') = u_B^{im}(\mathbf{r}, \boldsymbol{\rho}') / u_0^{im}(\mathbf{r}, \boldsymbol{\rho}')$ is the first-order Rytov approximation for the complex scattered phase at the image plane for which $u_B^{im}(\mathbf{r}, \boldsymbol{\rho}') = h(\mathbf{r}) * u_0(\mathbf{r}, \boldsymbol{\rho}') \psi(\mathbf{r})$ is the first-order Born approximation for the normalized scattered wave field at the image plane.

Under this approximation, the normalized intensity at the image plane can be expressed as

$$I_R^{im}(\mathbf{r}, \boldsymbol{\rho}') = |u_0^{im}(\mathbf{r}, \boldsymbol{\rho}')|^2 \exp\{2\text{Re}[\psi_R^{im}(\mathbf{r}, \boldsymbol{\rho}')]\}, \quad (\text{A.3})$$

in which $I_R^{im}(\mathbf{r}, \boldsymbol{\rho}')$ is the normalized intensity at the image plane under the first-order Rytov approximation. By the sifting property of the delta function, the Fourier transform of $u_0^{im}(\mathbf{r}, \boldsymbol{\rho}')$ may be written as

$$u_0^{im}(\boldsymbol{\rho}, \boldsymbol{\rho}') = P(\boldsymbol{\rho}')\sqrt{S(\boldsymbol{\rho}')}\delta(\boldsymbol{\rho} - \boldsymbol{\rho}'), \quad (\text{A.4})$$

so that in real space $u_0^{im}(\mathbf{r}, \boldsymbol{\rho}') = P(\boldsymbol{\rho}')u_0(\mathbf{r}, \boldsymbol{\rho}')$. Since the Fourier transform of $u_B^{im}(\mathbf{r}, \boldsymbol{\rho}')$ is given by

$$u_B^{im}(\boldsymbol{\rho}, \boldsymbol{\rho}') = P(\boldsymbol{\rho})\sqrt{S(\boldsymbol{\rho}')}\psi(\boldsymbol{\rho} - \boldsymbol{\rho}'), \quad (\text{A.5})$$

then the Fourier transform of $\psi_R^{im}(\mathbf{r}, \boldsymbol{\rho}')$ is given by

$$\psi_R^{im}(\boldsymbol{\rho}, \boldsymbol{\rho}') = \frac{P(\boldsymbol{\rho} + \boldsymbol{\rho}')}{P(\boldsymbol{\rho})}\psi(\boldsymbol{\rho}), \quad (\text{A.6})$$

so that Eq. (3.19) is derived.

In Eq. (3.19a), $\exp\{2\text{Re}[\psi_R^{im}(\mathbf{r}, \boldsymbol{\rho}')]\}$ may be expanded in a Taylor series so that

$$\exp\{2\text{Re}[\psi_R^{im}(\mathbf{r}, \boldsymbol{\rho}')]\} \approx 1 + 2\text{Re}[\psi_R^{im}(\mathbf{r}, \boldsymbol{\rho}')], \quad (\text{A.7})$$

on the condition that

$$|2\text{Re}[\psi_R^{im}(\mathbf{r}, \boldsymbol{\rho}')]| \ll 1. \quad (\text{A.8})$$

Since $\psi(\boldsymbol{\rho}) = -A(\boldsymbol{\rho}) + i\phi(\boldsymbol{\rho})$, then the Fourier transform of $2\text{Re}[\psi_R^{im}(\mathbf{r}, \boldsymbol{\rho}')]$ may be given as

$$\begin{aligned} \mathcal{F}\{2\text{Re}[\psi_R^{im}(\mathbf{r}, \boldsymbol{\rho}')]\} = & -\left[\frac{P(\boldsymbol{\rho} + \boldsymbol{\rho}')}{P(\boldsymbol{\rho}')} + \frac{P^*(\boldsymbol{\rho}' - \boldsymbol{\rho})}{P^*(\boldsymbol{\rho}')}\right]A(\boldsymbol{\rho}) \\ & + i\left[\frac{P(\boldsymbol{\rho} + \boldsymbol{\rho}')}{P(\boldsymbol{\rho}')} - \frac{P^*(\boldsymbol{\rho}' - \boldsymbol{\rho})}{P^*(\boldsymbol{\rho}')}\right]\phi(\boldsymbol{\rho}), \end{aligned} \quad (\text{A.9})$$

in which $P(\boldsymbol{\rho} + \boldsymbol{\rho}')/P(\boldsymbol{\rho}')$ is divided into Hermitian and anti-Hermitian parts in order to evaluate the real component. Careful inspection reveals that the two terms in Eq. (A.9) produce the second and third terms in the 2D WOTF [Eq. (3.14)], corresponding to the

amplitude and phase optical transfer functions respectively, upon evaluating the integral in Eq. (3.19a). Multiplying Eq. (A.9) by $|P(\boldsymbol{\rho}')|^2$ and taking the inverse Fourier transform demonstrates that Eqs. (3.20) and (3.21) in Section 3.2.2, in concert with the first-order Rytov approximation for the wave field at the image plane, are sufficient conditions for linearizing the WOTF.

REFERENCES

- [1] R. Yuste, "Fluorescence microscopy today," *Nat. Meth.*, vol. 2, pp. 902-904, Dec. 2005.
- [2] F. Zernike, "Phase contrast, a new method for the microscopic observation of transparent objects part II," *Physica*, vol. 9, pp. 974-986, Dec. 1942.
- [3] G. Nomarski and A. R. Weill, "Application a la metallographie des methodes interferentielles a deux ondes polarisees," *Rev. Metall.*, vol. 52, pp. 121-128, 1955.
- [4] R. Hoffman and L. Gross, "Modulation contrast microscope," *Appl. Opt.*, vol. 14, pp. 1169-1176, May 1, 1975.
- [5] K. G. Phillips, S. L. Jacques, and O. J. McCarty, "Measurement of single cell refractive index, dry mass, volume, and density using a transillumination microscope," *Phys. Rev. Lett.*, vol. 109, pp. 118105-1--118105-5, Sep. 14, 2012.
- [6] G. Popescu, *Quantitative Phase Imaging of Cells and Tissues*. New York: McGraw Hill Professional, 2011.
- [7] C. Zuo, Q. Chen, W. Qu, and A. Asundi, "High-speed transport-of-intensity phase microscopy with an electrically tunable lens," *Opt. Express*, vol. 21, pp. 24060-24075, Oct. 7, 2013.
- [8] W. F. Scherer, J. T. Syverton, and G. O. Gey, "Studies on the propagation in vitro of poliomyelitis viruses IV. Viral multiplication in a stable strain of human malignant epithelial cells (strain HeLa) derived from an epidermoid carcinoma of the cervix," *J. Exp. Med.*, vol. 97, pp. 695-710, May 1, 1953.
- [9] W. Choi, C. Fang-Yen, K. Badizadegan, S. Oh, N. Lue, R. R. Dasari, and M. S. Feld, "Tomographic phase microscopy," *Nat. Meth.*, vol. 4, pp. 717-719, Aug. 12, 2007.
- [10] P. Bon, S. Lécart, E. Fort, and S. Lévêque-Fort, "Fast label-free cytoskeletal network imaging in living mammalian cells," *Biophys. J.*, vol. 106, pp. 1588-1595, Apr. 15, 2014.
- [11] M. Mir, Z. Wang, Z. Shen, M. Bednarz, R. Bashir, I. Golding, S. G. Prasanth, and G. Popescu, "Optical measurement of cycle-dependent cell growth," *Proc. Nat. Acad. Sci.*, vol. 108, pp. 13124-13129, July 25, 2011.
- [12] Y. Park, C. A. Best, T. Auth, N. S. Gov, S. A. Safran, G. Popescu, S. Suresh, and M. S. Feld, "Metabolic remodeling of the human red blood cell membrane," *Proc. Nat. Acad. Sci.*, vol. 107, pp. 1289-1294, Jan. 26, 2010.

- [13] Y. Sung, W. Choi, N. Lue, R. R. Dasari, and Z. Yaqoob, "Stain-free quantification of chromosomes in live cells using regularized tomographic phase microscopy," *PLoS One*, vol. 7, p. e45902, Nov. 2012.
- [14] R. Wang, Z. Wang, L. Millet, M. U. Gillette, A. J. Levine, and G. Popescu, "Dispersion-relation phase spectroscopy of intracellular transport," *Opt. Express*, vol. 19, pp. 20571-20579, Oct. 10, 2011.
- [15] D. Claus, A. M. Maiden, F. Zhang, F. G. R. Sweeney, M. J. Humphry, H. Schluesener, and J. M. Rodenburg, "Quantitative phase contrast optimised cancerous cell differentiation via ptychography," *Opt. Express*, vol. 20, pp. 9911-9918, Apr. 16, 2012.
- [16] M. Hunter, V. Backman, G. Popescu, M. Kalashnikov, C. W. Boone, A. Wax, V. Gopal, K. Badizadegan, G. D. Stoner, and M. S. Feld, "Tissue self-affinity and polarized light scattering in the Born approximation: A new model for precancer detection," *Phys. Rev. Lett.*, vol. 97, pp. 138102-1--138102-4, Sep. 29, 2006.
- [17] M. Mir, Z. Wang, K. Tangella, and G. Popescu, "Diffraction phase cytometry: blood on a CD-ROM," *Opt. Express*, vol. 17, pp. 2579-2585, Feb. 16, 2009.
- [18] Z. Wang, K. Tangella, A. Balla, and G. Popescu, "Tissue refractive index as marker of disease," *J. Biomed. Opt.*, vol. 16, pp. 116017-1--116017-7, Nov. 2011.
- [19] C. L. Zheng, K. Scheerschmidt, H. Kirmse, I. Hausler, and W. Neumann, "Imaging of three-dimensional (Si, Ge) nanostructures by off-axis electron holography," *Ultramicroscopy*, vol. 124, pp. 108-116, Jan. 2013.
- [20] R. A. Gonsalves, "Phase Retrieval And Diversity In Adaptive Optics," *Opt. Eng.*, vol. 21, pp. 215829-215832, Sep./Oct. 1982.
- [21] S. Gasilov, A. Mittone, E. Brun, A. Bravin, S. Grandl, and P. Coan, "On the possibility of quantitative refractive-index tomography of large biomedical samples with hard X-rays," *Biomed. Opt. Express*, vol. 4, pp. 1512-1518, Aug. 2, 2013.
- [22] B. L. Bachim and T. K. Gaylord, "Microinterferometric optical phase tomography for measuring small, asymmetric refractive-index differences in the profiles of optical fibers and fiber devices," *Appl. Opt.*, vol. 44, pp. 316-327, Jan. 20, 2005.
- [23] G. Rego, P. Marques, J. Santos, and H. Salgado, "Arc-induced long-period gratings," *Fiber Integrated Opt.*, vol. 24, pp. 245-259, 2005.
- [24] Y. Wang, "Review of long period fiber gratings written by CO₂ laser," *J. Appl. Phys.*, vol. 108, pp. 081101-1--081101-18, Oct. 22, 2010.

- [25] B. H. Kim, Y. Park, T. J. Ahn, D. Y. Kim, B. H. Lee, Y. Chung, U. C. Paek, and W. T. Han, "Residual stress relaxation in the core of optical fiber by CO₂ laser irradiation," *Opt. Lett.*, vol. 26, pp. 1657-1659, Nov. 1, 2001.
- [26] A. Yablon, M. Yan, P. Wisk, F. DiMarcello, J. Fleming, W. Reed, E. Monberg, D. DiGiovanni, J. Jasapara, and M. Lines, "Refractive index perturbations in optical fibers resulting from frozen-in viscoelasticity," *Appl. Phys. Lett.*, vol. 84, pp. 19-21, Jan. 5, 2004.
- [27] G. Humbert and A. Malki, "Characterizations at very high temperature of electric arc-induced long-period fiber gratings," *Opt. Commun.*, vol. 208, pp. 329-335, Jul. 15, 2002.
- [28] S. G. Kosinski and A. M. Vengsarkar, "Splicer-based long-period fiber gratings," in *Optical Fiber Communication Conference and Exhibit*, 1998, pp. 278-279.
- [29] G. Kakarantzas, T. E. Dimmick, T. A. Birks, R. Le Roux, and P. S. J. Russell, "Miniature all-fiber devices based on CO₂ laser microstructuring of tapered fibers," *Opt. Lett.*, vol. 26, pp. 1137-1139, Aug. 1, 2001.
- [30] I. K. Hwang, S. H. Yun, and B. Y. Kim, "Long-period fiber gratings based on periodic microbends," *Opt. Lett.*, vol. 24, pp. 1263-1265, Sep. 15, 1999.
- [31] M. R. Hutsel and T. K. Gaylord, "Concurrent three-dimensional characterization of the refractive-index and residual-stress distributions in optical fibers," *Appl. Opt.*, vol. 51, pp. 5442-5452, Aug. 1, 2012.
- [32] S. Aknoun, P. Bon, J. Savatier, B. Wattellier, and S. Monneret, "Quantitative retardance imaging of biological samples using quadriwave lateral shearing interferometry," *Opt. Express*, vol. 23, pp. 16383-16406, Jun. 15, 2015.
- [33] M. W. Conklin, J. C. Eickhoff, K. M. Riching, C. A. Pehlke, K. W. Eliceiri, P. P. Provenzano, A. Friedl, and P. J. Keely, "Aligned collagen is a prognostic signature for survival in human breast carcinoma," *Am. J. Pathol.*, vol. 178, pp. 1221-1232, Mar. 3, 2011.
- [34] P. Bon, G. Maucort, B. Wattellier, and S. Monneret, "Quadriwave lateral shearing interferometry for quantitative phase microscopy of living cells," *Opt. Express*, vol. 17, pp. 13080-13094, Jul. 20, 2009.
- [35] M. R. Arnison, K. G. Larkin, C. J. R. Sheppard, N. I. Smith, and C. J. Cogswell, "Linear phase imaging using differential interference contrast microscopy," *J. Microsc.*, vol. 214, pp. 7-12, Apr. 1, 2004.
- [36] W. C. Warger Ii and C. A. DiMarzio, "Computational signal-to-noise ratio analysis for optical quadrature microscopy," *Opt. Express*, vol. 17, pp. 2400-2422, Feb. 16, 2009.

- [37] N. Lue, W. Choi, G. Popescu, T. Ikeda, R. R. Dasari, K. Badizadegan, and M. S. Feld, "Quantitative phase imaging of live cells using fast Fourier phase microscopy," *Appl. Opt.*, vol. 46, pp. 1836-1842, Apr. 1, 2007.
- [38] Z. Wang, L. Millet, M. Mir, H. Ding, S. Unarunotai, J. Rogers, M. U. Gillette, and G. Popescu, "Spatial light interference microscopy (SLIM)," *Opt. Express*, vol. 19, pp. 1016-1026, Jan. 17, 2011.
- [39] E. Sanchez-Ortiga, A. Doblaz, G. Saavedra, M. Martinez-Corral, and J. Garcia-Sucerquia, "Off-axis digital holographic microscopy: practical design parameters for operating at diffraction limit," *Appl. Opt.*, vol. 53, pp. 2058-2066, Apr. 1, 2014.
- [40] T. Ikeda, G. Popescu, R. R. Dasari, and M. S. Feld, "Hilbert phase microscopy for investigating fast dynamics in transparent systems," *Opt. Lett.*, vol. 30, pp. 1165-1167, May 15, 2005.
- [41] D. C. Ghiglia and M. D. Pritt, *Two-Dimensional Phase Unwrapping: Theory, Algorithms, and Software*: Wiley New York., 1998.
- [42] G. Popescu, T. Ikeda, R. R. Dasari, and M. S. Feld, "Diffraction phase microscopy for quantifying cell structure and dynamics," *Opt. Lett.*, vol. 31, pp. 775-777, Mar. 3, 2006.
- [43] B. Bhaduri, H. Pham, M. Mir, and G. Popescu, "Diffraction phase microscopy with white light," *Opt. Lett.*, vol. 37, pp. 1094-1096, Mar. 15, 2012.
- [44] J. R. Fienup, "Phase retrieval algorithms - a comparison," *Appl. Opt.*, vol. 21, pp. 2758-2769, Aug. 1, 1982.
- [45] L. J. Allen, W. McBride, N. L. O'Leary, and M. P. Oxley, "Exit wave reconstruction at atomic resolution," *Ultramicroscopy*, vol. 100, pp. 91-104, Jul. 2004.
- [46] M. R. Teague, "Deterministic phase retrieval: a Green's function solution," *J. Opt. Soc. Am.*, vol. 73, pp. 1434-1441, Nov. 1, 1983.
- [47] D. Paganin, A. Barty, P. J. McMahon, and K. A. Nugent, "Quantitative phase-amplitude microscopy. III. The effects of noise," *J. Microsc.*, vol. 214, pp. 51-61, Apr. 2004.
- [48] C. Zuo, Q. Chen, Y. Yu, and A. Asundi, "Transport-of-intensity phase imaging using Savitzky-Golay differentiation filter-theory and applications," *Opt. Express*, vol. 21, pp. 5346-5362, Mar. 11, 2013.
- [49] S. S. Kou, L. Waller, G. Barbastathis, P. Marquet, C. Depeursinge, and C. J. R. Sheppard, "Quantitative phase restoration by direct inversion using the optical transfer function," *Opt. Lett.*, vol. 36, pp. 2671-2673, Jul. 15, 2011.

- [50] J. P. Guigay, M. Langer, R. Boistel, and P. Cloetens, "Mixed transfer function and transport of intensity approach for phase retrieval in the Fresnel region," *Opt. Lett.*, vol. 32, pp. 1617-1619, Jun. 15, 2007.
- [51] M. Langer, P. Cloetens, J. P. Guigay, and F. Peyrin, "Quantitative comparison of direct phase retrieval algorithms in in-line phase tomography," *Med. Phys.*, vol. 35, pp. 4556-66, Sep. 18, 2008.
- [52] I. Yamaguchi and T. Zhang, "Phase-shifting digital holography," *Opt. Lett.*, vol. 22, pp. 1268-1270, Aug. 15, 1997.
- [53] U. Schnars and W. Jüptner, "Direct recording of holograms by a CCD target and numerical reconstruction," *Appl. Opt.*, vol. 33, pp. 179-181, Jan. 10, 1994.
- [54] E. D. Barone-Nugent, A. Barty, and K. A. Nugent, "Quantitative phase-amplitude microscopy I: Optical microscopy," *J. Microsc.*, vol. 206, pp. 194-203, Jun. 2002.
- [55] M. A. Choma, A. K. Ellerbee, C. Yang, T. L. Creazzo, and J. A. Izatt, "Spectral-domain phase microscopy," *Opt. Lett.*, vol. 30, pp. 1162-1164, May 15, 2005.
- [56] A. C. Kak and M. Slaney, *Principles of Computerized Tomographic Imaging*: Society for Industrial and Applied Mathematics, 2001.
- [57] F. Macias-Garza, K. R. Diller, and A. C. Bovik, "Missing cone of frequencies and low-pass distortion in three-dimensional microscopic images," *Opt. Eng.*, vol. 27, pp. 276461-276465, Jun. 1988.
- [58] B. P. Medoff, W. R. Brody, M. Nassi, and A. Macovski, "Iterative convolution backprojection algorithms for image reconstruction from limited data," *J. Opt. Soc. Am.*, vol. 73, pp. 1493-1500, Nov. 1, 1983.
- [59] A. J. Devaney, "A filtered back-projection algorithm for diffraction tomography," *Ultrasonic Imaging*, vol. 4, pp. 336-350, 1982.
- [60] S. X. Pan and A. C. Kak, "A computational study of reconstruction algorithms for diffraction tomography: Interpolation versus filtered backpropagation," *IEEE Trans. Acous. Speech Sig. Process.*, vol. 31, pp. 1262-1275, Oct. 1983.
- [61] Y. Sung, W. Choi, C. Fang-Yen, K. Badizadegan, R. R. Dasari, and M. S. Feld, "Optical diffraction tomography for high resolution live cell imaging," *Opt. Express*, vol. 17, pp. 266-277, Jan. 5, 2009.
- [62] G. Gbur and E. Wolf, "Relation between computed tomography and diffraction tomography," *J. Opt. Soc. Am. A*, vol. 18, pp. 2132-2137, Sep. 2001.
- [63] T. Kim, R. Zhou, M. Mir, S. D. Babacan, P. S. Carney, L. L. Goddard, and G. Popescu, "White-light diffraction tomography of unlabelled live cells," *Nat. Photon.*, vol. 8, pp. 256-263, Mar. 2014.

- [64] P. Bon, S. Aknoun, S. Monneret, and B. Wattellier, "Enhanced 3D spatial resolution in quantitative phase microscopy using spatially incoherent illumination," *Opt. Express*, vol. 22, pp. 8654-8671, Apr. 7, 2014.
- [65] P. Bon, S. Aknoun, J. Savatier, B. Wattellier, and S. Monneret, "Tomographic incoherent phase imaging, a diffraction tomography alternative for any white-light microscope," *Proc. SPIE*, vol. 8589, pp. 858918-1--858918-5, 2013.
- [66] N. Streibl, "Three-dimensional imaging by a microscope," *J. Opt. Soc. Am.*, vol. 2, pp. 121-127, Feb. 1, 1985.
- [67] J. Lim, K. Lee, K. H. Jin, S. Shin, S. Lee, Y. Park, and J. C. Ye, "Comparative study of iterative reconstruction algorithms for missing cone problems in optical diffraction tomography," *Opt. Express*, vol. 23, pp. 16933-16948, Jun. 29, 2015.
- [68] F. Charriere, E. Cucho, P. Marquet, and C. Depeursinge, "Biological cell (pollen grain) refractive index tomography with digital holographic microscopy," *Proc. SPIE*, vol. 6090, pp. 609008-1--609008-8, 2006.
- [69] F. Charriere, J. Kuhn, T. Colomb, E. Cucho, P. Marquet, and C. Depeursinge, "Sub-cellular quantitative optical diffraction tomography with digital holographic microscopy," *Proc. SPIE*, vol. 6441, pp. 64410K-1--64410K-6, 2007.
- [70] A. D. Yablon, "Advanced fiber characterization technologies for fiber lasers and amplifiers," in *Advanced Solid State Lasers*, Shanghai, 2014, p. ATh2A.45.
- [71] M. Young, "Optical fiber index profiles by the refracted-ray method (refracted near-field scanning)," *Appl. Opt.*, vol. 20, pp. 3415-3422, Oct. 1, 1981.
- [72] G. Summer, "A new technique for refractive index profile measurement in multimode optical fibres," *Opt. Quant. Electron.*, vol. 9, pp. 79-82, 1977.
- [73] A. D. Yablon, "Multifocus tomographic algorithm for measuring optically thick specimens," *Opt. Lett.*, vol. 38, pp. 4393-4396, Nov. 1, 2013.
- [74] M. Jenkins and T. K. Gaylord, "3D characterization of the refractive-index and residual-stress distributions in optical fibers," in *Frontiers in Optics*, 2012, p. FTh3C.2.
- [75] W. Gorski and W. Osten, "Tomographic imaging of photonic crystal fibers," *Opt. Lett.*, vol. 32, pp. 1977-1979, Jul. 15, 2007.
- [76] A. D. Yablon, "New transverse techniques for characterizing high-power optical fibers," *Opt. Eng.*, vol. 50, pp. 111603-1--111603-6, Nov. 2011.
- [77] A. D. Yablon, "Measuring the spatial distribution of rare-earth dopants in high-power optical fibers," *Proc. SPIE*, vol. 7914, pp. 79141N-1--79141N-8, 2011.

- [78] T. Feng, M. Jenkins, F. Yan, and T. K. Gaylord, "Joint residual stress and refractive index characterization of polarization-maintaining optical fibers," in *Frontiers in Optics*, 2013, p. FTu3A.34.
- [79] F. Just, M. Jager, and H. Bartelt, "The influence of the drawing process on the intrinsic stress in optical fibers and the arising possibility to optimize the birefringence of PM fibers," *Proc. SPIE*, vol. 8426, pp. 84260K-1--84260K-9, 2012.
- [80] P. Kniazewski, T. Kozacki, and M. Kujawinska, "Inspection of axial stress and refractive index distribution in polarization-maintaining fiber with tomographic methods," *Opt. Laser Eng.*, vol. 47, pp. 259-263, May 9, 2009.
- [81] N. M. Dragomir, X. M. Goh, and A. Roberts, "Three-dimensional quantitative phase imaging: Current and future perspectives," *Proc. SPIE*, vol. 6861, pp. 686106-1--686106-11, 2008.
- [82] X. M. Goh, S. S. Kou, B. P. Kouskousis, N. M. Dragomir, S. F. Collins, G. W. Baxter, and A. Roberts, "Non-destructive three-dimensional optical imaging of a fiber Bragg grating," *IEEE Photon. J.*, vol. 6, p. 6900207, Sep. 25, 2014.
- [83] X. M. Goh, N. M. Dragomir, D. N. Jamieson, A. Roberts, and D. X. Belton, "Optical tomographic reconstruction of ion beam induced refractive index changes in silica," *Appl. Phys. Lett.*, vol. 91, pp. 181102-1--181102-3, Oct. 29, 2007.
- [84] N. M. Dragomir, X. M. Goh, and A. Roberts, "Three-dimensional refractive index reconstruction with quantitative phase tomography," *Microsc. Res. Tech.*, vol. 71, pp. 5-10, Sep. 20, 2008.
- [85] G. Xiao Ming, N. Dragomir, and A. Roberts, "Axial stress changes in optical fibres on fusion splicing," in *Optical Internet, 2007 and the 2007 32nd Australian Conference on Optical Fibre Technology*, 2007, pp. 1-3.
- [86] A. D. Yablou and R. Bise, "Low-loss high-strength microstructured fiber fusion splices using GRIN fiber lenses," in *Optical Fiber Communication Conference*, 2004, p. MF14.
- [87] W. Shin, M. J. Han, U. C. Paek, D. Y. Kim, and K. Oh, "Longitudinal distribution of stress along the splice between dissimilar optical fibers," in *Optical Fiber Communication Conference*, 2004, p. MF7.
- [88] F. Abrishamian, N. Dragomir, and K. Morishita, "Refractive index profile changes caused by arc discharge in long-period fiber gratings fabricated by a point-by-point method," *Appl. Opt.*, vol. 51, pp. 8271-8276, Dec. 1, 2012.

- [89] F. Durr, G. Rego, P. Marques, S. L. Semjonov, E. M. Dianov, H. G. Limberger, and R. P. Salathe, "Tomographic stress profiling of arc-induced long-period fiber gratings," *J. Lightwave Technol.*, vol. 23, pp. 3947-3953, Nov. 2005.
- [90] B. Sévigny, M. Leduc, M. Faucher, N. Godbout, and S. Lacroix, "Characterization of the large index modification caused by electrical discharge in optical fibers," in *Lasers and Electro-Optics. Conference on Quantum Electronics and Laser Science*, 2009, pp. 2-4.
- [91] M. R. Hutsel and T. K. Gaylord, "Residual-stress relaxation and densification in CO₂-laser-induced long-period fiber gratings," *Appl. Opt.*, vol. 51, pp. 6179-6187, Sep. 1, 2012.
- [92] J. J. Koponen, H. J. Hoffman, and S. K. Tammela, "Measuring photodarkening from single-mode ytterbium doped silica fibers," *Opt. Express*, vol. 14, pp. 11539-11544, Nov. 27, 2006.
- [93] F. Just, H.-R. Müller, S. Unger, J. Kirchhof, V. Reichel, and H. Bartelt, "Ytterbium-doping related stresses in preforms for high-power fiber lasers," *J. Lightwave Technol.*, vol. 27, pp. 2111-2116, Jun. 15, 2009.
- [94] K. Lyytikainen, S. Huntington, A. Carter, P. McNamara, S. Fleming, J. Abramczyk, I. Kaplin, and G. Schötz, "Dopant diffusion during optical fibre drawing," *Opt. Express*, vol. 12, pp. 972-977, Mar. 22, 2004.
- [95] A. D. Yablon, "Optical and mechanical effects of frozen-in stresses and strains in optical fibers," *IEEE J. Sel. Top. Quant.*, vol. 10, pp. 300-311, Mar./Apr. 2004.
- [96] O. Schmidt, J. Rothhardt, T. Eidam, F. Röser, J. Limpert, A. Tünnermann, K. P. Hansen, C. Jakobsen, and J. Broeng, "Single-polarization ultra-large-mode-area Yb-doped photonic crystal fiber," *Opt. Express*, vol. 16, pp. 3918-3923, Mar. 17, 2008.
- [97] L. Fu, H. A. McKay, and L. Dong, "Extremely large mode area optical fibers formed by thermal stress," *Opt. Express*, vol. 17, pp. 11782-11793, Jun. 29, 2009.
- [98] T. Schreiber, H. Schultz, F. Röser, O. Schmidt, J. Limpert, R. Iliew, A. Petersson, C. Jacobsen, K. Hansen, and J. Broeng, "Design and high power operation of a stress-induced single-polarization single-transverse mode LMA Yb-doped photonic crystal fiber," in *Lasers and Applications in Science and Engineering*, 2006, pp. 61020C-1--61020C-9.
- [99] A. D. Yablon, *Optical Fiber Fusion Splicing* vol. 103: Springer Science & Business Media, 2005.
- [100] H. Y. Tam, "Simple fusion splicing technique for reducing splicing loss between standard singlemode fibres and erbium-doped fibre," *Electron. Lett.*, vol. 27, pp. 1597-1599, Aug. 15, 1991.

- [101] J. Luo, "Modeling dissimilar optical fiber splices with substantial diffusion," *J. Lightwave Technol.*, vol. 25, pp. 3575-3579, Nov. 2007.
- [102] D. D. Davis, T. K. Gaylord, E. N. Glytsis, S. G. Kosinski, S. C. Mettler, and A. M. Vengsarkar, "Long-period fibre grating fabrication with focused CO₂ laser pulses," *Electron. Lett.*, vol. 34, pp. 302-303, Feb. 5, 1998.
- [103] M. D. Feit and J. A. Fleck, "Light-propagation in graded-index optical fibers," *Appl. Opt.*, vol. 17, pp. 3990-3998, Dec. 15, 1978.
- [104] G. Sztefka and H. P. Nolting, "Bidirectional eigenmode propagation for large refractive index steps," *IEEE Photon. Tech. Lett.*, vol. 5, pp. 554-557, May 1993.
- [105] M. R. Hutsel, "Characterization of the stress and refractive-index distributions in optical fibers and fiber-based devices," Ph.D. thesis, School of Electrical and Computer Engineering, Georgia Institute of Technology, Atlanta, Georgia, 2011.
- [106] H. H. Hopkins, "On the diffraction theory of optical images," *Proc. R. Soc. A*, vol. 217, pp. 408-432, 1953.
- [107] L. Waller, "Phase imaging with partially coherent light," *Proc. SPIE*, vol. 8589, pp. 85890K-1--85890K-6, 2013.
- [108] J. C. Petrucci, L. Tian, and G. Barbastathis, "The transport of intensity equation for optical path length recovery using partially coherent illumination," *Opt. Express*, vol. 21, pp. 14430-14441, Jun. 17, 2013.
- [109] T. Erdogan, "Fiber grating spectra," *J. Lightwave Technol.*, vol. 15, pp. 1277-1294, Aug. 1997.
- [110] T. Erdogan, "Cladding-mode resonances in short- and long-period fiber grating filters," *J. Opt. Soc. Am. A*, vol. 14, pp. 1760-1773, Aug. 1997.
- [111] M. H. Jenkins, J. M. Long, and T. K. Gaylord, "Multifilter phase imaging with partially coherent light," *Appl. Opt.*, vol. 53, pp. D29-D39, Jun. 1, 2014.
- [112] M. H. Jenkins and T. K. Gaylord, "Systems and methods for quantitative phase imaging with partially coherent illumination," U. S. Provisional Patent Application no. 61/886,879, Oct. 3, 2014.
- [113] J. R. Fienup, "Reconstruction of an object from the modulus of its Fourier transform," *Opt. Lett.*, vol. 3, pp. 27-29, Jul. 1, 1978.
- [114] R. Bie, X.-H. Yuan, M. Zhao, and L. Zhang, "Method for estimating the axial intensity derivative in the TIE with higher order intensity derivatives and noise suppression," *Opt. Express*, vol. 20, pp. 8186-8191, Mar. 26, 2012.

- [115] M. Soto and E. Acosta, "Improved phase imaging from intensity measurements in multiple planes," *Appl. Opt.*, vol. 46, pp. 7978-7981, Nov. 20, 2007.
- [116] L. Waller, L. Tian, and G. Barbastathis, "Transport of intensity phase-amplitude imaging with higher order intensity derivatives," *Opt. Express*, vol. 18, pp. 12552-12560, Jun. 7, 2010.
- [117] J. Long, M. Jenkins, and T. K. Gaylord, "Comparison of transport-of-intensity derivative methods for optical fibers under partially coherent illumination," in *Frontiers in Optics*, 2013, p. FTh1F.3.
- [118] A. Pogany, D. Gao, and S. W. Wilkins, "Contrast and resolution in imaging with a microfocus x-ray source," *Rev. Sci. Instr.*, vol. 68, pp. 2774-2782, Apr. 21, 1997.
- [119] M. Langer, P. Cloetens, J. P. Guigay, S. Valton, and F. Peyrin, "Quantitative evaluation of phase retrieval algorithms in propagation based phase tomography," in *4th IEEE International Symposium on Biomedical Imaging: Macro to Nano*, Piscataway, NJ, 2007, pp. 552-525.
- [120] C. J. R. Sheppard, "Defocused transfer function for a partially coherent microscope and application to phase retrieval," *J. Opt. Soc. Am.*, vol. 21, pp. 828-831, May 1, 2004.
- [121] L. Tian and L. Waller, "Quantitative differential phase contrast imaging in an LED array microscope," *Opt. Express*, vol. 23, pp. 11394-11403, May 4, 2015.
- [122] A. M. Zysk, R. W. Schoonover, P. S. Carney, and M. A. Anastasio, "Transport of intensity and spectrum for partially coherent fields," *Opt. Lett.*, vol. 35, pp. 2239-2241, Jul. 1, 2010.
- [123] C. J. R. Sheppard, "Three-dimensional phase imaging with the intensity transport equation," *Appl. Opt.*, vol. 41, pp. 5951-5955, Oct. 1, 2002.
- [124] J. Martinez-Carranza, K. Falaggis, T. Kozacki, and M. Kujawinska, "Effect of imposed boundary conditions on the accuracy of transport of intensity equation based solvers," *Proc. SPIE*, vol. 8789, pp. 87890N-1--87890N-14, 2013.
- [125] V. V. Volkov, Y. Zhu, and M. De Graef, "A new symmetrized solution for phase retrieval using the transport of intensity equation," *Micron*, vol. 33, pp. 411-416, Feb. 2002.
- [126] C. Zuo, Q. Chen, H. Li, W. Qu, and A. Asundi, "Boundary-artifact-free phase retrieval with the transport of intensity equation II: applications to microlens characterization," *Opt. Express*, vol. 22, pp. 18310-18324, Jul. 28, 2014.
- [127] J. P. Guigay, "Fourier-transform analysis of Fresnel diffraction patterns and in-line holograms," *Optik*, vol. 49, pp. 121-125, 1977.

- [128] C. J. Bellair, C. L. Curl, B. E. Allman, P. J. Harris, A. Roberts, L. M. D. Delbridge, and K. A. Nugent, "Quantitative phase amplitude microscopy IV: imaging thick specimens," *J. Microsc.*, vol. 214, pp. 62-69, Apr. 1, 2004.
- [129] M. H. Jenkins and T. K. Gaylord, "Quantitative phase microscopy via optimized inversion of the phase optical transfer function," *Appl. Opt.*, (in press) 2015.
- [130] M. H. Jenkins and T. K. Gaylord, "Bright-field quantitative phase microscopy," U. S. Provisional Patent Application no. 62/174,948, Jun. 8, 2015.
- [131] J. Marrison, L. Raty, P. Marriott, and P. O'Toole, "Ptychography - a label free, high-contrast imaging technique for live cells using quantitative phase information," *Sci. Repts.*, vol. 3, pp. 1-7, Aug. 2013.
- [132] T. H. Nguyen, S. Sridharan, V. Macias, A. K. Balla, M. N. Do, and G. Popescu, "Prostate cancer diagnosis using quantitative phase imaging and machine learning algorithms," *Proc. SPIE*, vol. 9336, pp. 933619-1--933619-10, 2015.
- [133] S. Kosmeier, P. Langehanenberg, S. Przibilla, G. von Bally, and B. Kemper, "Multi-wavelength digital holographic microscopy for high resolution inspection of surfaces and imaging of phase specimen," *Proc. SPIE*, vol. 7718, pp. 77180T-1-77180T-7, 2010.
- [134] J. A. Rodrigo and T. Alieva, "Rapid quantitative phase imaging for partially coherent light microscopy," *Opt. Express*, vol. 22, pp. 13472-13483, Jun. 2, 2014.
- [135] G. Popescu, L. P. Deflores, J. C. Vaughan, K. Badizadegan, H. Iwai, R. R. Dasari, and M. S. Feld, "Fourier phase microscopy for investigation of biological structures and dynamics," *Opt. Lett.*, vol. 29, pp. 2503-2505, Nov. 11, 2004.
- [136] B. Bhaduri, K. Tangella, and G. Popescu, "Fourier phase microscopy with white light," *Biomed. Opt. Express*, vol. 4, pp. 1434-1441, Aug. 1, 2013.
- [137] B. Kemper, D. Carl, A. Hoink, G. von Bally, I. Bredebusch, and J. Schnekenburger, "Modular digital holographic microscopy system for marker free quantitative phase contrast imaging of living cells - art. no. 61910T," *Proc. SPIE*, vol. 6191, pp. 61910T-1-61910T-8, 2006.
- [138] N. T. Shaked, "Quantitative phase microscopy of biological samples using a portable interferometer," *Opt. Lett.*, vol. 37, pp. 2016-2018, Jun. 1, 2012.
- [139] T. Yamauchi, H. Iwai, and Y. Yamashita, "Label-free imaging of intracellular motility by low-coherent quantitative phase microscopy," *Opt. Express*, vol. 19, pp. 5536-5550, Mar. 14, 2011.
- [140] K. Kim, Z. Yaqoob, K. Lee, J. W. Kang, Y. Choi, P. Hosseini, P. T. C. So, and Y. Park, "Diffraction optical tomography using a quantitative phase imaging unit," *Opt. Lett.*, vol. 39, pp. 6935-6938, Dec. 15, 2014.

- [141] K. Lee and Y. Park, "Quantitative phase imaging unit," *Opt. Lett.*, vol. 39, pp. 3630-3633, Jun. 15, 2014.
- [142] M. Mir, S. D. Babacan, M. Bednarz, M. N. Do, I. Golding, and G. Popescu, "Visualizing escherichia coli sub-cellular structure using sparse deconvolution spatial light interference tomography," *PLoS One*, vol. 7, p. e39816, Jun. 28, 2012.
- [143] S. Monneret, P. Bon, G. Baffou, P. Berto, J. Savatier, S. Aknoun, and H. Rigneault, "Quadriwave lateral shearing interferometry as a quantification tool for microscopy. Application to dry mass determination of living cells, temperature mapping, and vibrational phase imaging," *Proc. SPIE*, vol. 8792, pp. 879209-1--879209-11, May 23, 2013.
- [144] H. Ding, F. Nguyen, S. A. Boppart, and G. Popescu, "Optical properties of tissues quantified by Fourier-transform light scattering," *Opt. Lett.*, vol. 34, pp. 1372-1374, May 1, 2009.
- [145] H. F. Ding, L. J. Millet, M. U. Gillette, and G. Popescu, "Actin-driven cell dynamics probed by Fourier transform light scattering," *Biomed. Opt. Express*, vol. 1, pp. 260-267, Aug. 2, 2010.
- [146] B. Kemper, A. Bauwens, A. Vollmer, S. Ketelhut, P. Langehanenberg, J. Muthing, H. Karch, and G. von Bally, "Label-free quantitative cell division monitoring of endothelial cells by digital holographic microscopy," *J. Biomed. Opt.*, vol. 15, pp. 036009-1--036009-6, May/June 2010.
- [147] B. Kemper, P. Langehanenberg, I. Bredebusch, J. Schnekenburger, and G. von Bally, "Techniques and applications of digital holographic microscopy for life cell imaging" *Proc. SPIE*, vol. 6633, pp. 66330D-1--66330D-9, 2007.
- [148] B. Kemper, J. Wibbeling, L. Kastl, J. Schnekenburger, and S. Ketelhut, "Multimodal label-free growth and morphology characterization of different cell types in a single culture with quantitative digital holographic phase microscopy," *Proc. SPIE*, vol. 9336, pp. 933617-1--933617-6, 2015.
- [149] T. Kim, S. C. Liu, R. Iyer, M. U. Gillette, and G. Popescu, "3D quantitative phase imaging of neural networks using WDT," *Proc. SPIE*, vol. 9336, pp. 93361V-1--93361V-5, 2015.
- [150] J. Klossa, B. Wattelier, T. Happillon, D. Toubas, L. de Laulanie, V. Untereiner, P. Bon, and M. Manfait, "Quantitative phase imaging and Raman micro-spectroscopy applied to malaria," *Diagn. Pathol.*, vol. 8, pp. S42-1--S42-4, 2013.
- [151] Y. Park, M. Diez-Silva, G. Popescu, G. Lykotrafitis, W. Choi, M. S. Feld, and S. Suresh, "Refractive index maps and membrane dynamics of human red blood cells parasitized by plasmodium falciparum," *Proc. Nat. Acad. Sci.*, vol. 105, pp. 13730-13735, Sep. 16, 2008.

- [152] H. V. Pham, B. Bhaduri, K. Tangella, C. Best-Popescu, and G. Popescu, "Real time blood testing using quantitative phase imaging," *PLoS One*, vol. 8, p. e55676, Feb. 2013.
- [153] G. Popescu, Y. Park, R. R. Dasari, K. Badizadegan, and M. S. Feld, "Coherence properties of red blood cell membrane motions," *Phys. Rev. E*, vol. 76, pp. 031902-1--031902-5, 2007.
- [154] S. Przibilla, S. Dartmann, A. Vollmer, S. Ketelhut, B. Greve, G. von Bally, and B. Kemper, "Sensing dynamic cytoplasm refractive index changes of adherent cells with quantitative phase microscopy using incorporated microspheres as optical probes," *J. Biomed. Opt.*, vol. 17, pp. 097001-1--097001-9, Sep. 2012.
- [155] C. E. Rommel, C. Dierker, L. Schmidt, S. Przibilla, G. von Bally, B. Kemper, and J. Schnekenburger, "Contrast-enhanced digital holographic imaging of cellular structures by manipulating the intracellular refractive index," *J. Biomed. Opt.*, vol. 15, pp. 041509-1--041509-10, Jul./Aug. 2010.
- [156] Y. Park, G. Popescu, K. Badizadegan, R. R. Dasari, and M. S. Feld, "Diffraction phase and fluorescence microscopy," *Opt. Express*, vol. 14, pp. 8263-8268, Sep. 4, 2006.
- [157] L. J. Allen, W. McBride, N. L. O'Leary, and M. P. Oxley, "Investigation of the effects of partial coherence on exit wave reconstruction," *J. Microsc.*, vol. 216, pp. 70-75, Oct. 2004.
- [158] K. Falaggis, "Single beam phase retrieval techniques for partial coherent illumination," in *Latin Am. Opt. Photon. Conf.*, Cancun, 2014, p. LTh2D.4.
- [159] I. L. Ho, M.-Y. Ng, K.-C. Chen, W.-Y. Li, and Y.-C. Chang, "Iterative phase retrieval with partially coherent beams," *J. Opt.*, vol. 15, p. 075712, 2013.
- [160] Z. Jingshan, L. Tian, J. Dauwels, and L. Waller, "Partially coherent phase imaging with simultaneous source recovery," *Biomed. Opt. Express*, vol. 6, pp. 257-265, Jan. 1, 2015.
- [161] P. Kner, "Phase diversity for three-dimensional imaging," *J. Opt. Soc. Am.*, vol. 30, pp. 1980-1987, Oct. 1, 2013.
- [162] J. A. Rodrigo, T. Alieva, G. Cristóbal, and M. L. Calvo, "Wavefield imaging via iterative retrieval based on phase modulation diversity," *Opt. Express*, vol. 19, pp. 18621-18635, Sep. 12, 2011.
- [163] R. Claus, Y.-G. Wang, M. Benk, K. A. Goldberg, P. Naulleau, A. Neureuther, and L. Waller, "Partially coherent quantitative phase retrieval for EUV lithography," in *Imaging Systems and Applications*, 2015, p. ITh2A.4.

- [164] J. Frank, J. Matrisch, J. Horstmann, S. Altmeyer, and G. Wernicke, "Refractive index determination of transparent samples by noniterative phase retrieval," *Appl. Opt.*, vol. 50, pp. 427-433, Feb. 1, 2011.
- [165] E. J. Candès, T. Strohmer, and V. Voroninski, "Phaselift: Exact and stable signal recovery from magnitude measurements via convex programming," *Commun. Pure Appl. Math.*, vol. 66, pp. 1241-1274, 2013.
- [166] D. Paganin and K. A. Nugent, "Noninterferometric phase imaging with partially coherent light," *Phys. Rev. Lett.*, vol. 80, pp. 2586-2589, Mar. 23, 1998.
- [167] A. Shanker, L. Tian, M. Sczyrba, B. Connolly, A. Neureuther, and L. Waller, "Transport of intensity phase imaging in the presence of curl effects induced by strongly absorbing photomasks," *Appl. Opt.*, vol. 53, pp. J1-J6, Dec. 1, 2014.
- [168] C. Edwards, B. Bhaduri, T. Nguyen, B. G. Griffin, H. Pham, T. Kim, G. Popescu, and L. L. Goddard, "Effects of spatial coherence in diffraction phase microscopy," *Opt. Express*, vol. 22, pp. 5133-5146, Mar. 10, 2014.
- [169] T. Kim, C. Edwards, L. L. Goddard, and G. Popescu, "Quantitative phase imaging with programmable illumination," *Proc. SPIE*, vol. 9336, pp. 93361F-1--93361F-8, 2015.
- [170] T. H. Nguyen, H. Majeed, C. A. Edwards, M. N. Do, L. L. Goddard, and G. Popescu, "Halo-free quantitative phase imaging with partially coherent light," *Proc. SPIE*, vol. 9336, pp. 93360N-1--93360N-5, 2015.
- [171] Z. Jingshan, R. A. Claus, J. Dauwels, L. Tian, and L. Waller, "Transport of intensity phase imaging by intensity spectrum fitting of exponentially spaced defocus planes," *Opt. Express*, vol. 22, pp. 10661-10674, May 5, 2014.
- [172] J. Martinez-Carranza, K. Falaggis, and T. Kozacki, "Optimum measurement criteria for the axial derivative intensity used in transport of intensity-equation-based solvers," *Opt. Lett.*, vol. 39, pp. 182-185, Jan. 15, 2014.
- [173] B. Xue, S. Zheng, L. Cui, X. Bai, and F. Zhou, "Transport of intensity phase imaging from multiple intensities measured in unequally-spaced planes," *Opt. Express*, vol. 19, pp. 20244-20250, Oct. 10, 2011.
- [174] K. Falaggis, T. Kozacki, and M. Kujawinska, "Optimum plane selection criteria for single-beam phase retrieval techniques based on the contrast transfer function," *Opt. Lett.*, vol. 39, pp. 30-33, Jan. 1, 2014.
- [175] J. M. Cowley, *Diffraction Physics*: Elsevier, 1995.
- [176] W. O. Saxton, "What is the focus variation method? Is it new? Is it direct?," *Ultramicroscopy*, vol. 55, pp. 171-181, Apr. 1994.

- [177] P. Schiske, "Phase determination from a focal series and corresponding diffraction pattern in electron-microscopy for strongly scattering objects," *J. Phys. D*, vol. 8, pp. 1372-1386, Feb. 20, 1975.
- [178] C. J. R. Sheppard and X. Q. Mao, "Three-dimensional imaging in a microscope," *J. Opt. Soc. Am.*, vol. 6, pp. 1260-1269, Sep. 1989.
- [179] M. Jenkins and T. K. Gaylord, "Bright-field quantitative phase microscopy (BFQPM) for accurate phase imaging using conventional microscopy hardware," *Proc. SPIE*, vol. 9336, pp. 933616-1--933616-7, 2015.
- [180] M. Born and E. Wolf, *Principles of Optics: Electromagnetic Theory of Propagation, Interference and Diffraction of Light*: Cambridge University Press, 1999.
- [181] S. B. Mehta and C. J. R. Sheppard, "Partially coherent image formation in differential interference contrast (DIC) microscope," *Opt. Express*, vol. 16, pp. 19462-19479, Nov. 24, 2008.
- [182] C. J. Cogswell, N. I. Smith, K. G. Larkin, and P. Hariharan, "Quantitative DIC microscopy using a geometric phase shifter," *Proc. SPIE*, vol. 2984, pp. 72-81, 1997.
- [183] S. B. Mehta and C. J. Sheppard, "Linear phase-gradient imaging with Asymmetric Illumination based Differential Phase Contrast (AIDPC)," in *Advances in Imaging*, Vancouver, 2009, p. NTuA5.
- [184] J. W. Goodman, *Introduction to Fourier Optics*: Roberts and Company Publishers, 2005.
- [185] C. Mack, *Fundamental Principles of Optical Lithography: the Science of Microfabrication*: John Wiley & Sons, 2008.
- [186] X. Wu, S. Liu, W. Liu, T. Zhou, and L. Wang, "Comparison of three TCC calculation algorithms for partially coherent imaging simulation," *Proc. SPIE*, vol. 7544, pp. 75440Z-1--75440Z-10, 2010.
- [187] P. A. Gorry, "General least-squares smoothing and differentiation of nonuniformly spaced data by the convolution method," *Anal. Chem.*, vol. 63, pp. 534-536, Mar. 1, 1991.
- [188] A. Buades, B. Coll, and J. M. Morel, "A non-local algorithm for image denoising," in *Computer Vision and Pattern Recognition*, vol. 2, 2005, pp. 60-65.
- [189] L. Zhao, C. Kroenke, J. Song, D. Piwnica-Worms, J. Ackerman, and J. Neil, "Intracellular water specific MR of microbead-adherent cells: the HeLa cell intracellular water exchange lifetime," *NMR Biomed.*, vol. 21, pp. 79-84, Nov. 29, 2008.

- [190] A. Fujioka, K. Terai, R. E. Itoh, K. Aoki, T. Nakamura, S. Kuroda, E. Nishida, and M. Matsuda, "Dynamics of the Ras/ERK MAPK cascade as monitored by fluorescent probes," *J. Biol. Chem.*, vol. 281, pp. 8917-8926, Mar. 31, 2006.
- [191] A. Kus, M. Dudek, B. Kemper, M. Kujawinska, and A. Vollmer, "Tomographic phase microscopy of living three-dimensional cell cultures," *J. Biomed. Opt.*, vol. 19, pp. 046009-1--046009-7, Apr. 2014.
- [192] I. H. Malitson, "Interspecimen comparison of the refractive index of fused silica," *J. Opt. Soc. Am.*, vol. 55, pp. 1205-1208, Oct. 1, 1965.
- [193] M. H. Jenkins and T. K. Gaylord, "Three-dimensional quantitative phase imaging via tomographic deconvolution phase microscopy (TDPM)," *Appl. Opt.*, (under review) 2015.
- [194] M. H. Jenkins and T. K. Gaylord, "Tomographic deconvolution quantitative phase microscopy system," U. S. Patent Georgia Tech Record of Invention No. 7076, Sep. 7, 2015.
- [195] R. Zhou, C. Edwards, G. Popescu, and L. Goddard, "Semiconductor defect metrology using laser-based quantitative phase imaging," *Proc. SPIE*, vol. 9336, pp. 93361I-1--93361I-6, 2015.
- [196] K. Lee, K. Kim, J. Jung, J. Heo, S. Cho, S. Lee, G. Chang, Y. Jo, H. Park, and Y. Park, "Quantitative phase imaging techniques for the study of cell pathophysiology: from principles to applications," *Sensors*, vol. 13, pp. 4170-4191, Mar. 28, 2013.
- [197] R. Barer, "Interference microscopy and mass determination," *Nature*, vol. 169, pp. 366-367, Mar. 1, 1952.
- [198] R. Chandramohanadas, Y. Park, L. Lui, A. Li, D. Quinn, K. Liew, M. Diez-Silva, Y. Sung, M. Dao, and C. T. Lim, "Biophysics of malarial parasite exit from infected erythrocytes," *PLoS One*, vol. 6, p. e20869, Jun. 2011.
- [199] T. Noda, S. Kawata, and S. Minami, "3-dimensional phase-contrast imaging by an annular illumination microscope," *Appl. Opt.*, vol. 29, pp. 3810-3815, Sep. 10, 1990.
- [200] M. A. Fiddy, "Inversion of optical scattered field data," *J. Phys. D*, vol. 19, pp. 301-317, Aug. 30, 1986.
- [201] F. Charrière, N. Pavillon, T. Colomb, C. Depeursinge, T. J. Heger, E. A. Mitchell, P. Marquet, and B. Rappaz, "Living specimen tomography by digital holographic microscopy: morphometry of testate amoeba," *Opt. Express*, vol. 14, pp. 7005-7013, Aug. 7, 2006.

- [202] M. Habaza, B. Gilboa, Y. Roichman, and N. T. Shaked, "Tomographic phase microscopy with 180 degrees rotation of live cells in suspension by holographic optical tweezers," *Opt. Lett.*, vol. 40, pp. 1881-1884, Apr. 15, 2015.
- [203] D. A. Agard, "Optical sectioning microscopy - Cellular architecture in 3 dimensions," *Ann. Rev. Biophys. Bioengr.*, vol. 13, pp. 191-219, 1984.
- [204] W. Wallace, L. H. Schaefer, and J. R. Swedlow, "A workingperson's guide to deconvolution in light microscopy," *Biotechniques*, vol. 31, pp. 1076-1097, Nov. 2001.
- [205] J. Bradl, M. Hausmann, V. Ehemann, D. Komitowski, and C. Cremer, "A tilting device for three-dimensional microscopy: Application to in situ imaging of interphase cell nuclei," *J. Microsc.*, vol. 168, pp. 47-57, Oct. 1992.
- [206] C. J. Cogswell, K. G. Larkin, and H. U. Klemm, "Fluorescence microtomography: Multi-angle image acquisition and 3D digital reconstruction," *Proc. SPIE*, vol. 2655, pp. 109-115, 1996.
- [207] R. Heintzmann and C. Cremer, "Axial tomographic confocal fluorescence microscopy," *J. Microsc.*, vol. 206, pp. 7-23, Apr. 2002.
- [208] P. J. Shaw, D. A. Agard, Y. Hiraoka, and J. W. Sedat, "Tilted view reconstruction in optical microscopy – 3-dimensional reconstruction of drosophila-melanogaster embryo nuclei," *Biophys. J.*, vol. 55, pp. 101-110, Jan. 1989.
- [209] F. Staier, H. Eipel, P. Matula, A. V. Evsikov, M. Kozubek, C. Cremer, and M. Hausmann, "Micro axial tomography: A miniaturized, versatile stage device to overcome resolution anisotropy in fluorescence light microscopy," *Rev. Sci. Instr.*, vol. 82, pp. 093701-1--093701-8, 2011.
- [210] W. Singer, M. Totzeck, and H. Gross, *Handbook of Optical Systems, Physical Image Formation* vol. 2. Weinheim: Wiley VCH, 2005.
- [211] M. Keuper, T. Schmidt, M. Temerinac-Ott, J. Padeken, P. Heun, O. Ronneberger, and T. Brox, "Blind deconvolution of widefield fluorescence microscopic data by regularization of the Optical Transfer Function (OTF)," in *Computer Vision and Pattern Recognition*, 2013, pp. 2179-2186.
- [212] L. Turner, B. Dhal, J. Hayes, A. Mancuso, K. Nugent, D. Paterson, R. Scholten, C. Tran, and A. Peele, "X-ray phase imaging: Demonstration of extended conditions for homogeneous objects," *Opt. Express*, vol. 12, pp. 2960-2965, Jun. 28, 2004.
- [213] A. T. Vouldis, C. N. Kechribaris, T. A. Maniatis, K. S. Nikita, and N. K. Uzunoglu, "Investigating the enhancement of three-dimensional diffraction tomography by using multiple illumination planes," *J. Opt. Soc. Am.*, vol. 22, pp. 1251-1262, Jul. 1, 2005.

- [214] P. Bon, B. Wattellier, and S. Monneret, "Modeling quantitative phase image formation under tilted illuminations," *Opt. Lett.*, vol. 37, pp. 1718-1720, May 15, 2012.
- [215] C. A. Balanis, *Advanced Engineering Electromagnetics*: Wiley Online Library, 2012.
- [216] L. Cherkezyan, H. Subramanian, V. Stoyneva, J. D. Rogers, S. Yang, D. Damania, A. Taflove, and V. Backman, "Targeted alteration of real and imaginary refractive index of biological cells by histological staining," *Opt. Lett.*, vol. 37, pp. 1601-1603, May 15, 2012.
- [217] K. Morishita and A. Kaino, "Adjusting resonance wavelengths of long-period fiber gratings by the glass-structure change," *Appl. Opt.*, vol. 44, pp. 5018-5023, Aug. 20, 2005.
- [218] K. Kim, K. S. Kim, H. Park, J. C. Ye, and Y. Park, "Real-time visualization of 3-D dynamic microscopic objects using optical diffraction tomography," *Opt. Express*, vol. 21, pp. 32269-32278, Dec. 30, 2013.
- [219] T. Feng, M. H. Jenkins, F. Yan, and T. K. Gaylord, "Joint Residual Stress/Refractive Index Characterization of Large-Mode-Area Erbium-Doped Fibers," *J. Lightwave Technol.*, vol. 31, pp. 2426-2433, Jul. 15, 2013.
- [220] T. Feng, F. Yan, Q. Li, W. Peng, S. Tan, S. Feng, P. Liu, and X. Wen, "A stable wavelength-tunable single frequency and single polarization linear cavity erbium-doped fiber laser," *Laser Phys.*, vol. 23, pp. 025101-1--025101-7, Dec. 14, 2013.
- [221] X. He, X. Fang, C. Liao, D. Wang, and J. Sun, "A tunable and switchable single-longitudinal-mode dual-wavelength fiber laser with a simple linear cavity," *Opt. Express*, vol. 17, pp. 21773-21781, Nov. 12, 2009.
- [222] X. He, D. Wang, and C. Liao, "Tunable and switchable dual-wavelength single-longitudinal-mode erbium-doped fiber lasers," *J. Lightwave Technol.*, vol. 29, pp. 842-849, Mar. 15, 2011.
- [223] S. K. Kim, G. Stewart, W. Johnstone, and B. Culshaw, "Mode-hop-free single-longitudinal-mode erbium-doped fiber laser frequency scanned with a fiber ring resonator," *Appl. Opt.*, vol. 38, pp. 5154-5157, Aug. 20, 1999.
- [224] M. Li, J. Ma, X. Zhang, Y. Song, and W. Du, "Investigation of black box model for erbium-doped fiber amplifiers in space radiation environment," *J. Lightwave Technol.*, vol. 30, pp. 3667-3671, Dec. 1, 2012.
- [225] Q. Li, F. Yan, W. Peng, T. Feng, S. Feng, S. Tan, P. Liu, and W. Ren, "DFB laser based on single mode large effective area heavy concentration EDF," *Opt. Express*, vol. 20, pp. 23684-23689, Oct. 8, 2012.

- [226] S. K. Varshney, K. Saitoh, M. Koshiba, B. P. Pal, and R. K. Sinha, "Design of s-band erbium-doped concentric dual-core photonic crystal fiber amplifiers with ASE suppression," *J. Lightwave Technol.*, vol. 27, pp. 1725-1733, Jun. 1, 2009.
- [227] J. Zhang and J. W. Lit, "Erbium-doped fiber compound-ring laser with a ring filter," *IEEE Photon. Tech. Lett.*, vol. 6, pp. 588-590, May 1994.
- [228] J. Zhou, J. Chen, X. Li, G. Wu, Y. Wang, and W. Jiang, "Robust, compact, and flexible neural model for a fiber Raman amplifier," *J. Lightwave Technol.*, vol. 24, pp. 2362-2367, Jun. 2006.
- [229] Z. Meng, G. Stewart, and G. Whitenett, "Stable single-mode operation of a narrow-linewidth, linearly polarized, erbium-fiber ring laser using a saturable absorber," *J. Lightwave Technol.*, vol. 24, pp. 2179-2183, May 2006.
- [230] T. Feng, F.-P. Yan, Q. Li, W.-J. Peng, S.-C. Feng, S.-Y. Tan, and X.-D. Wen, "Stable single longitudinal mode erbium-doped silica fiber laser based on an asymmetric linear three-cavity structure," *Chin. Phys. B*, vol. 22, pp. 014208-1--014208-5, Jun./Jul. 2013.
- [231] T. Feng, F.-P. Yan, Q. Li, W.-J. Peng, S.-C. Feng, X.-D. Wen, P. Liu, and S.-Y. Tan, "Stable and high OSNR compound linear-cavity single-longitudinal-mode erbium-doped silica fiber laser based on an asymmetric four-cavity structure," *Chin. Phys. Lett.*, vol. 29, pp. 104205-1--104205-4, Jun./Jul. 2012.
- [232] H. Huang, R. M. Miura, and J. J. Wylie, "Optical fiber drawing and dopant transport," *SIAM J. Appl. Math.*, vol. 69, pp. 330-347, Oct. 29, 2008.
- [233] Y. Yan and R. Pitchumani, "Numerical study on the dopant concentration and refractive index profile evolution in an optical fiber manufacturing process," *Int. J. Heat Mass. Tran.*, vol. 49, pp. 2097-2112, Mar. 23, 2006.
- [234] P. K. Bachmann, W. Hermann, H. Wehr, and D. U. Wiechert, "Stress in optical waveguides. 1: Preforms," *Appl. Opt.*, vol. 25, pp. 1093-1098, Apr. 1, 1986.
- [235] P. K. Bachmann, W. Hermann, H. Wehr, and D. U. Wiechert, "Stress in optical waveguides. 2: Fibers," *Appl. Opt.*, vol. 26, pp. 1175-1182, Apr. 1, 1987.
- [236] Y. Park, U.-C. Paek, S. Han, B.-H. Kim, C.-S. Kim, and D. Y. Kim, "Inelastic frozen-in stress in optical fibers," *Opt. Commun.*, vol. 242, pp. 431-436, Dec. 8, 2004.
- [237] D. J. Wissuchek, C. W. Ponader, and J. J. Price, "Analysis of residual stress in optical fiber," in *Photonics East*, 1999, pp. 34-43.
- [238] M. R. Hutsel, R. Ingle, and T. K. Gaylord, "Accurate cross-sectional stress profiling of optical fibers," *Appl. Opt.*, vol. 48, pp. 4985-4995, Sep. 10, 2009.

- [239] I. H. Shin, B. H. Kim, S. P. Veetil, W.-T. Han, and D. Y. Kim, "Residual stress relaxation in cleaved fibers," *Opt. Commun.*, vol. 281, pp. 75-79, Jan. 1, 2008.
- [240] B. Wang and E. Mies, "Advanced topics on fusion splicing of specialty fibers and devices," in *Asia-Pacific Optical Communications*, 2007, pp. 678130-1--678130-14.
- [241] M. Ikeda, M. Tateda, and H. Yoshikiyo, "Refractive index profile of a graded index fiber: measurement by a reflection method," *Appl. Opt.*, vol. 14, pp. 814-815, Apr. 1975.
- [242] P. L. Chu and T. Whitbread, "Measurement of stresses in optical fiber and preform," *Appl. Opt.*, vol. 21, pp. 4241-4245, Dec. 1, 1982.
- [243] C. C. Montarou, T. K. Gaylord, and A. I. Dachevski, "Residual stress profiles in optical fibers determined by the two-waveplate-compensator method," *Opt. Commun.*, vol. 265, pp. 29-32, Mar. 2006.
- [244] Y. Park, T.-J. Ahn, Y. H. Kim, W.-T. Han, U.-C. Paek, and D. Y. Kim, "Measurement method for profiling the residual stress and the strain-optic coefficient of an optical fiber," *Appl. Opt.*, vol. 41, pp. 21-26, Jan. 1, 2002.
- [245] K. W. Raine, R. Feced, S. E. Kanellopoulos, and V. A. Handerek, "Measurement of axial stress at high spatial resolution in ultraviolet-exposed fibers," *Appl. Opt.*, vol. 38, pp. 1086-1095, Mar. 1, 1999.
- [246] M. R. Hutzel, R. R. Ingle, and T. K. Gaylord, "Technique and apparatus for accurate cross-sectional stress profiling of optical fibers," *IEEE Trans. Instrum. Meas.*, vol. 60, pp. 971-979, Mar. 2011.
- [247] J. Peng, L. Liu, H. Wei, J. Sun, Z. Kang, and S. Jian, "Theoretical analysis and experiment on a novel kind of single mode large-mode-area erbium-doped fiber," *Mod. Phys. Lett. B*, vol. 25, pp. 1193-1202, Jan. 2011.
- [248] J. J. Koponen, L. Petit, T. Kokki, V. Aallos, J. Paul, and H. Ihalainen, "Progress in direct nanoparticle deposition for the development of the next generation fiber lasers," *Opt. Eng.*, vol. 50, pp. 111605-1--111605-11, Nov. 2011.
- [249] J. Knight, T. Birks, P. S. J. Russell, and D. Atkin, "All-silica single-mode optical fiber with photonic crystal cladding," *Opt. Lett.*, vol. 21, pp. 1547-1549, Oct. 1, 1996.
- [250] B. Kim, Y. Park, D. Kim, U. Paek, and W.-T. Han, "Observation and analysis of residual stress development resulting from OH impurity in optical fibers," *Opt. Lett.*, vol. 27, pp. 806-808, May 15, 2002.

- [251] I. H. Shin, S. Ju, S. P. Veetil, W.-T. Han, and D. Y. Kim, "Simple model for frozen-in viscoelastic stress in optical fibers," *Opt. Commun.*, vol. 281, pp. 2504-2508, May 1, 2008.
- [252] W. Primak and D. Post, "Photoelastic constants of vitreous silica and its elastic coefficient of refractive index," *J. Appl. Phys.*, vol. 30, pp. 779-788, May 1959.
- [253] G. W. Scherer, "Stress-induced index profile distortion in optical waveguides," *Appl. Opt.*, vol. 19, pp. 2000-2006, Jun. 15, 1980.
- [254] P. L. Chu and T. Whitbread, "Stress transformation due to fusion splicing in optical fibre," *Electron. Lett.*, vol. 20, pp. 599-600, Jul. 5, 1984.
- [255] J. Yamauchi, Y. Akimoto, M. Nibe, and H. Nakano, "Wide-angle propagating beam analysis for circularly symmetric waveguides: comparison between FD-BPM and FD-TDM," *IEEE Photon. Tech. Lett.*, vol. 8, pp. 236-238, Feb. 1996.
- [256] T. Feng, M. H. Jenkins, F. Yan, and T. K. Gaylord, "Arc fusion splicing effects in large-mode-area single-mode ytterbium-doped fibers," *Appl. Opt.*, vol. 52, pp. 7706-7711, Nov. 10, 2013.
- [257] D. Richardson, J. Nilsson, and W. Clarkson, "High power fiber lasers: current status and future perspectives [Invited]," *J. Opt. Soc. Am. B*, vol. 27, pp. B63-B92, Nov. 2010.
- [258] N. Shahabuddin, M. Ismail, M. C. Paul, S. Damanhuri, S. Harun, H. Ahmad, M. Pal, and S. K. Bhadra, "Multi-wavelength ytterbium doped fiber laser based on longitudinal mode interference," *Laser Phys.*, vol. 22, pp. 252-255, Nov. 28, 2012.
- [259] F. Yin, S. Yang, H. Chen, M. Chen, and S. Xie, "Tunable single-longitudinal-mode ytterbium all fiber laser with saturable-absorber-based auto-tracking filter," *Opt. Commun.*, vol. 285, pp. 2702-2706, May 15, 2012.
- [260] Y. Zhou, P. Chui, and K. K. Wong, "Multiwavelength single-longitudinal-mode ytterbium-doped fiber laser," *IEEE Photon. Tech. Lett.*, vol. 25, pp. 385-388, Feb. 15, 2013.
- [261] S. Yin, P. Yan, and M. Gong, "Influence of fusion splice on high power ytterbium-doped fiber laser with master oscillator multi-stage power amplifiers structure," *Opt. Laser Eng.*, vol. 49, pp. 1054-1059, Apr. 20, 2011.
- [262] P. Yan, J. Hao, Q. Xiao, Y. Wang, and M. Gong, "The influence of fusion splicing on the beam quality of a ytterbium-doped fiber laser," *Laser Phys.*, vol. 23, pp. 045109-1--045109-9, Mar. 12, 2013.

- [263] S. S. Kou and C. J. R. Sheppard, "Comparison of three dimensional transfer function analysis of alternative phase imaging methods," *Proc. SPIE*, vol. 6443, pp. 64430Q-1--64430Q-6, 2007.
- [264] J. D. Ingle and S. R. Crouch, *Spectrochemical Analysis*: Prentice Hall, 1988.
- [265] C. Zuo, Q. Chen, L. Huang, and A. Asundi, "Phase discrepancy analysis and compensation for fast Fourier transform based solution of the transport of intensity equation," *Opt. Express*, vol. 22, pp. 17172-17186, Jul. 14, 2014.
- [266] A. Burvall, U. Lundström, P. A. C. Takman, D. H. Larsson, and H. M. Hertz, "Phase retrieval in X-ray phase-contrast imaging suitable for tomography," *Opt. Express*, vol. 19, pp. 10359-10376, May 23, 2011.
- [267] S. Bajt, A. Barty, K. A. Nugent, M. McCartney, M. Wall, and D. Paganin, "Quantitative phase-sensitive imaging in a transmission electron microscope," *Ultramicroscopy*, vol. 83, pp. 67-73, May 2000.
- [268] L. J. Allen and M. P. Oxley, "Phase retrieval from series of images obtained by defocus variation," *Opt. Commun.*, vol. 199, pp. 65-75, Nov. 2001.
- [269] K. A. Nugent and D. Paganin, "Matter-wave phase measurement: A noninterferometric approach," *Phys. Rev. A*, vol. 61, pp. 063614-1--063614-9, May 17, 2000.
- [270] T. K. Gaylord and M. H. Jenkins, "Single-shot parallel-defocus quantitative phase imaging system," U. S. Provisional Patent Application no. 62/065,394, Oct. 2, 2014.
- [271] S. B. Mehta and C. J. Sheppard, "Sample-less calibration of the differential interference contrast microscope," *Appl. Opt.*, vol. 49, pp. 2954-2968, May 20, 2010.
- [272] C. Preza, "Rotational-diversity phase estimation from differential-interference-contrast microscopy images," *J. Opt. Soc. Am. A*, vol. 17, pp. 415-424, Mar. 2000.
- [273] S. Zabler, P. Cloetens, J.-P. Guigay, J. Baruchel, and M. Schlenker, "Optimization of phase contrast imaging using hard x rays," *Rev. Sci. Instr.*, vol. 76, pp. 073705-1--073705-7, Jun. 29, 2005.
- [274] L. Tian, J. C. Petrucci, Q. Miao, H. Kudrolli, V. Nagarkar, and G. Barbastathis, "Compressive x-ray phase tomography based on the transport of intensity equation," *Opt. Lett.*, vol. 38, pp. 3418-3421, Sep. 1, 2013.
- [275] Y.-J. He, "Long-period fiber grating using the finite element method and eigenmode expansion method," *Sensor. Actuat. B-Chem.*, vol. 183, pp. 319-331, Apr. 13, 2013.

VITA



Micah H. Jenkins was born in 1987 in Columbia, South Carolina. Prior to attending the Georgia Institute of Technology, he received his Bachelor of Science in Electrical Engineering from Brigham Young University in 2011. During his time at Brigham Young, Micah served for two years as a volunteer representative for the Church of Jesus Christ of Latter-day Saints in India. While at Georgia Tech, Micah was a recipient of a National Science Foundation Graduate Research Fellowship. He is a member of the Optical Society of America and the International Society for Optical Engineering.